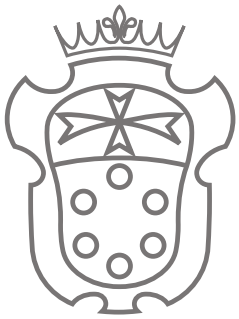

SCUOLA
NORMALE
SUPERIORE

CLASSE DI SCIENZE MATEMATICHE E NATURALI

Corso di Perfezionamento in NANOSCIENZE

THERMAL TRANSPORT IN STATIC AND DRIVEN NANOSCALE QUANTUM SYSTEMS

TESI DI PERFEZIONAMENTO

Candidato

BIBEK BHANDARI

Relatori

PROF. ROSARIO FAZIO

DR. FABIO TADDEI

Anno Accademico 2019/2020

PUBLICATIONS

Bibek Bhandari, Giuliano Chiriaco, Paolo Andrea Erdman, Rosario Fazio and Fabio Taddei, *Thermal drag in electronic conductors*, Phys. Rev. B, 98, 035415 (2018)

Paolo Andrea Erdman, Bibek Bhandari, Rosario Fazio, Jukka Pekola and Fabio Taddei, *Absorption refrigerators based on Coulomb-coupled single-electron systems*, Phys. Rev. B, 98, 045433 (2018)

Paolo A Erdman, Joonas T Peltonen, Bibek Bhandari, Bivas Dutta, Herve Courtois, Rosario Fazio, Fabio Taddei, Jukka P Pekola, *Nonlinear thermovoltage in a single-electron transistor*, Phys. Rev. B, 99, 165405 (2019)

Olivier Maillet, Paolo A Erdman, Vasco Cavina, Bibek Bhandari, Elsa T Mannila, Joonas T Peltonen, Andrea Mari, Fabio Taddei, Christopher Jarzynski, Vittorio Giovannetti, Jukka P Pekola, *Optimal probabilistic work extraction beyond the free energy difference with a single-electron device*, Phys. Rev. Lett, 122, 150604, (2019).

Bibek Bhandari, Pablo Terren Alonso, Fabio Taddei, Liliana Arrachea, Felix Von Oppen and Rosario Fazio, *Geometric properties of adiabatic quantum thermal machines*, Phys. Rev. B, 102, 155407 (2020).

Michele Governale, Bibek Bhandari, Fabio Taddei, Ken-Ichiro Umura and Uli Zülicke, *Finite-size effects in cylindrical topological insulators*, New Journal of Physics, 22, 063042 (2020).

Bibek Bhandari, Rosario Fazio, Fabio Taddei and Liliana Arrachea, *Quantum coherent adiabatic dynamics: Derivation of quantum master equations from Keldysh NEGF*, in progress.

Bibek Bhandari, Paolo Andrea Erdman, Rosario Fazio, Elisabetta Paladino and Fabio Taddei, *Heat Rectification in low-dimensional quantum systems*, in progress.

RINGRAZIAMENTI

Desidero esprimere la mia sincera gratitudine a tutti coloro che mi hanno aiutato durante il mio dottorato.

Ringrazio infinitamente il professor Rosario Fazio, e il Dr. Fabio Taddei: senza il loro supporto e la lora guida non sarei mai arrivato a questo traguardo.

Vorrei ringraziare tutte le persone che mi hanno dato una mano quando ne avevo bisogno: i miei amici e insegnanti sia in Italia che in Nepal, la mia famiglia e la mia fidanzata.

Infine, dedico questo lavoro a mio 'pitaji' e a mia 'ammijaan'.

CONTENTS

1

INTRODUCTION

Quantum transport and thermodynamics at nanoscale has been a subject of growing interest in modern research for some time. It is a widely studied field and ranges from the theoretical study of nanoscale devices using the principles of statistical and quantum mechanics to the experimental realisation of those devices. In addition, the field of nanoscience has represented itself as a common playground for physicists, chemists, material scientists, biologists as well as engineers. The main motivation being the theoretical proposal and experimental realisation of devices with novel properties emerging at the nanoscale. Moreover, the interest in this field has been further bolstered by the fact that the nanoscale devices have a wide range of application, from electronic and thermal devices to quantum computers. The inevitable application of quantum mechanics at this scale gives rise to interesting physics not observed in the classical regime. For instance, quantum Hall effect, quantized adiabatic pumping and so on. On the other hand, transistors used in contemporary computers and other electronic devices have the size of around 20 nm. Therefore, modern devices are already at the nanoscale and further miniaturisation of these devices makes the understanding of energy dynamics in this regime essential. The fabrication and application of devices at such a small scale entails serious technical challenges: noise and heat dissipation are the most significant ones.

When the system is attached to two reservoirs, thermal transport can be mediated by maintaining a thermal or potential bias, or by driving in time the system parameters. When it comes to nanoscale devices, thermal transport becomes as significant as particle transport. This has led to the invention of devices based on thermal transport such as thermal transistors and thermal diodes. Quantum thermodynamics governs the statistics, work production, entropy and other thermodynamic quantities in the quantum regime. To summarize, the study of thermal transport and thermodynamics at nanoscale not only helps in understanding the physics at nanoscale but also presents novel direction for technological advancement along with the miniaturisation of devices. Arguably, quantum transport and quantum thermodynamics have become the leading subject of interest in nanoscience.

In this thesis, we shall study quantum transport and quantum thermodynamics in nanoscale using different techniques (quantum master equation[1, 2], non-equilibrium Green's function[3, 4], linear response theory[5, 6]). We will be mainly focused on heat dynamics in the static as well as driven systems (for example quantum dots, metallic islands, resonators and qubits) attached to thermal reservoirs.

When we discuss about a modern field in science, for example thermal transport in nanoscale which has been so widely studied, there is always a problem of being too specific or too general. When we are too specific, there is a good chance we miss the forest for the details of the trees. On the other

hand, being too general might give us an over all comprehensive picture, but might render the discussion impractical or even inapplicable due to the lack of technical details. Although a balance between these two fronts is highly desirable, mostly it becomes inevitable to sacrifice one for the other. In order to address this issue, in the first three chapters we shall provide a general but a brief review on thermal transport and thermodynamics in nanoscale systems. In the last six chapters (from Chapter IV to Chapter IX), we will discuss about the specific properties and applications of thermal transport in static and driven nanoscale devices.

In particular, in Chapter II we will introduce different models of nanoscale devices that will be studied in the forthcoming chapters. We will also present a microscopic derivation of heat current for static as well as driven systems using Keldysh non-equilibrium Green's function.

In Chapter III, we will give a brief review of thermodynamics and thermal machines. We will talk about both theoretical and experimental developments in the field of classical as well as quantum thermodynamics, thermal transport and thermoelectrics.

In chapter IV, we will study the electronic thermal drag in two different Coulomb-coupled systems, the first one composed of two Coulomb blockaded metallic islands and the second one consisting of Coulomb coupled quantum dots. The two conductors of each system are electrically isolated and placed in the two circuits (the drive and the drag) of a four-electrode setup. The systems are biased, either by a temperature ΔT or a voltage V difference, on the drive circuit, while no biases are present on the drag circuit. We will use a master equation approach to determine the general properties of the dragged heat current, accounting also for co-tunneling contributions and the presence of large biases. Analytic results will be obtained in the sequential tunneling regime for small biases, finding, in particular, that the drag heat current is quadratic in ΔT or V and non-monotonous as a function of the inter-island coupling. Finally, by replacing one of the electrodes in the drag circuit with a superconductor or taking charge state dependent transition rates (in the case of quantum dots), we will find that heat can be extracted from the other normal electrode.

In chapter V, we will analyze a simple implementation of an absorption refrigerator, a system that requires heat and not work to achieve refrigeration, based on two Coulomb-coupled single-electron systems. We will determine the general condition to achieve cooling-by-heating. We will propose two possible experimental setups based on quantum dots or metallic islands that implement the nontrivial cooling condition. Using realistic parameters, we will show that these systems, which resemble existing experimental setups, can develop an observable cooling power.

In chapter VI, we will study thermal rectification. We will present a comprehensive and systematic study of thermal rectification in low-dimensional quantum systems. Focusing on various prototypical systems - a qubit, a non-linear harmonic oscillator and a Coulomb coupled quantum dot system - we identify necessary conditions to observe thermal rectification and we discuss strategies to maximize it. In particular, in the qubit case we will derive general upper bounds on rectification which hold in the weak system-bath coupling regime, and we show how the Lamb shift can be exploited to enhance rectification. We then go beyond the weak coupling regime using the non-equilibrium Green's function formalism and the Feynman-Vernon path integral approach. We will find that the strong coupling regime allows us to violate the bounds derived in the weak coupling regime, providing us

with clear signatures of high order coherent processes visible in the thermal rectification. In the non-linear harmonic oscillator, we will study the heat rectification using two different approximate schemes 1) mean field Hartree approximation and 2) equation of motion method that goes beyond mean field. The mean field calculations reproduces the results of the equation of motion method when the interaction is small compared to other energy scales of the system. Thermal rectification is enhanced in the large interaction limit, making equation of motion better suited to study thermal rectification in non-linear resonators. Finally, we will study non-local thermal rectification in Coulomb coupled quantum dots. For a suitable choice of parameters, we will show that a perfect non-local thermal rectification can be obtained.

In chapter VII, we will study thermal transport in two different single electron devices using master equations. In the first section, we will theoretically reproduce the experimental results of thermovoltage measurements in a single-electron transistor, both in the linear and non-linear regimes. Using a model which accounts for co-tunneling, we will find excellent agreement with the experimental data with no free parameters even when the temperature difference is larger than the average temperature (far-from-linear regime). This will allow us to confirm the sensitivity of the thermovoltage on co-tunneling and to find that in the non-linear regime the temperature of the metallic island is a crucial parameter. In the second section, using master equations we will theoretically match the experimental results for work extraction (beyond the free energy difference) from a single electron transistor at the single thermodynamic trajectory level. With a carefully designed out-of-equilibrium driving cycles featuring kicks of the control parameter, we will demonstrate work extraction up to large fractions of $k_B T$, despite zero free energy difference over the cycle. Our results are explained in the framework of nonequilibrium fluctuation relations. We thus shall show that irreversibility can be used as a resource for optimal work extraction even in the absence of feedback from an external operator.

In chapter VIII, we will present a general unified approach for the study of quantum thermal machines, including both heat engines and refrigerators, operating under periodic adiabatic driving and in contact with thermal reservoirs kept at different temperatures. We will show that many observables characterizing this operating mode and the performance of the machine are of geometric nature. Heat-work conversion mechanisms and dissipation of energy can be described, respectively, by the antisymmetric and symmetric components of a thermal geometric tensor defined in the space of time-dependent parameters generalized to include the temperature bias. The antisymmetric component can be identified as a Berry curvature, while the symmetric component defines the metric of the manifold. We will show that the operation of adiabatic thermal machines, and consequently also their efficiency, are intimately related to these geometric aspects. We will illustrate these ideas by discussing two specific cases: a slowly driven qubit asymmetrically coupled to two bosonic reservoirs kept at different temperatures, and a quantum dot driven by a rotating magnetic field and strongly coupled to electron reservoirs with different polarizations. Both examples are already amenable for an experimental verification.

In chapter IX, we will present a systematic derivation of the quantum master equation which describes the adiabatic dynamics of a driven quantum system weakly coupled to reservoirs kept at different temperatures. Starting from the microscopic Hamiltonian, we will derive such quantum master equation by means of the Schwinger-Keldysh non-equilibrium Green's functions

performing a perturbation expansion in the coupling between the system and the reservoirs. We will also calculate the charge and energy fluxes, as well as the power developed by the driving forces within the same framework. We will analyze the instantaneous as well as adiabatic contributions to the diagonal and off-diagonal elements of the density matrix in two specific examples, namely a qutrit attached to bosonic reservoirs and a pair of coupled quantum dot attached to fermionic reservoirs. Finally, we will also study heat rectification in adiabatically driven systems.

In Appendices A, B and C, we shall give a brief introduction of all the formulations used in the thesis to study thermal transport in nanoscale quantum devices: quantum master equation formulation based on Fermi golden rule will be presented in Appendix A, Keldysh-Schwinger formulation based on non-equilibrium Green's functions will be presented in Appendix B and Kubo formulation based on Luttinger theory of thermal transport in Appendix C.

2

MODEL AND FORMULATION

In this chapter, we will present different nanoscale devices that will be studied in the upcoming chapters. We will also present a microscopic derivation of heat current for static and driven systems which would be essential to study thermal transport properties of specific devices in upcoming chapters.

2.1 MODEL

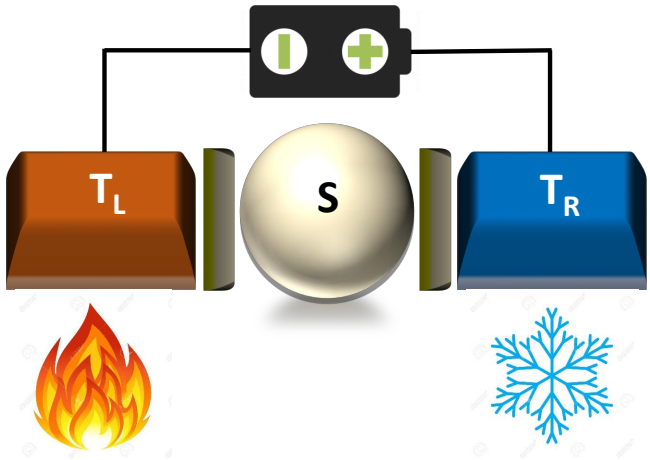

Figure 2.1: A nanoscale system S connected to baths L and R. A thermal and a potential bias has been maintained between the two baths.

As shown in Fig. (2.1), a nanoscale device is composed of three components, 1) system, 2) baths and 3) contacts. The baths represented by red and blue blocks on the two sides of the system (S) can be maintained at a thermal or potential bias. The total Hamiltonian is given by

$$H = H_S + H_B + H_C, \tag{2.1}$$

where H_S represents the Hamiltonian for the system, H_B represents the bath Hamiltonian and H_C gives the coupling between the system and the baths.

2.1.1 *System*

We will generally consider three different type of systems: 1) fermionic, for example quantum dots and metallic islands, 2) bosonic, for example resonators. The Hamiltonian for a quantum dot is given by:

$$H_{QD} = \sum_i \epsilon_i a_i^\dagger a_i + \sum_i w_i \left(a_i^\dagger a_{i+1} + h.c. \right) + \sum_{i \neq j} U_{ij} n_i^\dagger n_j, \tag{2.2}$$

where $a_i(a_i^\dagger)$ represent the fermionic annihilation (creation) operator of the electron in the quantum dot (QD) labelled by i, U_{ij} represents the inter-dot Coulomb interaction between QDs i and j, ϵ_i is the onsite potential of quantum dot i and w_i gives the tunneling strength between QD i and $i+1$. The inter-dot Coulomb interaction will serve for studying non-local thermoelectric phenomena. The fermionic annihilation and creation operators satisfy the commutation relations, $\{a_i, a_i^\dagger\} = 1$. The Hamiltonian for Coulomb coupled metallic islands is given by

$$H_{MD} = \sum_{k,i=1,2} \epsilon_{ki} a_{ki}^\dagger a_{ki} + U \sum_{k,k'} n_{k1} n_{k'2}. \tag{2.3}$$

The strength of inter-metallic island Coulomb interaction is given by U, ϵ_{ki} represents the energy of mode k in the metallic island i and $a_{ki}(a_{ki}^\dagger)$ is the fermionic annihilation (creation) operator of an electron in metallic island i.

The Hamiltonian for a single mode harmonic resonator is

$$H_R = \Delta b^\dagger b + U b^\dagger b^\dagger b b, \tag{2.4}$$

where Δ gives the frequency of the resonator, the strength of non-linearity is determined by U and $b(b^\dagger)$ represents the bosonic annihilation (creation) operator of the resonator. The bosonic operators satisfy the commutation relation, $\left[b, b^\dagger\right] = 1$.

Finally, the qubit Hamiltonian is

$$H_Q = \frac{\Delta}{2}\sigma_z, \tag{2.5}$$

where Δ gives the qubit gap.

2.1.2 *Baths*

The baths are considered to be macroscopic systems with continuous degrees of freedom. The baths have a large enough heat capacity and are at thermal equilibrium with a fixed temperature T_α and chemical potential μ_α. Since the baths are kept at thermal equilibrium, the statistics of the baths can be defined by a thermal Gibbs state $\rho_\alpha = e^{-H_\alpha / k_B T_\alpha} / \mathcal{Z}_\alpha$, where H_α is the Hamiltonian of the bath α with partition function $\mathcal{Z}_\alpha = \mathrm{Tr}\left[e^{-H_\alpha / k_B T_\alpha}\right]$. When the baths maintained at a thermal or potential gradient are connected to a system, thermal conduction takes the bath out of thermal equilibrium. Due to the presence of inelastic scattering, the baths quickly attain thermal equilibrium. We consider that the time scale corresponding to the attainment of thermal equilibrium is the smallest time scale. In other words, the dynamics of bath is fast enough compared to the dynamics of the system. In this scenario, the coarse grained Markov approximation will be valid, provided the system-bath coupling is weak. The Hamiltonian of the Bosonic (B) and Fermionic (F) baths are given by

$$H_\alpha^{\mathrm{B}} = \sum_k \epsilon_{k\alpha} b_{k\alpha}^\dagger b_{k\alpha}, \tag{2.6}$$

$$H_\alpha^{\mathrm{F}} = \sum_k (\epsilon_{k\alpha} - \mu_\alpha) c_{k\alpha}^\dagger c_{k\alpha}, \tag{2.7}$$

where $b_{k\alpha}(c_{k\alpha})$ and $b_{k_\alpha}^\dagger(c_{k_\alpha}^\dagger)$ are the creation and annihilation operators for bosons (fermions) with energy $\epsilon_{k\alpha}$ for bath α. These operators satisfy the usual commutator and anti-commutator relations, $\left[b_{k\alpha}, b_{k'\alpha'}^\dagger\right] = \delta_{kk'}\delta_{\alpha\alpha'}$ and $\left\{c_{k\alpha}, c_{k'\alpha'}^\dagger\right\} = \delta_{kk'}\delta_{\alpha\alpha'}$.

2.1.3 *Coupling*

In general, we will consider a linear system-bath coupling. The coupling acts as a medium for the exchange of energy and particle between the system and the baths. The coupling contains both system and bath degrees of freedom, so it changes when either the system or bath changes. In the case of quantum dot i attached to fermionic bath α, the coupling Hamiltonian takes the form

$$H_{\alpha,QD} = \sum_k V_{k\alpha} a_i^\dagger c_{k\alpha} + h.c. \tag{2.8}$$

For the case of a metallic island, the coupling Hamiltonian should be modified to address the continuous energy modes in the system, i.e.

$$H_{\alpha,MD} = \sum_{k,q} V_{kq,\alpha} a_{ki}^\dagger c_{q\alpha} + h.c. \tag{2.9}$$

In the case of single mode harmonic resonator attached to bosonic bath the Hamiltonian takes the form

$$H_{\alpha,R} = \sum_k V_{k\alpha} \left(b_{k\alpha}^\dagger + b_{k\alpha} \right) \left(b^\dagger + b \right). \tag{2.10}$$

For the sake of simplicity, in some cases we will take only the particle conserving term in the latter contact Hamiltonian such that the coupling Hamiltonian for a single mode resonator connected to bosonic baths reduces to

$$H_{\alpha,R} = \sum_k V_{k\alpha} b_{k\alpha}^\dagger b + h.c. \tag{2.11}$$

Finally, the most general system-bath interaction for a qubit is given by

$$H_{\alpha,Q} = \sum_k V_k \left(b_{k\alpha} \otimes \sigma^+ + b_{k\alpha}^\dagger \otimes \sigma^- \right) + B_{\alpha z} \otimes \sigma_z + B_{\alpha 1} \otimes \mathbb{1}, \tag{2.12}$$

where $B_{\alpha z}$ and $B_{\alpha \mathbb{1}}$ are Hermitian operators acting on the space of bath α. When we shall consider arbitrary spin coupling between the qubit and the bosonic baths, we will use a modified version of coupling Hamiltonian given by

$$H_{\alpha,Q} = \sum_k V_{k\alpha} \sum_{i=x,y,z} m_{i,\alpha} \sigma_i \otimes \left(b_{k\alpha} + b_{k\alpha}^\dagger \right), \tag{2.13}$$

where $\mathbf{m}_\alpha = (\sin\theta_\alpha \cos\phi_\alpha, \sin\theta_\alpha \sin\phi_\alpha, \cos\theta_\alpha)$ is a unit vector parameterized by the angles θ_α and ϕ_α.

As we will see in the following chapters, the system-bath interaction can be conveniently characterized by the spectral density

$$\Gamma_\alpha(\epsilon) = 2\pi \sum_k \delta(\epsilon - \epsilon_{\alpha k}) V_{\alpha k} V_{\alpha k}^*. \tag{2.14}$$

In the following, we will consider generic spectral densities for the two baths. In the cases of bosonic baths, we will consider Ohmic spectral densities with an exponential cut-off energy ϵ_C (unless mentioned otherwise), i.e.

$$\Gamma_\alpha(\epsilon) = \pi K_\alpha \epsilon\, e^{-\epsilon/\epsilon_C} \equiv K_\alpha I(\epsilon), \tag{2.15}$$

where K_α is the dimensionless Ohmic coupling strength [7]. And for the fermionic baths, we will generally consider characterless spectral density given by

$$\Gamma_\alpha(\epsilon) = 2\pi |V_\alpha|^2 \rho_\alpha(\epsilon) = \Gamma_\alpha. \tag{2.16}$$

2.2 HEAT CURRENT

We are interested in studying the steady-state heat current flowing across the device when a temperature bias is imposed between the baths. Specifically, as depicted in Fig. 2.1, we fix $T_L = T + \Delta T/2$ and $T_R = T - \Delta T/2$, where T is the average temperature. Even in the fermionic case, we will consider the case of zero chemical potential. Furthermore, since we consider steady state currents, the heat flowing out of one bath is equal to the one flowing into the other bath. In addition, in the absence of chemical potential the heat current and energy current are the same, i.e. $J_\alpha^{(h)} = J_\alpha^{(E)}$. Therefore, for simplicity we define the heat flowing out of the left lead as

$$J_\alpha^{(h)}(\Delta T) \equiv -\lim_{t\to+\infty} \frac{d}{dt} \langle H_\alpha \rangle (t), \tag{2.17}$$

where $\langle \ldots \rangle (t) = \mathrm{Tr}[\rho(t) \ldots]$, $\rho(t)$ being the density matrix representing the state of the total system at time t. Notice that the time variation of the energy associated with the coupling Hamiltonian vanishes in steady state [8]. In addition, since the energy current is conserved we have, $J_L^{(E)} = -J_R^{(E)} = J^{(E)}$.

Starting from the formal definition of the heat current given in Eq. (2.17), we can simplify the calculation of the heat current using a standard procedure known as "bath embedding"[4], which is valid whenever the operators of the bath appear linearly in $H_{\alpha,S}$. This approach applies to all models with linear coupling between the system and the baths. Under such hypothesis, the formally exact Meir-Wingreen-type formula [9] for the heat current can be written as [10, 11, 12, 13, 14]

$$J_\alpha^{(h)}(t) = \mp 2 \sum_k \epsilon_{k\alpha} |V_{k\alpha}|^2 \int dt_1 \mathrm{Re}\left[G^r_{SS}(t,t_1) g^<_{k\alpha}(t_1,t) + G^<_{SS}(t,t_1) g^a_{k\alpha}(t_1,t) \right], \tag{2.18}$$

where S is the system degree of freedom in the contact Hamiltonian $H_{\alpha,S}$ (see Subsection (2.1.3)): in the quantum dot case $S \equiv a_i$ where a_i is the annihilation operator of the quantum dot i attached to bath α, in the case of metallic islands $S \equiv a_{ki}$ where a_{ki} is the annihilation operator of the metallic island i attached to bath α, in the case of resonator with resonator bath coupling defined through Eq (2.10), $S \equiv b^\dagger + b$ where $b^\dagger (b)$ are the creation (annihilation) operator for the resonator attached with bath α and for the case of qubit $S = \sum_{i,\alpha} m_{i,\alpha} \sigma_i$ where $m_{i,\alpha}$ associated with coupling to bath α is defined below Eq. (2.13). The minus sign in front of the integral applies only when both the system and the baths are fermionic. The greater and lesser Green's functions for the system are respectively defined as

$$\begin{aligned} G^>_{SS}(t,t') &= -i \left\langle S(t) S^\dagger(t') \right\rangle \\ G^<_{SS}(t,t') &= \pm i \left\langle S^\dagger(t') S(t) \right\rangle, \end{aligned} \tag{2.19}$$

with the retarded Green's function $G^r_{SS}(t,t') = \theta(t-t')[G^>_{SS}(t,t') - G^<_{SS}(t,t')]$. The greater and lesser Green's function for the bath α can be similarly defined as

$$\begin{aligned} g^>_{k\alpha}(t,t') &= -i \langle d_{k\alpha}(t) d^\dagger_{k\alpha}(t') \rangle \\ g^<_{k\alpha}(t,t') &= \pm i \langle d^\dagger_{k\alpha}(t') d_{k\alpha}(t) \rangle, \end{aligned} \tag{2.20}$$

respectively with the retarded Green's function $g^r_{k\alpha}(t,t') = \theta(t-t')[g^>_{k\alpha}(t,t') - g^<_{k\alpha}(t,t')]$ and the advanced Green's function $g^a_{k\alpha}(t,t') = \left[g^r_{k\alpha}(t',t)\right]^*$. The plus sign in lesser Green's function applies for fermionic systems attached to fermionic baths.

2.2.1 *Static case*

For time-independent systems, one can use the relative time Fourier transformation

$$G(\epsilon) = \int dt' G(t,t') e^{i\epsilon(t-t')} \tag{2.21}$$

After some calculations (the details are presented in the Appendix B), we arrive at the final expression for heat current written in terms of lesser and greater Green's function

$$J_\alpha^{(h)}(\Delta T) = \pm \int \frac{d\epsilon}{2\pi\hbar}\, \epsilon \left[G^<(\epsilon)\Sigma_\alpha^>(\epsilon) - G^>(\epsilon)\Sigma_\alpha^<(\epsilon) \right]_{SS}, \tag{2.22}$$

where the integration is performed over $[0,+\infty]$ ($[-\infty,+\infty]$) for bosonic (fermionic) baths. $G_{SS}^{\lessgtr}(\epsilon)$ is the Fourier transform of the lesser/greater Green's function of the system in the presence of the baths, while $\Sigma_{\mathrm{L}}^{\lessgtr}(\epsilon)$ is the Fourier transform of the lesser/greater *embedded* self energy induced by the left bath. The lesser and greater embedded self energies can be determined from the Keldysh contour components $\Sigma_\alpha(z,z') = \int d\epsilon_k/(2\pi)\, \Gamma_\alpha(\epsilon_k) g_{k\alpha}(z,z')$, where $g_{k\alpha}(z,z') = -i\,\langle \mathcal{T}_c\{d_{k\alpha}(z) d_{k\alpha}^\dagger(z')\}\rangle$ is the *free* contour Green function of bath α, $\mathcal{T}_c$ denoting the contour ordering. The only quantities which must be determined in Eq. (2.22) are $G_{SS}^{\lessgtr}(\epsilon)$.

There is a typical situation in which Eq. (2.22) can be written as a simpler and more transparent form. Namely, if the spectral densities $\Gamma_\alpha(\epsilon)$ of the baths are proportional, i.e. $\Gamma_{\mathrm{L}}(\epsilon) \propto \Gamma_{\mathrm{R}}(\epsilon)$, we can write Eq. (2.22) as [15]

$$J_{\mathrm{L}}^{(h)}(\Delta T) = \int \frac{d\epsilon}{2\pi\hbar}\, \epsilon\, \mathcal{T}(\epsilon, T, \Delta T) \left[n_{\mathrm{L}}(\epsilon) - n_{\mathrm{R}}(\epsilon) \right], \tag{2.23}$$

where

$$\mathcal{T}(\epsilon, T, \Delta T) = i \left\{ \frac{\Gamma_{\mathrm{L}}(\epsilon)\Gamma_{\mathrm{R}}(\epsilon)}{\Gamma_{\mathrm{L}}(\epsilon) + \Gamma_{\mathrm{R}}(\epsilon)} [G^>(\epsilon) - G^<(\epsilon)] \right\}_{SS} \tag{2.24}$$

and $n_\alpha(\epsilon)$ denotes the energy distribution of bath α. Therefore, $n_\alpha(\epsilon) = (e^{\epsilon/(k_{\mathrm{B}}T_\alpha)} - 1)^{-1}$ for bosonic baths, while $n_\alpha(\epsilon) = (e^{(\epsilon-\mu_\alpha)/(k_{\mathrm{B}}T_\alpha)} + 1)^{-1}$ for fermionic baths. The dependence of $\mathcal{T}(\epsilon, T, \Delta T)$ on the temperatures may arise from $G^{\lessgtr}(\epsilon)$, which are indeed correlation functions of the system computed in the presence of the baths. For non-interacting systems, Eq. (2.24) reduces to the well known scattering formula with a transmission function that does not depend on the temperature of the baths.

2.2.2 *Driven case*

In this subsection, we will discuss the dynamics of a driven quantum system using Floquet formulation along with non-equilibrium Green's functions. Considering periodic driving with period Ω, we apply the Floquet-Fourier transform given by:

$$\begin{aligned} G(t,\epsilon) &= \int dt' G(t,t') e^{i\epsilon(t-t')}, \\ G(n,\epsilon) &= \frac{1}{\tau}\int_0^\tau G(t,\epsilon) e^{in\Omega t}, \end{aligned} \tag{2.25}$$

where $G(t,\epsilon)$ and $G(n,\epsilon)$ are the Fourier transformed and Floquet-Fourier transformed Green's functions respectively. Using the Floquet Fourier trans-

form in Eq. (B.8) and after some calculations (see Appendix B for details) we arrive at following expression for heat current

$$J_\alpha^{(h)} = J_{\alpha,1}^{(h)} + J_{\alpha,2}^{(h)}, \tag{2.26}$$

where

$$J_{\alpha,1}^{(h)}(t) = \sum_{ln} \int \frac{d\epsilon}{2\pi} e^{-il\Omega t} \Big\{ \mathcal{Z}_\alpha^h(\epsilon) \Big[G^r(l+n, \epsilon - n\Omega) \Big[\Sigma^>(\epsilon - n\Omega) - \hat{\Sigma}^<(\epsilon - n\Omega) \Big] G^{r^*}(n, \epsilon - n\Omega) \Big] + \Big(\mathcal{Z}_\alpha^h(\epsilon - l\Omega) - \mathcal{Z}_\alpha^h(\epsilon) \Big) G^{r^*}(-l, \epsilon) \Big\}_{SS} \tag{2.27}$$

and

$$J_{\alpha,2}^{(h)}(t) = \mp \sum_{ln} \int \frac{d\epsilon}{2\pi} e^{-il\Omega t} \Big\{ G^r(l+n, \epsilon) \Sigma^<(\epsilon) G^{r^*}(n, \epsilon) \Big[\mathcal{Y}_\alpha^h(\epsilon + n\Omega) - \mathcal{Y}_\alpha^{h^*}(\epsilon + n\Omega + l\Omega) \Big] \Big\}_{SS}, \tag{2.28}$$

where

$$\mathcal{Y}_\alpha^h(\epsilon) = \int \frac{d\epsilon'}{2\pi} \epsilon' \Gamma_\alpha(\epsilon') \left[\mathcal{P} \left\{ \frac{1}{\epsilon - \epsilon'} \right\} + i\pi\delta(\epsilon - \epsilon') \right], \tag{2.29}$$

and $\mathcal{P}$ represents the principal value, while $\mathcal{Z}_\alpha^h(\epsilon) = -i\epsilon n_\alpha(\epsilon)\Gamma_\alpha(\epsilon)$. Summing Eq. (B.22) and Eq. (B.24), one obtains the final expression for heat current flowing in individual lead at time t. For driven systems, a finite amount of heat is stored in the contact region, however, on average this current goes to zero. The heat current stored in the contact between bath α and the system at time t given by

$$J_{\alpha,C}^{(h)}(t) = \frac{d}{dt} \langle H_{C,\alpha} \rangle = \pm 2 \sum_k V_{k\alpha} \operatorname{Im} \left[\frac{d}{dt} G_{S\alpha}^<(t,t) \right]. \tag{2.30}$$

From Eq. (B.26), we have:

$$J_{\alpha,C}^{(h)} = \pm 2 \sum_k |V_{k\alpha}|^2 \int dt_1 \operatorname{Im} \Big[\frac{d}{dt} \Big(G_{SS}^r(t,t_1) g_\alpha^<(t_1,t) + G_{SS}^<(t,t_1) g_\alpha^a(t_1,t) \Big) \Big] \tag{2.31}$$

The second term in the right hand side goes to zero (the lesser Green's function is imaginary by definition and we neglect the Lamb shift component of the self energy for time being) giving:

$$J_{\alpha,C}^{(h)} = \mp i \sum_k |V_{k\alpha}|^2 \int \frac{d\epsilon}{2\pi} \frac{d}{dt} \Big(G_{SS}^r(t,\epsilon) + G_{SS}^{r^*}(t,\epsilon) \Big) g_\alpha^<(\epsilon). \tag{2.32}$$

After Fourier transformation, we obtain:

$$J_{\alpha,C}^{(h)} = \mp 2i\Omega \sum_k |V_{k\alpha}|^2 \int \frac{d\epsilon}{2\pi} \sum_l l \operatorname{Im} \Big(G_{SS}^r(l,\epsilon) e^{-il\Omega t} \Big) g_\alpha^<(\epsilon). \tag{2.33}$$

The time averaged heat current over one cycle flowing in lead α is given by:

$$J_\alpha^{(h)} = \sum_n \int \frac{d\epsilon}{2\pi} \Big\{ \Big[G^r(n,\epsilon) \Sigma^<(\epsilon) G^{r^*}(\epsilon) \Big]_{SS} \Big(\mp 2i \operatorname{Im} \Big[\mathcal{Y}_\alpha^h(\epsilon + n\Omega) \Big] - \mathcal{Z}_\alpha^h(\epsilon + n\Omega) \Big) \Big[G^r(n,\epsilon) \Sigma^>(\epsilon) G^{r^*}(\epsilon) \Big]_{SS} \mathcal{Z}_\alpha^h(\epsilon + n\Omega) \Big\}. \tag{2.34}$$

The adiabatic contribution can be obtained by expanding Eq. (2.34), upto first order in driving frequency.

$$\begin{aligned}\mathcal{Z}^h_\alpha(\epsilon + n\Omega) &= \mathcal{Z}^h_\alpha(\epsilon) + n\Omega\frac{\partial \mathcal{Z}^h_\alpha(\epsilon)}{\partial\epsilon} \\ \mathcal{Y}^h_\alpha(\epsilon + n\Omega) &= \mathcal{Y}^h_\alpha(\epsilon) + n\Omega\frac{\partial \mathcal{Y}^h_\alpha(\epsilon)}{\partial\epsilon}.\end{aligned} \tag{2.35}$$

In order to calculate the adiabatic contribution, it is sufficient to take only the zeroth order contribution for the Green's functions[8], $G^r(n,\epsilon) \equiv G^{r,f}(n,\epsilon)$, where $G^{r,f}(n,\epsilon)$ is the Green's function which evolves with the instantaneous Hamiltonian.

3

THERMODYNAMICS AND THERMAL MACHINES: A BRIEF REVIEW

The advent of thermal machines can be traced back to prehistoric times when fire piston was used by tribes in Southeast Asia and Pacific islands to make fire[16]. It was an ingenuous invention, where the gas in a cylinder was rapidly compressed with the help of a piston creating high temperature which in turn lit the tinder attached to the piston. Intriguingly, the practical application of ideal gas law which was later developed by Boyle, Charles and Émile Clapeyron was already experimented in the prehistoric times. There were many extra-ordinary inventions from the prehistoric times to the 17th century however the 17-19th centuries were arguably the golden years for the field of thermodynamics and thermal machine. In the following we will try to outline the significant breakthroughs in the field of thermodynamics and thermal machines from the 17th century till now. The first major experiment was done by Boyle[17] and Mariotte[18] in the 16th century where they proved that the volume of a gas with fixed mass is inversely proportional to pressure at constant temperature. Then as early as 1698, steam engine was first patented by Thomas Savery, later James Watt presented a more efficient version of steam engine with a separate condensing chamber in 1769. The steam engines were used for pumping water, driving sawmills, for transport like trains, driving factories and other purposes. In 1824, Sadi Carnot analyzed the efficiency of steam engine using Caloric theory and proposed the maximum efficiency a heat engine can have: these days it is known as Carnot efficiency. The steam engine were the only heat engines until 1876 when Otto proposed the first four-stroke petrol engine[19]. Along with the diesel engine developed by Rudolf Diesel in 1890s[19], these inventions brought a revolutionary trend in the field of thermal machines. The importance of these inventions can be clearly illustrated by the fact that modern vehicles still include a 4-stroke engine proposed by Otto, although modifications have been done to increase the efficiency and performance. A heat engine always suffers from inevitable and irreversible loss of heat in terms of dissipation. One of the main criteria in the advancement of thermal machines has been to increase efficiency by reducing dissipation.

On the other side, the field of thermodynamics was observing its own glorious days. Both first and second law of thermodynamics were developed in the first half of the 19th century. During the same period, ideal gas law was developed combining Boyle's and Charle's law. The later half of the century brought many significant observations into light when Clausis introduced the concept of entropy and Maxwell proposed the distribution law of molecular velocities. In the same period, Boltzmann proposed that the probability for a system to be in a certain energy state depends only on the energy of the state and the temperature known as Boltzman distribution law. Till the beginning of the 20th century, thermodynamics and statistical

mechanics were largely considered separate fields of study. In the early 1900s, Gibbs introduced the statistical mechanics definition of entropy where the entropy was related to the probability distribution of energy microstates[20]. One other important development regarding the connection between the statistical mechanics and thermodynamics was the fluctuation dissipation theorem used by Johnson and Nyquist in 1928 to characterize the fluctuation intrinsic to the system[21, 22]. The fluctuation-dissipation theorem brings into attention the importance of environment since every irreversible process is accompanied with dissipation.

Most of the studies until the first half of the 19th century were based on thermal machines and thermodynamics of systems with continuous degrees of freedom. For macroscopic systems, much of the statistical and transport properties are calculated using the "thermodynamic limit". In these devices, quantum interference and coherence effects are insignificant as the particles undergo many inelastic collision before being observed. However in the 1980s, with miniaturization of devices, the interest shifted to quantum interference and quantum coherence effects in microscopic devices. This led to the experimental realisation of Aharonobov-Bohm oscillations in normal-metal rings in 1985 by Webb et al[23]. The discovery of quantum effects in the microscopic devices motivated further experimental and theoretical research in nanoscale systems. In the 1990s, the technology became advanced enough for the experimental study of transport properties in tiny devices with discrete energy states, for example the single electron transistor. At low temperature, when the classical dynamics becomes suppressed quantum mechanics governs the dynamics. The nanoscale devices has been successfully used as necessary ingredients in quantum computers. They have been used to study quantum effects in various fields ranging from quantum information[24], cryptography[25, 26] to quantum thermodynamics[27, 28]. In this thesis, we shall study the thermal transport and thermodynamics in nanoscale quantum devices. But mostly, we would be motivated to understand the nature and dynamics of heat transfer in nanoscale device.

3.1 TRANSPORT THEORIES AND THERMOELECTRICS IN NANOSCALE QUANTUM SYSTEMS

In this section, we will discuss about different thermoelectric coefficients associated with nanoscale electronic thermal machines. But before diving deeper into thermoelectrics, we deem it necessary to discuss the classical and quantum transport theories which would be necessary to express the thermoelectric parameters in manageable form. In the following, we give a brief introduction of the main formulations used to study transport properties in solid state devices and their regime of validity. We start with the Boltzmann transport theory. The charge and energy carriers in macroscopic objects like metal or semiconductors move under the application of a bias (thermal or potential) or when an external time-dependent driving field is applied. The movement of carriers redistributes the particle as well as energy density of the carriers as well as makes the particles scatter among themselves[29]. A transport theory has to take into account all these effects. It also has to balance out different processes, for instance if the carriers move from one point in space to another after acquiring a momentum, they can scatter with other particles and lose this momentum. The simplest approach was studied by Boltzman[29], where he considered three different processes by which the local concentration of carriers can change 1) diffusion, 2) redistribution due

to the presence of external field and 3) scattering. The net balance between the above mentioned three different processes in steady state gives the Boltzman transport equations. The Boltzman transport equations describe the semi-classical transport processes but fails to address the quantum mechanical nature of the carriers. The quantum interference effects and quantum coherence are not addressed by the Boltzman transport equations and require more advanced techniques such as Green's function or Kubo formalism.

A transport theory for non-interacting mesoscopic devices based on scattering matrices was developed by Rolf Landauer, Yoseph Imry and Markus Büttiker[30, 31]. This approach is known as scattering formalism and gives a correct description of coherent transport (when a single wave function can be defined extending from one lead to another) in non-interacting nanoscale devices. This formulation has been widely used to study current and noise in nanoscale devices when the device size is effectively shorter than the phase relaxation length.

Another way to study dynamics in nanoscale devices (even with interactions present) is to use the Pauli master equation where the semi-classical transition rates are calculated using the Fermi Golden rule which can describe one as well as many electron tunneling processes. However, the semi-classical master equations are inadequate to study the quantum dynamics. In order to address the quantum effects in nanoscale devices, quantum master equation can be employed which is obtained by studying the dynamics of reduced density matrix of the system[1, 2]. The quantum master equation method has been employed in a wide range of fields, for instance quantum thermodynamics, quantum optics and quantum information. The quantum master equation serves as a significant tool for studying the transport properties in the weak coupling limit but fails to address the dynamics when the coupling between the bath and system is strong enough. In order to address the problem of strong coupling, the Schwinger-Keldysh formulation based on perturbation theory employing non-equilibrium Green's function is often applied[3, 4]. On the other hand, when the bias as well as driving are weak and when the linear response becomes sufficient to describe the dynamics, Kubo formalism can be used[5, 6]. Using the Kubo linear response theory, one can calculate the linear response coefficients which holds for both weak and strong system-bath coupling. The linear response coefficient satisfy some special set of relations known as Onsager relations.

After we have pointed out different formulations that can be applied to calculate the observables related to thermal transport, we are ready to define the different thermoelectric coefficients. Thermoelectricity has been studied in a variety of nanoscale devices ranging from single electron transistors[32, 33] to devices based on topological insultators[34]. Let us consider a microscopic system attached to two thermal fermionic baths as shown in Fig. 2.1. The two baths L and R have temperatures T_{L} and T_{R} respectively and chemical potentials $\mu_{\mathrm{L}} = eV_{\mathrm{L}}$ and $\mu_{\mathrm{R}} = eV_{\mathrm{R}}$ respectively. V_{L} and V_{R} are the voltage applied to left and right bath, where $V_{\mathrm{L}} - V_{\mathrm{R}} = \Delta V$ is the voltage bias maintained between the two baths. In addition to voltage bias, a thermal bias ΔT can also be maintained between the two baths, where $\Delta T = T_{\mathrm{L}} - T_{\mathrm{R}}$. The charge and energy currents flowing into the bath α are defined as $J_{\alpha}^{(\mathrm{c})}$ and $J_{\alpha}^{(\mathrm{E})}$. In the steady state for the conservation of charge and energy, we have $J_{\mathrm{L}}^{(\mathrm{c})} = -J_{\mathrm{R}}^{(\mathrm{c})} = J^{(\mathrm{c})}$ and $J_{\mathrm{L}}^{(\mathrm{E})} = -J_{\mathrm{R}}^{(\mathrm{E})} = J^{(\mathrm{E})}$. In addition, the heat current is defined as the difference between the total energy current and the electrochemical potential energy current, $J_{\alpha}^{(\mathrm{h})} = J_{\alpha}^{(\mathrm{E})} - \frac{\mu_{\alpha}}{e} J_{\alpha}^{(\mathrm{c})}$. When the device acts as a thermal machine, a power P is either extracted from the

machine or provided to the machine depending on whether the machine acts as a heat engine or a refrigerator, respectively.

In the linear response regime, where $|\Delta T| \ll T_{L/R}$ and $|\Delta V| \ll k_B T_{L/R}$, the charge and heat currents flowing out of the left lead can be expressed as

$$\begin{aligned} J^{(c)} &= L_{cc}\frac{\Delta V}{T} + L_{ch}\frac{\Delta T}{T^2} \\ J_L^{(h)} &= L_{hc}\frac{\Delta V}{T} + L_{hh}\frac{\Delta T}{T^2}, \end{aligned} \tag{3.1}$$

where $T = (T_R + T_L)/2$ is the average temperature of the two baths (assuming symmetric thermal bias) and the coefficients $L_{ab}(a, b = c, h)$ are the Onsager coefficients. Different thermoelectric parameters can be written in terms of Onsager coefficients in the linear response regime.

The electrical conductance (G) is defined as the ratio of charge current and the applied potential bias when the thermal bias goes to zero

$$G = \left|\frac{J^{(c)}}{\Delta V}\right|_{\Delta T=0}, \tag{3.2}$$

where $\Delta V = V_L - V_R$ is the potential bias maintained between the two baths and $J^{(c)}$ is the charge current flowing in the device. The thermal conductance (κ) is defined as the ratio between the heat current and the applied thermal bias, provided the charge current is zero.

$$\kappa = \left|\frac{J^{(h)}}{\Delta T}\right|_{J^{(c)}=0}, \tag{3.3}$$

where for $J^{(c)} = 0$, $J_L^{(h)} = -J_R^{(h)} = J^{(h)}$. The thermovoltage V_{th} is defined as the potential bias for which the charge current goes to zero in the presence of a fixed thermal bias, i. e.

$$J^{(c)}\left(V_{th}\right)\Big|_{\Delta T\neq 0} = 0. \tag{3.4}$$

We will study the thermovoltage of single electron transistor in a highly non equilibrium regime in Chapter VII. The thermovoltage is related to the thermopower (S) where the later is defined as the ratio between the potential bias and thermal bias, provided the charge current is zero.

$$S = \left|\frac{\Delta V}{\Delta T}\right|_{J^{(c)}=0}. \tag{3.5}$$

And finally the Peltier Π coefficient can be expressed as

$$\Pi = \left|\frac{J_L^{(h)}}{J^{(c)}}\right|_{\Delta T=0}. \tag{3.6}$$

For a review on the relationships between different thermoelectric parameters, the figure of merit and efficiency in the linear response, we ask the readers to consult the review by Benenti et al[35].

3.2 HEAT TRANSFER AND THERMODYNAMICS IN NANOSCALE DEVICES

In this section, we will present a general discussion on thermal transport in nanoscale devices. Nanoscale devices are generally composed of a microscopic system connected to macroscopic baths as shown in Fig. 2.1. The

system can exchange particles or energy with the baths. Generally, a system is connected to two or more baths in order to have a particle or energy flow by maintaining a thermal and potential bias. Work can be either done by the system or on the system. Heat engines are obtained by extracting work from the system by maintaining a thermal bias between the baths. However, when the heat is transported from the cold bath to hot bath by doing work on the system, the device is called a refrigerator. If the work output is given by W_{out} and Q_{H} is the heat out of the hot source, the efficiency of the heat engine is defined through the expression

$$\eta_{\text{H}} = \frac{W_{\text{out}}}{Q_{\text{H}}}. \tag{3.7}$$

In the case of two baths, the Carnot efficiency which is the efficiency of a perfect thermal machine is given by

$$\eta_{\text{H}}^{\text{c}} = 1 - \frac{T_{\text{C}}}{T_{\text{H}}}, \tag{3.8}$$

where $T_{\text{C/H}}$ is the temperature of the cold/hot bath. Similarly, the efficiency of the refrigerator which is known as the 'coefficient of performance' is expressed as

$$\eta_{\text{R}} = \frac{Q_{\text{C}}}{W_{\text{in}}}, \tag{3.9}$$

where Q_{C} is the amount of heat extracted from the cold reservoir and W_{in} is the input work done on the system. The maximum coefficient of performance of a perfect refrigerator is given by

$$\eta_{\text{R}}^{\text{c}} = \frac{T_{\text{C}}}{T_{\text{H}} - T_{\text{C}}}. \tag{3.10}$$

In this thesis, we will generally consider a quantum thermal machine, where the work is performed on the system, either by driving the system by an external ac supply (for example, see Chapters VIII and IX) or by means of a coupled system (for example, see Chapters IV and V where the system under study is Coulomb coupled to another system maintained at a thermal bias). In these cases, depending on the energy exchanges in the system, the details of the system, bath and coupling, the device can act as thermal machines of different sorts, for example refrigerator, thermal accelerator, heat pump, etc.

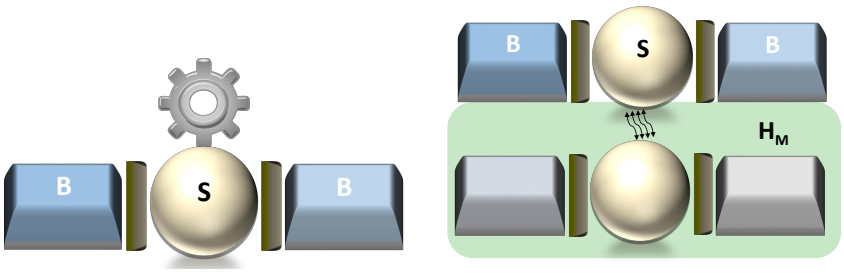

Figure 3.1: A nanoscale system S connected to baths B. The work can be performed on the system either (left panel) by driving the system or (right panel) by coupling the system to another system (indicated by a light green shade and represented by Hamiltonian H_M) through Coulomb interaction.

Now, we will discuss about different thermodynamic parameters that define the properties of a thermal machine when the system is both driven

as well as coupled to an external system. As sketched in Fig. 3.1, we define the total Hamiltonian

$$H_{\text{tot}} = H + H_{\text{M}} \tag{3.11}$$

where H is the Hamiltonian for the device under consideration as defined in Eq. (2.1), the system Hamiltonian, $H_S \equiv H_S(t)$ is time dependent (see the left panel of Fig. 3.1), $H_{\text{B}} = \sum_\alpha H_\alpha$ describes the baths (α labels the different baths) and $H_{\text{C}} = \sum_\alpha H_{\text{C},\alpha}$ describes the coupling between the system and the baths. H_M gives the Coulomb coupled part, when the work is performed on the system by means of a Coulomb coupled system (see the right panel of Fig. 3.1).

Let's start from the energy currents. To study the energy flux entering and exiting different parts of the device, we consider the time evolution of total Hamiltonian

$$\frac{d\langle H\rangle}{dt} = \frac{d\langle H_{\text{S}}\rangle}{dt} + \frac{d\langle H_{\text{B}}\rangle}{dt} + \frac{d\langle H_{\text{C}}\rangle}{dt}. \tag{3.12}$$

The energy current entering the baths is given by

$$J_\alpha^{(\text{E})}(t) = i\langle[H(t), H_\alpha(t)]\rangle\,. \tag{3.13}$$

The energy current flowing in the contact region is

$$J_{\text{C},\alpha}^{(\text{E})}(t) = i\langle[H(t), H_{\text{C},\alpha}(t)]\rangle\,. \tag{3.14}$$

And finally the energy current flowing through the system is expressed as

$$J_{\text{S}}^{(\text{E})}(t) = i\langle[H(t), H_{\text{S}}(t)]\rangle\,. \tag{3.15}$$

On the other hand,

$$\begin{aligned}
\frac{d\langle H\rangle}{dt} &= i\langle[H_{\text{tot}}, H]\rangle + \left\langle\frac{\partial H_{\text{S}}}{\partial t}\right\rangle,\\
\frac{d\langle H_{\text{S}}\rangle}{dt} &= i\langle[H_{\text{tot}}, H_{\text{S}}]\rangle + \left\langle\frac{\partial H_{\text{S}}}{\partial t}\right\rangle,\\
\frac{d\langle H_\alpha\rangle}{dt} &= i\langle[H, H_\alpha]\rangle\,,\\
\frac{d\langle H_{\text{C},\alpha}\rangle}{dt} &= i\langle[H, H_{\text{C},\alpha}]\rangle\,,
\end{aligned} \tag{3.16}$$

where $\left\langle\frac{\partial H_{\text{S}}}{\partial t}\right\rangle = 0$ for static systems. We define the power developed by the ac source as

$$P_{\text{ac}}(t) = \left\langle\frac{\partial H_{\text{S}}}{\partial t}\right\rangle \tag{3.17}$$

and define the power introduced by coupling

$$P_{\text{M}}(t) = i\langle[H_{\text{M}}, H_{\text{S}}]\rangle\,. \tag{3.18}$$

Eq. (3.12) reduces to

$$P_{\text{ac}}(t) + P_{\text{M}}(t) = J_{\text{S}}^{(\text{E})}(t) + P_{\text{M}}(t) + P_{\text{ac}}(t) + \sum_\alpha J_\alpha^{(\text{E})}(t) + \sum_\alpha J_{\text{C},\alpha}^{(\text{E})}(t), \tag{3.19}$$

where we used the fact that $[H_{\text{tot}}, H] = [H_{\text{M}}, H_{\text{S}}]$ and $[H_{\text{tot}}, H_{\text{S}}] = [H_{\text{M}}, H_{\text{S}}] + [H_{\text{C},\alpha}, H_{\text{S}}]$. We obtain

$$J_{\text{S}}^{(\text{E})}(t) + \sum_\alpha J_\alpha^{(\text{E})}(t) + \sum_\alpha J_{\text{C},\alpha}^{(\text{E})}(t) = 0. \tag{3.20}$$

Upon time averaging, the heat current flowing in the contact region

$$J_{C,\alpha}^{(\mathrm{E})} = \frac{1}{\tau}\int_0^\tau J_{C,\alpha}^{(\mathrm{E})}(t)dt = 0, \tag{3.21}$$

and the conservation of energy in the steady state is given by

$$J_{\mathrm{S}}^{(\mathrm{E})} + \sum_\alpha J_\alpha^{(\mathrm{E})} = 0. \tag{3.22}$$

Eqs. (3.20) and (3.22) establish the first law of thermodynamics for the nanoscale devices we will be considering in this thesis. Next we would like to define entropy (S). The power developed by ac source and the power introduced by coupling to a different system are non-conservative and hence associated with dissipation. Therefore, when the baths are kept at a temperature T or have a relatively small thermal bias $\Delta T \ll T$, the net rate of entropy production is given by

$$T\dot{S} = P_{\mathrm{ac}} + P_{\mathrm{M}}. \tag{3.23}$$

Since both effects are dissipative in nature, $P_{\mathrm{ac}}, P_{\mathrm{M}} > 0$ and hence $\dot{S} > 0$. This establishes the second law of thermodynamics for our quantum nanoscale devices.

3.3 EXPERIMENTS ON NANOSCALE QUANTUM THERMAL DEVICES

We shall start with one of the basic properties of nanoscale thermal devices: the quantum of thermal conductance. The quantization of thermal conductance is analogous to the quantization of electrical conductance in nanoscale ballistic devices at low temperature. The limit value of thermal condutance was first proposed theoretically by J. B. Pendry in 1983[36] employing the relation between entropy and the quantum limit of information flow for a finite size system in contact with a reservoir. Later, limiting value of thermal conductance given by $\kappa = \pi^2 k_{\mathrm{B}}^2 T/3h$ in single mode systems was observed in a range of experimental devices: ballistic one dimensional nanostructure[37], metallic islands[38] and single electron transistor[39] to name a few.

Single electron transistors are possible setups for studying quantum properties of thermal transport in nanoscale devices. The possibility of microfabrication has led to the realisation of metallic tunneling junctions with capacitances of the order of $10^{-15}F$. This capacitance corresponds to a charging energy (E_c) of $100\mu eV \approx k_{\mathrm{B}} \times 1.16K$. So, in the sub-Kelvin temperature regime, one would have to overcome the charging energy in order to realize the transport of electrons. This regime, known as Coulomb blockade regime, enables the study of single electron transport. A metallic island is characterized by the "charge state" which is defined through the number of electrons (n) present in the island. Thermometry based on N-I-S tunnel junction[40] can be operated at millikelvin regime and are widely used for thermal analysis in single electron devices. Apart from thermal conductance, single electron transistors have been used to experimentally observe dissipation[41] and transport of heat[27, 42] in nanoscale devices, thermoelectric coefficients[32, 35], negative entropy processes[43], maxwell demon[27] and the rate of information flow[44]. Single electron transistors have also been used to engineer nanoscale thermal machines[42]. On the other hand, thermal transport has also been widely studied in photon based thermal devices. Josephson junctions and LC resonator circuits based on metal-island junctions are the basic components of these devices. Recently,

experiments based on photon based devices have led to the observation of thermal rectification[45] and quantum heat valve[46].

Thermal machines have been miniaturized down to atomic scale, utilizing cold atoms[47], colloidal particles[48, 49], single molecules[50], and moreover even a single atom[51]. The recent experiments are precise up to the level of single particle transport which would have been an impossible tasks some decades back. Regarding refrigerators, absorption refrigeration was recently observed in trapped ions [52]. On a different note, quantum dot based energy harvester was recently observed experimentally by Thierschmann et al [53].

4

THERMAL DRAG IN COULOMB COUPLED SINGLE ELECTRON SYSTEMS

Two electrically isolated conductors placed close together can still be coupled via the Coulomb interaction. As a result, when a bias is only applied to one conductor, electronic currents can be generated in the unbiased one in such a way that a charge current is dragged in this second conductor. This phenomenon, *the Coulomb drag*, arises because the carriers in the two conductors are subject to a "mutual friction", i.e. to scattering processes mediated by the Coulomb interaction between the two conductors, and can exchange momentum and/or energy. The phenomenon of drag, first proposed in 1977 by Pogrebinskii [54] in layered conductors, has so far been studied in a large variety of systems and it is still the subject of an intense research activity (see Ref. [55] for a recent review).

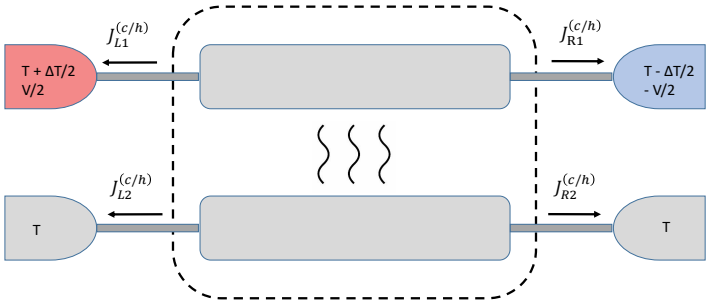

Figure 4.1: Sketch of Coulomb-coupled systems, which consists of an upper (drive) biased circuit, and a lower (drag) unbiased circuit. The conductors are represented as grey rectangles and are attached to two leads each. The two conductors are coupled only through the Coulomb interaction. As indicated by the black arrows, the sign of charge and heat currents is positive when they enter an electrode.

So far most of the attention has been devoted to the effect of drag on the charge current. More recently, the drag of charge between zero-dimensional systems have been theoretically considered for single-level Quantum Dots (QDs) in Refs. [56, 57, 58, 59]. Experimental investigations in systems composed of two capacitively coupled QDs are reported in Ref. [60] (emphasizing the importance of co-tunneling processes [58]) and in Refs. [61, 62] for the case of graphene-based QDs. The drag of charge in coupled double QDs systems has been also experimentally addressed in Ref. [63]. In addition, energy harvesting from thermal and voltage fluctuations in coupled QDs systems attached to three terminals has been considered theoretically [64, 65, 66, 67, 35] and experimentally [68, 69, 70, 71].

Another consequence of the Coulomb coupling between two nearby conductors is the fact that a flow of heat can also be induced in the unbiased

conductor. This phenomenon, which is distinguished from the drag of charge that is constrained by the charge conservation within individual conductors, has been hardly considered in the literature so far [72]. In the case of metallic islands, heat currents can be induced in the unbiased circuit as a result of energy transfer, through the capacitive coupling, from the upper island. Such energy transfer has been recently considered for the implementation of a heat diode [73], of a minimal self-contained quantum refrigeration machine [74], of a three-terminal QD refrigerator [75], of an autonomous Maxwell demon [76], of a Szilard engine [27], of a nanoscale thermocouple heat engine [72], and for the study of a correlation-induced in SINIS refrigerator [77]. In this chapter we will investigate another important case of this kind, *thermal drag*.

The setup we consider is represented in Fig. 4.1. Two mesoscopic conductors, represented by grey rectangles, are coupled through Coulomb interactions, but cannot exchange electrons. One conductor is contained in the upper (drive) circuit, which is either voltage or thermal biased, while the other conductor is part of the lower (drag) circuit, which is unbiased. As specified in Fig. 4.1, the left (right) electrode in the drive circuit is kept at a voltage $\pm V/2$ and temperature $T \pm \Delta T/2$, while the electrodes in the drag circuit are kept at the same temperature T and at zero voltage. Our goal is to study the general properties of the heat currents flowing in the drag circuit, $I^{(\mathrm{h})}_{\mathrm{L2}}$ and $I^{(\mathrm{h})}_{\mathrm{R2}}$, as a result of energy transfer between upper and lower circuits, due to Coulomb interaction.

We define the drag currents as

$$J^{(\mathrm{c/h})}_{\mathrm{drag}} = \frac{J^{(\mathrm{c/h})}_{\mathrm{L2}} - J^{(\mathrm{c/h})}_{\mathrm{R2}}}{2}, \tag{4.1}$$

where $J^{(\mathrm{c})}_{\mathrm{L2}}$ and $J^{(\mathrm{c})}_{\mathrm{R2}}$ are charge currents in the drag circuit. Notice that the charge current is conserved separately on the upper and lower circuit ($J^{(\mathrm{c})}_{\mathrm{L1}} + J^{(\mathrm{c})}_{\mathrm{R1}} = 0$ and $J^{(\mathrm{c})}_{\mathrm{L2}} + J^{(\mathrm{c})}_{\mathrm{R2}} = 0$, respectively). We will focus on the following two cases:

i) A pair of capacitively-coupled metallic islands in the Coulomb blockade regime

ii) A pair of capacitively-coupled quantum dots in the Coulomb blockade regime.

Regarding system i) and ii), we study the general properties of the dragged heat using a master equation approach up to second order tunnelling events (co-tunneling)[78]. We find that the dragged heat current $J^{(\mathrm{h})}_{\mathrm{drag}}$ is finite, even in the cases where the dragged charge vanishes (i. e. when the island-electrode couplings are energy-independent). We study the behavior of the dragged heat current, driven by either a voltage bias V or a thermal bias ΔT, as a function of the various parameters characterizing the system, such as the gate voltages and the capacitive coupling C_{I} between the islands. We find, in particular, that $J^{(\mathrm{h})}_{\mathrm{drag}}$ exhibits a maximum as a function of C_{I}. By expanding the dragged heat current for small values of V or ΔT, we find analytic expressions for $J^{(\mathrm{h})}_{\mathrm{drag}}$ which result quadratic in V or ΔT. We find, moreover, that co-tunneling events yield an important impact on the dragged

heat current, though not changing the quadratic dependence on V or ΔT. Finally, we find that the behavior of the dragged heat current can change qualitatively if one replaces one of the electrodes in the drag circuit with a superconductor. More precisely, under appropriate conditions we find that heat can be extracted from the normal electrode in the drag circuit ($J^{(\mathrm{h})}_{\mathrm{L}2} < 0$). Additionally, the superconductor allows a finite dragged charge current whose sign can be controlled by the gate voltages.

As far as system ii) is concerned, we find similar dependence of the drag heat current on the thermal or potential bias as in system i). However, in the case of QDs, the energy filtering mechanism can be made more efficient. We observe a significant heat flow from one bath to another in the drag when one of the system-bath coupling in the drag is made energy dependent.

The chapter is organized as follows: In the next Section we will discuss the case i) in which the thermal drag occurs in the case of two coupled metallic islands. We will consider the contribution to the drag due to sequential tunneling and co-tunneling. In Section 4.2 we move to consider the second setup of Coulomb coupled quantum dots.

4.1 THERMAL DRAG IN COULOMB COUPLED METALLIC ISLANDS

The first system considered, depicted in Fig. 4.2, consists of two metallic islands (labeled 1 and 2), each one tunnel-coupled to two electrodes and capacitively-coupled to a gate kept at a voltage V_{gi}, with $i = 1, 2$. C_α is the capacitance and $\mathcal{R}_\alpha$ is the resistance associated to the tunnel junction between lead α =Li, Ri and the island i, while C_{gi} is the capacitance associated to the gate. The two metallic islands (assumed to be at equilibrium temperature T) are coupled through a capacitance C_{I}, which does not allow electron transfer. We assume that all capacitances are small so that the charging energies relevant for transport (see below) are the largest energy scales in the system and the islands are in the Coulomb blockade regime. Single electron tunneling processes in each metallic island, thus, are associated to an increase or decrease in the electrostatic energy of the system, which is given by

$$\begin{aligned} E_U(n_1, n_2) = E_{C,1}\,(n_1 - n_{x_1})^2 + E_{C,2}\,(n_2 - n_{x_2})^2 + \\ + E_{\mathrm{I}}\,(n_1 - n_{x_1})\,(n_2 - n_{x_2})\,. \end{aligned} \tag{4.2}$$

Here n_1 and n_2 represent the number of electrons present on island 1 and 2, respectively. $E_{C,i} = e^2/(2C_i)$ is the charging energy of island i (where $C_i = C_{\mathrm{L}i} + C_{\mathrm{R}i} + C_{\mathrm{g}i} + C_{\mathrm{I},i}$, with $C^{-1}_{\mathrm{I},1} = \tilde{C}_2^{-1} + C_{\mathrm{I}}^{-1}$, $C^{-1}_{\mathrm{I},2} = \tilde{C}_1^{-1} + C_{\mathrm{I}}^{-1}$ and $\tilde{C}_i = C_{\mathrm{L}i} + C_{\mathrm{R}i} + C_{\mathrm{g}i}$) and E_{I} is the inter-island interaction energy given by $E_{\mathrm{I}} = e^2(\tilde{C}_1 + \tilde{C}_2 + \tilde{C}_1\tilde{C}_2/C_{\mathrm{I}})^{-1}$. The symbols n_{x1} and n_{x2} represent the "external charges" determined by the gate potentials, $V_{\mathrm{g}1}$ and $V_{\mathrm{g}2}$ respectively, and dependent on the voltage bias V as

$$n_{x1} = \frac{V/2\; C_{\mathrm{L}1} - V/2\; C_{\mathrm{R}1} + V_{\mathrm{g}1}C_{\mathrm{g}1}}{e} \tag{4.3}$$

and

$$n_{x2} = \frac{V_{\mathrm{g}2}C_{\mathrm{g}2}}{e}. \tag{4.4}$$

For the sake of simplicity, we will assume that $C_{\mathrm{g}1} = C_{\mathrm{g}2} \equiv C_{\mathrm{g}}$ and that all the capacitances relative to the tunnel junctions are equal, namely $C_{\mathrm{L}1} = C_{\mathrm{R}1} = C_{\mathrm{L}2} = C_{\mathrm{R}2}$, so that $C_1 = C_2 \equiv C$ and we can define the charging energy $E_C = e^2/(2C)$. Note that n_{x1} becomes independent of V and takes the same form as n_{x2}.

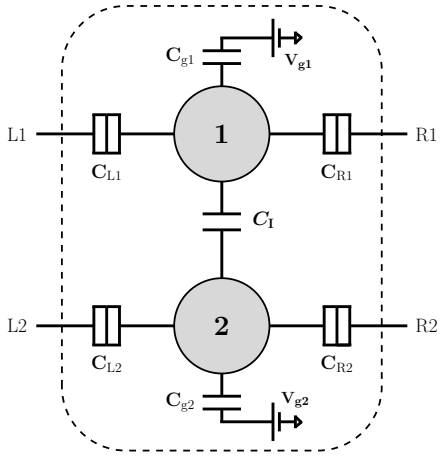

Figure 4.2: Sketch of the first system under consideration composed of two capacitively-coupled metallic islands labeled by 1 (in the drive circuit) and 2 (in the drag circuit). L1, L2, R1 and R2 labels the four electrodes which are tunnel-coupled to the islands.

Charge $J_\alpha^{(c)}$ and heat $J_\alpha^{(h)}$ currents can be expressed in terms of the probability for the occupation of the islands, and the transition rates for electrons to be exchanged between the islands and an electrodes. The actual expressions for the currents depend on whether one has to account for only first order tunneling processes (sequential tunneling regime) or second order processes have to be considered too (co-tunneling). The probability $p(n_1, n_2)$ for the occupation of island 1 with n_1 electrons and island 2 with n_2 electrons is determined through a set of master equations (see App. D) which accounts for all possible tunneling processes in the system.

4.1.1 *Sequential tunneling regime*

Within the sequential tunneling regime, we have that the charge and heat currents in the lower circuit take the form

$$J_\alpha^{(c/h)} = Q^{(c/h)}\Big[\Gamma_{\alpha,2}^{(c/h)}(n_1,n_2)\,p(n_1,n_2) + \Gamma_{\alpha,2}^{(c/h)}(n_1+1,n_2)\,p(n_1+1,n_2) - \Gamma_{2,\alpha}^{(c/h)}(n_1,n_2)\,p(n_1,n_2+1) - \Gamma_{2,\alpha}^{(c/h)}(n_1+1,n_2)\,p(n_1+1,n_2+1)\Big], \quad (4.5)$$

respectively, where $\alpha =$ L2, R2 and $Q^{(c)} = e$, $Q^{(h)} = 1$. We have assumed small temperatures and biases so that only four charge states contribute to transport, namely (n_1, n_2), (n_1+1, n_2), (n_1, n_2+1) and (n_1+1, n_2+1). In Eq. (4.5), $\Gamma_{\alpha,i}^{(c/h)}(n_1, n_2)$ is the particle/heat transition rate for an electron to reach island i from lead α [with the island initially in the state (n_1, n_2)], and $\Gamma_{i,\alpha}^{(c/h)}(n_1, n_2)$ is the particle/heat transition rate for an electron leaving island i to reach lead α [with the island in the final state (n_1, n_2)]. As long as the energy-dependence of the lead-island couplings[1] can be disregarded (see Sec. 4.1.3, where this assumption will be lifted), the particle and heat transition rates can be written as

$$\Gamma_{\alpha,i}^{(c/h)}(n_1,n_2) = \frac{1}{e^2\mathcal{R}_\alpha} F_{\alpha i}^{(c/h)}[\delta E_{Ui}(n_1,n_2) - eV_\alpha], \quad (4.6)$$

1 Lead-island couplings are energy-dependent when their tunnelling matrix elements depend on energy or when at least one density of states (of the lead or of the island) depend on energy.

and

$$\Gamma^{(c/h)}_{i,\alpha}(n_1,n_2) = \frac{1}{e^2\mathcal{R}_\alpha} G^{(c/h)}_{i\alpha}[\delta E_{Ui}(n_1,n_2) - eV_\alpha]. \tag{4.7}$$

In Eqs. (4.6) and (4.7) the functions $F^{(c/h)}_{\alpha i}$ and $G^{(c/h)}_{i\alpha}$ are defined as

$$F^{(c/h)}_{\alpha i}(E) = \int_{-\infty}^{+\infty} d\epsilon\, z^{(c/h)} f_\alpha(\epsilon)[1 - f_i(\epsilon - E)], \tag{4.8}$$

$$G^{(c/h)}_{i\alpha}(E) = \int_{-\infty}^{+\infty} d\epsilon\, z^{(c/h)} f_i(\epsilon - E)[1 - f_\alpha(\epsilon)], \tag{4.9}$$

where $f_k(\epsilon) = (1 + e^{\epsilon/k_B T_k})^{-1}$ is the Fermi distribution at temperature T_k, and $z^{(c)} = 1$, $z^{(h)} = \epsilon$. The two quantities

$$\begin{aligned} \delta E_{U1}(n_1,n_2) &= E_U(n_1+1,n_2) - E_U(n_1,n_2) \\ \delta E_{U2}(n_1,n_2) &= E_U(n_1,n_2+1) - E_U(n_1,n_2) \end{aligned} \tag{4.10}$$

represent the jumps in the electrostatic energy related to the transitions [note that they appear in Eqs. (4.8-4.9) as chemical potentials of the islands]. In the case where all temperatures are equal to T, Eqs. (4.6) and (4.7) for the charge reduce to

$$\Gamma^{(c)}_{\alpha,2}(n_1,n_2) = \frac{1}{e^2\mathcal{R}_\alpha} \frac{\delta E_{U2}(n_1,n_2)}{\exp\left[\frac{\delta E_{U2}(n_1,n_2)}{k_B T}\right] - 1}, \tag{4.11}$$

and

$$\Gamma^{(c)}_{2,\alpha}(n_1,n_2) = \frac{1}{e^2\mathcal{R}_\alpha} \frac{-\delta E_{U2}(n_1,n_2)}{\exp\left[\frac{-\delta E_{U2}(n_1,n_2)}{k_B T}\right] - 1}. \tag{4.12}$$

The assumption of energy-independent couplings allows us to make general statements thanks to the fact that the currents $J^{(c/h)}_\alpha$ are proportional to $1/\mathcal{R}_\alpha$. In the lower circuit, in particular, the proportionality constants are equal for the two leads (i. e., $J^{(c)}_{L2}\mathcal{R}_{L2} = J^{(c)}_{R2}\mathcal{R}_{R2}$ and $J^{(h)}_{L2}\mathcal{R}_{L2} = J^{(h)}_{R2}\mathcal{R}_{R2}$) since no biases are applied. As far as charge is concerned, current conservation in the lower circuit ($J^{(c)}_{L2} + J^{(c)}_{R2} = 0$) implies that the individual charge currents in the lower circuit vanish identically, and therefore $J^{(c)}_{drag}$ is zero even in the case of asymmetric barriers ($\mathcal{R}_{L2} \neq \mathcal{R}_{R2}$). On the other hand, no conservation holds for the heat currents[2] in the lower circuit so that the two heat currents, $J^{(h)}_{L2}$ and $J^{(h)}_{R2}$, are in general non-vanishing. In particular, for symmetry reasons they are equal when $\mathcal{R}_{L2} = \mathcal{R}_{R2}$, and therefore $J^{(h)}_{drag}$ is finite only in the case of asymmetric barriers. The presence of heat currents in the lower circuit is a result of the energy transferred from the upper circuit, thanks to the capacitive coupling. Indeed, as detailed in the following, this energy transfer occurs through the dependence of δE_{U2}, which controls the transition rates for the lower island, on the charge state of the upper island n_1, see Eq. (4.10).

For the sake of definiteness, let us assume that the relevant charge states are $(0,0)$, $(0,1)$, $(1,0)$ and $(1,1)$. Thus the jumps in electrostatic energy related to the currents in the lower island are

$$\delta E_{U2}(0,0) = E_C(1 - 2n_{x2}) - E_I n_{x1}, \tag{4.13}$$

2 The energy current, defined as $J^{(e)}_{\alpha i} = J^{(h)}_{\alpha i} + eV_{\alpha i} J^{(c)}_{\alpha i}$, is not conserved even globally (apart from specific values of the temperatures of the islands). Indeed, fixing the temperature of the islands is equivalent to connect the islands to electrodes, thus allowing them to exchange energy with the "environment".

for the case where the upper island is empty, and

$$\delta E_{U2}(1,0) = E_C(1-2n_{x2}) + E_I(1-n_{x1}), \tag{4.14}$$

for the case where the upper island is occupied. Equations (4.13) and (4.14) express the fact that the position of the two chemical potentials $\delta E_{U2}(0,0)$ and $\delta E_{U2}(1,0)$ of the lower island, with respect to common equilibrium electrochemical potential of the lower leads (set to zero), is expressed in terms of n_{x1} and n_{x2}. When $n_{x1} = n_{x2} = 1/2$ we obtain $\delta E_{U2}(0,0) = -E_I/2$ and $\delta E_{U2}(1,0) = +E_I/2$. The energy scheme for the lower island is represented in Fig. 4.3a) for the former case and in panel Fig. 4.3b) for the latter case. If we assume a small temperature T, an electron can jump on the island from one of the electrodes only when the upper island is empty, since the corresponding chemical potential $\delta E_{U2}(0,0)$ is below the electrochemical potential of the leads, see panel a). Such an electron can jump out of the island only when the upper island gets occupied, since the chemical potential $\delta E_{U2}(1,0)$ is now greater than zero. This sequence of processes allows the heat currents $J^{(h)}_{L2}$ and $J^{(h)}_{R2}$ to be finite as long as the interaction energy $E_I \neq 0$. Such heat currents can be modulated by varying n_{x1} and n_{x2}, which produces a rigid shift of the position of the two chemical potentials $\delta E_{U2}(0,0)$ and $\delta E_{U2}(1,0)$, see Eqs. (4.13) and (4.14). Note that the difference $\delta E_{U2}(1,0) - \delta E_{U2}(0,0) = E_I$, independently of n_{x1} and n_{x2}.

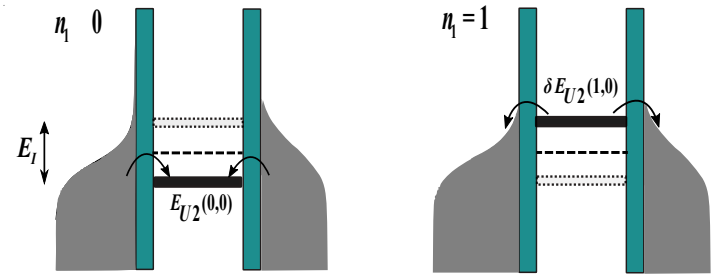

Figure 4.3: Energies scheme for the lower, drag, circuit. Green rectangles represent the tunnel barriers. Grey areas represent the Fermi distribution functions of the leads, whose common equilibrium electrochemical potential, set to zero, is indicated by a dashed line. Thick horizontal black lines indicate the position of the chemical potential of the island for $n_{x1} = n_{x2} = 1/2$. a) The upper island is empty and the chemical potential is $\delta E_{U2}(0,0)$: electrons can jump on the island. b) The upper island is occupied and the chemical potential is $\delta E_{U2}(1,0)$: electrons can jump out of the island.

Analytic, even though cumbersome, expressions for the heat currents could be derived in the limit of small biases V and ΔT. Interestingly, heat currents turn out to be second order in V and ΔT (note that the heat currents in the upper circuit are first order in V and ΔT). In particular, when $n_{x1} = n_{x2} = 1/2$, the dragged heat current takes the simple form

$$J^{(h)}_{drag} = \frac{\xi \mathcal{R}_\parallel}{16\mathcal{R}}\left[\frac{1}{\mathcal{R}_{L2}} - \frac{1}{\mathcal{R}_{R2}}\right] \operatorname{csch}\xi\,[\xi \operatorname{csch}\xi - \operatorname{sech}\xi]\,V^2, \tag{4.15}$$

when $\Delta T = 0$ and expanding in V/E_C, while

$$J^{(h)}_{drag} = \frac{\xi \mathcal{R}_\parallel}{6e^2\mathcal{R}}\left[\frac{1}{\mathcal{R}_{L2}} - \frac{1}{\mathcal{R}_{R2}}\right] \operatorname{csch}\xi\left[2\xi\left(\frac{\pi^2}{4}+\xi^2\right)\operatorname{csch}\xi - \left(\frac{\pi^2}{2}+3\xi^2\right)\operatorname{sech}\xi\right](k_B\Delta T/2)^2, \tag{4.16}$$

when $V = 0$ and expanding in $\Delta T/T$ (only the leading terms in $k_B\Delta T/E_C$ are retained)[3] In Eqs. (4.15) and (4.16) we have defined $\xi = E_I/(4k_BT)$ and

$$\mathcal{R}_{\parallel} = \left(\frac{2}{\mathcal{R}} + \frac{1}{\mathcal{R}_{L2}} + \frac{1}{\mathcal{R}_{R2}}\right)^{-1}, \tag{4.17}$$

and assumed $\mathcal{R}_{L1} = \mathcal{R}_{R1} = \mathcal{R}$. Eqs. (4.15) and (4.16) show that the dragged heat current is finite only when the interaction energy $E_I \neq 0$ and depends on E_I only through the ratio $E_I/(k_BT)$ (this is true only when $n_{x1} = n_{x2} = 1/2$). Moreover, we mention that in the presence of both voltage and thermal biases the contribution to the dragged heat current is proportional to the product $V\Delta T$ and exhibits the same qualitative behavior as for the voltage or thermal bias only case. For $n_{x1} = n_{x2} = 1/2$ such contribution vanishes. More manageable expressions can be obtained by further expanding in

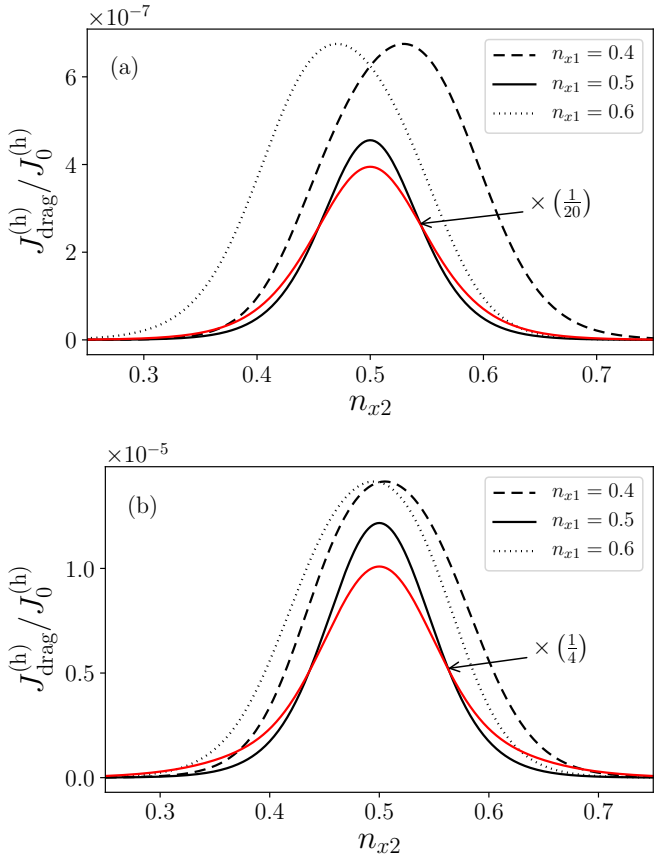

Figure 4.4: Dragged heat currents plotted as functions of n_{x2} for different values of n_{x1}. The results accounting for sequential tunneling only are plotted in black, while results including co-tunneling contributions are plotted in red. $\mathcal{R}_{L1} = \mathcal{R}_{R1} = \mathcal{R}_{L2} = 5\mathcal{R}_Q$, $\mathcal{R}_{R2} = 10\mathcal{R}_Q$, $k_BT = 0.05E_C$, and $E_I = 0.4E_C$. (a) $\Delta T = 0$ and $V = 0.08E_C/e$; (b) $V = 0$ and $\Delta T = 0.08E_C/k_B$. The solid curves have been multiplied by a factor $1/20$ in panel (a) and by a factor $1/4$ in panel (b). The heat current is given in units of $J_0^{(h)} = e^2/(4C^2\mathcal{R})$.

powers of the interaction energy E_I, namely we get

$$J^{(h)}_{drag} = \left[\frac{1}{\mathcal{R}_{L2}} - \frac{1}{\mathcal{R}_{R2}}\right]\frac{\mathcal{R}_{\parallel}\xi^2}{48\mathcal{R}}V^2, \tag{4.18}$$

3 Note that the cross-term $V\Delta T$ vanishes when $n_{x1} = n_{x2} = 1/2$.

when $\Delta T = 0$, and

$$J^{(\mathrm{h})}_{\mathrm{drag}} = \left[\frac{1}{\mathcal{R}_{\mathrm{L2}}} - \frac{1}{\mathcal{R}_{\mathrm{R2}}}\right] \frac{\left(\pi^2 - 6\right)\mathcal{R}_{\parallel}\xi^2}{36e^2\mathcal{R}} \left(k_B \Delta T/2\right)^2 \tag{4.19}$$

when $V = 0$. Note that both expressions are second order in E_{I}.

Let us now concentrate on the dependence of the dragged heat current $J^{(\mathrm{h})}_{\mathrm{drag}}$ on the external charges, i. e. on the gate voltages, and show numerical results for the asymmetric barriers case specified by $\mathcal{R}_{\mathrm{R2}} = 10\mathcal{R}_{\mathrm{Q}}$, $\mathcal{R}_{\mathrm{L2}} = 5\mathcal{R}_{\mathrm{Q}}$ ($\mathcal{R}_{\mathrm{Q}} = e^2/h$ is the resistance quantum), while setting $k_B T = 0.05 E_C$, $\mathcal{R} = \mathcal{R}_{\mathrm{L1}} = \mathcal{R}_{\mathrm{R1}} = 10\mathcal{R}_{\mathrm{Q}}$, and $E_{\mathrm{I}} = 0.4 E_C$. In Fig. 4.4 we plot the dragged heat current as a function of n_{x2} (determined by the gate voltage acting on island 2) for three different fixed values of n_{x1}. The black curves accounts for sequential tunneling processes only (solid $n_{x1} = 0.5$, dashed $n_{x1} = 0.4$ and dotted $n_{x1} = 0.6$), while the red solid curve accounts also for co-tunneling contributions (see below). In Fig. 4.4a) and 4.4b) the currents are, respectively, a result of a voltage bias V (with $\Delta T = 0$) or a thermal bias ΔT (with $V = 0$).

Fig. 4.4a) shows that when $n_{x1} = 1/2$, solid curve, $J^{(\mathrm{h})}_{\mathrm{drag}}$ exhibits a peak at $n_{x2} = 1/2$, while the peak is shifted to a larger (smaller) value of n_{x2} when $n_{x1} = 0.4$ ($n_{x1} = 0.6$). This effect can be understood by noticing that the dragged heat current is expected to be maximal when the two chemical potentials of the lower island $\delta E_{U2}(1,0)$ and $\delta E_{U2}(0,0)$ are *equidistant* with respect to the equilibrium electrochemical potential set by the electrodes [see Fig. 4.3]. In this case, in fact, the heat transition rate for an electron to enter the island from the left lead (non-vanishing only if $n_1 = 0$) is equal to the heat transition rate for an electron to leave the island to go to the left lead (non-vanishing only if $n_1 = 1$). By departing from the equidistant configuration, one of the two rates gets suppressed resulting in a suppression of the heat current.[4] For $n_{x1} = 1/2$ the equidistant configuration occurs when $n_{x2} = 1/2$, while when $n_{x1} = 0.4$ ($n_{x1} = 0.6$) the equidistant configuration occurs when $n_{x2} = 0.5 + 0.05\, E_{\mathrm{I}}/E_{\mathrm{C}} > 1/2$ ($n_{x2} = 0.5 - 0.05\, E_{\mathrm{I}}/E_{\mathrm{C}} < 1/2$). Notice that the value of $J^{(\mathrm{h})}_{\mathrm{drag}}$ is over one order of magnitude bigger in the case $n_{x1} = 1/2$, with respect to the cases $n_{x1} = 0.4$ and $n_{x1} = 0.6$. The reason for this behavior is related to the fact that in the former case the heat current in the drive circuit (and therefore the energy transferred in the lower circuit) is maximum.

We checked that the position and the shape of the peaks does not change by varying the value of V, while the maximum value increases with it. On the contrary, an increase in the temperature T produces a proportional increase in the width of the peaks ($\Delta n_{x2} \simeq 2k_B T/E_C$), on the one hand, and a decrease in the separation between the peaks at $n_{x2} = 0.4$ and at $n_{x2} = 0.6$, on the other. Thus, temperature seems to have a less intuitive effect on the dragged heat current. Remarkably, the width of the peaks is virtually independent of E_{I}. In Fig. 4.4b) we show plots of the dragged heat current in the presence of a thermal bias in the drive circuit. The behavior of $J^{(\mathrm{h})}_{\mathrm{drag}}$ in this case is similar to the one in the presence of a voltage bias, with the following little differences: i) the value of the heat current for the cases $n_{x1} = 0.4$ and $n_{x1} = 0.6$ is not dramatically suppressed with respect to the $n_{x1} = 1/2$ case (a factor 4 with respect to a factor 20); ii) the shift in the positions of the peaks for the cases $n_{x1} = 0.4$ and $n_{x1} = 0.6$ is smaller with respect to the voltage-bias case.

4 For $n_{x2} > 1/2$ the two chemical potentials shift downwards, thus reducing the rate for exiting the island. For $n_{x2} < 1/2$ the two chemical potentials shift upwards, thus reducing the rate for entering the island.

Let us now concentrate on the role of E_I on the dragged heat current. Notice that the interaction energy can be expressed as

$$E_I = E_C \frac{2}{1 + \frac{\tilde{C}}{C_I}}, \tag{4.20}$$

where $\tilde{C} \equiv \tilde{C}_1 = \tilde{C}_2$, and that it is bounded by the inequality $E_I \leq 2E_C$. In Fig. 4.5, $J^{(h)}_{drag}$ is plotted as a function of E_I for the voltage bias case (dashed red line) and for the thermal bias case (solid black line) for $n_{x1} = n_{x2} = 1/2$. As a general feature, we note that the dragged heat current is maximal for intermediate values of E_I. This agrees with the fact that, on the one hand, $J^{(h)}_{drag}$ must decrease for large values of E_I as a consequence of the fact that the probability $p(1,1)$, thus the occurrence of the process depicted in Fig. 4.3(b), gets suppressed (indeed, E_I represents the inter-island Coulomb repulsion which hinders the occupation of the lower island when the upper island is occupied). On the other hand, $J^{(h)}_{drag}$ vanishes for $E_I = 0$ due to the absence of electrostatic coupling. In Fig. 4.5, while the thick lines are numerical results, the thin lines are the analytical solutions for small voltage and temperature biases, Eqs. (4.15) and (4.16). It worthwhile stressing that while the red curves coincide, the black curves closely match only for $E_I < 0.2E_C$ and thereafter depart significantly. This is due to the fact that, despite $k_B\Delta T$ is small with respect to E_C, $k_B\Delta T$ is larger than k_BT and Eq. (4.16) does not hold. Nevertheless, the position of the maxima E_I^{max} are well predicted by the analytical expressions, Eqs. (4.15) and (4.16), even for larger values of ΔT and V. The solution of a transcendent equation yield $E_I^{max} \simeq 5.5k_BT$, for the voltage bias case, and $E_I^{max} \simeq 8.5k_BT$, for thermal bias case. Finally, unlike Eqs. (4.15) and (4.16), we notice that $J^{(h)}_{drag}$ at $n_{x1} = n_{x2} = 1/2$ for large enough V and ΔT depends on E_I not only through the ratio $E_I/(k_BT)$.

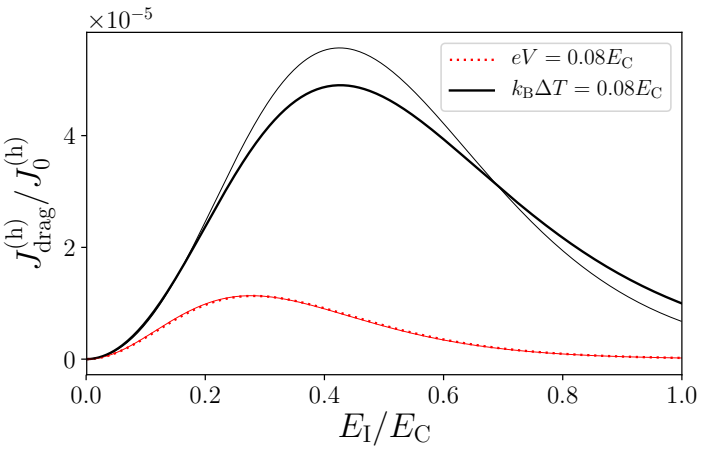

Figure 4.5: Dragged heat current (sequential tunneling only) plotted as a function of E_I for the case $V = 0.08E_C$ and $\Delta T = 0$ (red lines) the case $\Delta T = 0.08E_C$ and $V = 0$ (black lines) for $n_{x1} = n_{x2} = 1/2$. Thin black and red curves are plots of the analytic expressions Eqs. (4.15) and (4.16), respectively. The other parameters are chosen as follows: $\mathcal{R}_{L1} = \mathcal{R}_{R1} = \mathcal{R}_{L2} = 5\mathcal{R}_Q$, $\mathcal{R}_{R2} = 10\mathcal{R}_Q$, and $k_BT = 0.05E_C$.

We conclude this section by comparing the heat current in the drive circuit, for example $J^{(h)}_{R1}$, with the one in the drag circuit, for example $J^{(h)}_{R2}$. In the

case of a thermal bias, it turns out that $J^{(\mathrm{h})}_{\mathrm{R2}} < J^{(\mathrm{h})}_{\mathrm{R1}}$, as expected from the fact that $J^{(\mathrm{h})}_{\mathrm{R1}}$ is linear in ΔT, while $J^{(\mathrm{h})}_{\mathrm{R2}}$ is quadratic in ΔT (at least for small values of ΔT). In the voltage-bias case, surprisingly, we find that $J^{(\mathrm{h})}_{\mathrm{R2}}$ is larger than $J^{(\mathrm{h})}_{\mathrm{R1}}$ for large enough interaction energy, as shown in Fig. 4.6, where the crossing occurs at $E_{\mathrm{I}}^{\mathrm{cross}} \simeq 0.4E_C$. More precisely, the value of $E_{\mathrm{I}}^{\mathrm{cross}}$ decreases linearly by decreasing T, thereafter saturating, for small T, to a finite value of $E_{\mathrm{I}}^{\mathrm{cross}} \sim eV$, i. e. very close to the applied voltage.

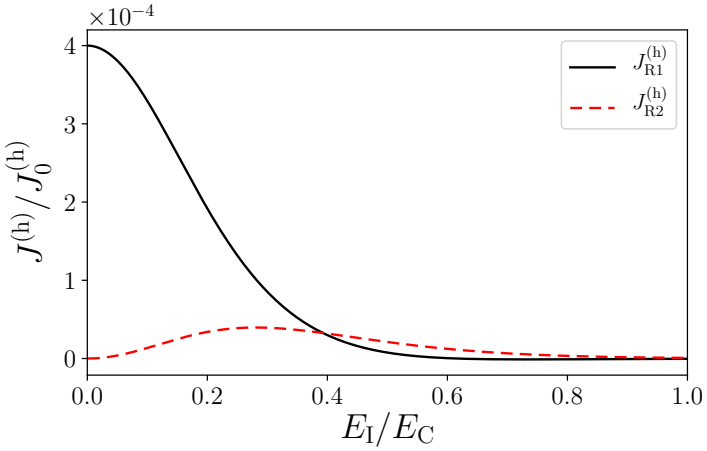

Figure 4.6: Heat currents $J^{(\mathrm{h})}_{\mathrm{R1}}$ (solid black curve) and $J^{(\mathrm{h})}_{\mathrm{R2}}$ (dashed red curve) plotted as a function of E_{I} for the case $\Delta T = 0$ and accounting for sequential tunneling only. The other parameters are chosen as follows: $\mathcal{R}_{\mathrm{L1}} = \mathcal{R}_{\mathrm{L2}} = \mathcal{R}_{\mathrm{R1}} = \mathcal{R}_{\mathrm{R2}} = 10\mathcal{R}_{\mathrm{Q}}$, $n_{x1} = n_{x2} = 1/2$, $V = 0.08E_C/e$, and $k_{\mathrm{B}}T = 0.05E_C$.

4.1.2 *Co-tunnelling contributions*

When the barriers' resistances do not largely exceed the resistance quantum $\mathcal{R}_Q$ and temperatures are low, it is important to account for second-order tunneling events (co-tunneling contributions). Given the large number of electrons in the islands, we will only consider inelastic co-tunneling. Co-tunneling contributions affect the expressions of the currents (4.5), see App. D.3, and the master equations, see App. D.1, by introducing additional terms. These are related to the co-tunneling particle and heat transition rates involving an electron entering or leaving island 1 through the upper leads and a second electron entering or leaving island 2 through the lower leads (see App. D.2). In the present situation, where there are no voltage and temperature biases applied to the drag (lower) circuit, the number of processes that contributes to the current in L2 (R2) is limited to the ones that involve a tunneling event between island 2 and its lead L2 (R2) and all possible tunneling events between island 1 and its leads L1 and R1 (see App. D.3 for the expression of the current $J^{(\mathrm{h})}_{\mathrm{R2}}$). We were able to obtain analytical expressions for charge and heat currents only in the voltage-biased case.

Due to the energy-independence of lead-island couplings, also in the presence of co-tunneling contributions the currents $J^{(\mathrm{c/h})}_{\alpha}$ remain proportional to $1/\mathcal{R}_\alpha$ in such a way that the charge currents in the drag circuit vanish also in the case of asymmetric barriers ($\mathcal{R}_{\mathrm{L2}} \neq \mathcal{R}_{\mathrm{R2}}$). On the contrary, the dragged heat currents, which are non-zero even for sequential tunneling, can give rise to quantitatively important changes (when resistances are small and

temperatures are low). As shown in Fig. 4.4 (red curves), co-tunneling gives rise to a broadening and lowering of the peaks with respect to the sequential tunneling only case (solid black curves), both in the voltage and thermal bias cases.

In Fig. 4.7, $J^{(\mathrm{h})}_{\mathrm{drag}}$ is plotted as a function of V, for $\Delta T = 0$, in a wide range of voltages up to $0.4E_C$. The solid black curve accounts for sequential tunneling only, while the red dashed curve includes co-tunneling events. Fig. 4.7 shows that co-tunneling events produce an increase of the dragged heat current for values of V in the lower range and a decrease in the upper range. This reflects the fact that, for low voltages, co-tunneling contributions becomes dominant since the Coulomb gap does not allow for first order transport processes (sequential tunneling) [60, 57]. Finally, we numerically check that, for small voltage and temperature biases, $J^{(\mathrm{h})}_{\mathrm{drag}}$ remains quadratic in V and ΔT even when co-tunneling contributions are important. For the specific choice of parameters used in Fig. 4.7, we get that $J^{(\mathrm{h})}_{\mathrm{drag}}$ remains proportional to V^2 up to $V \sim 0.05E_C/e$, when sequential tunneling only is accounted for, while up to $V \sim 0.1E_C/e$, when co-tunneling is also included.

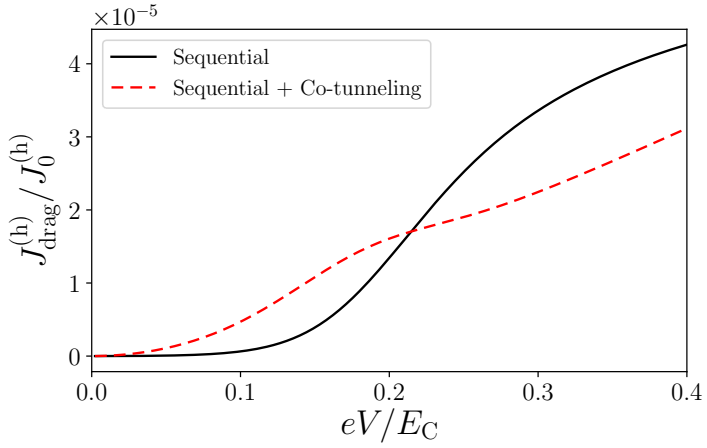

Figure 4.7: Dragged heat current $J^{(\mathrm{h})}_{\mathrm{drag}}$ plotted as a function of V accounting for sequential tunneling only (solid black line) and including co-tunneling contributions (dashed red line) for $\Delta T = 0$ and $n_{x1} = n_{x2} = 0.478$. The other parameters are chosen as follows: $\mathcal{R}_{\mathrm{L1}} = \mathcal{R}_{\mathrm{R1}} = \mathcal{R}_{\mathrm{L2}} = 2\mathcal{R}_{\mathrm{Q}}$, $\mathcal{R}_{\mathrm{R2}} = 4\mathcal{R}_{\mathrm{Q}}$, $E_{\mathrm{I}} = 0.1E_C$ and $k_{\mathrm{B}}T = 0.01E_C$.

4.1.3 *Superconducting electrode*

In this section we assume that one of the electrodes in the drag circuit (the right-hand one, R2, for definiteness) is superconducting. This case is interesting since the transition rates cannot be written as in Eqs. (4.6) and (4.7). Indeed, the particle transition rates $\Gamma^{(\mathrm{c})}_{R2,2}(n_1, n_2)$ can be written as [79]

$$\Gamma^{(\mathrm{c})}_{R2,2}(n_1, n_2) = \frac{4\pi}{\hbar}\int d\epsilon \int d\epsilon' \, |t(\epsilon)|^2 \rho_{R2}(\epsilon)\rho_2(\epsilon') f_{R2}(\epsilon) \times \left[1 - f_2(\epsilon')\right] \delta\left[\epsilon' - \epsilon + \delta U_2(n_1, n_2)\right], \tag{4.21}$$

where $\rho_{R2}(\epsilon)$ [$\rho_2(\epsilon)$] is the density of states (DOS) of the superconducting lead R2 (island 2) and $t(\epsilon)$ is the tunneling matrix element of the junction

(the heat transition rates are defined analogously). The DOS of the electrode R2 is given by

$$\rho_{\mathrm{R2}}(\epsilon) = \rho_{\mathrm{R2}}^{\mathrm{nor}} \Theta\left[|\epsilon| - \Delta\right] \frac{|\epsilon|}{\left(\epsilon^2 - \Delta^2\right)^{1/2}}, \tag{4.22}$$

where $\rho_{\mathrm{R2}}^{\mathrm{nor}}$ is the DOS of the electrode in the normal state, Θ is the Heaviside step function, and Δ is the superconducting gap. We assume that $\Delta \ll E_C$, so that Andreev reflection is largely suppressed [79], and $\mathcal{R}_{\mathrm{R2}}^{\mathrm{nor}} \gg \mathcal{R}_Q$, so that sequential tunneling of quasi-particles becomes the dominant process. $\mathcal{R}_{\mathrm{R2}}^{\mathrm{nor}}$ is defined as the normal state tunnel resistance of the junction R2, namely

$$\frac{1}{\mathcal{R}_{R2}^{\mathrm{nor}}} = \frac{4\pi e^2}{\hbar} \rho_2 \, \rho_{R2}^{\mathrm{nor}} \, |t|^2 , \tag{4.23}$$

since the tunneling matrix element is energy-independent. Notice that Eq. (4.21) reduces to Eq. (4.6) when the energy-dependence of the tunneling matrix elements and of the DOS of lead and island can be disregarded.

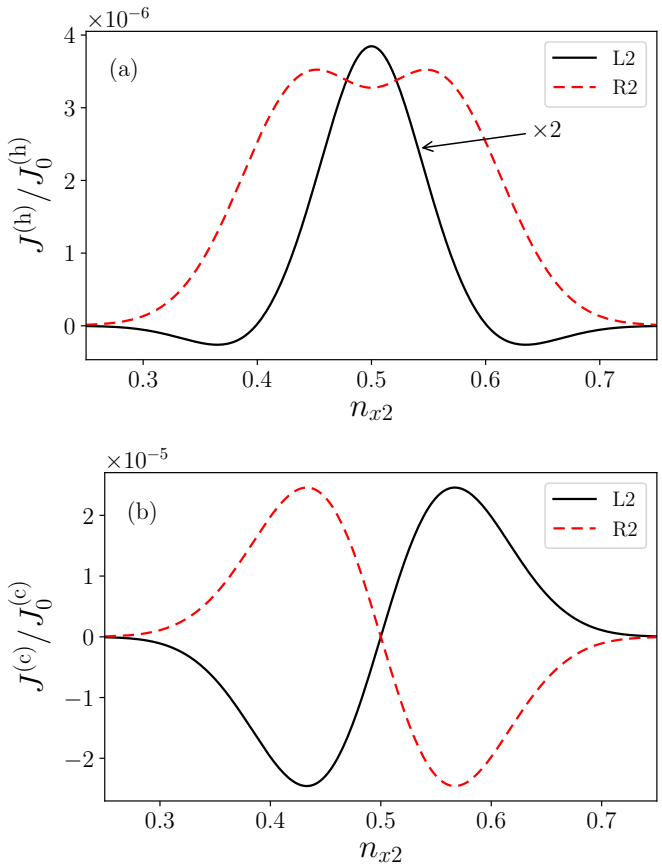

Figure 4.8: Heat (a) and charge (b) drag currents versus n_{x2} for fixed $n_{x1} = 1/2$ in the case where R2 is a superconducting electrode. The other parameters are chosen as follows: $\mathcal{R}_{\mathrm{L1}} = \mathcal{R}_{\mathrm{R1}} = \mathcal{R}_{\mathrm{R2}} = \mathcal{R} = 5\mathcal{R}_{\mathrm{Q}}$, $\mathcal{R}_{\mathrm{L2}} = 200\mathcal{R}_{\mathrm{Q}}$, $E_{\mathrm{I}} = 0.3E_C$, $k_BT = 0.05E_C$, $\Delta = 0.4E_C$. The charge current is given in units of $J_0^{(\mathrm{c})} = e/(2C\mathcal{R})$. Charge drag current (b) is obtained by applying a thermal bias $k_B\Delta T = 0.08E_C$, whereas the heat drag current (a) is obtained by applying a voltage bias $\Delta V = 0.08E_{\mathrm{C}}/e$.

As shown in Fig. 4.8(a), the heat currents in the drag circuit (due to a voltage bias in the drive circuit) plotted as a function of n_{x2}, with $n_{x1} = 1/2$,

exhibit a qualitatively different behavior when compared with the energy-independent case. Namely, $J^{(h)}_{R2}$ [dashed red curve in Fig. 4.8(a)] is not a bell-shape function, but rather presents two maxima, symmetric with respect to $n_{x2} = 1/2$, separated by a shallow dip. This behaviour is a result of the peculiar energy-dependence of the DOS of the superconductor, which presents a gap around the equilibrium electrochemical potential and narrow peaks at $\epsilon = \pm\Delta$ [see Eq. (4.22)]. The former, on the one hand, suppresses the transfer of quasi-particles in and out of the right electrode R2 when $n_{x2} \simeq 1/2$, see Fig. 4.9(a), thus producing a dip in $I^{(h)}_{R2}$. The narrow peaks, on the other hand, promote such transfer when $n_{x2} = 1/2 - \Delta/(2E_C) + E_I/(4E_C)$, i. e. when n_{x2} is such that $\delta E_{U2(0,0)}$ $[\delta U_2(1,0)]$ is close to $\mp\Delta$ [see the sketch in Fig. 4.9(c)], inducing an enhancement of the heat flow into the electrode R2.

Let us now consider the behavior of $J^{(h)}_{L2}$, represented by the solid black curve in Fig. 4.8(a). Remarkably, $J^{(h)}_{L2}$ takes negative values for $n_{x2} \simeq 0.6$ and $n_{x2} \simeq 0.4$, which means that heat is extracted from electrode L2. We observe that such heat extraction is related (occurring roughly at the same values of n_{x2}) to the peaks in the heat current entering R2. One could intuitively imagine that the heat extracted from L2 results from a "compensation" of the enhanced heat flow entering R2. We point out that heat extraction occurs only when three conditions are met, namely when $k_B T < E_I$, $E_I \approx \Delta$ and $\mathcal{R}_{L2}$ is larger than the other tunnel resistances.

Furthermore, we find that the superconducting electrode R2 allows a finite thermoelectric drag of charge current. Fig. 4.8(b) shows the dragged charge thermocurrent (i. e. due to a thermal bias in the drive circuit) plotted as a functions of n_{x2}, for a fixed $n_{x1} = 1/2$. The dragged charge thermocurrent, on the one hand, vanishes at $n_{x2} = 1/2$ because of the symmetric energy configuration [see Fig. 4.9(a)]. For $n_{x2} < 1/2$, however, the two chemical potentials shift up [see Fig. 4.9(c))] so that the up most one matches the peak of the DOS of the superconductor, thus favouring a charge current flowing towards the right, i. e. $J^{(c)}_{R2}$ becomes positive. For $n_{x2} > 1/2$, an analogous argument holds for which the transfer of holes towards the right is favoured when the down most chemical potential matches the peak of the DOS of the superconductor [see Fig. 4.9(b)], so that $J^{(c)}_{R2}$ takes negative values.

We remark that the necessity for energy-dependent lead-island couplings in the drag circuit, in order to obtain a drag of charge, was discussed for single-level QD-based Coulomb-coupled systems in Refs. [57], [58], [60], [61] and [62], in the presence of a voltage bias. Energy-dependent couplings were introduced through the dependence on the charge state of the QDs of the transition rates between leads and QD, in Refs. [57] and [60], and through the linear energy dependence of the DOS of graphene in Refs. [61] and [62]. These mechanisms, however, are not realistic for metallic islands.

Finally, we wish to mention that, in the limit of small biases, both $J^{(c)}_{drag}$ and $J^{(h)}_{drag}$ are second order in V or ΔT, independently of the values of n_{x1} and n_{x2} (analogously to what found in Ref. [57] and [58] for the drag of charge in the biased-voltage case of QD-based systems). We checked that first order contributions in V or ΔT appear when an additional superconducting electrode is included in the drive circuit, i. e. when energy-dependent lead-island couplings are present in the drive circuit as well as in the drag circuit (analogously to what found in Ref. [57] for the drag of charge in the biased-voltage case of QD-based systems). Furthermore, the heat currents in the

drag circuit are proportional to V or ΔT when energy-dependent couplings are present at least in the drive circuit.

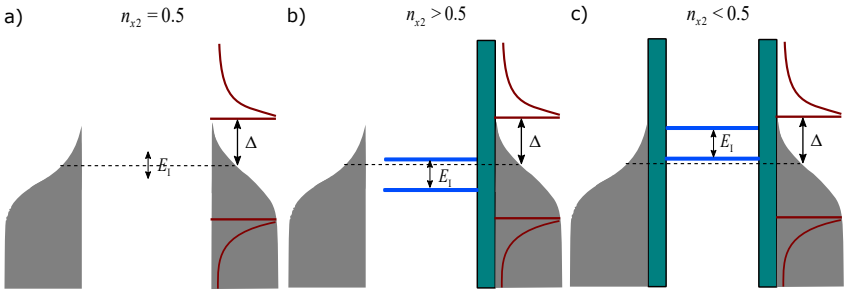

Figure 4.9: Sketch of the energies in the presence of a superconducting electrode on R2, for $n_{x1} = 1/2$. The red line represent the superconducting DOS, with a gap equal to Δ centered at the equilibrium electrochemical potential of the electrodes (dashed thin line). Blue lines represent the two chemical potentials of the lower island, $\delta E_{U2}(1,0)$ and $\delta E_{U2}(0,0)$. Such chemical potentials, according to Eqs. (4.13) and (4.14), are symmetric with respect to the electrochemical potential of the electrodes when $n_{x2} = 0.5$ [(panel a)], shift downwards [(panel b)] when $n_{x2} > 0.5$, and shift upwards [(panel c)] when $n_{x2} < 0.5$.

4.2 THERMAL DRAG IN COULOMB COUPLED QUANTUM DOTS

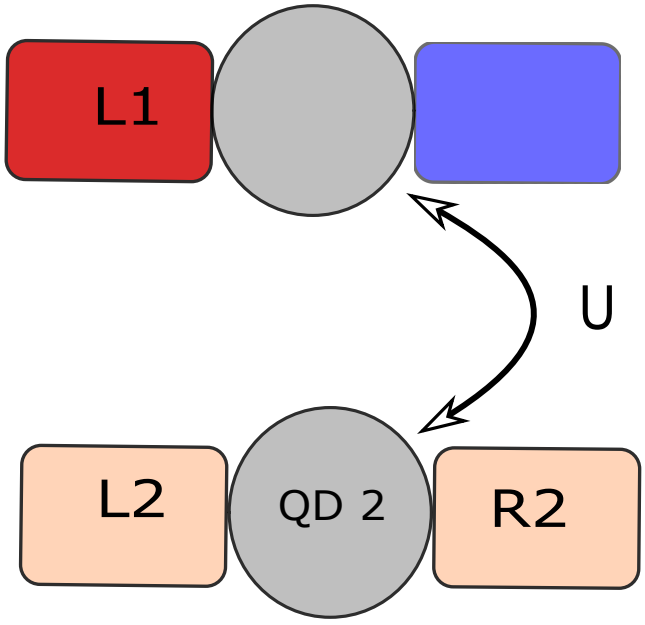

Figure 4.10: Sketch of second system under consideration composed of two Coulomb coupled quantum dots (QDs) labeled by QD 1 (in the drive circuit) and QD 2 (in the drag circuit).

The second system considered, depicted in Fig. 4.10, consists of two quantum dots (labeled QD 1 and QD 2), each one tunnel-coupled to two electrodes. Quantum dots (QDs) present an ideal setup for studying quantum effects at nano-scale. The recent experimental as well as theoretical progress on

thermo-electric properties of Coulomb coupled systems have been primarily motivated by their possible application as non-local thermoelectric devices. We discussed the case of metallic islands in the previous section where we observed that for energy independent tunneling, the unbiased system favorably gets heated whereas cooling can be obtained by introducing energy dependent parameters, for instance, by taking superconducting electrode or engineering energy dependence in the transition amplitudes. The energy dependence filters the allowed energy for transition and hence can be suitably engineered only to allow specific processes. Since the quantum dot has only one energy state, the filtering process can be made more strict. We expect the quantum dot setup to provide higher magnitude of heat extraction from one of the electrode in the drag compared to the metallic island case.

4.2.1 *Formulation*

The Hamiltonian for the double quantum dot system is given by Eq. (2.2) with $i = 1, 2$ and $w_i = 0$ and $U_{12} = U$. The baths are fermionic as defined in Eq. (2.7). The contact Hamiltonian for dot-electrode coupling is given by Eq. (2.8).

We study the thermoelectric dynamics using Pauli master equation approach. The coupled QDs are considered to be in Coulomb blockade regime and hence the dynamics of the system can be described by four charge states. For brevity, we represent the empty state by $(0,0)$, singly occupied states by $(1,0)$ and $(0,1)$ and doubly occupied state by $(1,1)$. The energy associated with the eigenstates mentioned above are given by $E(0,0) = 0$, $E(1,0) = \epsilon_1$, $E(0,1) = \epsilon_2$ and $E(1,1) = \epsilon_1 + \epsilon_2 + U$ respectively. The transition rates are obtained by solving the Fermi's golden rule where the tunneling Hamiltonian is treated as a perturbation and different order contribution can be calculated using the perturbative T-matrix approach. The first order contribution includes the tunneling of only one particle and will be discussed in the following.

The change in energy of the QD system, when an electron tunnels into or out of the system can be expressed as

$$\begin{aligned} \delta E_1(n_1, n_2) &= E(n_1 + 1, n_2) - E(n_1, n_2), \\ \delta E_2(n_1, n_2) &= E(n_1, n_2 + 1) - E(n_1, n_2). \end{aligned} \tag{4.24}$$

The transition rates between the QD system and the electrode α can be expressed as,

$$\Gamma^{(c/h)}_{\alpha,i}(n_1, n_2) = \hbar^{-1} z^{(c/h)}_{\alpha} \left(\delta E_i(n_1, n_2) - eV_\alpha\right) f_\alpha \left(\delta E_i(n_1, n_2) - eV_\alpha\right) \tag{4.25}$$

for tunneling from electrode α into the QD system and,

$$\Gamma^{(c/h)}_{i,\alpha}(n_1, n_2) = \hbar^{-1} z^{(c/h)}_{\alpha} \left(\delta E_i(n_1, n_2) - eV_\alpha\right) f_\alpha \left(-\delta E_i(n_1, n_2) + eV_\alpha\right) \tag{4.26}$$

for the reverse process, i.e. when an electron tunnels from the QD i into the electrode α. We have introduced,

$$\begin{aligned} z^{(c)}_{\alpha}(\epsilon) &= \Gamma_\alpha(\epsilon) \\ z^{(h)}_{\alpha}(\epsilon) &= \epsilon \Gamma_\alpha(\epsilon), \end{aligned} \tag{4.27}$$

where $\Gamma_\alpha(\epsilon)$ is the spectral density of the bath α as defined in Eq. (2.16). The occupation probabilities and the currents can be obtained using the master equation formulation (see previous section on metallic islands for details).

4.2.2 *Energy dependent tunneling – Charge-state-dependent transition amplitudes*

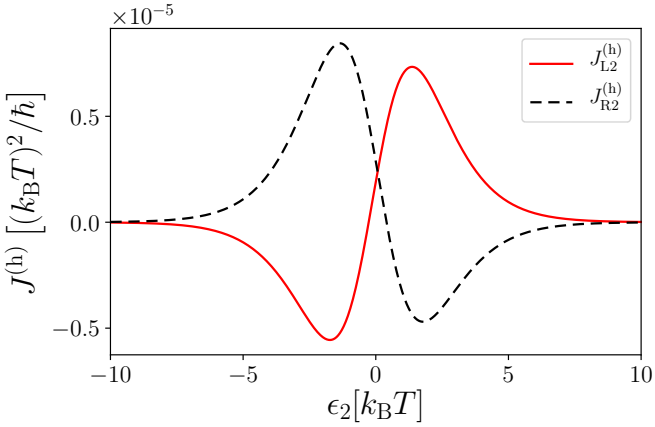

Figure 4.11: Heat currents in the case of QDs flowing in the two leads of drag system as a function of ϵ_2 considering charge state dependent transition rate. Parameters: $\epsilon_1 = 0$; $\Delta T = 0.8T$; $eV = 0$; $U = 0.1k_\mathrm{B}T$; $\Gamma_{L1} = \Gamma_{R1} = \Gamma_{L2} = \frac{1}{30}k_\mathrm{B}T$ and $\Gamma^{(0)}_{R2} = \frac{1}{10}k_\mathrm{B}T$.

In Ref. [60] the energy-dependence of the lead-island couplings was implemented assuming that the transition rate between the QD and one electrode in the lower branch circuit depends on the charge state of the upper QD (see Fig. 4.10). In this section we consider the case where for all the electrodes, except for the lower right R2, we assume energy-independent coupling. On the contrary, for the lower right electrode R2 we implement an energy-dependence by setting an "effective resistance" which depends on the charge state of the upper island. This can be done by assuming the spectral density to have the form

$$\begin{aligned} 2\pi|V^{(0)}_{\mathrm{R2}}|^2\rho_{\mathrm{R2}}(0) &= \Gamma^{(0)}_{\mathrm{R2}} \\ 2\pi|V^{(1)}_{\mathrm{R2}}|^2\rho_{\mathrm{R2}}(0) &= \Gamma^{(1)}_{\mathrm{R2}} = \frac{1}{2}\Gamma^{(0)}_{\mathrm{R2}} \end{aligned} \tag{4.28}$$

where $V^{(0)}_{\mathrm{R2}}$ and $V^{(1)}_{\mathrm{R2}}$ represent the tunneling matrix element between the QD2 and right electrode R2, which depend on the charge state of the QD1, either empty (0) or occupied (1). Charge state dependent transition rates provides selective transport of energetic particles across the tunnel barriers. The high energy particles can get picked up from one of the electrode (R1 or R2) in the right side and get dropped to the other electrode in the same side. As a consequence, one of the electrode gets cooled whereas the other one gets heated as shown in Fig. 4.11. The electrode that is cooled (R1 or R2) depends on the sign of ϵ_2 when everything else is kept constant (see Fig. (4.11)). Note that negative heat current implies extraction of heat (cooling) from the corresponding electrode.

The mechanism which allows a drag heat current to flow can be described through the energy scheme in Fig. 4.12, where panel (i) refers to the case $\epsilon_2 > 0$ and panel (ii) refers to $\epsilon_2 < 0$. For simplicity, we consider the case when $\Gamma_{\mathrm{L2}} = \Gamma^{(0)}_{\mathrm{R2}}$. 1) For small temperatures and $E_I < k_B T$, an electron jumps to QD2 when the QD1 is empty (panel (i)) (this step is facilitated by keeping the bare energy level of the QD2 close to the Fermi-level (dashed line) of the electrodes). When $n_1 = 0$, an electron from the electrodes (L2 or R2) has

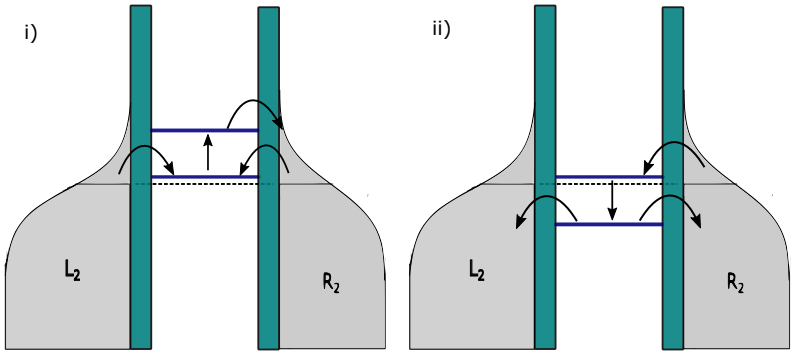

Figure 4.12: Sketch for the cooling process with charge state dependent transition rates

equal chance of tunneling into QD2 as $\Gamma_{L2} = \Gamma^{(0)}_{R2}$. 2) An electron tunnels into QD1 from one of the electrodes in the drive circuit raising the energy of the electron in QD2 by E_I as shown by the upward arrow in Fig. (4.12). Eventually, the electron in QD2 tunnels out to one of the electrodes, but more preferentially to the electrode R2, as when the QD1 is occupied it is more easier to exit to R2 than L2 ($\Gamma^{(1)}_{R2} = \frac{1}{2}\Gamma^{(0)}_{R2}$). This asymmetry in tunneling into the left and the right electrode when QD1 has an electron leads to finite cooling of one of the electrode in the drag system. When $\epsilon_2 > 0$ (panel (i)), hot electrons tunnel into the electrode R2 whereas when $\epsilon_2 < 0$ (panel (ii)), hot electrons tunnel out of the electrode R2 (see Fig. 4.12). This leads to heating of the electrode R2 when $\epsilon_2 > 0$ and cooling of the electrode R2 when $\epsilon_2 < 0$ (see Fig. 4.11).

4.2.3 *Energy Dependent Tunneling - Superconducting Electrode*

In this subsection, we will consider the electrode R2 to be superconducting. The density of state for the superconducting electrode is energy dependent and is given by the superconducting density of states:

$$\rho_{R2}(\epsilon) = \left| \mathrm{Re}\left(\frac{\epsilon + i\eta}{\sqrt{(\epsilon + i\eta)^2 - \Delta^2}} \right) \right| \tag{4.29}$$

where, η (Dyne's parameter) represents the inverse life time for the quasiparticles and Δ is the superconducting gap. Eqs. (4.25) and (4.26) for transition rates hold with the spectral density given by:

$$\Gamma_\alpha(\epsilon) = 2\pi|t|^2\rho_\alpha(\varepsilon). \tag{4.30}$$

As shown in Fig. 4.13, the presence of superconducting electrode leads to the extraction of heat from one electrode and heating of the other electrode in the drag system for suitable values of ϵ_2. The cooling mechanism can be described similarly as in the case of charge-state dependent transition rates. However, in the case of superconducting electrode, selective tunneling of electrons in the drag system is led by the superconducting gap.

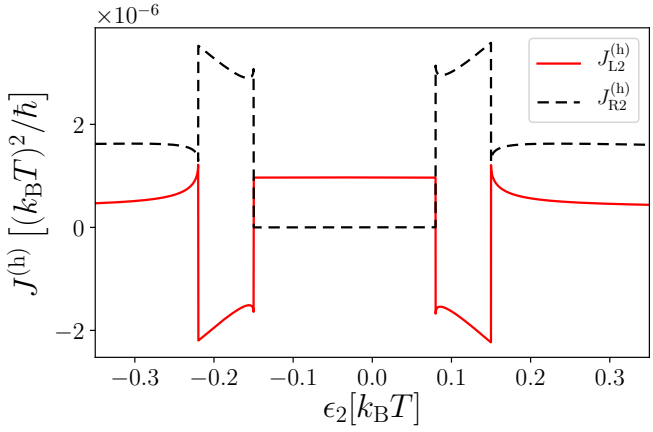

Figure 4.13: Heat currents in the coupled QDs case flowing in the two leads of drag system as a function of ϵ_2 taking the lead R2 to be superconducting. Parameters: $\epsilon_1 = 0$; $\Delta T = 0.8T$; $eV = 0$; $U = 0.07k_\mathrm{B}T$; $\Gamma_{\mathrm{L1}} = \Gamma_{\mathrm{R1}} = \Gamma_{\mathrm{L2}} = \frac{1}{40}k_\mathrm{B}T$; $\gamma_{\mathrm{R2}} = \frac{1}{10}k_\mathrm{B}T$.

Different Set Ups	**Energy Dependence in tunneling rates**	**Order dependence of heat drag on the bias**
Potential bias	None / in the drag	2nd order in V
Thermal bias (symmetric)	None / in the drag	2nd order in ΔT
Thermal bias (asymmetric)	None / in the drag	1st order in ΔT
Potential bias	Each in the drive and drag	1st order in V
Thermal bias (symmetric)	Each in the drive and drag	1st order in ΔT
Thermal bias (symmetric) + potential bias	None / In the drag	1st order in V ΔT

Table 4.1: Order dependence on thermal and potential bias under different scenarios.

4.2.4 *Order dependence on bias*

In Table 4.1, we list the order dependence of thermal drag on potential and thermal bias under different conditions. Firstly, we observe that the heat currents flowing in leads of the drag system are second order in the potential or thermal bias when they are applied symmetrically. Indeed we find that, for the charge state dependent transition rates with $\varepsilon_1 = \varepsilon_2 = \frac{-U}{2}$, $V_{\mathrm{L1}} = -V_{\mathrm{R1}} = \frac{V}{2}$ for potential bias and $T_{\mathrm{L1/R1}} = T \pm \Delta T$ for thermal bias,

$$J^{(h)}_{\mathrm{L2}} = \frac{7\Gamma^{(0)}}{832}U^2 \operatorname{sech}\left[\frac{U}{4k_\mathrm{B}T}\right]^2 \left(4k_\mathrm{B}T - U\tanh\left[\frac{U}{4k_\mathrm{B}T}\right]\right)\frac{\Delta T^2}{k_\mathrm{B}^2T^4},$$
$$J^{(h)}_{L2} = \frac{7\Gamma^{(0)}}{832}U \operatorname{sech}\left[\frac{U}{4k_\mathrm{B}T}\right]^2 \tanh\left[\frac{U}{4k_\mathrm{B}T}\right]\left(\frac{eV}{k_\mathrm{B}T}\right)^2. \tag{4.31}$$

Interestingly, a linear in ΔT or ΔV term can be obtained in the drag heat current, by introducing asymmetry (energy dependent tunneling or asymmetric bias) in the driven system.

Taking asymmetric thermal bias $T_{L1} = T + \Delta T$ and $T_{R1} = T$, we find:

$$J_{L2}^{(h)} = -\frac{7\Gamma^{(0)}}{416} U^2 \operatorname{sech}\left[\frac{U}{4k_B T}\right]^2 \frac{\Delta T}{k_B T^2} + \frac{7\Gamma^{(0)}}{1664} U^2 \operatorname{sech}\left[\frac{U}{4k_B T}\right]^2 \left(4k_B T - U \tanh\left[\frac{U}{4k_B T}\right]\right) \frac{\Delta T^2}{k_B^2 T^4} \tag{4.32}$$

4.3 SUMMARY

In summary, in this chapter we have studied the phenomenon of electronic thermal drag in two different setups, namely for capacitively-coupled metallic islands and for Coulomb-coupled quantum dots. In the metallic island case, using the master equation approach we have studied both the sequential and the co-tunneling contributions to thermal drag in the presence of either a voltage bias or a temperature bias. In the sequential tunneling regime we have obtained analytical results for small biases, finding, in particular, that $I_{\text{drag}}^{(h)}$ is quadratic in ΔT or V and non-monotonous as a function the coupling between the islands (inter-island repulsion). We have found that such behavior holds even when co-tunneling processes are included. Finally, we have explored the consequences of energy-dependent island-electrode coupling by replacing one of the electrodes in the drag circuit with a superconductor. Apart from allowing a finite dragged charge current, we have found that the presence of the superconducting electrode can cause the extraction of heat from the remaining normal electrode in the drag circuit.

In the case of Coulomb coupled quantum dots, we have derived an analytic expression for the heat current flowing in the drag circuit using the master equation formulation. Similar to metallic island case, we find that for symmetric bias condition, the first order contribution in the bias vanishes and the second order contribution becomes the leading contribution. However, if either the thermal bias is asymmetric or if the tunneling rate in the drive circuit is energy dependent, a finite contribution to thermal drag is obtained even from the first order terms. On a separate note, the non-local cooling effects are significantly enhanced in the quantum dot case compared to the metallic island case.

As argued in the following, both setups are experimentally feasible with current technology. In both cases, the Coulomb coupling between two such islands has been realised by placing close together two single electron transistors, while making sure that no electron transfer occurs between them, see for example Refs. [76] and [43]. In both cases, heat currents can be determined by making use of heat budget models which account for all possible heat exchanges between the systems and their environment. See, for example, Ref. [39].

We believe that the results obtained in this chapter can be also relevant for the implementation of non-local thermal machines. Indeed, the four-terminal system depicted in Fig. 4.1 can be operated as a non-local heat engine where the temperature difference between the two upper electrodes can be used to extract work from the lower circuit. Likewise, a non-local refrigerator uses the work performed on the upper circuit to cool one of the lower electrodes. Autonomous refrigerators, where heat is provided instead of work in the upper circuit, can also be envisaged (see Refs. [35, 80]). Moreover, the four-terminal setup can be operated as a thermal gating system, similarly to the three-terminal setups of Refs. [69, 81], where the heat or charge flow in the

upper circuit is controlled by changing the temperature of the electrodes in the lower circuit.

5

ABSORPTION REFRIGERATORS BASED ON COULOMB COUPLED SINGLE-ELECTRON DEVICES

Absorption refrigerators, also known in literature as self-contained or autonomous refrigerators, are systems that extract heat from a cold thermal bath only by exploiting the incoherent interaction with other two thermal baths held at higher temperatures. No work is provided to the system, i. e. *cooling is achieved by heating*. The exploration for solid state implementations of absorption refrigerators has been recently attracting a considerable attention [82, 83, 84, 85, 86, 87, 88, 89, 90, 91, 92, 93, 94, 95, 96, 97, 98, 99]. The question of identifying the smallest absorption quantum refrigerators was addressed by Linden et al. in Ref. [83], where systems such as two qubits, a qubit and a qutrit, or a single qutrit were considered. It has been later shown that these "minimal" systems can operate at Carnot efficiency[84, 85], and the role of quantum coherence and entanglement has been addressed [88, 89, 92, 93, 94, 96]. Besides being of fundamental interest in quantum thermodynamics, absorption refrigeration is also appealing for practical reasons: waste heat can be used to achieve cooling at the nanoscale without providing work nor requiring any external control of the system. There are already few experimental proposals[100, 86, 101, 74, 102, 103, 104, 35, 81], but the only experimental realization so far has been performed with trapped ions [52]. In Ref. [35], in particular, it was pointed out that the very simple setup consisting of two capacitively-coupled quantum dots could act as an absorption refrigerator, and the conditions under which its coefficient of performance (COP) can reach Carnot's limit were discussed (no entanglement or quantum coherence is required).

In this chapter, we analyze in detail a setup consisting of two capacitively-coupled quantum dots. we propose two experimental realizations, based either on quantum dots (QDs) or metallic islands, which can implement the non-trivial requirements for the system to behave as an absorption refrigerator. We demonstrate that these systems, which closely resemble existing experimental setups [105, 63, 106, 61, 68, 76, 53, 62, 60, 43], can attain an observable cooling power using realistic parameters.

5.1 MODEL

The system under investigation, depicted in Fig. 5.1(a), consists of two electronic reservoirs [upper left (L) and upper right (R)] tunnel coupled to a QD, denoted by 1. A second QD, 2, capacitively coupled to 1, is tunnel coupled to a third electronic reservoir (C). The number of electrons occupying each Coulomb-blockaded QD can be controlled through a gate of capacitance C_{gi} and applied voltage V_{gi}, with $i = 1, 2$. Reservoir L is kept at a higher temperature, $T_{\mathrm{L}} = T + \Delta T$, with respect to the other reservoirs which are kept at temperature $T_{\mathrm{R}} = T$ and $T_{\mathrm{C}} = T - \Delta T_{\mathrm{C}}$. The heat current leaving reservoir

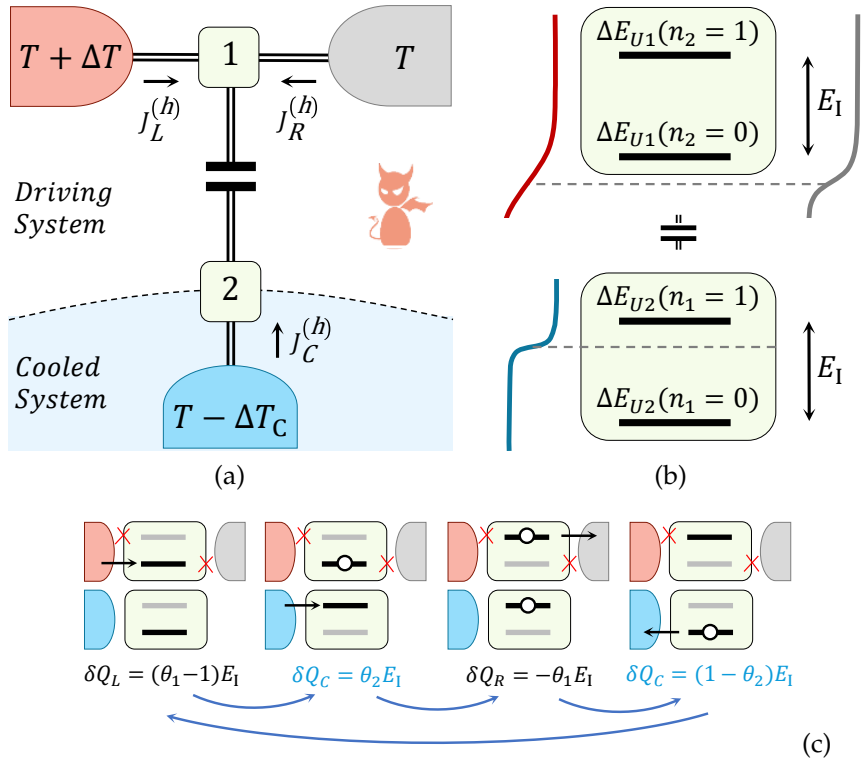

Figure 5.1: Panel (a): schematic representation of the system. Panel (b): the Fermi distribution of the leads (red upper left, gray upper right and blue lower left) is shown vertically. The black thick lines represent the transition energies $\Delta E_{U_1}(n_2)$ and $\Delta E_{U_2}(n_1)$ [Eq. (5.2)] that are measured with respect to common chemical potential of the leads (black dashed line). Panel (c): sequence of system states and electron transitions that provide cooling when conditions (5.7) and (5.8), represented by the red crosses, are satisfied. The black horizontal lines represent the actual transition energies as determined by the occupation of the other QD, while the grey horizontal lines represent the transition energies when the other QD has opposite occupation. δQ_α, for α=L,R,C, represents the heat extracted from reservoir α during the corresponding electron transition.

α = L,R,C is denoted by $J_\alpha^{(h)}$, and the charge current flowing between reservoirs L and R is denoted by $J^{(c)}$. We describe the transport in the entire system using a master equation approach in the sequential tunneling limit. Although we expect higher order tunneling processes, such as co-tunneling, to decrease the cooling power, these corrections are suppressed if the conductances of the junctions are much smaller than the conductance quantum and temperature is not too small. The electrostatic energy of the system is given by

$$E_U(n_1, n_2) = E_{C1}(n_1 - n_{x1})^2 + E_{C2}(n_2 - n_{x2})^2 + E_I(n_1 - n_{x1})(n_2 - n_{x2}), \tag{5.1}$$

where n_i (for $i = 1, 2$) is the number of electrons in QD i, $n_{xi} = V_{gi}C_{gi}/e$, and $E_{Ci} = e^2/(2C_i)$ is its charging energy. C_i is the capacitance of QD i to its surroundings, and E_I is the inter-system charging energy which is controlled by the capacitive coupling between the QDs. By assuming that $E_{Ci} \gg k_B T$ and constraining the values of n_{xi} to an appropriate range, we can restrict our analysis to 4 charge states, described by $n_1, n_2 = 0, 1$. The "transition energy",

i.e. the energy necessary to add an electron to QD 1 (2), which also depends on the occupation of QD 2 (1), is given by $\Delta E_{U1}(n_2) = E_U(1,n_2) - E_U(0,n_2)$ [$\Delta E_{U2}(n_1) = E_U(n_1,1) - E_U(n_1,0)$]. Since $\Delta E_{Ui}(1) - \Delta E_{Ui}(0) = E_I$, we can write

$$\Delta E_{Ui}(n) = \theta_i E_I + (n-1)E_I, \tag{5.2}$$

where

$$\theta_1 = 1 - n_{x2} + \frac{E_{C1}}{E_I}(1-2n_{x1}), \tag{5.3}$$

$$\theta_2 = 1 - n_{x1} + \frac{E_{C2}}{E_I}(1-2n_{x2}), \tag{5.4}$$

can be varied using the gate voltages. The transition energies are schematically represented in Fig. 5.1(b) and 5.1(c) as black thick lines. Let $\Gamma_{L/R,1}(n_2)$ [$\Gamma_{1,L/R}(n_2)$] be the rate of electrons tunneling from (to) reservoir L/R to (from) QD 1, and let $\Gamma_{C,2}(n_1)$ [$\Gamma_{2,C}(n_1)$] be the rate of electrons tunneling from (to) reservoir C to (from) QD 2. Note that the tunneling rates satisfy the detailed balance conditions

$$\Gamma_{i,\alpha}(n) = \exp\left\{\left[\frac{\delta_\alpha(n)}{k_B T_\alpha}\right]\right\}\Gamma_{\alpha,i}(n), \tag{5.5}$$

where $\delta_L(n) = \delta_R(n) = \Delta E_{U1}(n)$ and $\delta_C(n) = \Delta E_{U2}(n)$. The currents can be calculated by specifying the tunneling rates for each process and by determining the probability P_{n_1,n_2} for the two QDs to have occupation numbers n_1 and n_2 (see App. E.1). We also use Eq. (5.5) to express $\Gamma_{\alpha,i}(0)$ in terms of $\Gamma_{i,\alpha}(0)$ and $\Gamma_{i,\alpha}(1)$ in terms of $\Gamma_{\alpha,i}(1)$. We emphasize, however, that the results we present in the next section do not depend on the specific form of the rates, as long as Eq. (5.5) is satisfied. Only a quantitative description of the cooling power will explicitly depend on the rates.

5.1.0.1 *The coefficient of performance*

The COP for refrigeration is defined as

$$\eta = \frac{J_C^{(h)}}{J_L^{(h)}}, \tag{5.6}$$

where $J_L^{(h)} > 0$ is the input heat and $J_C^{(h)} > 0$, the cooling power, is the heat extracted from reservoir C (their expressions are reported in App. E.1). Considering generic rates that are only constrained by satisfying the detailed balance condition [Eq. (5.5)], we find that the cooling power is maximized, at fixed values of E_I, θ_1 and θ_2, when

$$\Gamma_{L,1}(1) = 0, \tag{5.7}$$

$$\Gamma_{1,R}(0) = 0, \tag{5.8}$$

and $\Gamma_{1,L}(0)$, $\Gamma_{R,1}(1)$, $\Gamma_{2,C}(0)$, $\Gamma_{C,2}(1)$, are as large as possible (see App. E.2 for details). In this situation [i. e. when Eqs. (5.7) and (5.8) hold and when $\theta_i > 1/2$, see App. E.1 for details] the condition for the positivity of I_C^h reduces to the simple inequality

$$\theta_1 > \theta_1^* \equiv 1 + \frac{1}{\eta_C^h \eta_C^r}, \tag{5.9}$$

where $\eta_C^h = 1 - T/T_L$ and $\eta_C^r = T_C/(T - T_C)$. Remarkably, in this situation the COP is also maximized (at least for $\Delta T_C = 0$), and takes a particularly simple (i. e. independent of temperatures) form

$$\eta = \frac{1}{\theta_1 - 1}, \tag{5.10}$$

that only depends on θ_1 (which is determined by both gate voltages V_{g1} and V_{g2}). Note that Eq. (5.9) implies that $\Delta E_{U1}(1) > 0$ and $\Delta E_{U1}(0) > 0$, i. e. both transition energies are above the common chemical potential of the reservoirs[1], as shown in Fig. 5.1(b). This observation holds also for generic rates that do not satisfy Eqs. (5.7) and (5.8), see App. E.2 for details.

Although the ideal condition of completely blocking the transitions as shown in Fig. (5.1) is not possible, one can include energy filters in the transition rates, for example including a quantum dot in the contact region, taking a superconducting reservoir or by considering charge state dependent transition rates. We will use these mechanisms to study cooling in two different set ups.

5.2 QUANTUM DOTS

The experimental realization of the proposed absorption refrigerator relies on the ability of implementing the crucial conditions (5.7) and (5.8). Such conditions could be, in principle, implemented by properly engineering the tunneling barrier which couple QD 1 to its reservoirs, in order to obtain tunneling rates for QD 1 that depend on the occupation of QD 2. In this section, we make use of an additional QD [107] to implement the crucial condition (5.7) that is found to be sufficient for obtaining heat extraction.

In the setup, schematically pictured in Fig. 5.2, we introduce an additional QD (3), tunnel-coupled to 1, and we require that its transition energy ΔE_{U3} is aligned with $\Delta E_{U1}(0)$ [see Fig. 5.2(b)]. This way, the "energy filtering" effect of QD 3 is used to suppress $\Gamma_{L,1}(1)$ with respect to $\Gamma_{1,L}(0)$. To perform a

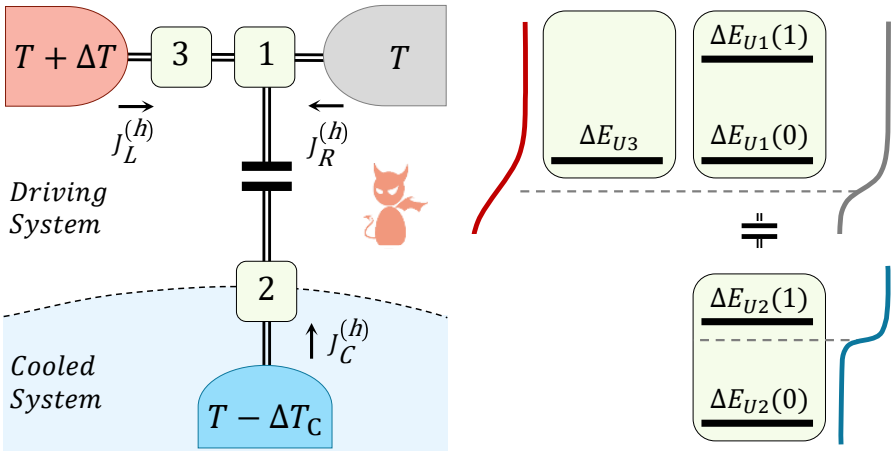

Figure 5.2: Left: schematic representation of the system, where 1, 2 and 3 represents either QDs or MIs. Right: representation of the transition energies in the case of the system with QDs. See Fig. 5.1 for details.

quantitative analysis, we study the dynamics of the system of the three QDs altogether under the assumption that the coupling between QDs 1 and 3

1

is much weaker than the coupling between such QDs are their reservoirs. The Hamiltonian for the QD system under study is given by Eq. (2.2) with $w_1 = w_2 = 0$ and $U_{31} = 0$ (note that $w_3 = t$, $\hat{a}_{3+1} = \hat{a}_1$). The baths and coupling are defined by Eq. (2.7) and Eq. (2.8) respectively. The electrostatic energy of the system [see Eq. (5.1) for two QDs] now takes the form

$$E_U(n_1, n_2, n_3) = E_{C1}(n_1 - n_{x1})^2 + E_{C2}(n_2 - n_{x2})^2 + E_{C_3}(n_3 - n_{x3})^2 + E_I(n_1 - n_{x1})(n_2 - n_{x2}), \quad (5.11)$$

where we have added the third term, relative to the additional QD (3). Analogously to the two-QD case, we define $\Delta E_{U1}(n_2) = E_U(1, n_2, n_3) - E_U(0, n_2, n_3)$, $\Delta E_{U2}(n_1) = E_U(n_1, 1, n_3) - E_U(n_1, 0, n_3)$ and $\Delta E_{U3} = E_U(n_1, n_2, 1) - E_U(n_1, n_2, 0)$, which can be written as

$$\begin{aligned} \Delta E_{U1}(n_2) &= E_I(\theta_1 + n_2 - 1) \\ \Delta E_{U2}(n_1) &= E_I(\theta_2 + n_1 - 1) \\ \Delta E_{U3} &= E_I(\theta_3 - 1), \end{aligned} \quad (5.12)$$

where we have defined the following 3 independent dimensionless parameters

$$\begin{aligned} \theta_1 &= (1 - 2n_{x1})E_{C1}/E_I + (1 - n_{x2}) \\ \theta_2 &= (1 - 2n_{x2})E_{C2}/E_I + (1 - n_{x1}) \\ \theta_3 &= (1 - 2n_{x3})E_{C3}/E_I + 1. \end{aligned} \quad (5.13)$$

If we assume that each QD can be only singly-occupied, we can restrict our analysis to the following 8 states: $|0,0,0\rangle$, $|0,0,1\rangle$, $|0,1,0\rangle$, $|1,0,0\rangle$, $|1,0,1\rangle$, $|0,1,1\rangle$, $|1,1,0\rangle$ and $|1,1,1\rangle$, where $|n_1, n_2, n_3\rangle$ is the state associated to the set of occupation numbers (n_1, n_2, n_3). The probability p_m for the system to be in the state $|m\rangle = |n_1, n_2, n_3\rangle$ is calculated by solving the master equation in the stationary case (see App. E.3 for details)

$$\dot{p}_m = \sum_{\alpha,l} \left(-\Gamma_{\alpha,ml}\, p_m + \Gamma_{\alpha,lm}\, p_l\right), \quad (5.14)$$

where $\Gamma_{\alpha,ml}$ is the rate for the transition from state $|m\rangle$ to state $|l\rangle$ accompanied by the bath α. The rates $\Gamma_{\alpha,ml}$ which account for the transfer of electrons between a QD and a reservoir can be expressed as [58]

$$\Gamma_{\alpha,ml} = \hbar^{-1}\Gamma_\alpha f_\alpha(\Delta\tilde{E}_{U,ml}), \quad (5.15)$$

where Γ_α is the coupling energy between the reservoir $\alpha = \alpha(m,l)$ and a QD, where $\alpha = \mathrm{L}, \mathrm{R}, \mathrm{C}$ depends on the initial state $|m\rangle$ and final state $|l\rangle$. In addition, $\Gamma_{mn} \equiv \Gamma_{\alpha,mn}$ since only one reservoir is attached to each quantum dot and hence removing the bath index does not introduce any ambiguity. In Eq. (5.15), $f_\alpha(\epsilon) = [1 + e^{\epsilon/(k_B T_\alpha)}]^{-1}$ is the reservoir Fermi distribution function, while $\Delta\tilde{E}_{U,ml} = \tilde{E}_U(l) - \tilde{E}_U(m)$ is the transition energy, where $\tilde{E}_U(m) = E_U(n_1, n_2, n_3)$ [see Eq. (5.11)] with the set of occupation numbers corresponding to the state $|m\rangle$. The inter-dot transition rates, which account for the transfer of electrons between QD 1 and 3 [namely, $\Gamma_{(0,0,1)(1,0,0)}$ and $\Gamma_{(0,1,1)(1,1,0)}$], are obtained using the procedure outlined in App. E.3 under the assumption that the hopping element t is much smaller than the coupling energy between QDs and reservoirs [108, 109, 110, 111, 112].

The relevant heat currents can now be written as

$$J_{\mathrm{C}}^{(h)} = \sum_{ml} \Delta\tilde{E}_{U,ml}\left(\Gamma_{ml}\, p_m - \Gamma_{lm}\, p_l\right), \quad (5.16)$$

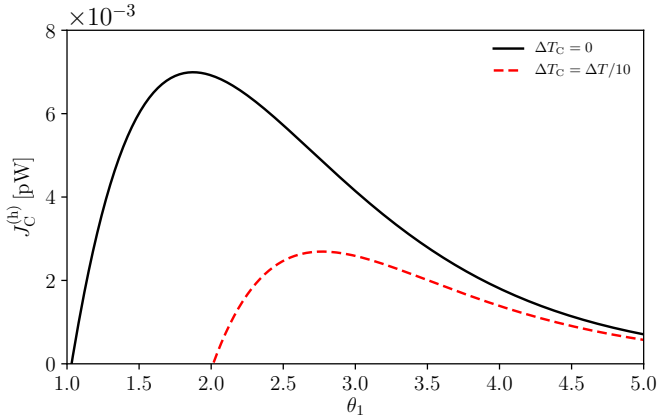

Figure 5.3: Cooling power $J_C^{(h)}$, relative to the system containing three QDs and represented in Fig. 5.2, under resonant condition [$\Delta E_{U3} = \Delta E_{U1}(0)$]. $J_C^{(h)}$ is plotted as a function of θ_1 for the case $\Delta T_C = 0$ (solid black curve) and the case $\Delta T_C = \Delta T/10$ (dashed red curve), setting $\theta_2 = 1/2$ and imposing $\theta_3 = \theta_1$. The parameters are of the order of the experimental ones reported in Ref. [60] and read: $E_I = 0.72$ meV, $\Gamma_L = \Gamma_R = \Gamma_C = 0.036$ meV, $t = 0.016$ meV, and $T = \Delta T = 4.17$ K.

where the sum runs over the states specified in App. E.3. In Fig. 5.3 we plot the cooling power $J_C^{(h)}$, as a function of θ_1, for realistic parameters and setting $\theta_3 = \theta_1$ in order to obtain the resonant condition [i. e. $\Delta E_{U3} = \Delta E_{U1}(0)$] which approximately implements condition (5.7). The solid black curve is relative to the case $\Delta T_C = 0$, while the dashed red curve refers to $\Delta T_C = \Delta T/10$. Fig. 5.3 shows that in both cases heat extraction is obtained and that $J_C^{(h)}$ takes a maximum value of the order of 10^{-2} pW. We notice that, as in the ideal case, the cooling power is weakly dependent on θ_2 in the range between 0 and 1, and that in this case $J_C^{(h)}$ is maximized for $\theta_2 \simeq 1/2$. Moreover, we check that when the difference between ΔE_{U3} and $\Delta E_{U1}(0)$ is not much larger than the coupling energies $\Gamma_{L/R/C}$, the condition $\theta_3 = \theta_1$ is essentially fulfilled and the curves in Fig. 5.3 do not change appreciably. We have demonstrated that the implementation of the crucial condition (5.7) alone is sufficient to obtain heat extraction. Cooling power, as seen above, is expected to be maximal when the additional condition (5.8) is also satisfied. This could be implemented by adding another filtering QD in series with 1, between R and 1, and aligning its transition energy to $\Delta E_{U1}(1)$. For experimental purposes, however, a simpler system is desirable, especially because the transition energies of the different QDs need to be tuned by individual gates (not shown in Fig. 5.2), operation that is further complicated by possible cross-couplings arising between them.

5.3 METALLIC ISLANDS

We will now explore the possibility of replacing the QDs in the setup depicted in Fig. 5.2 with MIs. These are systems still characterized by a large charging energy but, as opposed to QDs, they present a continuous distribution of energy levels (the level spacing is much smaller than $k_B T$) so that electrons within the island are thermalized and distributed according to the Fermi distribution. Due to the absence of discrete levels, the sharp

"filtering effect" discussed above in the QD system and exploited to satisfy the crucial conditions (5.7) and (5.8) is not possible. As we will show below, however, heat extraction can nonetheless be obtained in the setup depicted in Fig. 5.2, where 1, 2 and 3 are now usual metals and reservoir R (grey element) is superconducting. Our aim is to approximately satisfy Eq. (5.7) by properly tuning the chemical potential of MI 3. Conversely, by exploiting the superconducting gap of reservoir R, we aim at approximately satisfying Eq. (5.8) in order to suppress the electron transfer with energy near $\Delta U_1(0)$. Unlike the case with QDs, here the detailed balance condition [Eq. (5.5)] is not satisfied by the rates between islands at different temperatures. As we shall see, however, this has only minor consequences.

The electrostatic energy of the system is equal to the one relative to the system of three QDs, Eq. (5.11). Also in this case we assume that each MI can only be singly-occupied so that our analysis can be restricted to the 8 states defined in the QD case. In the sequential tunneling regime, the stationary probability p_m that the system is in the state m is computed by solving the master equation (5.14), where, unlike in the QDs case, the rate for the transition from state m to state l is given by

$$\Gamma_{ml} = \frac{1}{e^2 \mathcal{R}_{\alpha\beta}} \int d\epsilon \mathcal{N}_\alpha(\epsilon) \mathcal{N}_\beta(\epsilon - \Delta\tilde{E}_{U,lm}) f_\alpha(\epsilon) \left[1 - f_\beta(\epsilon - \Delta\tilde{E}_{U,lm})\right]. \quad (5.17)$$

Here, $\mathcal{R}_{\alpha\beta}$ is the resistance of the tunneling barrier associated with the tunneling process, while α and β identify the indices of the reservoirs or the metallic island involved in the tunneling process respectively. In Eq. (6.6), $\mathcal{N}_\alpha$ denote the normalized density of states, which takes the value $\mathcal{N}_\alpha = 1$ for $\alpha =$ 1,2,3,L,C, and

$$\mathcal{N}_R(\epsilon) = \left| Re\left(\frac{\epsilon + i\eta}{\sqrt{(\epsilon + i\eta)^2 - \Delta^2}} \right) \right|, \quad (5.18)$$

for the superconducting reservoir [113, 114]. Here η is a phenomenological inverse quasi-particle lifetime, and Δ is the superconducting gap. As before, the heat currents $J_L^{(h)}$ and $J_C^{(h)}$ are defined as the heat currents extracted from reservoirs L and C, and are computed in App. E.4.

In Fig. 5.4 the cooling power is plotted, using realistic parameters, as a function of θ_1, for $\Delta T_C = 0$ (solid black curve) and for $\Delta T_C = 5$ mK (dashed red curve) and setting $\theta_2 = 1/2$. We assume that MIs 1 and 3 are at temperature T, while MI 2 is at temperature $T - \Delta T_C$. Aiming at implementing the condition (5.7), we place the electrochemical potential ΔE_{U3} half way between $\Delta E_{U1}(0)$ and $\Delta E_{U1}(1)$, i. e. we set $\theta_3 = \theta_1 + 1/2$. In fact, this guarantees that (if $k_B T \lesssim E_I$) the electron energy distribution in MI 3 is such that electron transfer to MI 1 is suppressed in the case where MI 2 is occupied.

Note, however, that the opposite process (electron transfer from 1 to 3) is not suppressed. Indeed, to obtain heat extraction we need to further assume that electrode R is superconducting. Figure 5.4 shows that cooling is achieved in both cases, $\Delta T_C = 0$ and $\Delta T_C = 5$ mK. In the former case, the maximum cooling power is of the order 10^{-2} fW, while in the latter heat extraction is still possible, but the maximum cooling power decreases roughly by a factor 4. Interestingly, heat extraction occurs even for $\theta_1 < 1$, contrary to the prediction of Eq. (5.9). This can be attributed to the fact that the detailed balance condition (5.5) is not satisfied for the tunneling rates coupling MIs or reservoirs having different temperatures. An amount of heat equal to

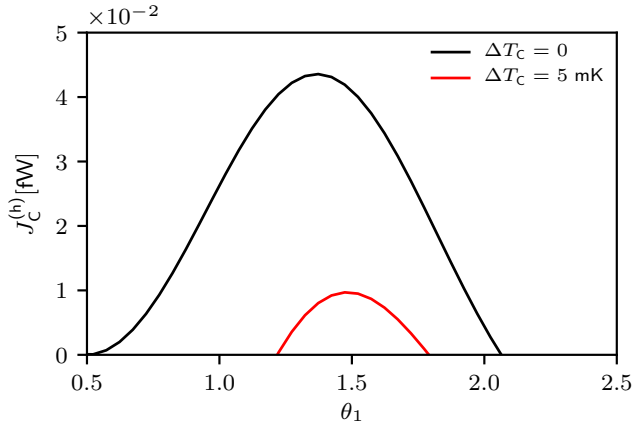

Figure 5.4: Cooling power, relative to the setup depicted in Fig. 5.2 for MIs, as a function of θ_1 for two different values of ΔT_C, and setting $\theta_2 = 1/2$ and $\theta_3 = \theta_1 + 1/2$. The parameters used are experimentally relevant, see for example Refs. [76, 39], and read: $E_I = 25$ μeV, $\Delta = 35$ μeV, $\eta = 10^{-3}$ μeV, $T = 100$ mK, $\Delta T = 200$ mK and $\mathcal{R}_{\alpha\beta} = 10$ kΩ for all barriers.

I_C^h is also extracted from MI 2 (see App. E.4 for details). Naturally no heat is extracted when reservoir R is in the normal state. We find that $J_C^{(h)}$ is maximized when $\theta_2 \simeq 1/2$ and $\theta_3 \simeq \theta_1 + 1/2$, and that its increase with ΔT is at most linear. Nevertheless, we wish to point out that there is no simple condition to identify the optimal values of E_I and Δ. Yet by scaling all energies and temperatures of a given factor, the cooling power scales as the square of such factor.

5.4 SUMMARY

We have studied several aspects of a minimal implementation of an absorption refrigerator based on two Coulomb coupled single-electron systems [35]. We have derived the general condition to guarantee cooling by heating and we have found the optimal rates that simultaneously maximize cooling power and coefficient of performance (COP). A simple relation between cooling power and charge current is also found. Analyzing the system as an autonomous Maxwell demon, we have shown that the efficiencies for information production and consumption can reach their upper bounds, and we have related the COP to these efficiencies. Finally, we have put forward two experimental proposals, based on quantum dots (QDs) and metallic islands (MIs). In both proposals we have introduce an additional QD or MI that implements the non-trivial condition required to achieve cooling-by-heating. By plugging in realistic parameters we have shown that these proposals, which resemble existing experiments, yield observable heat currents [46].

6

THERMAL RECTIFICATION

Improving thermal mangagement at nanoscale is necessary to prevent overheating of the electronic circuitry. Research in this field is growing thanks to recent advances in the experimental realization of nanoscale thermal devices [115, 116, 117, 46, 28, 118]. An intriguing phenomenon which may arise in nanoscale devices is thermal rectication, i. e. the asymmetric conduction of heat, whereby the heat flow in one direction is different with respect to the heat flow in the opposite direction, see Fig. 6.1. Thermal rectification, first observed experimentally by Starr in 1935[119], has been studied in a variety of setups since then, both theoretically[120, 121, 73, 122, 123, 124, 125, 126, 127, 128, 129, 130, 124, 127, 131, 132, 133, 134, 135, 136, 137, 138, 139] and experimentally[140, 141, 45, 142, 143].

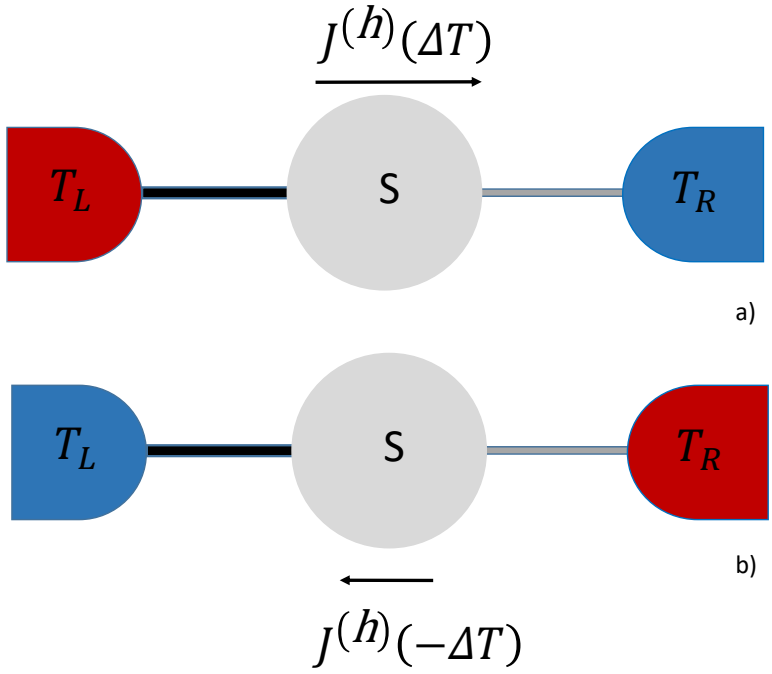

Figure 6.1: Schematic representation of a central quantum system S (gray circle) coupled to the two heat baths. The left and right baths are characterized respectively by the temperatures T_L and T_R. Panel (a) represents the positive bias case, i.e. $T_L = T + \Delta T/2$ and $T_R = T - \Delta T/2$ with $\Delta T > 0$, while panel (b) represents the negative bias configuration where the sign of ΔT is reversed. In the presence of some asymmetry in the coupling to the baths (represented by the different thickness of the dashed lines), the magnitude of the heat currents flowing through the device may depend on the sign of ΔT, leading to thermal rectification.

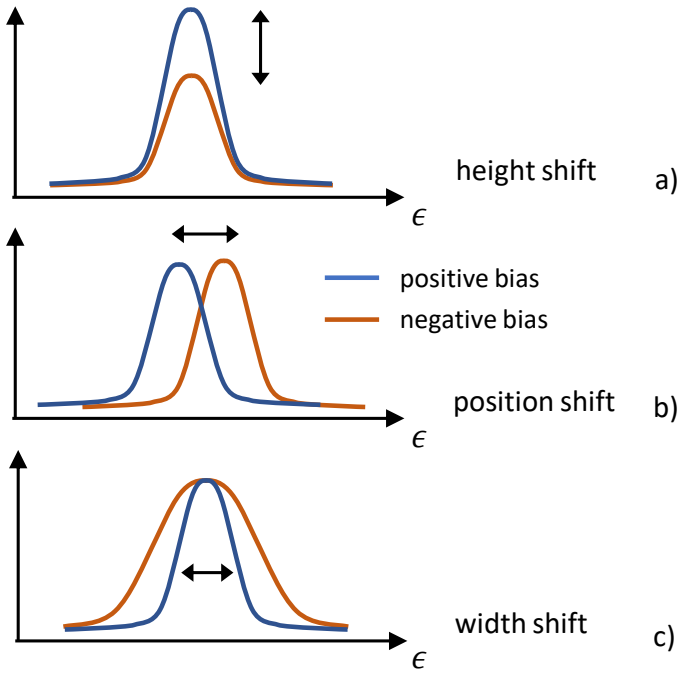

Figure 6.2: Scematic representation of the transmission function, as a function of the energy ϵ, for the positive and negative bias case. Each panel corresponds to a different variations of the transmission function which can realize heat rectification.

Thermal rectification is interesting both from a practical and from a fundamental point of view. On the one hand, it can be used in a nanoscale device to evacuate heat from sensitive areas, while preventing it from flowing back in. On the other hand, from a conceptual point of view, it is interesting to understand what are the fundamental physical requirements for a system to exhibit thermal rectification, and what are the strategies to maximize this phenomenon. In this chapter we study thermal rectification through a low-dimensional quantum system (S) coupled to two thermal baths at different temperatures as schematically sketched in Fig. 6.1. In panel (a) and panel (b), we depict the positive and negative bias cases. One bias condition is obtained from the other by inverting the temperature of the baths.

As we shall see in the following, in order to observe thermal rectification, the presence of inelastic scattering is necessary, and the baths must be asymmetrically coupled to the system. In the absence of inelastic scattering, the current can be described by the Landauer-Büttiker scattering approach [30, 31], expressed as an energy integral of a transmission function (which does not depend on temperature) multiplied by the difference of energy distribution of the baths. In this situation, no rectification is possible, since the temperatures of the baths enter only through their distributions. Inelastic processes occur naturally in the presence of non-linearities, for example induced by interactions, or by time dependent driving in the Hamiltonian describing the system [144]. In the presence of interactions, at least when the spectral density of the baths have identical energy dependence, one can formally express the heat current analogous to the scattering theory with a “transmission function" which now depends also on the temperatures of the baths [10, 125]. If, in addition, the quantum system S is coupled asymmetrically to the two baths, thermal rectification can take place.

Within this framework we can identify three possible ways the transmission probability can change upon inverting the temperature bias (from positive to negative). As schematically shown in Fig. 6.2, the transmission functions can change in height (a), position (b) and width (c). The height shift is the main mechanism that allows rectification even in the weak coupling regime, and it is present whenever one accounts for inelastic processes. The position shift is caused by the real part of the self energy, known as Lamb shift, which accounts for the renormalization of the system energy scales due to the system-bath coupling. Finally, the width of the transmission probability may change when the system is strongly coupled to the baths. In most cases we consider, the width and height shift occur together.

In the literature, thermal rectification has been studied in different nanoscale systems, such as quantum dots [73, 120, 121], spin-boson models [125, 123], non-linear harmonic resonators [126], and hybrid quantum devices [124, 127, 136], to name a few. In most cases, the weak coupling wide band approximation is used to study thermal rectification. It has been shown in Ref. [124] that asymmetric system-bath coupling and the presence of non-linearities are sufficient conditions to observe thermal rectification. Studying the spin-boson model [123, 125] and the non-linear harmonic resonator [126], it has been observed that thermal rectification increases as a function of the temperature difference and as a function of the asymmetry between the system-bath coupling strenghts. The spin-boson model has been studied also beyond the weak coupling regime in Ref. [125] using non equilibrium Green's function, and an enhancement in thermal rectification was observed.

Although thermal rectification has been studied in various specific systems, strategies to *maximize* rectification remain unclear. Moreover, it is not known if there are any fundamental bounds to the maximum rectification that can be obtained, and what is the impact of higher order coherent processes on rectification.

In this chapter, we address these issues studying different quantum systems, namely a qubit (two-level systems), a non-linear harmonic resonator and a Coulomb coupled quantum dot system employing three different formalisms: (1) the master equation (ME) taking cotunneling into account, (2) non-equilibrium Green's functions (NEGF) and (3) exact calculations based on Feynman-Vernon path integral approach in the qubit case. Our results are summarized in the following for the three different systems.

In the qubit case, without assuming any specific model for the bath and system-bath Hamiltonian, we study how to maximize rectification and we derive general upper bounds valid within the weak coupling regime. Furthermore, we find that the rectification can be enhanced by exploiting the temperature dependence of the Lamb-shift, together with gapped density of states in the baths. We then perturbatively go beyond the weak coupling regime generalizing the calculation of Ref. [125] by addressing general spin couplings between the system and the baths, as well as the effect of the Lamb shift. Furthermore, employing the Feynman-Vernon path integral approach, we are able to exactly study the strong coupling regime. Thanks to these methods, we find that many bounds and limitations emerging in the weak coupling regime can be overcome, and that rectification can be enhanced by higher order quantum coherent processes. These violations provide clear and simple "strong coupling signatures" which are experimentally observable.

The second system we consider is a non-linear harmonic resonator. Ruokola et al[126] studied thermal rectification in a non-linear harmonic resonator using the mean-field Hartree approximation. Such approximation gives accu-

rate results when the strength of non-linearity is significantly small compared to other energy scales of the system. In this chapter, we go beyond mean-field approximation employing the equation of motion (EOM) method to study thermal rectification in the strong coupling and large-interaction regime. We find better thermal rectification going beyond the mean field Hartree approximation. Finally, we also study the non-local thermal rectification effect in Coulomb coupled quantum dots. We will study the system proposed in Chapter 4, and employ non-local cooling effect to obtain thermal rectification in the drag system when the bias in the drive in switched.

The chapter is organized as follows. In Sec. 6.1 we present the model and in Sec. 6.2 we define the rectification coefficient. In Sec. 6.3 we study the qubit case in the weak coupling regime, while in Sec. 6.4 we study the qubit beyond the weak coupling regime. In Sec. 6.5, we study thermal rectification in a non-linear harmonic resonator. In Sec. 6.6, we study thermal rectification based on Coulomb coupled quantum dot device. At last, in Sec. 6.7 we draw the conclusions.

6.1 MODEL

We consider a system S arbitrarily coupled to two thermal baths denoted by L (left) and R (right) [see Fig. 6.1 for a sketch]. The total Hamiltonian is given by

$$H = H_{\mathrm{L}} + H_{\mathrm{R}} + H_{\mathrm{S}} + H_{\mathrm{L,S}} + H_{\mathrm{R,S}}, \tag{6.1}$$

where H_α, for $\alpha = \mathrm{L}, \mathrm{R}$, is the Hamiltonian of bath α, H_{S} is the Hamiltonian of the system S and $H_{\alpha,\mathrm{S}}$ describes the coupling between bath α and S. Each of these components - the baths, the system, and the couplings - contribute in different ways to the thermal properties of the device.

6.2 HEAT CURRENT AND RECTIFICATION

We are interested in studying the steady-state heat current flowing across the device when a temperature bias is imposed between the baths. Specifically, as depicted in Fig. 6.1, we fix $T_{\mathrm{L}} = T + \Delta T/2$ and $T_{\mathrm{R}} = T - \Delta T/2$, where T is the average temperature. Since no work is performed on the system (in the fermionic case, we will either consider no chemical potential bias, or configurations where the charge current is zero), the first principle of thermodynamics tell us that heat will flow from left to right if $\Delta T > 0$ (positive bias case, see Fig. 6.1a), otherwise it will flow from right to left (negative bias case, see Fig. 6.1b). Furthermore, since we consider steady state currents, the heat flowing out of one bath is equal to the one flowing into the other bath. Therefore, for simplicity we define the heat flowing out of the left lead as

$$J_{\mathrm{L}}^{(\mathrm{h})}(\Delta T) = -J_{\mathrm{R}}^{(\mathrm{h})}(\Delta T) = J^{(\mathrm{h})}(\Delta T) \equiv -\lim_{t\to+\infty} \frac{d}{dt} \langle H_{\mathrm{L}} \rangle (t), \tag{6.2}$$

where $\langle \ldots \rangle (t) = \mathrm{Tr}[\rho(t) \ldots]$, $\rho(t)$ being the density matrix representing the state of the total system at time t. Notice that the time variation of the energy associated with the coupling Hamiltonian vanishes in steady state [8].

As discussed in the introduction, it is possible to construct devices where the magnitude of the heat current depends on the sign of the temperature bias. Specifically, if the left-right symmetry is broken, the magnitude of the heat current $|J^{(\mathrm{h})}(\Delta T)|$ induced by a positive bias may be different respect

to $|J^{(\mathrm{h})}(-\Delta T)|$, which is the heat current induced by a negative bias. We therefore define the rectification coefficient R as

$$R = \frac{\left|J^{(\mathrm{h})}(\Delta T)\right| - \left|J^{(\mathrm{h})}(-\Delta T)\right|}{\left|J^{(\mathrm{h})}(\Delta T)\right| + \left|J^{(\mathrm{h})}(-\Delta T)\right|}, \tag{6.3}$$

for $\Delta T > 0$. The definition is such that $|R| \leq 1$. Furthermore, $R = 0$ means that no rectification takes place, while $|R| = 1$ means that we have perfect rectification (i.e. the heat current is finite in one direction, and null in the other). Positive (negative) values of R indicate that the heat flow is greater for positive (negative) temperature biases.

6.3 QUBIT: WEAK COUPLING REGIME

In this section, we derive general properties and upper bounds to the rectification coefficient R only assuming that the baths are weakly coupled to the qubit. The weak coupling regime is obtained by performing a leading order expansion in $\mathcal{H}_{\alpha,\mathrm{Q}}$ and assuming that the baths are Markovian [2]. This scheme leads to the so-called master equation for the reduced density matrix of the system. The approximation performed in this section allows us to consider height and position shift in the transmission function (see Fig. 6.2), but it neglects any width shift. Indeed, in this regime the width of the transmission function is the smallest energy scale, so it is infinitesimal. In the following sections, we will be able to observe also the impact of width shifts performing calculations beyond the weak-coupling regime.

Neglecting for the moment the Lamb-shift (which we discuss in Sec. 6.3.3) we find that (see App. F for details)

$$R = \frac{1 - C}{1 + C}, \tag{6.4}$$

where

$$C = \frac{\gamma_{\mathrm{L}}^{+}(\Delta, T_{\mathrm{H}})\gamma_{\mathrm{R}}^{+}(\Delta, T_{\mathrm{C}})}{\gamma_{\mathrm{L}}^{+}(\Delta, T_{\mathrm{C}})\gamma_{\mathrm{R}}^{+}(\Delta, T_{\mathrm{H}})} \cdot \frac{\gamma_{\mathrm{L}}^{+}(\Delta, T_{\mathrm{C}}) + \gamma_{\mathrm{R}}^{+}(\Delta, T_{\mathrm{H}})}{\gamma_{\mathrm{L}}^{+}(\Delta, T_{\mathrm{H}}) + \gamma_{\mathrm{R}}^{+}(\Delta, T_{\mathrm{C}})}, \tag{6.5}$$

$\gamma_{\alpha}^{+}(\Delta, T_{\alpha}) = \gamma_{\alpha}(\Delta, T_{\alpha}) + \tilde{\gamma}_{\alpha}(\Delta, T_{\alpha})$ is the total dissipation rate induced by bath α and $T_{\mathrm{H/C}} = T \pm \Delta T/2$ for $\Delta T > 0$. $\gamma_{\alpha}(\Delta, T_{\alpha})$ [$\tilde{\gamma}_{\alpha}(\Delta, T_{\alpha})$] represents the rate with which the qubit, being in the ground (excited) state, transits to the excited (ground) state by exchanging energy with bath α. Since bath α is prepared in a thermal state, these two rates are in general related by the detailed balance condition $\gamma_{\alpha}(\Delta, T_{\alpha}) = e^{-\Delta/(k_{\mathrm{B}}T_{\alpha})}\tilde{\gamma}_{\alpha}(\Delta, T_{\alpha})$ [see App. F for details]. The dissipation rate can then be calculated by evaluating

$$\tilde{\gamma}_{\alpha}(\Delta, T_{\alpha}) = \frac{1}{\hbar^2}\int_{-\infty}^{+\infty} dt\, e^{i\Delta t/\hbar}\left\langle B_{\alpha}(t)B_{\alpha}^{\dagger}(0)\right\rangle_{\alpha}, \tag{6.6}$$

where the expectation value is taken with respect to the *equilibrium* thermal state ρ_{α} of the bath, Δ is the energy spacing of the qubit [see Eq. (2.5)], and the operators $B_{\alpha}(t)$ and $B_{\alpha}^{\dagger}(t)$ are interaction picture operators (they evolve through $\mathcal{H}_{\alpha}$), thus the coupling to the qubit is neglected [see App. F for a derivation of Eq. (6.6)].

We can now study R for any weakly coupled system using Eqs. (6.4) and (6.6), which are generally easy to compute (we will consider various models explicitly in the following subsections). Interestingly, as a consequence of the weak coupling assumption, the coupling term $\sigma_z \otimes B_{\alpha z}$ [see Eq. (2.12)] does not contribute to $J(\Delta T)$, therefore neither to R. Intuitively, this is due to the

fact that the heat current is mediated by transitions in the weak coupling regime. Therefore, the heat current only depends on the population of the qubit, which in turn is solely determined by the coupling terms proportional to σ^+ and σ^- (see App. F for more details).

The rest of the section is organized as follows: in Sec. 6.3.1, we derive general bounds assuming that the baths are "similar" (this is a weak hypothesis; a proper definition will be given). In Sec. 6.3.2, we study a generic spin coupling to the bath. At last, in Sec. 6.3.3 we show how the Lamb-shift can be exploited to further enhance rectification.

6.3.1 *Rectifying with "similar" system-bath coupling*

In this section we assume that the left and right baths are "similar", i.e. we assume that the dissipation rate can be decomposed as

$$\gamma^+(\Delta, T_\alpha) = \Gamma_\alpha(\Delta) g(\Delta, T_\alpha), \tag{6.7}$$

where $\Gamma_\alpha(\Delta)$ is the spectral density of bath α, given by Eq. (2.15), and $g(\Delta, T_\alpha) \geq 0$ is an arbitrary non-negative function. Equation (6.7) implies that the dissipation rates of the two baths, as a function of temperature, are equal up to a prefactor. However, the rates may have *any dependence* on the gap of the qubit through the spectral densities. Two baths are similar whenever the coupling Hamiltonians relative to the two baths are distinct linear combinations of the *same operators*. For example, two bosonic baths, with distinct density of states, both coupled to the system through a linear or non-linear coupling, are similar baths.

Let us define the "asymmetry coefficient" λ as

$$\lambda = \frac{\Gamma_L(\Delta) - \Gamma_R(\Delta)}{\Gamma_L(\Delta) + \Gamma_R(\Delta)}, \tag{6.8}$$

such that $|\lambda| \leq 1$. Using Eq. (6.7), we can cast Eq. (6.4) into the simple form

$$R = \lambda \frac{g(\Delta, T_C) - g(\Delta, T_H)}{g(\Delta, T_C) + g(\Delta, T_H)}. \tag{6.9}$$

Without specifying the precise model, we can derive the following general properties of R:

- If $\lambda > 0$, R is a decreasing function of $g(\Delta, T_H)$, and an increasing function of $g(\Delta, T_C)$ (the monotonicity is inverted if $\lambda < 0$). Therefore, if $g(\Delta, T)$ is monotonous with respect to T, then R is monotonous with respect to ΔT.
- R is linear, therefore monotonous, with respect to λ.
- Given the first property, we can maximize the possible rectification by taking the limits where $g(\Delta, T_H)$ and $g(\Delta, T_C)$ respectively tend to zero and infinity. This yields the following bound

  $$|R| \leq |\lambda|. \tag{6.10}$$

  As a consequence, the maximum rectification is severely limited by the asymmetry ratio λ. As expected, for $\lambda = 0$ we find that there is no rectification, and the only way to obtain perfect rectification is to have a vanishingly small coupling to one bath.
- Given the second property, $|R|$ is bounded by $|(g(\Delta, T_C) - g(\Delta, T_H))/(g(\Delta, T_C) + g(\Delta, T_H))|$. We therefore have stronger rectification when $g(\Delta, T)$ has a strong temperature dependence.

6.3.1.1 *Linear system-bath tunnel couplings*

In this subsection we study heat rectification through a qubit where the coupling to the baths is linear, i.e. defined by Eq. (2.12). For fermionic baths weakly coupled to the qubit, we have that (see App. F, for details)

$$g(\Delta, T) = 1. \tag{6.11}$$

Plugging this value into Eq. (6.9) shows us that no rectification is possible. This is indeed expected, since a qubit coupled to fermionic reservoirs can be described by a non-interacting fermionic Hamiltonian, where the Landauer-Büttiker formula can be used to compute the heat current. Next, we consider bosonic baths. In this case, as shown in App. F, we have that

$$g(\Delta, T) = \coth\left[\Delta/(2k_{\mathrm{B}}T)\right], \tag{6.12}$$

so rectification is possible. In particular, we find the following properties:

- Since $g(\Delta, T)$ is a monotonous increasing function of T, λ and R have opposite signs. This means that more heat flows out of the weakly coupled lead.
- Since $g(\Delta, T)$ is a monotonous function of T, the rectification increases with ΔT.
- Since $g(\Delta, T)$ is never zero, but it diverges for $T \to \infty$, the bound in Eq. (6.10) is saturated only in the limit of infinitely hot reservoir ($T_{\mathrm{H}} \to \infty$).
- It can be explicitly seen that R is a decreasing function of the gap Δ, so it is maximum in the limit $\Delta \to 0$. In this limit, we can expand the cotangent, finding the following bound

$$|R| \leq \lambda \, \frac{T_{\mathrm{H}} - T_{\mathrm{C}}}{T_{\mathrm{H}} + T_{\mathrm{C}}}. \tag{6.13}$$

6.3.2 *Arbitrary baths with different spin couplings to the system*

In this section, we investigate what happens when the qubit is coupled to the baths through the same arbitrary bath operators, but through different Pauli spin matrices. As an example, we consider the coupling Hamiltonian given in Eq. (2.13) with $V_{\mathrm{L}k} = V_{\mathrm{R}k}$, although also non-linear couplings can be treated on the same footing. As shown in App. F, this system can be mapped into the "similar baths" case with an effective $\Gamma_\alpha(\Delta) \propto \sin^2\theta_\alpha$. Therefore, all the properties derived in Sec. 6.3.1 hold in this case, where the asymmetry coefficient is given by

$$\lambda = \frac{\sin^2\theta_{\mathrm{L}} - \sin^2\theta_{\mathrm{R}}}{\sin^2\theta_{\mathrm{L}} + \sin^2\theta_{\mathrm{R}}}, \tag{6.14}$$

while the function $g(\Delta, T)$ depends on the bath and system-bath Hamiltonian [in the specific case of Eq. (2.13), we have $g(\Delta, T) = \coth\left[\Delta/(2k_{\mathrm{B}}T)\right]$, see Eq. (6.12)]. Interestingly, the rectification does not depend on the angle ϕ_α; as we will show, this property does not hold beyond the weak coupling regime thanks to coherent transport effects. The only relevant angle is θ_α, which is the angle between the coupling term and the qubit Hamiltonian (which is proportional to σ_z). Since the rectification is linear in λ, we find that the rectification is maximum when θ_{L} is 0 and θ_R is $\pi/2$, or viceversa.

6.3.3 *Rectification enhanced by the Lamb-Shift*

Until now we have ignored the Lamb shift, i.e. the renormalization of the energy gap of the qubit induced by the presence of the baths. The renormalization of the qubit gap depends on both bath temperatures, thus it may influence the rectification properties of the device. As we now show, this allows us to achieve rectification beyond the bounds derived in the previous sections.

As shown in App. F, if the system-bath Hamiltonian does not contain terms proportional to σ_z (i.e. $B_{\alpha z} = 0$), the Lamb shift Hamiltonian (which has to be summed to the "bare" Hamiltonian $H_{\rm Q}$) takes the following form [2]:

$$H_{\rm LS} = \left[\delta\Delta_{\rm L}(\Delta, T_{\rm L}) + \delta\Delta_{\rm R}(\Delta, T_{\rm R})\right]\sigma_z, \tag{6.15}$$

where

$$\delta\Delta_\alpha(\epsilon, T_\alpha) = \frac{1}{2\pi}\mathcal{P}\int_{-\infty}^{+\infty}\frac{\gamma_\alpha^+(\epsilon', T_\alpha)}{\epsilon - \epsilon'}d\epsilon'. \tag{6.16}$$

In Eq. (6.16), $\mathcal{P}$ indicates a Cauchy principal value integration. We recall that the Δ appearing in Eq. (6.15) is the *bare gap*, neglecting the Lamb shift.

The renormalized gap is therefore given by

$$\tilde{\Delta}(\Delta T) = \Delta + \delta\Delta_{\rm L}(\Delta, T + \Delta T/2) + \delta\Delta_{\rm R}(\Delta, T - \Delta T/2), \tag{6.17}$$

and it may change upon inverting the temperature bias ($\Delta T \to -\Delta T$). In the presence of a Lamb shift, R is still given by Eq. (6.4) provided that we replace $\Delta \to \tilde{\Delta}(\Delta T)$.

In general, we notice that the renormalization terms $\delta\Delta_\alpha(\Delta, T_\alpha)$ is of the same order in the coupling strength as the rates $\gamma_\alpha^+(\epsilon, T_\alpha)$ (which are evaluated at leading order in the coupling). Therefore, if the rates $\gamma_\alpha^+(\epsilon, T_\alpha)$ are smooth functions of ϵ, their variation due to the Lamb shift will be beyond leading order in the coupling strength. Therefore, the effect of the Lamb shift on rectification is negligible in the weak coupling regime when the spectral density of the baths is a smooth function of the energy (on the $\hbar\gamma_\alpha^+$ scale).

However, the Lamb shift may become relevant for rectification whenever there is a strong energy dependence in $\gamma_\alpha^+(\epsilon, T_\alpha)$, for example, if the density of states of the baths has a gap. As we will show in detail in the following, even a small renormalization of the gap can have a large impact on the current.

We consider two bosonic Ohmic baths with a cutoff frequency $\epsilon_{\rm C}$, but we add a gap in the density of states between zero and a certain value ϵ_0. We thus have that

$$\gamma_\alpha^+(\epsilon, T_\alpha) = \frac{\pi}{\hbar}K_\alpha\,\theta(\epsilon - \epsilon_0)\,\epsilon\,e^{-\epsilon/\epsilon_{\rm C}}\coth\left[\epsilon/(2k_{\rm B}T_\alpha)\right], \tag{6.18}$$

where $\theta(\epsilon)$ is the Heaviside function which describes the gap in the density of states. In the upper panel of Fig. 6.3 we show the bare gap Δ (black curve), the renormalized gap $\tilde{\Delta}(\Delta T)$ for the positive bias case (blue curve), and the renormalized gap $\tilde{\Delta}(-\Delta T)$ for the negative bias case (green curve), as a function of the bare gap Δ. As we can see, the renormalized gaps are different in the positive and negative bias cases. In particular, in the highlighted region $\tilde{\Delta}(-\Delta T)$ is inside the gap, i.e. it is smaller than ϵ_0 (dashed gray line), while $\tilde{\Delta}(\Delta T)$ is outside the gap; we therefore expect a finite heat current in the latter case, and a zero heat current in the former. This is confirmed in the lower panel of Fig. 6.3 where $J^{(h)}(\Delta T)$ and $J^{(h)}(-\Delta T)$ are plotted as a function of the bare gap. The heat currents are computed using Eq. (F.7) with $\Delta \to \tilde{\Delta}(\Delta T)$

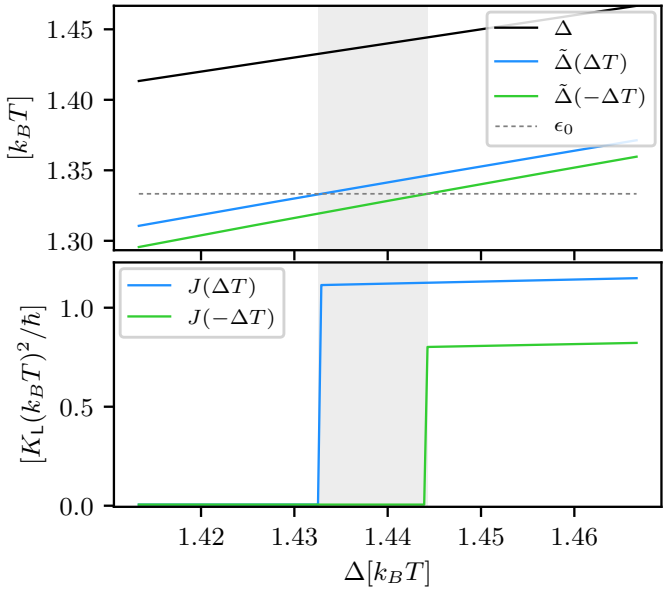

Figure 6.3: Upper panel: the bare gap Δ, the renormalized gap $\tilde{\Delta}(\Delta T)$ in the positive bias case and the renormalized gap $\tilde{\Delta}(-\Delta T)$ in the negative bias case, as a function of the bare gap Δ. The dashed gray line corresponds to the gap ϵ_0 in the density of states of the baths, while the region highlighted in gray shows where the renormalized gaps are respectively larger and smaller than ϵ_0. Lower panel: the heat currents $J^{(h)}(\Delta T)$ and $J^{(h)}(-\Delta T)$. In the highlighted region we have perfect rectification (up to higher order corrections in the coupling strength). The parameters are: $K_R = 5K_L$, $\epsilon_C = (20/3)\, k_B T$, $\epsilon_0 = (4/3)\, k_B T$ and $\Delta T/T = 2/3$.

to account for the Lamb shift. As we can see, within the highlighted region we have perfect rectification. However, we expect that the inclusion of higher order effects in the coupling strength (for example co-tunneling effects) will reduce the rectification. Indeed, the perfect rectification visible in the gray region in the lower panel of Fig. 6.3 is a consequence of the current $J^{(h)}(-\Delta T)$ being directly proportional to the density of states, therefore exactly zero for $\tilde{\Delta}(-\Delta T) < \epsilon_0$; on the other hand, higher order effects create small yet finite currents even in this parameter range. Nonetheless, we have identified a mechanism to enhance rectification exploiting the Lamb shift.

6.4 QUBIT: BEYOND WEAK COUPLING REGIME

As we have seen, the weak coupling regime puts strong constraints on the rectification coefficient R. In this section, we show that some of these bounds can be overcome by going beyond the weak coupling regime. This implies that coherent quantum effects - beyond "sequential tunneling" - can be beneficial for rectification. From the point of view of the transmission function, see Fig. 6.2, going beyond the weak coupling regime allows us to consider also width shifts, which were neglected in the previous section.

We perform calculations beyond the weak coupling regime using three different techniques. First, we include co-tunneling effects in the master equation (ME), which allows us to intuitively interpret our results; next, we employ a perturbative approach based on non equilibrium Green's function (NEGF) theory which yields results beyond sequential and co-tunneling effects. Finally, we perform an exact calculation employing the Feynman-

Vernon path integral approach which gives the heat current for general spectral densities and coupling conditions.

For concreteness, we consider bosonic baths, and a general spin coupling to the baths as defined in Eq. (2.13). We will then mainly consider two different couplings: the "XX coupling", where both left and right baths are coupled to the system through σ_x, i.e. $\theta_L = \theta_R = \pi/2$, $\phi_L = 0$, $\phi_R = 0$, and the "YX coupling", i.e. $\theta_L = \theta_R = \pi/2$, $\phi_L = \pi/2$, $\phi_R = 0$. Since the XX and YX couplings only differ by the angle ϕ_α [see Eq. (2.13)], both cases display identical rectification within the weak coupling regime (see Sec. 6.3.2). As we will see, this property is violated beyond the weak coupling regime, signaling the effect of higher order coherent quantum effects. We will also consider arbitrary spin coupling in the $\Delta \to 0$ limit. This particular choice exhibits no current in the sequential tunneling limit. Hence, thermal current and thermal rectification becomes solely due to higher order processes.

In the following, we describe the ME technique including co-tunneling in Sec. 6.4.1, the NEGF method in Sec. 6.4.2, exact calculations based on Feynman-Vernon path integral approach in Sec. 6.4.3 and we discuss the impact on rectification in Sec. 6.4.4. The results for arbitrary spin coupling in the $\Delta \to 0$ limit will be presented in Sec. 6.4.5.

6.4.1 *Master equation with co-tunneling*

In this subsection we describe how to perform calculations beyond the weak coupling regime by adding rates to the ME that arise from second order processes in the coupling Hamiltonian. It can be shown that, both for the XX and YX couplings, only elastic cotunneling processes contribute, i.e. only those processes that coherently transfer an excitation from one bath to the other - via a virtual state - without changing the state of the qubit.

We find that the heat current, including co-tunneling effects, can be expressed as (see App. F for details)

$$J^{(h)}(\Delta T) = J^{\mathrm{seq(h)}}(\Delta T) + J^{\mathrm{cot(h)}}(\Delta T), \tag{6.19}$$

where $J^{\mathrm{seq(h)}}(\Delta T)$ is the heat current expected in the weak coupling regime, given by Eq. (F.7), and

$$J^{\mathrm{cot(h)}}(\Delta T) = \int_0^\infty \frac{d\epsilon}{2\pi\hbar}\epsilon\Gamma_L(\epsilon)\Gamma_R(\epsilon) \times \left|\frac{1}{\Delta+\epsilon+i\eta} \pm \frac{1}{\Delta-\epsilon+i\eta}\right|^2 [n_R(\epsilon) - n_L(\epsilon)] \tag{6.20}$$

is the contribution due to co-tunneling, where η is an infinitesimal positive quantity, and $n_\alpha(\epsilon)$ is the Bose-Einstein distribution relative to bath α. The plus sign in Eq. (6.20) refers to the XX coupling, while the minus sign to the YX coupling.

Crucially, since the temperatures only enter through the Bose-Einstein distributions, $J^{\mathrm{cot(h)}}(\Delta T)$ is an *anti-symmetric* function, i.e. $J^{\mathrm{cot(h)}}(-\Delta T) = -J^{\mathrm{cot(h)}}(\Delta T)$. Therefore the contribution of cotunneling to the heat current is the same both for the positive and negative bias case. Mathematically, Eq. (6.20) diverges logarithmically in the limit $\eta \to 0^+$. The co-tunneling rates can be "regularised" in a proper manner[145, 146, 32]. Assuming that the qubit is in the ground state, the first term inside the square modulus of Eq. (6.20) arises by virtually transferring an excitation from one bath to the qubit, and then from the qubit to the other bath. The second term instead

arises by virtually creating an excitation both in one bath and in the qubit, and then by destroying an excitation in the qubit and in the other bath. The different XX and YX couplings produce opposite interference effects between these two processes. If we had neglected the "counter rotating" terms in $\mathcal{H}^{(\mathrm{sb})}_{\alpha,\mathrm{Q}}$ [Eq. (2.13)], the second term inside the square modulus would have vanished and the co-tunneling rates would have become the same in the XX and YX cases.

Exploiting the anti-symmetry of $J^{\mathrm{cot(h)}}(\Delta T)$, the impact of co-tunneling on rectification can be easily appreciated by plugging Eq. (6.19) into Eq. (6.3):

$$R = \frac{|J^{\mathrm{seq(h)}}(\Delta T)| - |J^{\mathrm{seq(h)}}(-\Delta T)|}{|J^{\mathrm{seq(h)}}(\Delta T)| + |J^{\mathrm{seq(h)}}(-\Delta T)| + 2J^{\mathrm{cot(h)}}(\Delta T)}, \tag{6.21}$$

where we fix $\Delta T > 0$. Notably, co-tunneling only appears at the denominator of Eq. (6.21). In addition, the cotunneling contribution of Eq. (6.20) represents an elastic process which would induce no rectification on its own. However, defining $R^{\mathrm{seq}} = (|J^{\mathrm{seq(h)}}(\Delta T)| - |J^{\mathrm{seq(h)}}(-\Delta T)|)/(|J^{\mathrm{seq(h)}}(\Delta T)| + |J^{\mathrm{seq(h)}}(-\Delta T)|)$, we see that if $J^{\mathrm{cot(h)}}(\Delta T) < 0$, then

$$|R| > |R^{\mathrm{seq}}|, \tag{6.22}$$

whereas $|R| < |R^{\mathrm{seq}}|$ if $J^{\mathrm{cot}}(\Delta T) > 0$. Therefore, co-tunneling can enhance rectification. Interestingly, the co-tunneling contribution $J^{\mathrm{cot}}(\Delta T)$ is usually *negative* when sequential tunneling dominates. Indeed, the transmission function due to sequential tunneling is a delta function peaked around resonant condition. The cotunneling contribution increases the width of the transmission function giving it an effective bell shape (as shown in Fig. 6.2). As we increase the width of the transmission function, we move the weight from the peak of the transmission function to its tails. Therefore, where sequential dominates, co-tunneling contribution *decreases* the heat flow. On the other hand, if sequential tunneling is suppressed, i.e. in the tails of the transmission function, co-tunneling increases the heat flow. Therefore, we expect the following behavior: when sequential tunneling is dominant, we expect co-tunneling to *enhance* rectification. Instead, when the currents are dominated by co-tunneling, we expect the rectification to decrease in comparison to the weak-coupling predictions. This qualitative argument is confirmed by the calculations performed in Sec. 6.4.4.

6.4.2 *Non-equilibrium Green's function method*

In this subsection we describe how to employ the NEGF method to compute heat currents beyond the weak coupling limit. Since Green functions for spin operators cannot be expanded in a perturbative series using Wick's theorem, we first perform the following transformation[147]

$$\sigma_a = -\frac{i}{2}\sum_{bc=x,y,z} \epsilon_{abc}\,\eta_b\eta_c, \tag{6.23}$$

where ϵ_{abc} is the Levi-Civita symbol, and η_a denotes three Majorana fermion operators (they satisfy the anticommutation relation $\{\eta_a, \eta_b\} = 0$ for $a \neq b$, $\eta_a^2 = 1$ and $\eta_a = \eta_a^\dagger$). The qubit and coupling Hamiltonians [see Eqs. (2.5) and (2.13)] therefore become (up to an irrelevant additive constant)

$$\begin{aligned} \mathcal{H}_{\mathrm{Q}} &= -i\frac{\Delta}{2}\eta_x\eta_y, \\ \mathcal{H}^{(\mathrm{sb})}_{\alpha,\mathrm{Q}} &= -\frac{i}{2}\sum_{abc}\hat{n}_{\alpha,a}\epsilon_{abc}\,\eta_b\eta_c \otimes \sum_k V_{\alpha k}(b_{\alpha k} + b^\dagger_{\alpha k}), \end{aligned} \tag{6.24}$$

where the indices a, b and c run over x, y and z in the sum. Notice that in this representation the qubit Hamiltonian is still quadratic (therefore "free"), while $\mathcal{H}^{(\mathrm{sb})}_{\alpha,\mathrm{Q}}$ is the product of three operators. Therefore, in the Majorana representation the system-bath coupling gives us the non-linear term which, as we discussed, is necessary to observe rectification.

Assuming that the spectral densities of the two baths are proportional, the heat current is given by Eq. (2.23) where $\mathcal{T}(\epsilon, T, \Delta T)$, in general, must be computed numerically. However, we are able to find an analytic expression for the transmission function by solving the Dyson equation for the Green's functions with an expression for the self energy expanded to leading order in the coupling Hamiltonian $\mathcal{H}^{(\mathrm{sb})}_{\alpha,\mathrm{Q}}$ (see App. F for details). In the XX coupling case, this method leads to

$$\mathcal{T}_{\mathrm{XX}}(\epsilon, T, \Delta T) = \frac{4\,\Delta^2 \Gamma_{\mathrm{L}}(\epsilon)\Gamma_{\mathrm{R}}(\epsilon)}{\left(\epsilon^2 - 2\epsilon\left(\delta\Delta_{\mathrm{L}}(\epsilon, T_{\mathrm{L}}) + \delta\Delta_{\mathrm{R}}(\epsilon, T_{\mathrm{R}})\right) - \Delta^2\right)^2 + \xi^2(\epsilon)} \tag{6.25}$$

where $\xi(\epsilon) = \epsilon \sum_\alpha \Gamma_\alpha(\epsilon)(1 + 2n_\alpha(\epsilon))$, and $\delta\Delta_\alpha(\epsilon, T_\alpha)$, which describes the Lamb shift induced by bath α, is defined in Eq. (6.16) with $\gamma^+_\alpha(\epsilon', T_\alpha) = \Gamma_\alpha(\epsilon') \coth\left[\epsilon'/(2k_{\mathrm{B}}T_\alpha)\right]$ [1]. Instead, in the YX coupling case we find

$$\mathcal{T}_{\mathrm{YX}}(\epsilon, T, \Delta T) = \frac{4\,\epsilon^2\,\Gamma_{\mathrm{L}}(\epsilon)\Gamma_{\mathrm{R}}(\epsilon)}{\left(\epsilon^2 - \mathcal{X}(\epsilon) - \Delta^2\right)^2 + \mathcal{Y}^2(\epsilon)}, \tag{6.26}$$

where

$$\mathcal{X}(\epsilon) = 2\epsilon\left(\delta\Delta_{\mathrm{L}}(\epsilon) + \delta\Delta_{\mathrm{R}}(\epsilon)\right) + \left(1 + 2n_{\mathrm{L}}(\epsilon)\right) \times \left(1 + 2n_{\mathrm{R}}(\epsilon)\right)\Gamma_{\mathrm{L}}(\epsilon)\Gamma_{\mathrm{R}}(\epsilon) - 4\delta\Delta_{\mathrm{L}}(\epsilon)\delta\Delta_{\mathrm{R}}(\epsilon), \tag{6.27}$$

and

$$\mathcal{Y}(\epsilon) = \sum_{\substack{\alpha,\beta=\mathrm{L},\mathrm{R} \\ \alpha\neq\beta}} \left(2\delta\Delta_\alpha(\epsilon) - \epsilon\right)\left(1 + 2n_\beta(\epsilon)\right)\Gamma_\beta(\epsilon). \tag{6.28}$$

As shown in App. F, this approach provides results which are more accurate with respect to the ME approach (including co-tunneling contributions), since it contains higher order processes beyond sequential and cotunneling thanks to the implicit re-summation performed by solving the Dyson equation.

6.4.3 *Spin-boson model: Exact calculation*

In this subsection we consider the XX coupling case, which allows the derivation of an exact formal expression for the heat current Eq. (2.22) for general spectral densities of the two baths within the Feynmann-Vernon path-integral approach to the spin-boson problem [7]. Calculations are reported in App. (F). When the spectral densities have the same energy dependence, i.e. $\Gamma_{\mathrm{L}}(\epsilon) \propto \Gamma_{\mathrm{R}}(\epsilon)$, the heat current takes the form of Eq. (2.23) with

$$\mathcal{T}^{(\mathrm{ex})}_{\mathrm{XX}}(\epsilon, T, \Delta T) = 2\frac{\Gamma_{\mathrm{L}}(\epsilon)\Gamma_{\mathrm{R}}(\epsilon)}{\Gamma_{\mathrm{L}}(\epsilon) + \Gamma_{\mathrm{R}}(\epsilon)}\mathrm{Im}\left[\chi(\epsilon)\right], \tag{6.29}$$

where $\chi(\epsilon)$ is the Fourier transform of the qubit dynamical susceptibility in the presence of the two baths, $\chi(t) = (i/\hbar)\Theta(t)\langle[\sigma_x(t), \sigma_x(0)]\rangle$, given in Eq. (F.115).

1 In order to account for the counter-rotating terms in the coupling Hamiltonian, in the calculation of the Lamb-shift the spectral density $\Gamma_\alpha(\epsilon')$ must be extended to negative values according to $\Gamma_\alpha(-\epsilon') = -\Gamma_\alpha(\epsilon')$.

We now focus on Ohmic spectral densities, defined as in Eq. (2.15). The dimensionless Ohmic coupling strength K_α enters the exact expression of the dynamical susceptibility in a form which allows the path summation in analytic form when $K_R + K_L = 1/2$, analogously to the Toulouse point of the Ohmic spin boson problem [7, 148], see Eq. (2.15). We obtain

$$\chi(t) = \frac{2\Delta^2}{\hbar^3\gamma}\Theta(t)e^{-\gamma t/2}\int_0^\infty d\tau P(\tau)\left[e^{-\gamma|t-\tau|/2} - e^{-\gamma|t+\tau|/2}\right], \tag{6.30}$$

where $\gamma = \pi\Delta^2/(2\hbar\epsilon_C)$ and

$$P(\tau) = \prod_\alpha \left(\frac{\epsilon_C}{\pi k_B T_\alpha}\sinh\left(\frac{\pi|\tau|k_B T_\alpha}{\hbar}\right)\right)^{-2K_\alpha}. \tag{6.31}$$

We note that $\chi(t)$ takes the same form of the spin-boson model at the Toulouse point with the only differnce that the bath-induced (dipole or intra-blip, see App. F) interactions involving the two baths enter $P(\tau)$ in factorized form. Indeed, in the limit $K_L = K_R = 1/4$ and $\Delta T = 0$ we recover the susceptibility of the Kondo problem at the Toulouse point. Under these conditions the heat current trivially vanishes. In the following we will evaluate heat rectification considering asymmetric couplings with the two baths under the"overal" strong coupling condition $K_L + K_R = 1/2$. All possible heat transfer processes are exactly included. To this end the heat current Eq. (2.23) with (6.30) is more conveniently written as

$$J = \frac{1}{\hbar}\frac{K_L K_R}{K_L + K_R}\,\mathrm{Im}\int_{-\infty}^{+\infty} dt\,\chi(t)F(-t), \tag{6.32}$$

where

$$F(-t) = (k_B T_R)^3\psi^{(2)}\left(1 + \frac{k_B T_R}{\epsilon_C}\left(1 - i\frac{\epsilon_C t}{\hbar}\right)\right) - (k_B T_L)^3\psi^{(2)}\left(1 + \frac{k_B T_L}{\epsilon_C}\left(1 - i\frac{\epsilon_C t}{\hbar}\right)\right) \tag{6.33}$$

and $\psi^{(2)}(z)$ denotes the second derivative of the digamma function.

6.4.4 *Rectification beyond the weak-coupling regime*

In this subsection we show that various general properties and bounds derived in Sec. 6.3 can be overcome, allowing the system to exibit stronger rectification than in the weak-coupling regime. We will also be able to identify the effect of higher order coherent transport on rectification. We will consider Ohmic spectral density, as in Eq. (2.15), for both baths.

In Fig. 6.4 we plot R as a function of K_L in the XX and YX case comparing the NEGF calculation, the ME calculation including cotunneling effects [ME(cot)] and the ME calculation in the weak coupling regime [ME(seq)]. The coupling constant $K_R = 0.005$ and the temperatures are fixed. First we notice that, for small values of K_L, i.e. in the weak coupling limit, all three curves coincide, as expected. As K_L increases, we notice that the NEGF and ME(cot) curves nicely agree up to $K_L \approx 0.025$, and then we see some deviations. Next, we notice that the rectification using NEGF and ME(cot) method is *different* in the XX and YX cases, whereas it is the same using the ME(seq) method. Indeed, in Sec. 6.3.2 we showed that, in the weak coupling regime, rectification only depends on the angle between the qubit (σ_z) and

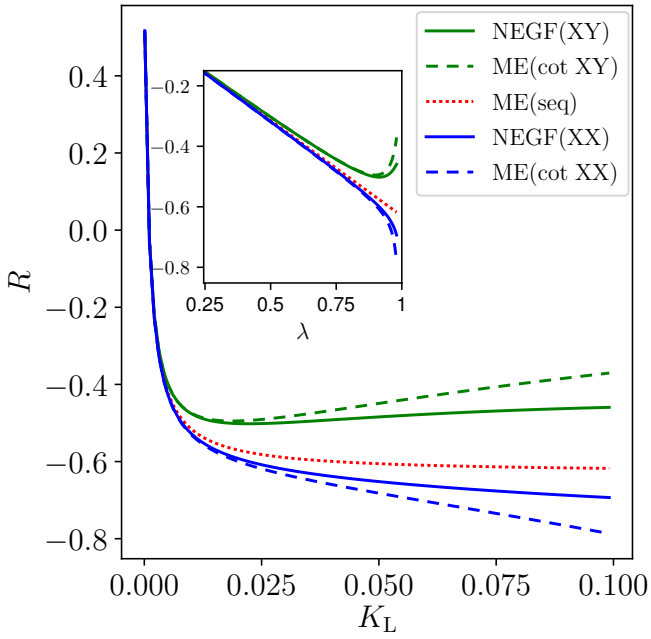

Figure 6.4: R, computed with the three methods described in the legend, as a function of K_L both for the XX and YX couplings; the ME(seq) case is the same for both couplings. The parameters are $K_R = 0.001$, $\Delta = 0.8 k_B T$, $\epsilon_C = 10 k_B T$ and $\Delta T/T = 8/5$. We denote with "NEGF" the calculations performed with the non-equilibrium Green's function method described in Sec. 6.4.2, with "ME(cot)" those performed with the master equation which includes co-tunneling described in Sec. 6.4.1, and with "ME(seq)" the calculations performed in the weak coupling limit as described in Sec. 6.3. The inset shows the same points plotted as a function of λ for $\lambda \in [0.25, 1]$. We neglect the Lamb shift in this plot.

the coupling term. Higher order coherent processes, instead, are able to distinguish these different couplings, as they produce different interference effects [see the $\pm$ in Eq. (6.20)]. Next, we notice that the rectification is *enhanced* in the XX coupling case thanks to higher order processes, while it is suppressed in the YX case (we will explain this behavior describing Fig. 6.5). In the inset of Fig. 6.4 we plot the same points as a function of the asymmetry coefficient $\lambda = (K_L - K_R)/(K_L + K_R)$ [see Eq. (6.8)]. We recall that, in the weak coupling regime, we proved that R is linear in λ (see Sec. 6.3.1). Indeed, for small values of λ, the behavior is linear. Interestingly, the behaviour becomes non-linear for larger values of λ, which correspond to larger values of the coupling constant K_L. This non-linearity is yet another signature of higher order coherent processes.

In Fig. 6.5 we plot R, computed with the three methods described above, as a function of Δ for fixed values of the temperatures and of the coupling constants. There are many interesting facts to notice. First, the coupling constants are not very small, so the NEGF and ME(cot) methods, which qualitatively agree with each other, provide visible corrections to the ME(seq) calculations. As we noticed also in Fig. 6.4, rectification is stronger in the XX case (blue curves), while it is weaker in the YX case (green curves) as compared to the ME(seq) calculations for $\Delta \leq 2 k_B T$. For $\Delta > 2 k_B T$, all the methods predict similar values of R. Interestingly, the value of R computed using the NEGF and ME(cot) methods in the XX case shows a violation of the

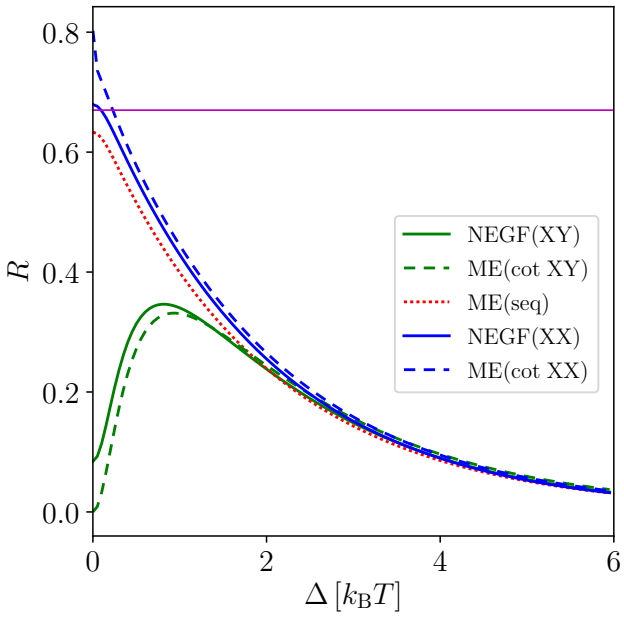

Figure 6.5: Rectification R, computed with the three methods described in the legend, as a function of the qubit gap Δ. The parameters are $K_L = 0.006$, $K_R = 0.03$, $\epsilon_C = 10 k_B T$ and $\Delta T/T = 1.9$. The horizontal magenta line shows $|\lambda| = |(K_L - K_R)/(K_L + K_R)| = 0.67$. We neglect the Lamb shift in this plot.

general weak-coupling bound of Eq. (6.10), i.e. we find that $|R| > |\lambda| = 0.67$ (denoted with a horizontal magneta line in Fig. 6.5) for small values of Δ. On the other hand, in the YX coupling case we notice that coherent processes decrease rectification. This different behavior is due to the following fact: the heat currents computed in the ME(seq) case tend to zero as $\Delta/(k_B T) \to 0$ (see App. F for details). In the XX case, the two terms inside the square modulus of Eq. (6.20) cancel each other, hence also the co-tunneling contribution vanishes; however, in the YX case, it remains finite. Therefore, in the $\Delta \to 0$ limit, sequential tunneling dominates over co-tunneling in the XX case, thus enhancing rectification (as discussed in Sec. 6.4.1). On the contrary, in the YX case co-tunneling dominates over sequential tunneling, thus suppressing rectification. This observation justifies also the large deviation between the ME(seq) curve and the other ones observed in the YX case for small Δ. At last, we notice that in the YX case, thanks to higher order processes, the NEGF and ME(cot) are non-monotonous with respect to Δ (as discussed in Sec. 6.3.1.1, R is monotonous in Δ in the weak coupling regime).

In Fig. 6.6 we plot the heat current (upper panel) and the rectification coefficient (lower panel) as a function of the qubit gap Δ fixing all other parameters as described in the caption. We compare the analytic results obtained in the XX case using the NEGF method including the Lamb-shift (see Sec. 6.4.2) with the exact calculation obtained using the Feynman-Vernon path integral approach (see Sec. 6.4.3). In doing so, we are constrained to fixing the coupling strength as $K_L + K_R = 1/2$. We observe that the exact and NEGF calculations for the heat current give quantitatively different results, i.e. the NEGF method tends to overestimate the magnitude of the heat current for values of $\Delta/(k_B T) \lesssim 10$, while it underestimates the heat current for larger

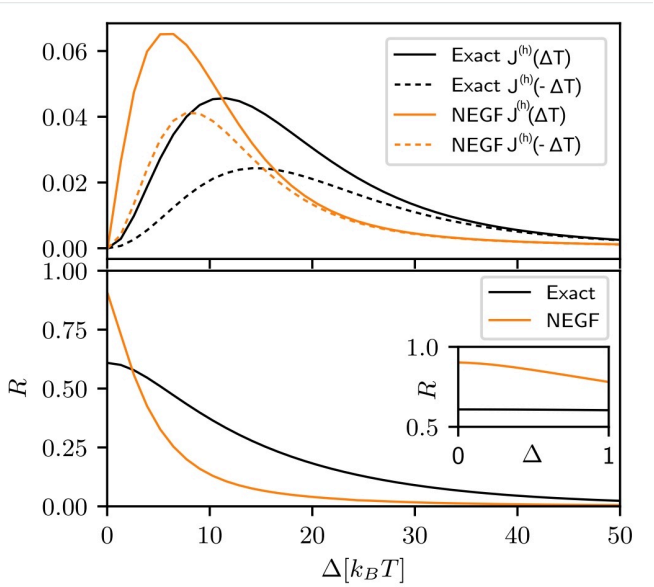

Figure 6.6: Comparison of thermal current (in units of $(k_B T)^2/\hbar$) and thermal rectification in the strong coupling regime computed using the two methods described in the legend, as a function of qubit gap Δ. The NEGF calculation includes the Lamb shift. The parameters are $K_L = 0.49$, $K_R = 0.01$, $\epsilon_C = 100 k_B T$ and $\Delta T/T = 1.9$.

values of $\Delta/(k_B T)$. However, qualitatively there is a reasonable agreement between the two calculations. This is in fact surprising: the NEGF approach is perturbative in the coupling strength. Therefore, strictly speaking, it is valid only for $K_L + K_R \ll 1$, while $K_L + K_R = 1/2$ (strong coupling regime). On the other hand, the rectification coefficient is very different for small values of $\Delta/(k_B T)$: the NEGF approach strongly overestimates the rectification. However, this behavior is inverted upon increasing the qubit gap. Then, for large enough values of Δ, the two methods predict a more similar rectification coefficient, with the exact calculation predicting higher thermal rectification compared to the NEGF calculations. At last, for even larger values of Δ, the rectification coefficient predicted by both methods tends to 1, i.e. no rectification.

6.4.5 *Rectification with arbitrary σ coupling*

In this subsection we study the impact on rectification of more general couplings respect to the XX and YX cases using the NEGF formalism previously described (see App. F for details about the calculation). We focus on the $\Delta/(k_B T) \to 0$ limit where heat transport is entirely due to higher order coherent processes. This is due to the fact that the heat current, computed in the weak coupling regime, tends to zero as $\Delta/(k_B T) \to 0$ (see App. F). We therefore consider the coupling Hamiltonian, given in Eq. (2.13), with an arbitrary coupling to the left bath, i.e. arbitrary $\theta_L = \theta$ and $\phi_L = \phi$, but with fixed σ_x coupling to the right lead, i.e. $\theta_R = \pi/2$ and $\phi_R = 0$. The XX and YX cases, considered in the previous subsections, can be recovered respectively by setting $\theta = \pi/2$ and $\phi = 0$, or $\theta = \pi/2$ and $\phi = \pi/2$. Notice that, by considering a coupling with $\theta \neq \pi/2$, we are including also a σ_z coupling to the left lead. We recall that, in the weak coupling regime, the σ_z coupling

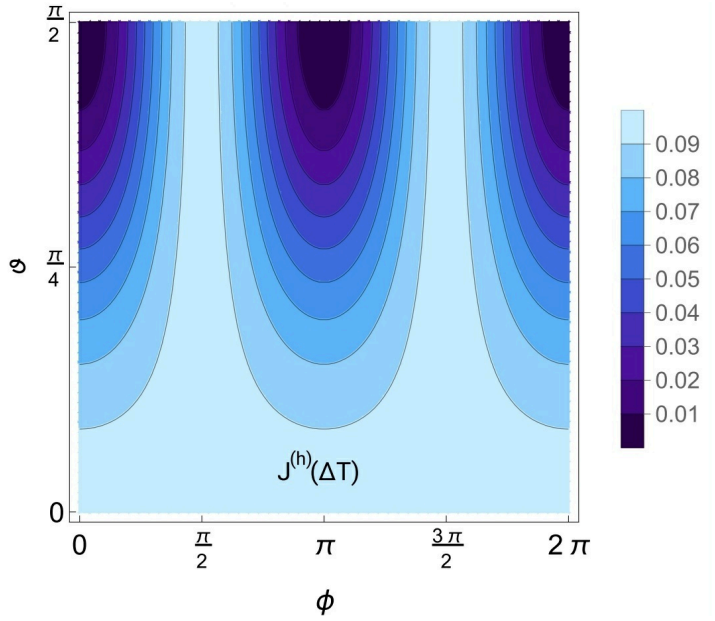

Figure 6.7: Contour plot of $J^{(h)}(\Delta T)$ in units of $(k_B T)^2/\hbar$ as a function of θ and ϕ. The parameters are: $\epsilon_C = 80 k_B T$, $K_L = K_R = 0.06$ and $\Delta T/T = 1.9$.

does not contribute to the heat current. In order to isolate the impact on rectification of different spin couplings, we consider the case of identical spectral densities for the two baths, i.e. $\Gamma_L(\epsilon) = \Gamma_R(\epsilon)$. Therefore, the only asymmetry in the coupling, which can give rise to rectification, is given by the different directions described by $\hat{n}_L$ and $\hat{n}_R$.

In Fig. 6.7 we show a contour plot of the heat current $J(\Delta T)$, at fixed temperatures and for equal Ohmic spectral densities [i.e. $K_L = K_R$, see Eq. (2.15)], as a function of the two angles θ and ϕ in the small gap limit, i.e. for $\Delta/(k_B T) \to 0$. For simplicity, we neglected the Lamb shift. Strikingly, the heat current is *maximum* when the left lead is coupled through σ_z, i.e. for $\theta = 0$ (lower part of Fig. 6.7). This is surprising for two reasons: first, in the weak coupling limit the heat current at $\theta = 0$ would be null even for finite values of Δ, since σ_z does not contribute to the heat currents; second, regardless of the coupling strength, a single bath coupled to S through σ_z cannot transfer heat to the system, since the Hamiltonian of S would commute with the total Hamiltonian (and thus it would be a conserved quantity). In this case, the σ_z coupling would only produce dephasing in the qubit state. We can therefore qualitatively describe transport in this regime as a direct transfer of heat from one bath to the other. As θ increases, and therefore as the σ_z component decreases, the heat current decreases monotonously, to the point that it is null in the XX case ($\phi = n\pi$), while it remain constant in the YX case (along $\phi = \pi/2 + n\pi$).

Interestingly, also the rectification coefficients roughly follows a similar trend, i.e. it is maximum where also the heat currents are maximum. This can be seen in Fig. 6.8, where R is contour-plotted as a function of θ and ϕ for the same parameters as in Fig. 6.7. Indeed, R is maximum for $\theta = 0$, i.e. when the left lead is coupled only through σ_z. As θ increases, R decreases monotonically along $\phi = n\pi$, just as the heat current itself. However, it remain constant along $\phi = \pi/2 + n\pi$, while for intermediate values of ϕ it displays a non-monotonic behavior.

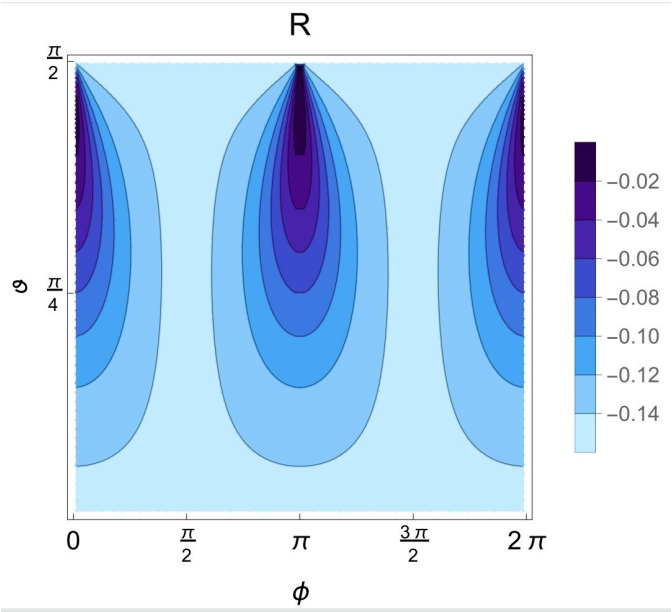

Figure 6.8: Contour plot of R as a function of θ and ϕ. The parameters are the same as in Fig. 6.7.

We can therefore conclude that the optimal operational points in the $\Delta/(k_B T) \to 0$ limit are the YX and the ZX coupling cases. These couplings simultaneously maximize the magnitude of the heat current and of the rectification coefficient. We emphasize that the heat current, which is solely due to coherent quantum processes, behaves in the opposite way respect to what would be expected from weak coupling calculations (the heat currents should be zero both because $\Delta = 0$ and because σ_z does not contribute to the heat current).

6.5 NON-LINEAR QUANTUM CIRCUIT

The Josephson junction in an electric circuit behaves as an inductance with a degree of non-linearity. Thanks to the superconductivity, the inductance is non-dissipative as well. Due to the aforementioned two characteristics, namely non-linearity and no dissipation, Josephson junctions are used as building blocks in superconducting quantum circuits. On the same note, Josephson junction is often inserted into a resonator circuit to obtain a non-linear resonator circuit. Consequently, the Hamiltonian for a split Cooper pair box which consists of an LC resonator circuit with a Josephson junction, under certain conditions, can be reduced to the Hamiltonian for a non-linear resonator defined in Eq. (2.4) (for details see Refs. [149, 150, 151]). In terms of the parameters of the split-pair cooper box, $\Delta = \sqrt{2E_{CP}E_J}$ and $U = E_{CP}/4$, where E_{CP} is the charging energy of the Cooper pair box and E_J is the Josephson energy. When the non-linearity factor U is very large compared to the photon decay rate, the Hamiltonian behaves as an effective two level system,

$$H_H \approx \frac{\Delta}{2}\hat{\sigma}_z. \tag{6.34}$$

A similar model was recently realized by Senior et al. in Ref. [45] to study thermal rectification.

In this section, we will study heat rectification in a non-linear resonator defined in Eq. (2.4) coupled to bosonic leads. We will employ the Keldysh non-equilibrium Green's function technique to obtain analytic expressions beyond mean field for heat current. Note that, as opposed to the qubit case, we shall keep only the non-rotating terms in the Hamiltonian. We can define the system Green's function as:

$$G^r_{b;b}(t,t') = -i\theta(t-t')\left\langle\left[b(t), b^\dagger(t')\right]\right\rangle. \tag{6.35}$$

For the sake of simplicity, we consider Ohmic spectral density with a sharp cut-off given by

$$\Gamma_\alpha(\epsilon) = \pi\theta(\epsilon)\theta(\epsilon_C - \epsilon)K_\alpha\,\epsilon, \tag{6.36}$$

ϵ_C being the cut-off frequency. In the presence of interaction, one cannot obtain exact expression for Green's function. Following Ref. [152], we use the equation of motion (EOM) method to obtain the Green's function for the system (see App. F for details):

$$G_{b;b}(\epsilon) = \frac{1 + 2I(\epsilon)\langle n\rangle}{\epsilon - \epsilon_0 - \Sigma^{(0)}(\epsilon) + 2I(\epsilon)\left(\Sigma^{(2)}(\epsilon) + \Sigma^{(3)}(\epsilon)\right)}, \tag{6.37}$$

where

$$I(\epsilon)/U = \left(\epsilon - \epsilon_0 - U\langle n\rangle - \left(2\Sigma^{(0)}(\epsilon) + \Sigma^{(1)}(\epsilon)\right)\right)^{-1}. \tag{6.38}$$

In deriving Eq. (6.37), we neglected terms involving correlation in the baths. Specifically, we set $\left\langle\left[b^\dagger(t)b_{\alpha k}(t)b_{\alpha k}(t), b^\dagger(t')\right]\right\rangle = 0$ and $\left\langle b^\dagger b_{k\alpha}\right\rangle = \left\langle b b^\dagger_{k\alpha}\right\rangle = 0$. The contribution from these terms become significant in the strong coupling regime [152]. In addition we truncated the Green's function at second order, i. e. we assume $G_{n,n,b;b}(\epsilon) = \langle n\rangle\, G_{n,b;b}(\epsilon)$. In Eq. (6.37), the usual embedded self-energy is defined through the expression

$$\Sigma^{(0)}_\alpha(\epsilon) = \int d\omega\left[\frac{\Gamma_\alpha(\omega)}{\epsilon - \omega + i\eta}\right]. \tag{6.39}$$

Our calculation goes beyond mean field (MF) and keeps also the processes involving virtual states in the system. The inclusion of self energies defined through the expressions

$$\begin{aligned}
\Sigma^{(1)}(\epsilon) &= \sum_\alpha \int \frac{d\omega}{2\pi}\left[\frac{\Gamma_\alpha(\omega)}{\epsilon + \omega - 2\epsilon_0 - 2U\langle n\rangle - U + i\eta}\right],\\
\Sigma^{(2)}(\epsilon) &= \sum_\alpha \int \frac{d\omega}{2\pi}\left[\frac{n_\alpha(\omega)\Gamma_\alpha(\omega)}{\epsilon - \omega + i\eta}\right],\\
\Sigma^{(3)}(\epsilon) &= \sum_\alpha \int \frac{d\omega}{2\pi}\left[\frac{\Gamma_\alpha(\omega)n_\alpha(\omega)}{\epsilon + \omega - 2\epsilon_0 - 2U\langle n\rangle - U + i\eta}\right].
\end{aligned}$$

ensure that the onsite correlation effects are correctly captured. The distribution function can be obtained from

$$\langle n\rangle = \sum_\alpha \int \frac{d\epsilon}{2\pi} G_{b;b}(\epsilon) n_\alpha(\epsilon)\Gamma_\alpha(\epsilon) G^*_{b;b}(\epsilon). \tag{6.40}$$

In order to obtain the Green's function ($G_{b;b}$), one would have to solve Eq. (6.37) and Eq. (6.40) self-consistently. Since the spectral densities for the

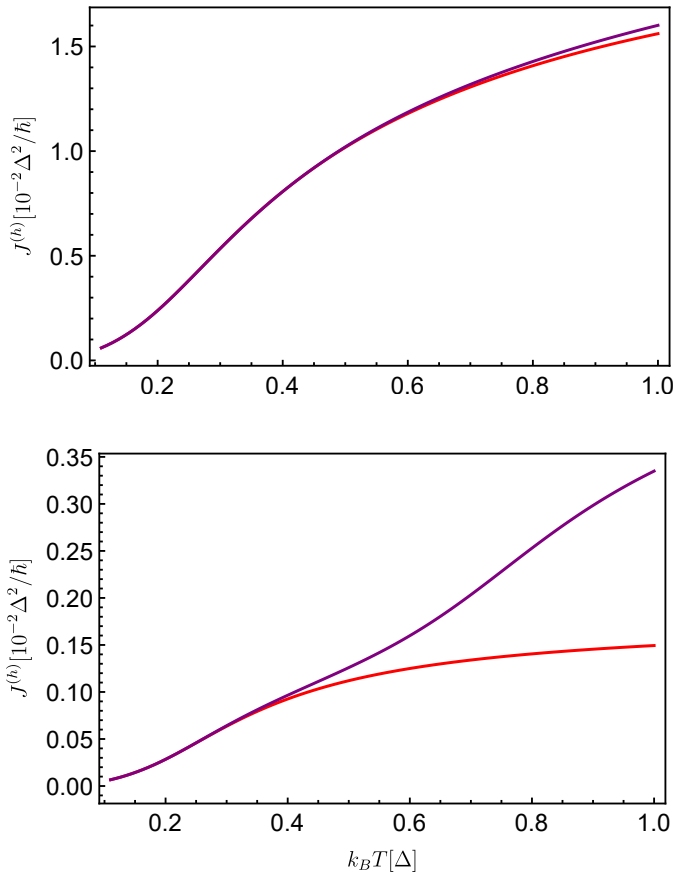

Figure 6.9: Heat current as a function of average temperature k_BT for different values of system-bath coupling strength (top panel $K_L = K_R = 0.05$ and bottom panel $K_L = K_R = 0.005$). The other parameters are $\epsilon_C = 100U$, $k_B\Delta T = 0.1\Delta$ and $U = 0.05\Delta$.

left and right lead are proportional to each other, the transmission function can be expressed as

$$\mathcal{T}(\epsilon) = \Gamma_L(\epsilon)\Gamma_R(\epsilon)G_{b;b}(\epsilon)G^*_{b;b}(\epsilon). \tag{6.41}$$

For $U = 0$, the transmission function is given by:

$$\mathcal{T}(\epsilon) = \frac{\epsilon\Gamma_L(\epsilon)\Gamma_R(\epsilon)}{(\epsilon^2 - \epsilon_0^2)^2 + \sum_\alpha \Gamma_\alpha^2(\epsilon)/4}. \tag{6.42}$$

Eq. (6.42) is temperature independent and hence, in the absence of interaction, a harmonic resonator does not induce thermal rectification.

6.5.0.1 *Mean-field approximation*

The MF results are obtained by truncating the EOM for the retarded Green's function at first order. In the MF approximation the retarded Green's function takes the form

$$G^{MF}_{b;b} = \frac{1}{\epsilon - \epsilon_0 - \frac{U}{2} - U\langle n\rangle - \Sigma^{(0)}(\epsilon)}. \tag{6.43}$$

The MF approximation renormalizes the energy of the resonator but the self-energy is unchanged compared to the non-interacting case. Consequently,

higher order effects resulting from correlation between system-bath coupling and the interaction are not taken into account. The self energy in Eq. (6.37) for Green's function calculated using the EOM takes into account onsite correlation effects but neglects correlations in the bath. Considering an average thermal energy $k_B T$ of the order of Δ, the onsite correlation effects become significant when the interaction is of the order of the coupling strength, i. e. $U \approx \pi K_\alpha \Delta$. For $U \ll \pi K_\alpha \Delta$, MF approximation and EOM give similar results. To illustrate this point, in Fig. 6.9 we plot heat current obtained using the above mentioned two approximations for different values of coupling strength. For a fixed value of interaction ($U = 0.05\Delta$), we observe that the MF (red curve) and the EOM (purple curve) method agree more in the strong system-bath coupling case (top panel) than the weak system-bath coupling case (bottom panel). The deviation between the two methods increases at increasing temperature. In the absence of interaction, both Eq. (6.37) and Eq. (6.43) reduce to the same expression for exact Green's function of a non-interacting harmonic resonator.

6.5.1 *Results*

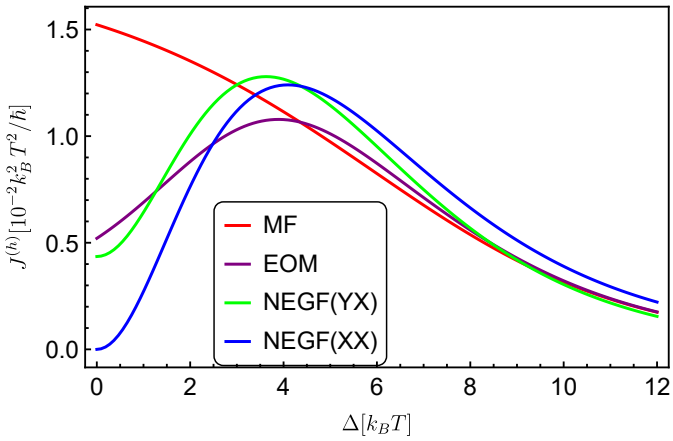

Figure 6.10: Heat current as a function of resonator energy Δ for $\Delta T/T = 8/5$, $\epsilon_C = 100U$, $U = 40k_B T$, $K_L = 0.06$ and $K_R = 0.003$.

In Fig. 6.10, we plot the heat current as a function of the resonator energy Δ. We fix the the coupling parameters to be within the weak coupling regime, $K_L = 0.06$ and $K_R = 0.003$. The interaction is taken large enough ($U = 40k_B T$) such that within the weak coupling regime only the first two eigenstates of the non-linear resonator become available for transport, and the non-linear resonator behaves as a qubit with Hamiltonian given by Eq. (6.34). We use two different expressions for Green's function to calculate the heat current: 1) Green's function described by Eq. (6.43) obtained by applying MF Hartree approximation, and 2) Green's function described by Eq. (6.37) obtained using the EOM. In addition, we compare the above mentioned heat currents with the heat current for a qubit [defined by Eq. (6.34)] calculated using NEGF method in the XX as well as the YX coupling case. As shown in Fig. 6.10, the heat currents obtained for the qubit case (blue curve for XX coupling and green curve for YX coupling) converge to the non-linear resonator case [both MF (red curve) and EOM (blue curve)] for $\Delta > 6k_B T$.

In addition, the NEGF and the EOM calculations both predict a peak in the heat current for $\Delta \sim 4k_BT$. The NEGF(XX) heat current goes to zero for $\Delta = 0$ whereas NEGF(YX) and EOM calculations predict a finite heat current even for $\Delta = 0$. On the other hand, heat current obtained using mean field approximation increases monotonously for $\Delta \to 0$, exhibiting completely different behavior than that of NEGF as well as EOM calculations. Above results can be explained on the basis of following arguments: 1) The system-bath coupling is different in the two cases (in the non-linear resonator case, the system bath coupling can be written in terms of σ^+ and σ^- operators which is a linear combination of σ_x and σ_y type couplings considered for the qubit). Indeed, for $\Delta \to 0$, the EOM calculations agrees more with the YX coupling case as the contribution due to XX coupling vanishes. 2) A one to one correspondence between the approximations applied in the qubit case and the non-linear resonator case can not be made. The MF as well as EOM correctly describe both the weak and strong coupling limit however the NEGF formulation in the qubit case (where the self energy is calculated undergoing perturbation upto first order in system bath coupling strength) is accurate only in the weak coupling limit. 3) The contribution from higher eigen states of the interacting resonator although relatively small could be significant. *The advantage of EOM is that it gives correct results in both weak and strong coupling regime.*

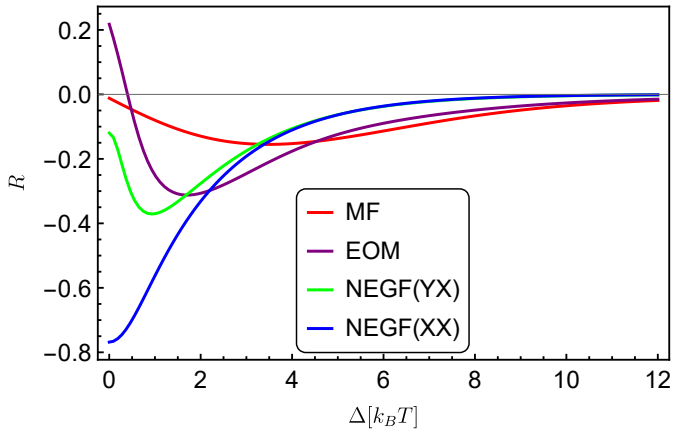

Figure 6.11: Rectification as a function of resonator energy or qubit gap Δ for similar parameters as in Fig. 6.10

In Fig. 6.11 we plot the rectification coefficient R as a function of resonator energy Δ for fixed thermal bias and coupling strength. The interaction U is chosen large enough to attain the qubit limit. EOM predicts maximum rectification of $\sim 32\%$ for $\Delta \sim 2k_BT$. For $\Delta < 2k_BT$, the rectification obtained using EOM for non linear resonator and NEGF(XX) for qubit exhibit different behavior: NEGF(XX) predicts a montonous increase in rectification with decreasing Δ whereas the rectification obtained using EOM decreases with decreasing Δ (agreeing qualitatively with the NEGF(YX) case) before changing direction around $\Delta \sim 0.4k_BT$. This is precisely because the heat current due to XX coupling vanishes for $\Delta \to 0$ and the contribution from YX coupling becomes dominant.

6.6 COULOMB COUPLED QUANTUM DOTS

In this section, we will study heat rectification in the drag circuit when the drive circuit is thermally biased (see Fig. 4.10). We take symmetric thermal bias in the drive, and calculate the heat current flowing in the drag for two different cases: 1) $T_{L1/R1} = T \pm \Delta T$ (the heat current flowing in bath α is given by $J_\alpha^{(\mathrm{h})}(T_{L1} = T_H)$), 2) $T_{L1/R1} = T \mp \Delta T$ (the heat current flowing in bath α is given by $J_\alpha^{(\mathrm{h})}(T_{L1} = T_C)$). We define the rectification factor as:

$$R_{L2/R2} = \frac{\left|J^{(\mathrm{h})}_{L2/R2}(T_{L1} = T_H)\right| - \left|J^{(\mathrm{h})}_{L2/R2}(T_{L1} = T_C)\right|}{\left|J^{(\mathrm{h})}_{L2/R2}(T_{L1} = T_H)\right| + \left|J^{(\mathrm{h})}_{L2/R2}(T_{L1} = T_C)\right|}. \tag{6.44}$$

When the tunneling in the drag circuit is energy independent, energy inevitably gets dissipated to both baths irrespective of the way the drive is biased. We obtain $\mathcal{R} = 0$, and there is no rectification. To obtain finite rectification, we consider two different possible ways of implementing energy dependence in the tunneling. We find that under suitable choice of parameters, a perfect non-local heat rectification, i.e $R = \pm 1$ can be obtained. The heat

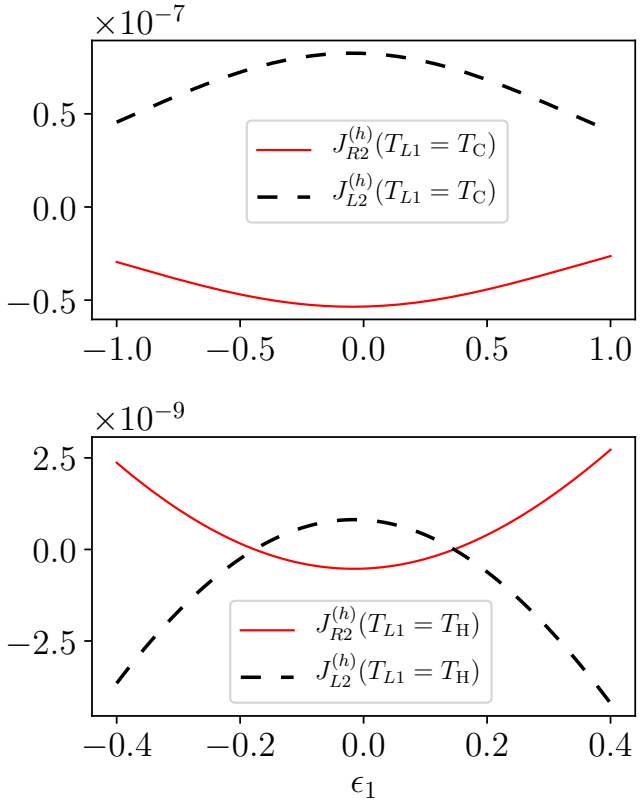

Figure 6.12: Heat currents flowing in the two leads of drag system as a function of ϵ_1 for $\epsilon_2 = 0.4 k_B T$ (charge state dependent transition rate). Parameters: $U = 0.03 k_B T$; $\Delta T = 0.068T$; $\Gamma_{L1} = 0.08 k_B T$; $\Gamma_{R1} = 0.07 k_B T$; $\Gamma_{L2} = 0.06 k_B T$; $\Gamma^{(0)}_{R2} = \frac{1}{5}\Gamma^{(1)}_{R2} = 0.05 k_B T$.

currents flowing to the two leads in the drag circuit are shown in Fig. (6.12) when the tunneling in or out of the lead $R2$ is dependent on the charge state of QD1. The upper panel is for $T_{L1} = T_H$, $T_{R1} = T_C$ (positive bias) whereas the lower panel is for the case when the bias is inverted, $T_{L1} = T_C$, $T_{R1} = T_H$

(negative bias). For a detailed analysis on the mechanism of heat flow in the drag circuit, we refer the readers to Chapter 4. The difference of the heat current flowing to the lead $R2$ in the above mentioned two cases gives us the rectification factor (see Eq. (6.44)). The heat currents are plotted as a function of energy of QD 1. The parameters were chosen such that heat is extracted from one of the reservoir in the drag circuit and deposited to the other one. We observe that both heat currents in the drag go to zero for a particular value of $\epsilon_1 (\approx 0.15 k_B T)$ in the positive bias case whereas for the same value of ϵ_1 we obtain a finite heat current in the negative bias case. This gives us a perfect non-local heat rectification for $\epsilon_1 (\approx 0.15 k_B T)$ (see Fig. 6.14, top panel).

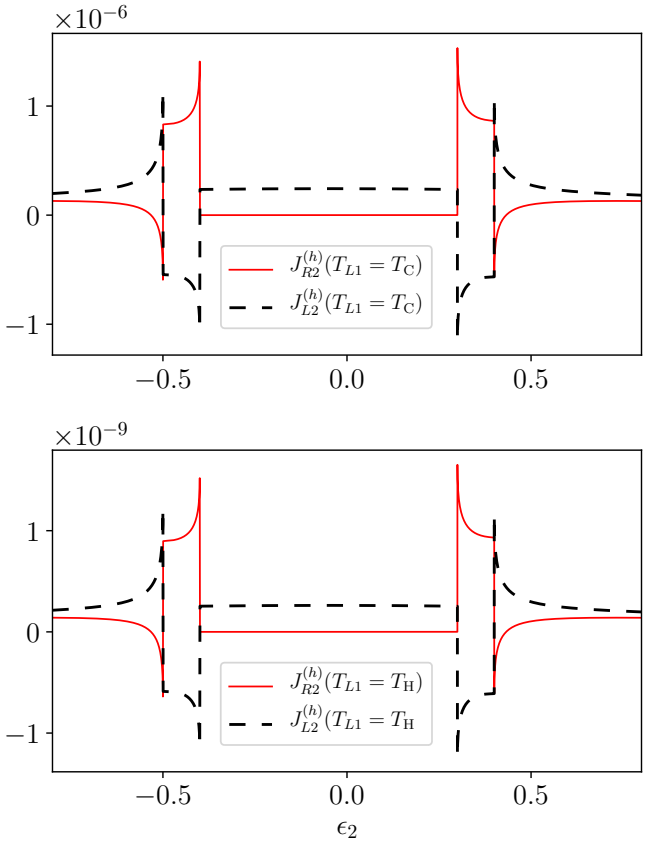

Figure 6.13: Heat currents flowing in the two leads of the drag as a function of ϵ_2 for $\epsilon_1 = 0.1 k_B T$ (superconducting reservoir). Parameters: $U = 0.1 k_B T$; $\Delta T = 0.068T$; $\Gamma_{L1} = 0.08 k_B T$; $\Gamma_{R1} = 0.07 k_B T$; $\Gamma_{L2} = 0.06 k_B T$; $\Gamma_{R2} = 0.05 k_B T$, $\Delta = 0.4 k_B T$

.

We plot heat currents flowing to the two leads in the drag when the lead $R2$ is superconducting in Fig. (6.13). We observe that for particular values of parameters, we obtain very small current in the positive bias case compared to the negative bias case giving a high magnitude of heat rectification. Note that, for the case of superconducting lead the amount of heat extracted from one of the reservoir is almost equal to the amount of heat deposited to the other one for a range of values of ϵ_2. In the bottom panel of Fig. 6.14, we plot thermal rectification as a function of thermal bias when the lead $R2$ is superconducting. We observe that for $\Delta T \approx 0.07T$, a perfect non-local thermal rectification ($R = -1$) is obtained. The parameters were carefully

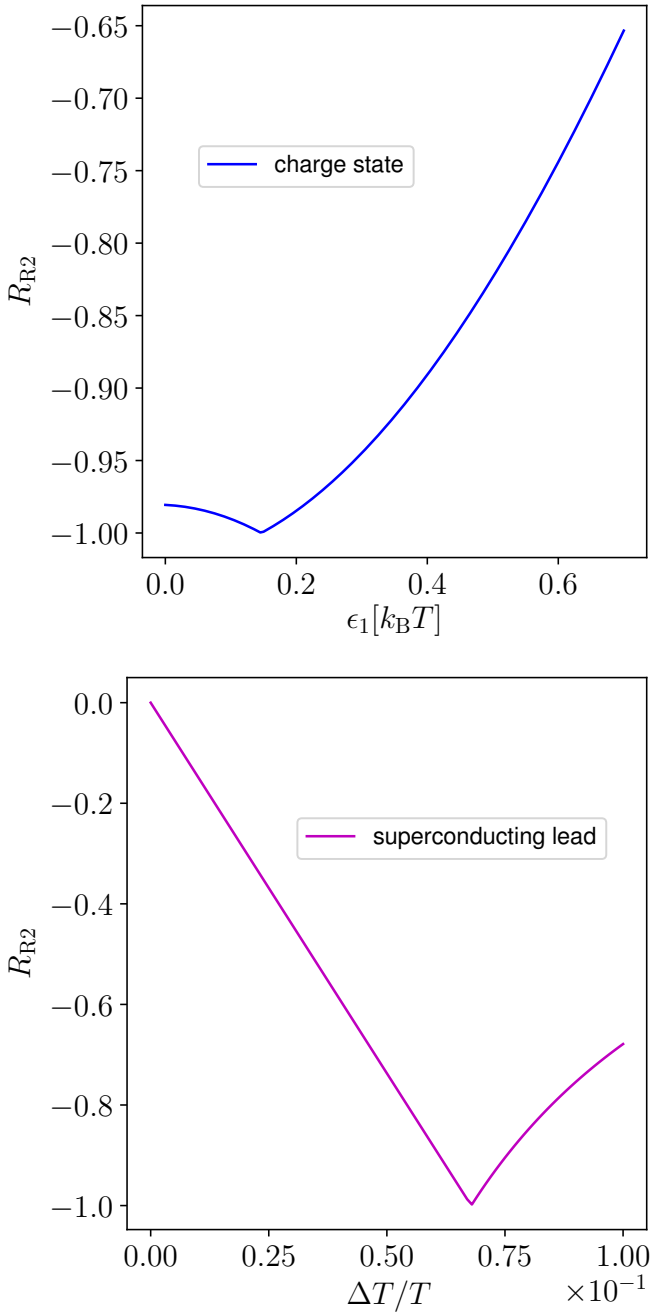

Figure 6.14: Non local thermal rectification as a function of ϵ_1 for charge state dependent transition rates (top panel, blue curve) and as a function of thermal bias ΔT for the case with superconducting lead $R2$. Parameters are chosen such that the heat current flows from one reservoir to the other in the drag circuit. For the top panel, $U = 0.03k_BT$; $\Delta T = 0.068T$; $\Gamma_{L1} = 0.08k_BT$; $\Gamma_{R1} = 0.07k_BT$; $\Gamma_{L2} = 0.06k_BT$; $\Gamma^{(0)}_{R2} = \frac{1}{5}\Gamma^{(1)}_{R2} = 0.05k_BT$ and for the bottom panel, $U = 0.1k_BT$; $\epsilon_1 = 0.1k_BT$; $\epsilon_2 = 0.3k_BT$; $\Gamma_{L1} = 0.08k_BT$; $\Gamma_{R1} = 0.07k_BT$; $\Gamma_{L2} = 0.06k_BT$; $\Gamma_{R2} = 0.05k_BT$ and $\Delta = 0.4k_BT$.

chosen such that the heat current always flows from one lead to another in the drag circuit. The “perfect thermal rectification" is obtained even in the presence of higher order terms like cotunneling as well as when the lamb

shift effect is taken into account. Hence, the effect is robust to system-bath coupling strength, provided perturbative treatment is allowed.

6.7 SUMMARY

In this chapter, we presented a comprehensive and systematic study of thermal rectification in low-dimensional quantum systems. Focusing on various prototypical systems - a qubit, a non-linear harmonic oscillator and a Coulomb coupled quantum dot system - we identified necessary conditions to observe thermal rectification and we discussed strategies to maximize it. In particular, in the qubit case we derived general upper bounds on rectification which hold in the weak system-bath coupling regime, and we showed how the Lamb shift can be exploited to enhance rectification. We then went beyond the weak coupling regime using the non-equilibrium Green's function formalism and the Feynman-Vernon path integral approach. We found that the strong coupling regime allows us to violate the bounds derived in the weak coupling regime, providing us with clear signatures of high order coherent processes visible in the thermal rectification. In the non-linear harmonic oscillator, we studied the heat rectification using two different approximate schemes 1) mean field Hartree approximation and 2) equation of motion method that goes beyond mean field. We observed that the mean field calculations converges to the equation of motion method when the interaction is small compared to other energy scales of the system. Thermal rectification is enhanced in the large interaction limit, making equation of motion better suited to study thermal rectification in non-linear resonators. Finally, we studied non-local thermal rectification in Coulomb coupled quantum. For a suitable choice of parameters, we showed that a perfect non-local thermal rectification can be obtained.

7

THERMAL TRANSPORT IN SINGLE ELECTRON DEVICES: EXPERIMENT AND THEORY

7.1 NONLINEAR THERMOVOLTAGE IN A SINGLE-ELECTRON TRANSISTOR

The use of nano-devices has emerged as one of the key technologies in the quest to establish a sustainable energy system, allowing at the same time the control of heat flow in small circuits [35]. So far, most of the investigations of thermal properties in nanostructures have focused on the thermal conductance [153, 37, 154, 38, 155, 156, 157, 39, 158, 159]. Conversely the thermovoltage, which describes the electrical response to a temperature difference and is directly related to both the power and efficiency of thermal machines [35], is much less studied. This is due to the difficulty in coupling local sensitive electron thermometers and heaters/coolers to the sample under study in order to have a well-defined, known temperature difference across the device. The thermovoltage has been measured in devices based on nanowires [160, 161] and on quantum dots [162, 163, 164, 165, 166, 167, 168, 169, 170, 171, 172, 173, 174]. In these experiments, however, the temperature of the electrodes were typically not measured directly, but rather determined as fitting parameters, and there are no experiments where the temperature of the electrodes and the thermovoltage are measured simultaneously. Furthermore, there are no experiments probing the thermovoltage in devices based on metallic islands, while theoretical works for these systems have focused only on the linear response regime [175, 176, 177, 178, 179, 180, 181]. The non-linear thermovoltage though has been theoretically studied in discrete-level systems in Refs. [182, 183, 120, 184, 185, 186, 187, 188, 189, 190].

In this section, we report on the theoretical prediction of experimental measurement of the thermovoltage in a metallic single-electron transistor (SET) based on on-chip, local tunnel-junction-based thermometers and electron temperature control. This system allows one to perform thermoelectric measurements with an unprecedented control, both within the linear and non-linear response regimes, imposing temperature differences exceeding the average temperature. Using a theoretical model which accounts for non-linear effects and co-tunneling processes, we find an excellent agreement with the experimental data with no free parameters. On one hand, this allows us to nail down quantitatively the role of co-tunneling processes on the thermovoltage. On the other hand, we find that in the non-linear regime the temperature of the island emerges as a crucial parameter. Surprisingly, although the thermovoltage is measured at zero net charge current, within the non-linear response the island tends to overheat to a temperature greater than the average lead temperature, which results in a suppression of the thermovoltage. We show, however, that the non-linear thermovoltage can be

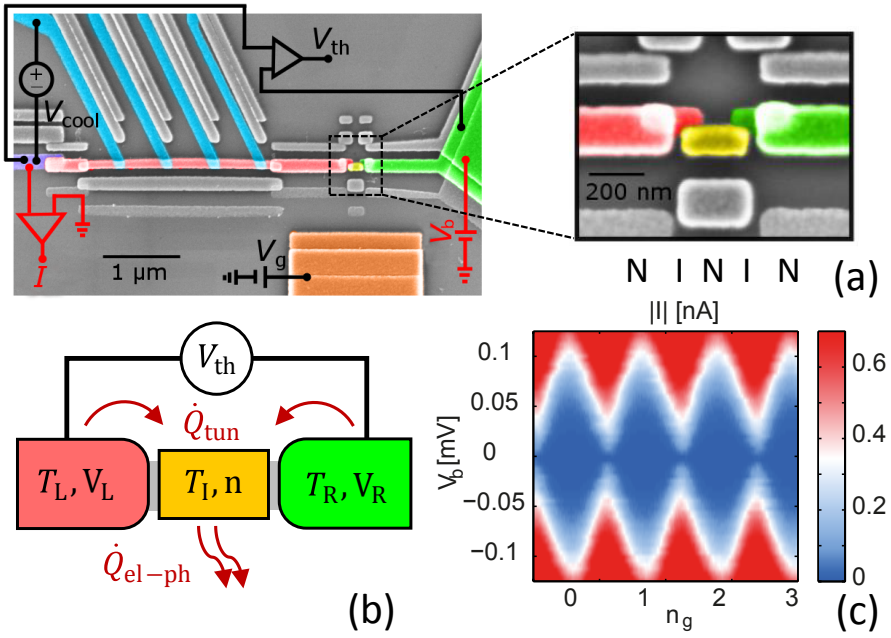

Figure 7.1: Representation and characterization of the single-electron transistor. a) False-colored SEM image of the full device and a zoomed in view around the metallic island (yellow) tunnel coupled to two normal leads (red and green). b) Schematic representation of the system with the same coloring as in the SEM image. The heat balance in the metallic island is represented by red arrows. c) Absolute value of the current through the SET as a function of the applied source drain voltage V_b and of the gate-induced charge n_g.

optimized up to a factor two with respect to the experimentally observed value by lowering the temperature of the island to the temperature of the cold lead. This could be achieved by exploiting the phonons in the island which act as a third thermal bath coupled to our system.

7.2 SETUP

Fig. 7.1a) is a colored scanning electron micrograph of the device and Fig. 7.1b) is a schematic representation of the experiment with the same colors highlighting the main elements of the fully normal-conducting SET. The left lead L (red) and right lead R (green) are tunnel and capacitively coupled to a central metallic island I (yellow), which is under the influence of a tunable gate electric field (orange). A voltage bias $V_b = V_L - V_R$ can be applied to the SET electrodes and the corresponding current I can be measured for an initial characterization of the device. The temperature T_R of the electrons in R is fixed to the bath temperature, given the strong electron-phonon coupling in the large and "bulky" lead. On the other hand, the electronic temperature T_L in the left lead (red) can both be varied and measured using the superconducting tunnel probes (blue). Electrons within the island are in local equilibrium at temperature T_I since the electron-electron interaction is much faster than the tunneling rates [115].

Figure 7.1c) shows the absolute value of the current I across the device at 65 mK as a function of the potential bias V_b and of the gate-induced charge $n_g = (C_L V_L + C_R V_R + C_g V_g)/e$, where C_L, C_R and C_g are, respectively, the

capacitances of the island to L, R and to the gate electrode, and V_g is the gate voltage. In the dark blue regions, Coulomb diamonds, single electron tunneling between the leads and the island is not allowed, and the current is very small. At half integer values of n_g, "degeneracy points", there are conductance peaks at zero bias since single electron tunneling is allowed for any finite voltage bias.

We consider both sequential and cotunneling contribution to the current. In the presence of a fixed temperature bias ($T_R \neq T_L$), the thermovoltage V_{th} is the solution to

$$J^{(c)}(V_{th}) = 0, \tag{7.1}$$

where $J^{(c)}$ is the total charge current due to both sequential and cotunneling contribution. Notice that the charge current also depends on the temperature of the island T_I. By imposing that the charge current and the net energy entering the island through electron tunneling are zero, we find that

$$T_I = \frac{T_L R_R + T_R R_L}{R_L + R_R}, \tag{7.2}$$

where R_L and R_R are respectively the resistance of the left and right tunnel junctions. Eq. (7.2), which is found performing a simple sequential tunneling calculation within linear response and in the two charge state approximation (valid for $E_C \gg k_B T$, E_C is the charging energy), reduces to $T_I = \bar{T} \equiv (T_L + T_R)/2$ in the present symmetric case where $R_L = R_R$.

7.3 RESULTS

We focus on two data sets which represent two different regimes: linear response (Fig. 7.2), i.e. when the modulus of the temperature difference $\Delta T = T_L - T_R$ is smaller than the average lead temperature $\bar{T} = (T_L + T_R)/2$, and non-linear response (Fig. 7.3). In both cases, using the model detailed above, we could accurately reproduce the experimental data without any free parameter. The system parameters $E_C = 100\mu$eV $\approx k_B \times 1.16$ K and $R_L = R_R = 26$ kΩ are independently extracted from charge current measurements. Figures 7.2 and 7.3a) present the same qualitative behavior, namely a periodic oscillation of the thermovoltage with the gate-induced charge n_g and a linear dependence around degeneracy points, but they exhibit different amplitudes (note that the sign of V_{th} is opposite in the two cases since the temperature biases are opposite).

We first analyze the linear response regime by choosing the set of data obtained when the temperature of the leads is $T_L = 134$ mK and $T_R = 190$ mK, such that $|\Delta T| < \bar{T}$. In Fig. 7.2 we compare the measured V_{th} (blue dots) as a function of n_g with different theoretical models. The red thin curve represents the typical sawtooth behavior which is predicted within linear response accounting only for sequential tunneling and two charge states. This is characterized by a linear function of n_g, crossing zero at the degeneracy points with slope $E_C \Delta T/\bar{T}$ [175]. The other two curves (red dashed and green solid) are instead determined by computing V_{th} using Eq. (7.1) and assuming that $T_I = \bar{T}$ [see Eq. (7.2)]. The red dashed curve, which only accounts for sequential tunneling, shows a smoothened sawtooth behavior as a consequence of including multiple charge states in the master equation and of a finite temperature. However, both models based on sequential tunneling (thin and dashed red curves) approximately fit the experimental data only near the degeneracy points (near half integer values of n_g). In this case, indeed, sequential tunneling is allowed and thus dominates over co-tunneling

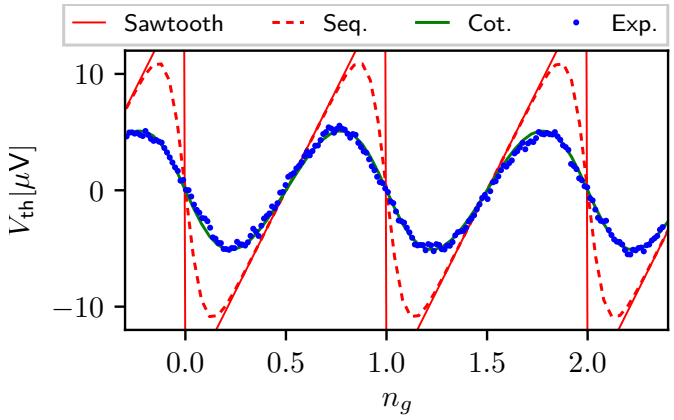

Figure 7.2: Experimental and theoretical thermovoltage as a function of n_g. The red thin curve represents the sawtooth behavior predicted with a sequential-tunneling calculation in linear response and accounting for two charge states. The dashed red curve is found by solving Eq. (7.1) including only sequential contributions, while the green curve includes also co-tunneling contributions. The temperatures of the leads are $T_{\mathrm{L}} = 134$ mK and $T_{\mathrm{R}} = 190$ mK and, according to Eq. (7.2), we assume that $T_{\mathrm{I}} = \bar{T}$.

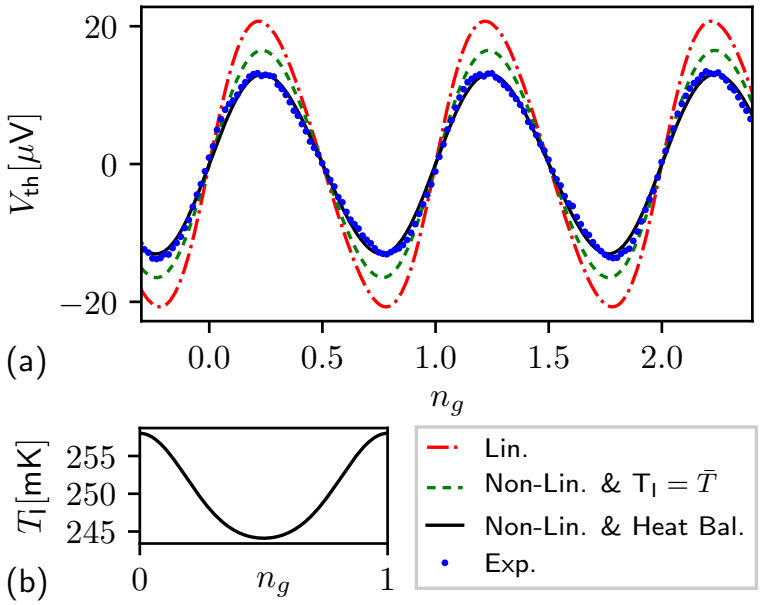

Figure 7.3: a) Experimental and theoretical thermovoltage as a function of n_g. All theoretical curves include co-tunneling. The red dashed-dotted curve corresponds to a linear response calculation around $\bar{T}$. The green dashed curve corresponds to a non-linear calculation where we fix $T_{\mathrm{I}} = \bar{T}$, while the black curve corresponds to a non-linear calculation where T_{I}, shown in b) as a function of n_g, is calculated solving the heat balance condition in Eq. (7.3) together with Eq. (7.1). The temperatures of the leads are $T_{\mathrm{L}} = 342$ mK and $T_{\mathrm{R}} = 63$ mK.

[177]. On the other hand the green solid curve, computed including co-tunneling contributions, shows a strong suppression of the thermovoltage as we move away from degeneracy points. The excellent agreement between this model and the experimental measurements pinpoints the critical dependence of the thermovoltage on inelastic co-tunneling processes.

We now move to the non-linear regime. In Fig. 7.3a) we show the measured thermovoltage as a function of n_g (blue dots) compared to theoretical calculations, all of which include co-tunneling contributions. The lead temperatures are $T_L = 342$ mK and $T_R = 63$ mK, such that $|\Delta T| > \bar{T}$. The red dashed-dotted curve is computed within the linear response regime choosing the average lead temperature $\bar{T}$ as the characteristic temperature. More precisely, we solve Eq. (7.1) setting $T_I = \bar{T}$ and choosing a small temperature difference of the leads δT around $\bar{T}$ to find the thermopower $S \equiv V_{th}/\delta T$ for $\delta T \to 0$. We then calculate the thermovoltage as $V_{th} = S(T_L - T_R)$, where now $T_L = 342$ mK and $T_R = 63$ mK are the actual lead temperatures. As we can see from Fig. 7.3a), this linear response model overestimates the thermovoltage almost by a factor two. A non-linear calculation (green dashed curve) improves the agreement with the experimental data. This calculation is performed by solving Eq. (7.1) using the actual lead temperatures and, as before, we fix the island temperature at $T_I = \bar{T}$. The difference between the red dashed-dotted and green dashed curves proves that we are indeed in the non-linear response regime, and it shows that the main effect of the nonlinear response is to decrease the amplitude of the thermovoltage. However, we still do not obtain a good agreement with the experimental data.

We find that we can get a perfect agreement with the experimental data if we further improve the model by determining also the island temperature T_I through a heat balance equation, rather than fixing it at $\bar{T}$. More precisely [see Fig. 7.1b)], we denote by $\dot{Q}_{tun}$ the heat current entering the island from sequential and co-tunneling events and by $Q_{el\text{-}ph} = \Sigma\mathcal{V}(T_I^5 - T_R^5)$ the heat current flowing from electrons in the island to the phonons (we assume that the electronic temperature T_R in the bulky right electrode is equal to the temperature of the phonons). $\mathcal{V}$ is the island volume and Σ is the electron-phonon coupling constant which only depends on the material. The temperature of the island can thus be determined by the following heat balance equation

$$\dot{Q}_{tun} = \dot{Q}_{el\text{-}ph}. \tag{7.3}$$

The values of the parameters entering $Q_{el\text{-}ph}$ that we use are determined independently: $\mathcal{V} = 225 \times 100 \times 29$ nm^3 is estimated from SEM images and Σ is obtained from Ref. [39] for this device (sample B). The value, $\Sigma = 2.8\,\mathrm{WK^{-5}m^{-3}}$, is close to the standard literature value for copper [115] and in agreement with measurements of other samples fabricated using the same Cu target.

The black curve in Fig. 7.3a) is thus determined by computing both V_{th} and T_I simultaneously by solving Eqs. (7.1) and (7.3) without any free parameters for each value of n_g. As we can see, the non-linear model, complemented with the heat balance equation, is in excellent agreement with the experimental measurements, demonstrating that T_I is indeed an important parameter in the non-linear regime. Conversely we have verified that, using the parameters of Fig. 7.2 which are within the linear response regime, V_{th} only weakly depends on the particular choice of T_I between T_L and T_R. In Fig. 7.3b) we plot the island temperature T_I, as a function of n_g over a single period, determined in the same calculation that leads to the black curve in Fig. 7.3a). Remarkably, despite the very low phonon temperature (63 mK), the calculated $T_I \approx 250$ mK is much larger than the average lead temperature $\bar{T} = 202.5$ mK. This means that while the net charge current across the SET is zero, the heat current due to electrons tunneling back and forth is overheating the island to a temperature that is significantly larger than the average temperature, resulting in a further decrease of the thermovoltage. This is another signature of

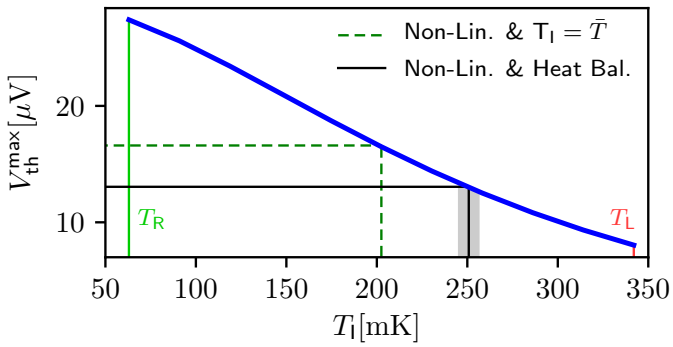

Figure 7.4: The maximum amplitude of the thermovoltage V_{th}^{max} is plotted as a function of the island temperature, for $T_R \leq T_I \leq T_L$. The green dashed lines point to the values of V_{th}^{max} and T_I found in the non-linear calculation at fixed $T_I = \bar{T}$ (see the green dashed curve of Fig. 7.3a) while the black solid lines and the gray area refer to the non-linear calculation including the heat balance equation (see the black solid curve of Fig. 7.3).

the non-linear response of the system, as it violates Eq. (7.2). We further find that the island temperature displays a weak n_g modulation of approximately 10 mK, but this prediction cannot be confirmed in the present experiment.

Finally we discuss how the thermovoltage depends on T_I. In Fig. 7.4 we plot V_{th}^{max}, the maximum amplitude of V_{th}, computed by solving Eq. (7.1) at fixed lead temperatures $T_L = 342$ mK and $T_R = 63$ mK and varying T_I between the lead temperatures. The black solid lines and the gray area point to the actual experimental value of V_{th}^{max} and to the corresponding computed T_I which differs from $\bar{T}$ [see black curves in Figs. 7.3a) and 7.3b)], while the dashed green lines point to V_{th}^{max} calculated setting $T_I = \bar{T}$ [see the green dashed curve in Fig. 7.3a)]. We find that V_{th}^{max} strongly depends on the choice of T_I and that it increases as T_I is lowered. Indeed, at $T_I = T_R = 63$ mK, the amplitude of the thermovoltage reaches 27 $\bar{}$eV, twice the experimental value [see blue dots in Fig. 7.3a)]. Thus, by increasing the energy exchange between the electrons and phonons in the island, for example by increasing the island's volume, we can lower the temperature of the island which in turn results in an increase of V_{th}.

7.4 OPTIMAL PROBILISTIC WORK EXTRACTION BEYOND FREE ENERGY DIFFERENCE

The ongoing miniaturization of physical systems, together with advances in techniques for the conception and manipulation of small biological objects, has made the investigation of devices with few degrees of freedom possible. In such systems fluctuations of physical quantities become comparable with or larger than their mean values. This property, in particular, has led to the theoretical [191, 192] and experimental [193, 194, 195] development of stochastic thermodynamics [196], which considers single realizations of work and heat relative to a given transformation rather than averaged quantities over an ensemble of realizations, as for the case of macroscopic systems. While the first law of thermodynamics (energy conservation) remains untouched, the second law (entropy increase over time) does not apply at the level of a single realization because of the stochastic nature of heat and work. Experimental platforms for stochastic thermodynamics include col-

loids [194, 197], single electron boxes [198], electronic double dots which allow entropy production measurements [199, 43] and recently experiments attained the quantum regime with e.g. NMR setups [200] and superconducting circuits [201, 202]. In this context, work and heat must be addressed in terms of probability distributions [196]. In particular, work fluctuations obey the equality [191]

$$\left\langle e^{-W/k_BT} \right\rangle = e^{-\Delta F/k_BT}. \tag{7.4}$$

Here W is the work *performed on a system* during a single realization of the process, ΔF is the free energy difference between the system's initial and final states, k_B is Boltzmann's constant and T the temperature of the heat bath to which the system is connected, and angular brackets denote an ensemble average over realizations. From this equality the second law of thermodynamics is recovered, $\langle W \rangle \geq \Delta F$. Additionally, Eq. (7.4) implies that for some realizations $W < \Delta F$, i.e. the extracted work $(-W)$ exceeds the decrease in free energy $(-\Delta F)$. Eq. (7.4) places no limits on the magnitude of such "violations" of the second law, nor on the net likelihood of observing these violations. Therefore it is interesting to consider how to design a process to maximize the amount of work that might be extracted during a single realization, or alternatively to maximize the net probability to extract work beyond the free energy difference.

With the exception of recent applications of one-shot methods in this context [203, 204], until now optimal control for a system coupled to a single heat bath has been mostly concerned with the trade-off between minimizing either fluctuations or average work [205, 206]. Recently, it has been shown with a quantum jump approach [207] that with a suitable far-from-equilibrium driving sequence, one can instead take advantage of fluctuations to force work extraction from a system by arbitrarily large value with a non-zero probability while still obeying Eq. (7.4). In particular, Ref. [207] discusses how to perform this task in the most efficient way, finding an optimal sequence that relies on two quasi-static tuning steps of the control parameter, separated by the sudden change of its energy level spacing, also referred to as a "quench". Such a protocol maximizes the probability of extracting work beyond a given quantity (i.e. $W \leq W^-$ where $W^- < \Delta F$ is fixed), while ensuring that we never perform work exceeding a selected threshold W^+.

In this section, in a single electron transistor (SET) setup [208], using master equations we theoretically reproduce the experimental results demonstrating a significant probability of extracting work arbitrarily bigger than the free energy difference in a single protocol realization. We also establish quantitative agreement between the nonequilibrium fluctuation relation [Eq. (7.4)] and the experimental results. These results are obtained without using the information on the system's state, unlike in a "Maxwell's demon" [209, 210] experiment.

The experimental set up is depicted in Fig. 7.5a) and 7.5b). We know the net heat transfer $\Delta E \equiv \Delta E_{0\to1} = H(1, n_g) - H(0, n_g)$ for an electron tunneling onto the island,

$$\Delta E_{0\to1}(n_g) = E_C(1 - 2n_g), \tag{7.5}$$

where E_C is the charging energy of the island and $n_g = C_{g,sys}V_{g,sys}\,\mathrm{e}$ is the reduced gate voltage. While the opposite heat transfer for an electron leaving the island is $\Delta E_{1\to0}(n_g) = -\Delta E_{0\to1}(n_g)$. By monitoring tunneling events during a driving cycle, and recording the corresponding jump times $\{t_k\}$

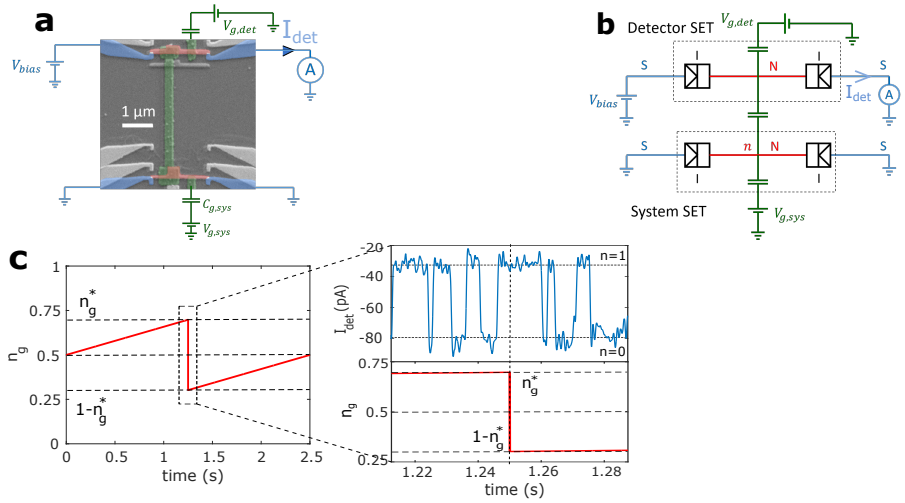

Figure 7.5: a) Scanning electron micrograph of the single-electron transistor (SET) capacitively coupled to a voltage biased detector SET. Leads (blue) made of superconducting aluminum are coupled through oxide (tunnel) barriers to the copper (red) island. b) Electrical circuit representation. c) Protocol used to maximize work extraction, with a zoom on the detector SET output current under system driving, around the quench event.

and gate voltage values $\{n_g(t_k)\}$, it is possible to experimentally determine the total heat absorbed by the system over the thermodynamic cycle: $Q = \sum_k \Delta E[n_g(t_k)]\Delta n_k$, where $\Delta n_k = \pm 1$ depending on whether the electron jumps in/out of the island. The initial and final values of n_g are both set to $1/2$ so that we operate on a closed thermodynamic cycle. This way the net energy change and the free energy difference ΔF over the entire cycle are both zero, and energy conservation ensures that $W = -Q$. Thus the experimental value of the work at the end of the cycle can be directly inferred based on the record of the transitions over the full cycle, see Fig. 7.5c).

The driving sequence $n_g(t)$ depicted in Fig. 7.5 c), referred to as protocol was first realized over a time t_f. For a given choice of W^- and W^+ satisfying $W^- < \Delta F < W^+$, the protocol [207] is designed to maximize the probability to observe a work value $W \leq W^-$ (successful event), while ensuring that we never observe $W^+ \geq \Delta F$ (failure events). For the sake of simplicity we consider the symmetric case, i.e. $W^- = -W^+$. First we prepare the system at charge degeneracy, i.e. $n_g(0) = 1/2$, at thermal equilibrium. Then we drive the system with a quasi-static ramp over a time $t_1 \gg \Gamma_d^{-1}$ up to a value $n_g^* \equiv n_g(t_1) = 1/2 + \Delta n_g$, with $0 < \Delta n_g < 1/2$. Next, a rapid swap of the energy splitting is operated by suddenly driving the system to a value $1 - n_g^*$. This "quench" must be realized over a time $\Delta t_q \ll \Gamma_d^{-1}$ so that no tunneling occurs in this time interval. Finally, we return the system to charge degeneracy through a quasi-static ramp, over a time t_1, such that $2t_1 + \Delta t_q = t_f$ and $n_g(t_f) = 1/2$. The total work output at the end of one cycle, obtained theoretically in the ideal quasi-static limit, writes

$$W(\overline{n}) = (1 - 2\overline{n})\Delta E(n_g^*), \tag{7.6}$$

where $\overline{n} \equiv n(t_1)$ is the charge state at the quench onset, and $\Delta E(n_g^*) < 0$. Therefore W is a stochastic variable taking two values $W^{\mp} = \pm\Delta E(n_g^*)$. Its distribution $P(W) = p^*\delta(W - W^+) + (1 - p^*)\delta(W - W^-)$ with $1/2 < p^* < 1$ [207] is solely dictated by the equilibrium occupation probabilities of the

two charge states before the quench, which obey the Gibbs ensemble: the ground state (one extra electron on the island) has a probability $p^* = (1 + e^{\Delta E(n_g^*)/k_B T})^{-1}$, while the excited state (zero extra electron) has a probability $1 - p^* = (1 + e^{-\Delta E(n_g^*)/k_B T})^{-1}$. The outcome is simple to interpret physically: as the two ramps are quasi-static, the amount of work performed during those segments can be considered merely in terms of the equilibrium occupation probabilities at each instant, and is here equal to zero because of the protocol's symmetry. On the other hand, the work performed during the quench does depend on the charge state at the quench onset: if the system is in the ground state $\overline{n} = 1$, the quench turns it into an energetically unfavorable state (since $\Delta E(1 - n_g^*) > 0$), and thus positive work has to be provided by the gate voltage source during the quench. If instead the system is in the excited state before the quench, the latter turns it into the ground state: thus energy is released by the system as work, since there is no heat exchange during the quench. Thus, counter-intuitively, the quench allows to realize $W < \Delta F = 0$ by a possibly large amount by deliberately introducing irreversibility.

Work histograms obtained for two different values of Δn_g (quench amplitudes) with the same ramp time are shown in Fig. 7.6a) and 7.6b). We indeed observe two peaks with maxima located at $\pm\Delta E(n_g^*)$. Their imbalance increases with the quench amplitude following Gibbs statistics as seen in Fig. 7.6c). This is expected since the probability $1 - p^*$ to be in the excited state decreases as n_g^* gets further away from charge degeneracy. Namely, the ratio between the weights of the two peaks follows the detailed balance condition for the two energy states $\pm\Delta E(n_g^*)$: $P\left[W = \Delta E(n_g^*)\right] / P\left[W = -\Delta E(n_g^*)\right] = e^{\Delta E(n_g^*)/k_B T}$. Irreversibility, introduced by the quench, can be quantified by computing the work $\langle W \rangle = \int P(W) W \mathrm{d}W$ performed on the system, averaged over all realizations:

$$\langle W \rangle = \Delta E(n_g^*) \tanh\left[\frac{\Delta E(n_g^*)}{2k_B T}\right]. \tag{7.7}$$

Indeed, $\langle W \rangle \geq 0$, as expected from the second law of thermodynamics. In Fig. 7.6d) we see that the averaged work is positive and increasing with the quench amplitude, in good agreement with Eq. (7.7). The inset of Fig. 7.6d) shows that our work histograms obey the nonequilibrium work relation (7.4).

Note that, in contrast to the theoretical situation depicted in Ref. [207], the peaks have a finite width in our results, which owes to the fact that a realistic ramp cannot be truly quasi-static, since one would need enough tunneling events between two infinitesimally close instants so that thermal equilibrium is properly defined at each instant t. Thus, the degree of reversibility is determined by the slope of the ramp with respect to the typical tunneling time, i.e. by $\Gamma_d^{-1} |\mathrm{d}n_g / \mathrm{d}t|$. For higher quench amplitudes but with the same ramping time, the residual irreversibility produces broader peaks [198], as Fig. 7.6a) and 7.6b) clearly show. We also run the protocol with constant quench amplitude but different ramp times. In Fig. 7.6e),f) work histograms for two different ramp times unambiguously demonstrate that a shorter ramp time results in a broadened distribution, as captured through a master equation approach [198]. Indeed, we see in Fig. 7.6 that the obtained histograms are very well reproduced by the theoretical expectation, which validates this approach.

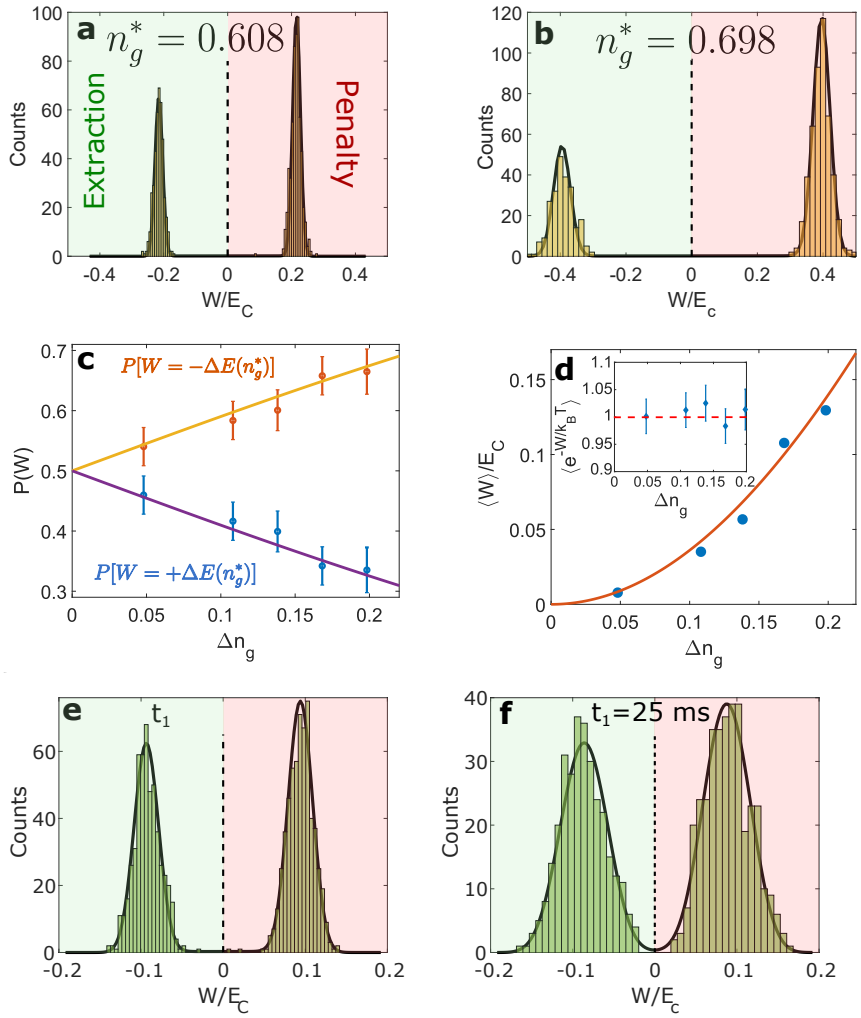

Figure 7.6: a) and b): work histograms obtained for a) $n_g^* = 0.608$ and b) $n_g^* = 0.698$, with the same ramp time $t_1 = 1.25$ s. c) Probability for $W = -\Delta E(n_g^*)$ (orange dots, mind the sign) and $W = \Delta E(n_g^*)$ (blue dots) events as a function of the quench amplitude. Solid lines are fits of Fermi functions (see text) with $E_C = 110$ μeV and $T = 670$ mK. Error bars are calculated from the number of protocol realizations. d) Work performed on the system averaged over all outcomes as a function of the quench peak amplitude $\Delta n_g = n_g^* - 1/2$. The solid line is obtained from Eq. (7.7). Inset: verification of Eq. (7.4) for all values of n_g. e),f): work histograms obtained for the same quench amplitude $\Delta n_g = 0.048$, but with ramp times $t_1 = 0.1$ s for e) and $t_1 = 0.025$ s for f), much shorter than in a). In a),b),e),f), solid lines are obtained by numerically solving the master equation. All work values are normalized to E_C.

7.5 SUMMARY

In this chapter, we theoretically studied two different experiments based on single electron transport in metallic islands. In the first section, we theoretically describe the measurements of thermovoltage in a metallic island tunnel coupled to normal leads. Within the linear regime we nail down the role of co-tunneling in determining the thermovoltage. Within the non-linear response regime we explore temperature biases even larger than the average lead temperature. Using a theoretical model which accounts for co-tunneling and non-linear effects, we find an accurate agreement with the experimental data without any free parameters. In particular, we find that the temperature of the metallic island becomes an important parameter which must be determined by solving a heat balance equation for the island. Surprisingly, even if the net charge current through the system is vanishing and the coupling to the leads is symmetric, the metallic island overheats to a temperature larger than the average lead temperature. As a consequence, the amplitude of the thermovoltage oscillations decreases.

In the second case, we have demonstrated that a substantial amount of work can be extracted with a non negligible probability from a two-level system *coupled to a single heat bath*, using a SET driven far from equilibrium with a rapid quench. The driving cycle is designed to maximize either the work or the probability of extracting work from the system on one trajectory, by strongly amplifying work fluctuations rather than minimizing them, which represents a new paradigm for work extraction in mesoscopic engines. The theoretical results based on a master equation approach which takes into account the irreversibility associated to finite time driving agrees with the experimental results satisfying the nonequilibrium work relation. We stress that even though work extraction can be favored, an external intervention (e.g. a Maxwell's Demon [209]) would still be required to select only the extraction events: it is thanks to this absence that the second law remains valid.

8

GEOMETRIC PROPERTIES OF ADIABATICALLY DRIVEN QUANTUM SYSTEMS

Thermodynamics in quantum nanoscale systems [211, 212, 213, 214, 215, 216, 217, 218] has been a rapidly growing research topic for some years now, emerging at the intersection of statistical mechanics, nanoscience, quantum information, as well as atomic and molecular physics. A paradigmatic goal in this field is to conceive of and realize thermal machines in the quantum realm, which, like the classical thermodynamic cycles, transform heat to useful work or use work to refrigerate [219, 220, 83, 221, 222, 223, 224, 225, 226, 227, 228, 229, 230]. The development of efficient thermal machines operating in the quantum realm is, in fact, of paramount importance also for quantum technologies. Numerous theoretical proposals [82, 231, 232, 233, 234, 235, 87, 103, 35, 236, 237] stimulated experimental efforts on several platforms [238, 239, 240], including solid-state electronics [241, 242, 243, 46] and nanomechanical systems [244, 245, 246, 247, 248], as well as cold atoms and trapped ions [249, 250, 251, 51, 252].

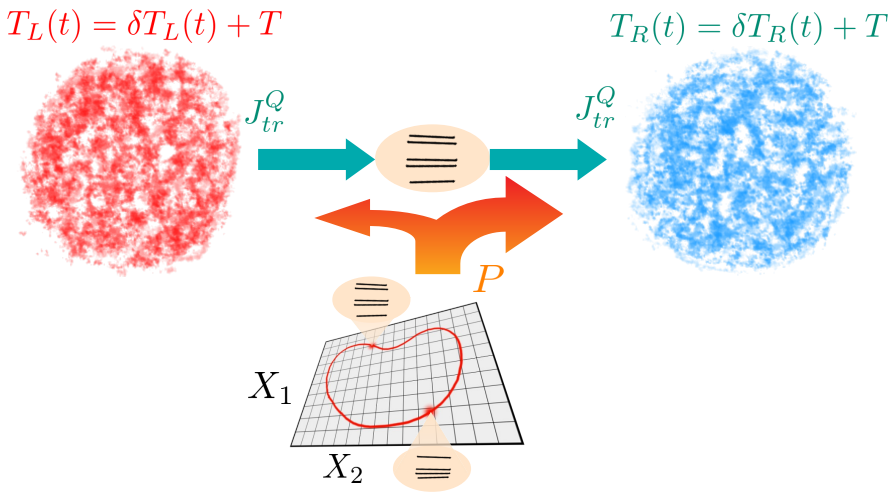

Figure 8.1: Geometrical thermal machine setup. A central, parametrically driven quantum system described by the Hamiltonian $\mathcal{H}_S$ is coupled to macroscopic reservoirs. A cycle of the machine is completely characterized by a closed path in the parameter space $\mathbf{X}$. After a complete cycle the averaged power P is dissipated as heat in the reservoirs. The net transported energy $J^Q_{\rm tr}$ flows from one reservoir to the other.

In its most simplified version a quantum thermal machine is composed of a working substance (typically a few-level quantum system) coupled to two or more thermal baths kept at different temperatures (and possibly at different chemical potentials). Engines and refrigerators can operate under steady-state conditions, as thermoelectric engines, or be controlled by time-

periodic perturbations which define a cycle, as in conventional macroscopic thermal machines. An example of the latter is the quantum Otto engine, which has been investigated theoretically [253, 220, 254, 255, 256, 257, 258, 259, 260, 261, 262, 263, 264, 265, 266, 267, 268, 269, 270, 224, 271] and realized experimentally [250, 252, 238]. Understanding how to discriminate and characterize useful work, heat, and dissipated energy in these systems is a fundamental step towards the realization of nanomachines. In fact, unlike the ideal classical thermodynamic cycles, quantum thermal machines typically operate out of equilibrium [272, 273], which necessarily implies entropy production and dissipation. In addition to its impact on emerging technologies, the study of quantum heat engines and refrigerators is also of fundamental importance to deepen our understanding of how energy flows and transforms at the nanoscale [274, 275, 276, 35, 277, 278, 279].

In the present chapter we will consider adiabatically driven thermal machines. Their cycle is controlled by time-periodic changes of a set of parameters which are slow compared to the typical time scales associated with the (quantum) working substance (see for example Refs. [280, 281]). The modulation can be associated with parameters of the baths (temperature, chemical potential, ...) or the working medium (external fields, coupling constants, ...), see Fig. 8.1. We will refer to these quantum machines as geometric thermal machines. In this regime and for small amplitude of the thermal bias, the operation has a purely geometric description. At the heart of this description is the thermal geometric tensor introduced in Section 8.2. Within the adiabatic linear response regime, the process of heat-work conversion is related to the antisymmetric component of the thermal geometric tensor, while the dissipation and entropy production are related to the symmetric component of the same tensor. Importantly, the antisymmetric component has the structure of a Berry curvature, which depends only on the geometry of the cycle in parameter space, and can be straightforwardly expressed in terms of a line integral in this space. This representation is very useful for identifying optimal protocols of heat-work conversion. Furthermore, the symmetric component has a geometric interpretation in terms of thermodynamic length and can also be represented as a line integral for cyclic protocols, which is useful in the design of efficient protocols. Our approach does not only allow one to describe a whole class of quantum machines in a unifying picture. It also has practical implications such as improved ways to optimize their performance, as we illustrate by two paradigmatic systems: a qubit and a quantum dot.

Starting from the seminal works of Aharonov and Bohm [282] as well as Berry [283], geometric effects have pervaded many areas of physics. In quantum transport, distinct contributions of geometric origin affect charge and energy currents. In the absence of an additional dc bias, the pumped charge in a periodically driven system was shown to be of geometric origin, and can thus be expressed in terms of a closed-path integral in parameter space [284, 285, 286, 287, 288, 289], akin to the Berry phase [283]. A similar approach was adopted to analyze heat transport in a driven two-level system weakly coupled to bosonic baths [290]. Closely related to these ideas is the geometric description of driving-induced forces [291, 292, 293, 294, 295, 296, 297, 298, 299], including geometric magnetism [300, 301], with the extension of geometric response functions to open systems also being discussed in relation to Cooper pair pumping [302]. Geometric concepts like a thermodynamic metric and a thermodynamic length were recently introduced as promising tools to characterize the dissipated energy and to design

optimal driving protocols [303, 304, 305, 306, 307, 308]. Similar ideas are behind the description of the adiabatic time-evolution of many-body ground states of closed systems in terms of a geometric tensor [309, 310, 311]. The topological characterization of mixed thermal states is also close to these concepts[312, 313].

This large body of work linking geometry to transport naturally hints at similar connections for thermal machines. First, thermal machines involve periodic variations of parameters and one may naturally expect geometric effects in the sense of Berry to play an important role. Second, the efficiency with which thermal machines operate is reduced by dissipation, and thus geometry enters the physics of thermal machines also in a second rather distinct way through the concept of thermodynamic length. In the present chapter, under quite general assumptions, we will show that the operation of quantum thermal machines and the underlying heat-work conversion is fundamentally tied to such geometric effects. We formulate a unified description in terms of a geometric tensor for all the relevant energy fluxes, which we refer to as thermal geometric tensor. Within this description, pumping and dissipation are, respectively, associated with the antisymmetric and symmetric components of this tensor. We also show that not only heat pumping but also the dissipated heat can be characterized in terms of an integral over a closed path in parameter space. These results apply universally to any periodically and adiabatically driven quantum system in contact with various reservoirs, irrespective of the statistics obeyed by the particles, the strength of the coupling between the system and the reservoir, or the presence of many-body interactions.

The chapter is organized as follows. In Section 8.1, we introduce the model of an adiabatic thermal machine. We also introduce the linear-response formalism to treat ac adiabatic and thermal driving. Section 8.2 is devoted to the analysis of the thermodynamic behavior of the heat engine. This section contains the principal results of the present work and shows how the performance characteristics of the engine (efficiency, output power, etc.) are of geometric origin. The central results of this approach are captured by Eqs. (8.5), (8.6), (8.14) and (8.16) which show that the pumped heat, the concomitant heat-work conversion and the dissipated power have a geometric interpretation. In the same section we will also analyze several classes of adiabatic machines depending on the various adiabatic drivings. Following this general formulation, Section. 8.3 focuses on two specific examples of thermal machines, which are particularly relevant for experimental implementations. We first consider a driven qubit which is asymmetrically and weakly coupled to two bosonic thermal baths. We then discuss a driven quantum dot coupled to two electron reservoirs. Conclusions and some additional perspectives related to our work are presented in Section 8.4. The Appendices C and E contain further details on the derivation of the main results of the chapter and explicit calculations for the examples presented in the main text.

8.1 MODEL OF A GEOMETRIC THERMAL MACHINE

A sketch of the geometric thermal machine that we analyze throughout this chapter is shown in Fig. 8.1. It consists of a central region containing the working substance, constituted by a few-level quantum system, coupled to two thermal baths. The quantum system is periodically driven by a set of N slowly-varying parameters $\vec{X}(t)$. The baths are macroscopic reservoirs of bosonic excitations or fermionic particles. The macroscopic variables

N	Number of slowly varying coupling parameters
N + 1	Number of slowly varying coupling parameters including thermal bias
$\vec{v}$	Arrows denote N-dimensional vectors
$\mathbf{v}$	Bold fonts denote $(N+1)$-dimensional vectors
ℓ , ℓ'	Labels of elements of N-dimensional vectors or matrices
μ , ν	Labels of elements of $(N+1)$-dimensional vectors or matrices
$\overleftrightarrow{M}$	$N \times N$ matrix
$\underline{\underline{\mathbf{M}}}$	$(N+1) \times (N+1)$ matrix

Table 8.1: Notation used in the text

characterizing the thermal environment such as the bath temperatures can also slowly vary in time. We parametrize the bath temperatures as $T_\alpha(t) = T + \delta T_\alpha(t)$ (with $\alpha = L, R$ referring to the left and right reservoirs) and define $\Delta T(t) = \delta T_L(t) - \delta T_R(t)$. A (possible) time dependence in the bath temperatures is only included in $\delta T_\alpha(t)$. We assume that the right reservoir R is the colder one.

Let us start with the simple observation that the thermal bias, without the action of the ac driving, induces a net heat flow from the hot to the cold reservoir. On the other hand, it is useful to consider an analogy with the operation of classical machines and notice that the modulation of the parameters $\vec{X}(t)$ is introduced by some mechanism, which is akin to a weight moving a wheel in the classical case. By the combined effects of thermal bias and ac driving forces, it is possible to realize heat-work conversion, which constitutes the key for the operation of the device as a thermal machine. Two main operational modes are possible. (i) In the heat engine mode, part of the heat flowing in the direction of the thermal bias is transformed into work performed against the mechanisms ruling the dynamics of $\vec{X}(t)$. (ii) In the refrigerator mode, part of the work induced by the action of the ac parameters can be used to extract heat from the cold reservoir, against the action of the thermal bias. In the latter case, the thermal bias plays the role of the weight. In the operation of the thermal machines, these processes come along with dissipation of energy leading to entropy production. The efficiency of the thermal machine relies on the appropriate balance between the heat-work conversion mechanism and dissipation.

8.1.1 *Heat, work, and operational modes*

As we are interested in the dynamics for slow driving and small temperature biases, it is convenient to define the $N+1$-dimensional vector of "velocities",

$$\dot{\mathbf{X}}(t) = \left\{ \dot{\vec{X}}(t), \Delta T(t)/T \right\} \tag{8.1}$$

These two types of vector notation (arrow and bold character) appear in several places throughout the chapter. For later reference, the Table I summarizes the different symbols used in the text.

A temperature bias as well as time-dependent system and bath parameters generally induce net heat transport between the reservoirs. At the same time,

any driving mechanism generates heat that is dissipated into the reservoirs. Hence, the total heat current entering a given reservoir has a component resulting from the net transport between the two reservoirs and a component originated in the dissipation because of the action of the driving forces. The net heat current $J^{(h)}_{\alpha,\mathrm{tot}}$, averaged over one cycle of period $2\pi/\Omega$, satisfies [314],

$$J^{(h)}_{\mathrm{L,tot}} + J^{(h)}_{\mathrm{R,tot}} = P, \tag{8.2}$$

where P is the total dissipative power generated by the driving forces, also averaged over one period. Identifying the component due to transport and that due to dissipation in $J^{(h)}_{\alpha,\mathrm{tot}}$ is a non trivial task in general. The transport component satisfies

$$J^{(h)}_{\mathrm{L}} = -J^{(h)}_{\mathrm{R}} \equiv J^{(h)}, \tag{8.3}$$

and we notice that only the total dissipative heat contributes to Eq. (8.2). In the next section, we exactly calculate $J^{(h)}_{\alpha}$ to linear order in $\dot{\mathbf{X}}(t)$ and we show that it satisfies Eq. (8.3). Hence, we identify it with the leading term of the transport current.

The net heat transported per cycle between the two reservoirs is

$$Q_{\mathrm{tr}} = -\frac{2\pi}{\Omega} J^{(h)}. \tag{8.4}$$

This component is defined such that $Q_{\mathrm{tr}} > 0$ when heat flows in the direction of the thermal bias (hot to cold). We also define the net work W performed on the system by the ac forces during one cycle. We take $W > 0$ when the ac forces exert work on the system. The balance between Q_{tr} and W is the key to the performance of the thermal machine, which may operate as a heat engine by transforming heat into work against the time-dependent driving or as a refrigerator, by using the work performed by the *ac* driving to pump heat from the cold to the hot reservoir. In the absence of heat-work conversion, one finds that both $Q_{\mathrm{tr}} \geq 0$ and $W \geq 0$. In the heat-engine mode, the heat–work conversion mechanism operates against the ac forces and consequently $W < 0$. In the refrigerator mode, the heat–work conversion mechanism operates by using part of the work done by the ac forces to pump heat against the thermal bias, so that $Q_{\mathrm{tr}} < 0$.

It is straightforward to generalize our considerations to multi-terminal devices or to include additional macroscopic variables beyond temperature such as an electrochemical potential difference between reservoirs.

8.1.2 *Adiabatic forces, currents, and entropy production over a cycle*

In the geometric description of the adiabatic thermal machines, the central role is played by integrals of the forces in Eq. (C.14) over a period, rather than by the instantaneous quantities. First consider the energy current $\langle \mathcal{J}^E_L \rangle(t)$ which leads to a description of the heat fluxes introduced in Eq. (8.3) within the adiabatic linear response formalism. The average of the instantaneous heat current over one period, $\langle \mathcal{J}^E_L \rangle(t)$, defines the transported heat flux within the adiabatic linear response formalism. In fact, evaluating this current with the adiabatic expansion of Eq. (C.10) and using the identities of Eqs. (C.23) and (C.24) we can see that the average over one period is identical in magnitude and opposite in signs at the two reservoirs. Hence, we eliminate the label α and write

$$J^{(h)} = -\frac{\Omega}{2\pi} \int_0^{2\pi/\Omega} \mathrm{d}t \sum_{\nu=1}^{N+1} \Lambda_{N+1,\nu}(\vec{X}) \dot{X}_\nu(t). \tag{8.5}$$

The term corresponding to the sum $\nu = 1, \ldots, N$ is the pumping contribution to the heat current. The literature on pumping of charge and heat, starting with the seminal paper by Thouless [315], is so vast that it would be impossible to give a proper account of it. A brief overview can be found in the reviews [316, 317]. One of the key results of the present chapter is to show how pumping affects the operation of a quantum thermal machine, thus paving the way to observe geometric effects in the operating mode of these systems. The last term of Eq. (8.5), corresponding to $\nu = N + 1$, is the heat current flowing in response to a finite temperature bias across the device.

For a single driving parameter and $\Delta T = 0$, it is straightforward to show that the pumped heat current vanishes. At least two parameters are necessary for pumping. This was originally noticed in the framework of scattering matrix theory for driven electron systems [286, 284]. Moreover, a spatially symmetric system has $\chi_t^{\rm ad}\left[\mathcal{J}_L^E, \mathcal{F}_\ell\right] = -\chi_t^{\rm ad}\left[\mathcal{J}_R^E, \mathcal{F}_\ell\right]$, so that these quantities should be zero in view of Eq. (C.24). Hence, breaking of spatial symmetry is another necessary condition for a non-vanishing pumping contribution to the heat current [318, 314].

The net generated power has components associated to the time-dependent driving forces as well as to the thermal bias,

$$P = \frac{\Omega}{2\pi}\int_0^{2\pi/\Omega} \mathrm{d}t \left(\sum_{\ell=1}^{N} \langle \mathcal{F}_\ell \rangle \dot{X}_\ell(t) + \sum_{\alpha,\beta=L,R} \langle \mathcal{J}_\alpha^E \rangle(t) \dot{\xi}_\alpha(t) \right) = \frac{\Omega}{2\pi}\int_0^{2\pi/\Omega} \mathrm{d}t \;\; \dot{\mathbf{X}} \cdot \underline{\underline{\mathbf{\Lambda}}}(\vec{X}) \cdot \dot{\mathbf{X}}, \quad (8.6)$$

The response matrix on the right-hand side of Eq. (8.6) was introduced through the definition of forces and the energy current in Eq. (C.14). While Eqs. (8.5) for the fluxes are linear in $\dot{\mathbf{X}}$, Eq. (8.6) is bilinear in these parameters. This reflects the fact that the dissipated heat, defined in Eq. (8.3) is at least second order in these quantities – equivalent to being $\mathcal{O}(\Omega^2)$ [318, 314]. The cross terms proportional to the thermal bias and ac driving usually have opposite signs and cancel one another when evaluating the total power. This happens, in particular, in the absence of a magnetic field with driving forces symmetric under time reversal, as a consequence of the Onsager relations (C.16).

From Eq. (8.2) for the total dissipated heat flux we have the following expression for the entropy production rate

$$T\dot{S} = J^{(h)}_{\rm L,tot} + J^{(h)}_{\rm R,tot} = P. \quad (8.7)$$

Substituting Eq. (8.6) we get

$$\dot{S} = \frac{\Omega}{2\pi T}\int_0^{2\pi/\Omega} \mathrm{d}t \;\; \dot{\mathbf{X}}(t) \cdot \underline{\underline{\mathbf{\Lambda}}}(\vec{X}) \cdot \dot{\mathbf{X}}(t). \quad (8.8)$$

We present an alternative derivation for the above expression in Appendix C.

The forces $\langle \mathcal{F}_\ell \rangle(t)$ enter the work performed by the thermal machine, as will be discussed in more detail in Sec. 8.2.2 below. We also find it useful to introduce average of the force over one period,

$$F_\ell = \frac{\Omega}{2\pi}\int_0^{2\pi/\Omega} \mathrm{d}t \langle \mathcal{F}_\ell \rangle(t) = F_{\ell,\rm BO} + F_{\ell,\rm ar}, \quad \ell, = 1, \ldots, N. \quad (8.9)$$

The first term of Eq. (8.9) corresponds to the instantaneous equilibrium (Born-Oppenheimer) description given by the first term of Eq. (C.14), while the second term is the first order adiabatic reaction force defined in Ref. [291].

8.2 GEOMETRIC CHARACTERIZATION

8.2.1 *Thermal geometric tensor*

It is instructive to decompose the tensor $\Lambda_{\mu,\nu}(\vec{X})$ into its symmetric and antisymmetric parts,

$$\Lambda^{S,A}_{\mu,\nu} = \frac{1}{2}\left(\Lambda_{\mu,\nu} \pm \Lambda_{\nu,\mu}\right). \tag{8.10}$$

Equation (8.8) for the entropy production implies that the symmetric component $\Lambda^{S}_{\mu,\nu}$ controls dissipation. Since the rate of entropy production $\dot{S}$ is non-negative, the symmetric part $\Lambda^{S}_{\mu,\nu}$ can be viewed as a metric tensor on the space of thermodynamic states [304, 303, 306]. Then, geodesics with respect to this metric correspond to adiabatic trajectories which minimize dissipation [304, 303, 306]. This contribution to $\Lambda_{\mu,\nu}(\vec{X})$ has also been referred to as geometric friction [300, 304, 301].

We can obtain an explicit expression for $\Lambda_{\mu,\nu}$ from the Lehmann representation (see details in App. C). The result for the symmetric component is

$$\begin{aligned}\Lambda^{S}_{\mu,\nu}(\vec{X}) = \quad & \hbar\pi \lim_{\omega\to 0} \sum_{n,m} p_m \frac{(\varepsilon_n - \varepsilon_m)^2}{\omega} \mathrm{Re}[\langle \partial_\mu m|n\rangle\langle n|\partial_\nu m\rangle] \\ & \times \left[\delta(\omega - (\varepsilon_m - \varepsilon_n)) - \delta(\omega - (\varepsilon_n - \varepsilon_m))\right].\end{aligned} \tag{8.11}$$

Here, $|m\rangle$ and ϵ_m denote the instantaneous eigenstates and eigenenergies of $\mathcal{H}_t$ and p_m is the corresponding thermal weight, with the same definitions as in Eq. (C.10). Similarly, the antisymmetric component can be expressed as

$$\Lambda^{A}_{\mu,\nu}(\vec{X}) = 2\hbar \sum_m p_m \,\mathrm{Im}\left[\langle \partial_\mu m|\partial_\nu m\rangle\right]. \tag{8.12}$$

In the limit of zero temperature, the sum over m is dominated by the ground state and $\Lambda^{A}_{\mu,\nu}(\vec{X})$ reduces to its Berry curvature. For $\Delta T = 0$, this component can be viewed as a velocity-dependent force, akin to a Lorentz force, which does not contribute to the net entropy production. This contribution has been referred to as geometric magnetism [300, 290, 293, 294, 295].

It is interesting to compare $\Lambda_{\mu,\nu}$ to the quantum geometric tensor for the instantaneous ground state $|\psi\rangle$ of a closed system as a function of parameters X_ℓ [310, 311],

$$g_{\ell,\ell'} = \langle \partial_\ell\psi\,|\partial_{\ell'}\psi\rangle - \langle\,\partial_\ell\psi|\,\psi\rangle\,\langle\psi\,|\partial_{\ell'}\psi\,\rangle. \tag{8.13}$$

Analogous to $\Lambda_{\mu,\nu}$, the symmetric part of $g_{\ell,\ell'}$ defines a metric on the manifold of ground states and the antisymmetric part equals the Berry curvature. The crucial difference between the two tensors is that the quantum geometric tensor is defined for a discrete spectrum, while $\Lambda_{\mu,\nu}$ assumes a continuous spectrum. This does not lead to essential differences for the antisymmetric components of the tensors which are non-dissipative. In contrast, the symmetric part of $\Lambda_{\mu,\nu}$ controls dissipation and therefore vanishes for a discrete (or gapped) spectrum. We can therefore view $\Lambda_{\mu,\nu}$ as the analog of the quantum geometric tensor for systems with continuous spectra. In view of this analogy, we refer to $\Lambda_{\mu,\nu}$ as the thermal geometric tensor.

In time reversal symmetric systems subject to driving parameters $\vec{X}$ which also respect time reversal symmetry, different parts of the thermal geometric tensor are either purely symmetric or antisymmetric. The Onsager relations (C.16) imply that $\Lambda_{\ell,\ell'} = \Lambda_{\ell',\ell}$ $(\ell, \ell' = 1, \ldots, N)$ is purely symmetric (corresponding to geometric friction without geometric magnetism). In contrast,

$\Lambda_{N+1,\ell} = -\Lambda_{\ell,N+1}$ (corresponding to geometric magnetism without geometric friction). In systems which break time reversal symmetry, both the symmetric and the antisymmetric components of the thermal geometric tensor are generally nonzero.

8.2.2 *Thermal machines and geometry*

The above analysis implies that there are several purely geometric quantities which enter into the operation of adiabatic quantum thermal machines. We will show in the following that in a very concrete sense, it is the geometric aspects (in the sense of Berry) which are responsible for the heat-work conversion underlying thermal machines. The Carnot limit of the efficiency is reached in a purely geometric thermal machine, and deviations from the Carnot limit are due to nongeometric contributions.

An essential quantity is the total heat transported between the leads per cycle, $Q_{\rm tr}$ defined in Eq. (8.4). In a heat engine, this heat is in part converted into useful work while in a refrigerator, this heat is extracted from the colder reservoir. The transported heat takes the form

$$Q_{\rm tr} = \oint \sum_{\ell=1}^{N} \Lambda_{N+1,\ell} \mathrm{d}X_\ell + \oint \mathrm{d}t \Lambda_{N+1,N+1} \frac{\Delta T}{T}. \tag{8.14}$$

The first term on the right hand side is geometric, depending only on the path, and has a simple physical interpretation. It is just the heat which is pumped between the reservoirs due to the periodic variation of the parameters $\vec{X}$,

$$Q_{\rm tr,ac} = \oint \sum_{\ell=1}^{N} \Lambda_{N+1,\ell} \mathrm{d}X_\ell. \tag{8.15}$$

The second term describes the heat current driven by the applied temperature bias as a result of the heat conductance $\Lambda_{N+1,N+1}$ of the system. Notice that the two terms typically have a different dependence on the period $2\pi/\Omega$. Due to its geometric nature, the first term is independent of the period. In contrast, the second term is in general proportional to the period.

The pumped heat per cycle is essential for the operation of adiabatic quantum thermal machines. To see this, we compute the work $W = \oint \mathrm{d}\vec{X} \cdot \vec{F}$ per period performed on the system during one cycle of the ac sources. The forces, as described by Eq. (C.14), have an instantaneous and a linear-response component. The instantaneous contribution depends only on the parameters $\vec{X}$ and is evaluated in the absence of the temperature bias. This equilibrium contribution to the force is necessarily conservative (in the mechanical sense) and thus gives a vanishing contribution to the work performed over a cycle. Thus, only the linear-response component contributes to the work per cycle,

$$W = \oint \mathrm{d}t \sum_{\ell,\ell'=1}^{N} \dot{X}_\ell \Lambda_{\ell,\ell'} \dot{X}_{\ell'} + \oint \sum_{\ell=1}^{N} \mathrm{d}X_\ell \Lambda_{\ell,N+1} \frac{\Delta T}{T}. \tag{8.16}$$

First consider the second term on the right hand side. For constant $\Delta T/T$, this term is again a purely geometric line integral over a closed contour. Unlike the contribution of the instantaneous component, this term is in general nonconservative and gives a finite contribution when integrated over a closed cycle. The reason is that this term originates from the nonequilibrium contribution to the force which is generated by the temperature bias. Along with Eq. (8.15) for the pumped heat, this geometric term is the essence of

heat-work conversion and hence crucial for the operation of the thermal machine. In contrast, the first term in Eq. (8.16) describes frictional losses. Unlike the second term, which can take either sign, this term is always positive. It then becomes evident that heat-work conversion is rooted in the geometric terms in Eqs. (8.14) and (8.16), and it is the nongeometric terms (in the sense of Berry) that are responsible for losses. We will see this again below when we discuss the efficiencies of quantum thermal machines.

As a result of the Onsager relations (C.16), the geometric contributions to the transported heat and the work are very closely related. If the system is time reversal invariant (which also requires that the parameters $\vec{X}$ couple to time-reversal-even operators), the Onsager relations imply that $\Lambda_{N+1,\ell} = -\Lambda_{\ell,N+1}$ and the prefactor of $\Delta T/T$ in Eq. (8.16) just equals minus the pumped heat between the reservoirs. We can then understand the operation of a heat engine as follows. During one cycle of the machine, the cyclic variation of the parameters pumps heat from the high-temperature to the low-temperature reservoir. The corresponding change in free energy is converted into work W performed on a load (i.e., $W < 0$). Here, the load corresponds to an external agent which couples to the dynamics of the parameters $\vec{X}$. This is analogous to the operation principle of inverted quantum pumps as adiabatic quantum motors [319, 320, 321, 322, 323]. Similarly, in a refrigerator work $W = -Q_{\mathrm{tr,ac}}\Delta T/T > 0$ must be supplied by the ac sources to overcome the thermal bias and to pump heat $Q_{\mathrm{tr,ac}}$ from the low-temperature to the high-temperature reservoir.

It is also interesting to discuss this heat-work conversion in the context of the entropy production rate defined in Eq. (8.7). With the definitions of this section, we can write

$$T\dot{S} = \frac{\Omega}{2\pi}\left(W + Q_{\mathrm{tr}}\frac{\Delta T}{T}\right). \tag{8.17}$$

The first term corresponds to the total power generated by the ac sources, while the second term corresponds to the power invested to transport the heat Q_{tr} per cycle in the presence of the thermal bias ΔT. Due to the heat-work conversion, the geometric component of W exactly cancels the component $Q_{\mathrm{tr,ac}}$ of Q_{tr} in the dissipated power (still assuming time-reversal invariance). Entropy production is then associated with the nongeometric contributions to heat and work. In a heat engine, a negative balance of the two terms contributing to Eq. (8.16), $W < 0$, can be used to work against the load. In a refrigerator, both terms are positive since one has to overcome the frictional losses in addition to pumping heat from the cold to the hot reservoir. It is important to notice that the two terms in Eq. (8.16) are typically of different orders in the period $2\pi/\Omega$. While the first, nongeometric contribution is inversely proportional to the period, the second, geometric contribution is independent of it. Thus, one can often neglect the nongeometric term when considering the limit of small frequency Ω. As we will show below, we note that under certain circumstances the first term in Eq. (8.16) can also be viewed as a geometric quantity even though it cannot be immediately rewritten as a line integral.

We close this section by a few additional remarks. The operation of a heat engine or refrigerator requires that a net amount of heat $Q_{\mathrm{tr,ac}}$ is pumped between the reservoirs during a cycle, requiring that the force is nonconservative. Above, we have focused on the case that $\Delta T/T$ is constant over the cycle. In principle, the conditions for the operation of adiabatic quantum thermal machines can be less stringent if one allows $\Delta T/T$ to vary along the

cycle, for instance by coupling the system to different reservoirs at different stages.

In the absence of time reversal symmetry, the Onsager relations connect the response functions $\Lambda_{\mu,\nu}$ at different magnetic fields. In this case, there is no general relation between $\Lambda_{N+1,\ell}$ and $\Lambda_{\ell,N+1}$ for a fixed magnetic field, and in addition to the antisymmetric contribution $\Lambda^A_{N+1,\ell} = -\Lambda^A_{\ell,N+1}$, there could also be a symmetric contribution, $\Lambda^S_{N+1,\ell} = \Lambda^S_{\ell,N+1}$. Unlike $\Lambda^A_{\mu,\nu}$, the symmetric $\Lambda^S_{\mu,\nu}$ is associated with entropy production and dissipation according to Eq. (8.6). Even if both the dissipative and the nondissipative contributions to the pumped heat flow from the hot to the cold reservoir, the work performed on a load would involve the difference between the antisymmetric and the symmetric contribution.

The time average of the forces $\vec{F}$ as defined in Eq. (8.9) also has contributions which are purely geometric. From Eq. (C.14), the first-order adiabatic reaction component can be readily rewritten as

$$F_{\ell,\mathrm{ar}} = \frac{\Omega}{2\pi}\left\{\oint \sum_{\ell'=1}^{N} \Lambda_{\ell,\ell'}\mathrm{d}X_{\ell'} + \oint \mathrm{d}t\Lambda_{\ell,N+1}\frac{\Delta T}{T}\right\} \tag{8.18}$$

Here, the first term on the right hand side is a line integral which is purely geometric in that it depends only on the path.

Finally, we remark that under certain conditions, the dissipated component of W, corresponding to the first term of Eq. (8.16), can also be formally represented in terms of a line integral over a closed path in parameter space. This is not as straightforward as for Eqs. (8.18), (8.14), and (8.16) since the power is bilinear in $\dot{\mathbf{X}}$. It is, however, possible when there exists a well-defined mapping between $\dot{\mathbf{X}}$ and $\mathbf{X}$ as the latter varies along the closed path γ. In particular, such a mapping exists for the case of periodic driving. For a smooth path γ, one can write the relations $\dot{X}_\mu = \Omega g_\mu(\vec{X})|_\gamma$ for all μ, where the functions $g_\mu(\vec{X})|_\gamma$ are defined by eliminating the parametrization in t between $X_\mu(t)$ and $\dot{X}_\mu(t)$. Then, we can write the dissipated power as a line integral by using this relation to eliminate one of the factors of $\dot{X}_\mu$ in Eq. (8.6) via these relations. Note that the resulting line integral has a prefactor of Ω, making it explicit that the dissipated power is inversely proportional to the period of the driving, as already mentioned above.

The line integrals controlling the operation of adiabatic thermal quantum machines are reminiscent of line integrals over Berry connections. This motivates us to introduce the vector fields

$$\vec{A}^{A/S}_\mu = \left(\Lambda^{A/S}_{\mu,1}(\vec{X}),\ldots,\Lambda^{A/S}_{\mu,N}(\vec{X})\right) \tag{8.19}$$

with $\mu = 1,\ldots,N+1$ for the rows of the thermal geometric tensor. Similarly, we introduce

$$\tilde{\vec{A}} \;=\; \sum_\ell \left(\tilde{\Lambda}^S_{\ell,1}(\vec{X}),\ldots,\tilde{\Lambda}^S_{\ell,N}(\vec{X})\right), \tag{8.20}$$

where $\tilde{\Lambda}^S_{\mu,\nu}(\vec{X}) = g_\mu(X_\mu)\Lambda^S_{\mu,\nu}(\vec{X})$. These vector fields control the pumped heat and the work performed on the system as well as the dissipated power. Thus, they are useful to illustrate the operation of the specific thermal machines which we discuss in Sec. 8.3. In terms of these vector potentials Eqs. (8.15) and (8.16) read, respectively,

$$Q_{\mathrm{tr,ac}} = \oint \vec{A}_{N+1}(\vec{X})\cdot d\vec{X}, \tag{8.21}$$

with $\vec{A}_\mu(\vec{X}) = \vec{A}^A_\mu(\vec{X}) + \vec{A}^S_\mu(\vec{X})$ and

$$W = \oint \left[\tilde{\vec{A}}(\vec{X}) - \frac{\Delta T}{T} \left(\vec{A}^A_{N+1}(\vec{X}) - \vec{A}^S_{N+1}(\vec{X}) \right) \right] \cdot d\vec{X}. \tag{8.22}$$

In the latter equation, the last term does not contribute for many systems. In particular, this is the case in the presence of time-reversal symmetry (including driving parameters $\vec{X}$ coupling to time-reversal-even operators). In such cases, we can write $W = \oint \tilde{\vec{A}}(\vec{X}) - (\Delta T/T) Q_{\mathrm{tr,ac}}$.

8.2.3 *Efficiencies*

8.2.3.1 *Heat engine*

In a heat engine, heat transported from the high to the low temperature reservoir is partially converted into useful work. We can then define an efficiency for the heat engine as

$$\eta^{(\mathrm{he})} = \frac{-W}{Q_{\mathrm{tr}}}. \tag{8.23}$$

This expression can be readily analyzed for a time-reversal-invariant system with constant $\Delta T/T$. In the limit of adiabatic operation of the heat engine, $\Omega \to 0$, we can neglect the frictional losses to leading order and only the second term on the right hand side of Eq. (8.16) contributes to the work performed against the load, $W \simeq -Q_{\mathrm{tr,ac}} \Delta T/T$. If the heat transfer across the system is dominated by the geometric contribution, one finds $Q_{\mathrm{tr}} \simeq Q_{\mathrm{tr,ac}}$, and hence that the efficiency approaches $\eta^{(he)} \simeq \Delta T/T$. Remarkably, this is just the Carnot efficiency. We thus find that a purely geometric quantum thermal machine reaches the optimal efficiency, and it is the nongeometric contributions to W and Q_{tr} (in the sense of Berry) which are responsible for deviations from the Carnot efficiency. Indeed, a finite heat conductance diminishes the efficiency of the heat engine, as do frictional losses described by the first term on the right hand side of Eq. (8.16). Note that the contribution of the heat conductance to the transferred heat is proportional to the period of the cycle. This implies that this term is less detrimental to the efficiency as the frequency at which the machine operates increases. Conversely, by increasing the frequency, the effect of the frictional losses becomes larger.

While the overall efficiency is fundamentally limited to the Carnot limit, there is no fundamental limit to reducing the detrimental effects of the nongeometric contributions. While the frictional forces become arbitrarily small as one approaches the truly adiabatic limit, the limit of a negligible heat conductance $\Lambda_{N+1,N+1} \simeq 0$ can be realized in a topological quantum pump. In such pumps, the ground state is separated from the excited states by a gap. Consequently, the symmetric contributions to $\Lambda_{\mu,\nu}$ – including the heat conductance – are strongly suppressed.

8.2.3.2 *Refrigerator*

A refrigerator uses work W performed on the system to remove heat from a cold to a hot reservoir. Thus, we can define a corresponding efficiency or coefficient of performance (COP) as

$$\eta^{(\mathrm{fr})} = \frac{-Q_{\mathrm{tr}}}{W}. \tag{8.24}$$

Again focusing on a time reversal invariant system with constant $\Delta T/T$, this efficiency approaches the Carnot limit $\eta^{fr} = T/\Delta T$ for zero heat conductance. The efficiency is reduced by a finite heat conductance since, for a refrigerator, its contribution to the numerator has the opposite sign compared to the pumped heat.

8.2.3.3 *Heat pump*

Of course, the device can also be used as an adiabatic heat pump in the absence of a thermal bias $\Delta T/T$. Heat is transported from left to right or vice versa due to the variation of $\vec{X}$. According to Eq. (8.16), we need to exert work W associated with dissipation, even if there is no temperature bias. We can then define a corresponding efficiency of heat pumping through

$$\eta^{(\text{pump})} = \frac{|Q_{\text{tr,ac}}|}{W}. \tag{8.25}$$

The denominator in this expression is proportional to Ω, so that the efficiency of the heat pump grows as it becomes more adiabatic.

8.3 EXAMPLES

We now illustrate the general formalism introduced in the previous sections by two driven systems coupled to thermals baths. One example is referred to as a driven qubit and consists of a generic two-level system with time-dependent energies and inter-level transition matrix elements, coupled to baths of bosonic excitations. This problem will be solved in the limit of weak coupling to the reservoirs. The second example is a driven quantum dot, which consists of a confined structure with two single-electron levels – one per spin orientation – driven by a rotating magnetic field. This problem is solved for weak as well as for strong coupling to spin-polarized electron reservoirs.

8.3.1 *Driven qubit*

We consider a generalization of the celebrated spin-boson model, which was introduced in Refs. [324, 325]. As in those works, we express the Hamiltonian in terms of the Pauli matrices $\hat{\vec{\sigma}} = (\hat{\sigma}_x, \hat{\sigma}_y, \hat{\sigma}_z)$ and a magnetic field $\vec{B}(t) = \big(B_x(t), B_y(t), B_z(t)\big)$. In our case, the latter varies periodically in time. The ensuing Hamiltonian reads

$$H_S(t) = \vec{B}(t) \cdot \hat{\vec{\sigma}}. \tag{8.26}$$

The qubit is attached to bosonic reservoirs L, R with Hamiltonians given by Eq. (2.6).

The coupling is described by the Hamiltonian $H_c = H_{c,L} + H_{c,R}$ given in Eq. (2.13). Our generalization with respect to previous works is to consider different types of couplings to the L and R reservoirs. This is motivated by the fact that spatial inversion symmetry has to be broken in order to obtain pumping, as mentioned in Section 8.1.2. Concretely, for the left lead we take $\theta_L = \pi/2$; $\phi_L = 0$ and for the right lead $\theta_R = 0$, such that the coupling Hamiltonians read

$$H_c = \sum_k \left[V_{kL} \hat{\tau}_L \left(b_{kL} + b_{kL}^\dagger \right) + V_{kR} \hat{\tau}_R \left(b_{kR} + b_{kR}^\dagger \right) \right], \tag{8.27}$$

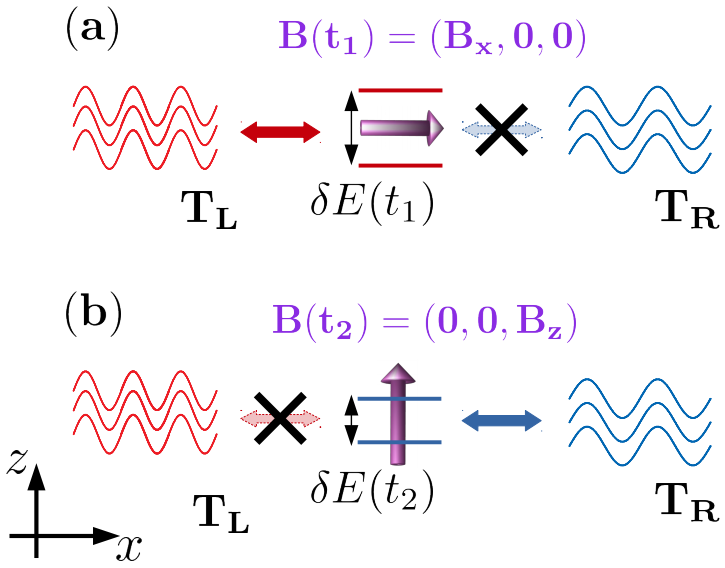

Figure 8.2: Illustration of the q-bit coupled to two bosonic reservoirs by the Hamiltonian of Eq. (8.27) with $\hat{\tau}_L = \hat{\sigma}_x$ and $\hat{\tau}_R = \hat{\sigma}_z$, operating as a heat engine. Panel (a): the q-bit is in one of the states $|x, \pm\rangle$ and couples to the reservoir L. Panel (b): the q-bit is in one of the states $|z, \pm\rangle$ and couples only to the reservoir R. The driving changes the energy difference between the two levels.

Hence, the q-bit couples to the L or R reservoir if it is in a state with a non-vanishing projection on the eigenstates $|x, \pm\rangle$ of $\hat{\sigma}_x$ or $|z, \pm\rangle$ of $\hat{\sigma}_z$, respectively. Any other combination of two Pauli matrices with $\hat{\tau}_L \neq \hat{\tau}_R$ would also be appropriate, as we will discuss in Section IV.A.3. Previous works related to heat engines based on q-bits considered the same type of coupling to the two reservoirs and non-adiabatic driving [326, 327, 328, 123, 329, 290, 330, 331, 266, 332, 333, 334, 335] .

The Hamiltonian for the system of Eq. (8.26) can be transformed to the basis of instantaneous eigenstates $|j\rangle$, such that $\mathcal{H}_S(t)|j\rangle = E_j(t)|j\rangle$, $j = 1, 2$, with $E_{1,2}(t) = \mp|\vec{B}|$. The resulting transformed Hamiltonian reads $\tilde{\mathcal{H}}_S(t) = \hat{U}^{-1}(t)\mathcal{H}_S(t)\hat{U}(t)$ with $\hat{U}(t)$ being a unitary transformation and

$$\tilde{\mathcal{H}}_S(t) = E_1(t)|1\rangle\langle 1| + E_2(t)|2\rangle\langle 2|, \tag{8.28}$$

Accordingly, the contact Hamiltonian can be also expressed in this basis as

$$\tilde{\mathcal{H}}_{c,\alpha}(t) = \sum_k \sum_{ij} V_{k\alpha} v_{\alpha,ij}(t) \hat{\rho}_{ij}(t) \left(b_{k\alpha} + b^\dagger_{k\alpha} \right), \tag{8.29}$$

with $v_{\alpha,ij}(t) = \left[\hat{U}^{-1}(t)\hat{\tau}_\alpha \hat{U}(t)\right]_{ij}$, $\hat{U}(t)$ being the unitary transformation which diagonalizes the Hamiltonian (8.26), and $\hat{\rho}_{ij} = |i\rangle\langle j|$.

Before proceeding to explicit calculations, we can gather some intuition on how the driven q-bit may work as a thermal machine by using the sketch of Fig. 8.2. As a consequence of the driving, the energy of the two levels as well as the coupling to the L and R reservoirs change in time according to Eqs. (8.28) and (8.29), respectively. Panel (a) represents a situation where the q-bit at a given time t_1 is in one of the eigenstates of $\hat{\sigma}_x$, hence, it couples to the L reservoir and it is completely decoupled from R. Panel (b) illustrates the situation where the q-bit is in an eigenstate of $\hat{\sigma}_z$ at a different time t_2, therefore it is coupled to R and decoupled from L. In an evolution from t_1

to t_2 the energy difference $\delta E(t) = E_2(t) - E_1(t)$ changes. A cycle can be realized when the protocol returns the q-bit to the state of the step (a). The paradigmatic Otto cycle corresponds to the extreme situation, where the q-bit is allowed to thermalize with L at the step (a) and with R at the step (b), while it evolves decoupled from the two reservoirs at intermediate times [266, 270]. For the case of adiabatic driving, the changes take place smoothly and the q-bit is coupled to the two reservoirs at all times. For suitable protocols, the setup may anyway operate as a heat engine or refrigerator, as well as a heat pump.

We will analyze in detail protocols with two time-dependent parameters of the form $\vec{B}(t) = (B_x(t), 0, B_z(t))$, with

$$\begin{aligned} B_x(t) &= B_{x,0} + B_{x,1}\cos(\Omega t + \phi), \\ B_z(t) &= B_{z,0} + B_{z,1}\cos(\Omega t). \end{aligned} \tag{8.30}$$

These two components of $\vec{B}(t)$ are identified with the time-dependent parameters of Eq. (C.1) as follows

$$\vec{X}(t) = (X_1(t), X_2(t)) \equiv (B_z(t), B_x(t))\,. \tag{8.31}$$

In addition, we will consider a constant difference of temperature ΔT, which defines $\dot{X}_3 = \Delta T/T$. We will solve the problem in the limit of very weak coupling between the qubit and the reservoirs (small $V_{k\alpha}$).

8.3.1.1 *Master equation approach*

We follow the procedure of Refs. [287, 233, 336], which consists in solving the time-dependent master equation by performing an adiabatic expansion along the lines of the general formalism of Section C.1.2. The basic idea is to describe the evolution of the population probabilities of the eigenstates of $\tilde{\mathcal{H}}_S(t)$, represented by the vector $\mathbf{p}(t) = (p_1(t), p_2(t))$, in terms of a master equation where the effect of the coupling to the reservoirs is treated at the lowest order of perturbation theory (first order in $|V_{k\alpha}|^2$). The master equation reads,

$$\frac{d}{dt}\mathbf{p}(t) = \sum_\alpha \mathbf{M}_\alpha(\vec{B}) \cdot \mathbf{p}(t), \tag{8.32}$$

where $\mathbf{M}_\alpha(\vec{B})$ is a 2×2 matrix representing the instantaneous transition rates corresponding to the reservoir α, which is given by

$$\mathbf{M}_\alpha(\vec{B}) = \begin{bmatrix} -\Gamma_{\alpha,12}(\vec{B}) & \Gamma_{\alpha,21}(\vec{B}) \\ \Gamma_{\alpha,12}(\vec{B}) & -\Gamma_{\alpha,21}(\vec{B}) \end{bmatrix}. \tag{8.33}$$

Here we stress that the instantaneous rates depend on time through the parameters $\vec{B}$, as indicated in Eq. (8.31). We have introduced the following definitions

$$\begin{aligned} \Gamma_{\alpha,12}(\vec{B}) &= \lambda_\alpha(\vec{B})\Big[\gamma_\alpha\Big(\delta E\left(\vec{B}\right)\Big) + \tilde{\gamma}_\alpha\Big(-\delta E\left(\vec{B}\right)\Big)\Big], \\ \Gamma_{\alpha,21}(\vec{B}) &= \lambda_\alpha(\vec{B})\Big[\tilde{\gamma}_\alpha\Big(\delta E(\vec{B})\Big) + \gamma_\alpha\Big(-\delta E(\vec{B})\Big)\Big], \end{aligned} \tag{8.34}$$

with

$$\begin{aligned} \gamma_\alpha(\varepsilon) &= n_\alpha(\varepsilon)\Gamma_\alpha(\varepsilon)/\hbar, \\ \tilde{\gamma}_\alpha(\varepsilon) &= [1 + n_\alpha(\varepsilon)]\Gamma_\alpha(\varepsilon)/\hbar, \end{aligned} \tag{8.35}$$

while $\delta E(\vec{B}) = E_2(\vec{B}) - E_1(\vec{B})$ and $\lambda_\alpha(\vec{B}) = v_{\alpha,12}(\vec{B})v_{\alpha,21}(\vec{B})$. For $\hat{\tau}_L = \hat{\sigma}_x$ and $\hat{\tau}_R = \hat{\sigma}_z$ we have

$$\lambda_L(\vec{B}) = \frac{B_x^2(t)}{B_z^2(t) + B_x^2(t)}, \qquad \lambda_R(\vec{B}) = \frac{B_z^2(t)}{B_z^2(t) + B_x^2(t)}. \tag{8.36}$$

$n_\alpha(\varepsilon)$ is the Bose-Einstein distribution for bath α and $\Gamma_\alpha(\epsilon)$ is the corresponding spectral density, which we assume to be Ohmic

$$\Gamma_\alpha(\epsilon) = \pi K_\alpha \, \epsilon \, e^{-\epsilon/\epsilon_C}, \quad \text{with } \epsilon > 0, \tag{8.37}$$

ϵ_C being the cut-off frequency. Since, according to Eq. (8.37), there are no negative-energy states in the bath, we set $\gamma_\alpha[-\delta E(\vec{B})] = \tilde{\gamma}_\alpha[-\delta E(\vec{B})] = 0$ (notice that $\delta E(\vec{B})$ is positive by definition).

Following Refs. [233, 336], the population can be expanded in different orders of the driving frequency Ω. Here we keep only the zeroth-order (instantaneous) term $\mathbf{p}^{(\mathrm{i})}$, and first-order (adiabatic) term $\mathbf{p}^{(\mathrm{a})}$ such that

$$\mathbf{p}(t) = \mathbf{p}^{(\mathrm{i})}(t) + \mathbf{p}^{(\mathrm{a})}(t). \tag{8.38}$$

The solution of the master equation (8.32) order by order in Ω, leads to

$$\sum_\alpha \mathbf{M}_\alpha(\vec{B}) \cdot \mathbf{p}^{(\mathrm{i})}(t) = 0, \tag{8.39}$$

and

$$\frac{d}{dt}\mathbf{p}^{(\mathrm{i})}(t) = \sum_\alpha \mathbf{M}_\alpha(\vec{B}) \cdot \mathbf{p}^{(\mathrm{a})}(t). \tag{8.40}$$

The adiabatic correction can be written in terms of instantaneous contributions as

$$\mathbf{p}^{(\mathrm{a})}(t) = \sum_\alpha \left[\bar{\mathbf{M}}_\alpha(\vec{B})\right]^{-1} \cdot \frac{d}{dt}\mathbf{p}^{(\mathrm{i})}(t), \tag{8.41}$$

where the matrix $\left[\bar{\mathbf{M}}_\alpha(\vec{B})\right]^{-1}$ includes the normalization condition for the adiabatic probabilities [287]. We obtain two additional equations from the conservation of the probability, namely $\sum_j p_j^{(\mathrm{i})}(t) = 1$ and $\sum_j p_j^{(\mathrm{a})}(t) = 0$.

The instantaneous (i), adiabatic (a) and thermal (th) contributions to the heat current flowing in reservoir α as functions of time are given by

$$\begin{aligned} J_\alpha^{(\mathrm{h}),\mathrm{i/a}}(t) &= \delta E(\vec{B}) \left[\mathbf{M}_\alpha(\vec{B}) \cdot \mathbf{p}^{(\mathrm{i/a})}(t)\right]_{11}, \\ J_\alpha^{(\mathrm{h}),\mathrm{th}}(t) &= \delta E(\vec{B}) \left[\mathbf{M}_\alpha(\vec{B}) \cdot \mathbf{p}_{\Delta T}^{(\mathrm{i})}(t)\right]_{11}, \end{aligned} \tag{8.42}$$

where $\mathbf{p}_{\Delta T}^{(\mathrm{i})}$ is the instantaneous probability vector in the presence of the thermal bias ΔT. We can now calculate the different linear-response components of the heat current defined in Eq. (8.5) as follows

$$J^{(\mathrm{h}),\mathrm{a/f}} = \frac{\Omega}{2\pi} \int_0^{2\pi/\Omega} dt \; J_{\mathrm{L}}^{(\mathrm{h}),\mathrm{th}}(t), \tag{8.43}$$

while the instantaneous component vanishes when averaged over the period.

On the other hand, the net work developed by the ac forces, corresponding to Eq. (8.16) can also be calculated in the master equation approach. To this end we write the total energy of the qubit at a particular time t as

$$E_{\mathrm{tot}}(t) = E_1(t)p_1(t) + E_2(t)p_2(t), \tag{8.44}$$

where the probabilities are given by the sum of the instantaneous $p_j^{(\mathrm{i})}$, the adiabatic $p_j^{(\mathrm{a})}$ and thermal $p_j^{(\mathrm{th})}$ components. The time derivative of the total energy contains two contributions,

$$\frac{dE_{\mathrm{tot}}}{dt} = \sum_{j=1}^{2}\left(\frac{dE_j(t)}{dt}p_j(t) + E_j(t)\frac{dp_j(t)}{dt}\right) \tag{8.45}$$

These are the power delivered by the ac sources

$$P(t) = \frac{dE_1(t)}{dt}p_1(t) + \frac{dE_2(t)}{dt}p_2(t), \tag{8.46}$$

and the heat temporarily stored in the q-bit. Thus, the total work over a cycle reads

$$W = \int_0^{2\pi/\Omega} dt\Big(\frac{dE_1}{dt}p_1(t) + \frac{dE_2}{dt}p_2(t)\Big), \tag{8.47}$$

where both instantaneous, adiabatic, and thermal components of the probabilities $\mathbf{p}(t)$ contribute. The contribution due to the instantaneous components represents the work done by the conservative forces, while the other terms will contribute to the non-conservative work defined in Eq. (8.16). The explicit expressions for the different components of $\mathbf{p}(t)$ for the driving protocol of Eq. (8.31) are presented in Appendix G. We notice that the terms originating from the coupling Hamiltonian in Eq. (8.29), could in principle contribute to W and can be calculated from the time average of $\langle\dot{\tilde{\mathcal{H}}}_{c,\alpha}\rangle$. However, this term is neglected in the limit of very small $V_{k\alpha}$. In fact, its contribution to the work per cycle is smaller (by at least a factor of $|V_{k\alpha}|$) than the contribution to the work due to $\tilde{H}_S(t)$.

8.3.1.2 *Geometrical properties*

We now derive the expressions corresponding to Eqs. (8.15) and (8.16) within the formalism of the master equation. These can be derived from Eqs. (8.43) and (8.47). We get

$$Q_{\mathrm{tr,ac}} = \int_0^{2\pi/\Omega} dt\ \mathbf{M}_R^{(h)}(\vec{B})\cdot\mathbf{p}^{(\mathrm{a})}(t), \tag{8.48}$$

$$W = \int_0^{2\pi/\Omega} dt\ \frac{d\mathbf{E}}{dt}\cdot\left[\mathbf{p}^{(\mathrm{a})}(t) + \mathbf{p}_{\Delta T}^{(\mathrm{i})}(t)\right], \tag{8.49}$$

where

$$\mathbf{M}_R^{(h)}(\vec{B}) = \delta E(\vec{B})\begin{bmatrix}-\Gamma_{R,12}(\vec{B})\\ \Gamma_{R,21}(\vec{B})\end{bmatrix}^T. \tag{8.50}$$

and $\mathbf{E}((\vec{B})) = (E_1(t),\ E_2(t))$. Using Eq. (8.41) and

$$\frac{d\mathbf{p}^{(i)}}{dt} = \sum_{\ell=1}^{2}\frac{\partial\mathbf{p}^{(i)}}{\partial B_\ell}\dot{B}_\ell \tag{8.51}$$

the pumped heat given by Eq. (8.48) can be written as in Eq. (8.15), by identifying

$$\Lambda_{3,\ell}(\vec{B}) = \mathbf{M}_R^{(h)}(\vec{B})\cdot\bar{\mathbf{M}}^{-1}(\vec{B})\cdot\frac{\partial\mathbf{p}^{(\mathrm{i})}}{\partial B_\ell},\quad \ell = 1,2. \tag{8.52}$$

In the present configuration, the explicit calculation of these coefficients show that $\Lambda_{3,\ell} = -\Lambda_{\ell,3}$, up to a function that vanishes upon integrating over the period. This means that these terms are components of the antisymmetric thermal tensor $\Lambda^A_{\mu,\nu}$. The other components of the tensor can be derived from the first terms ($\propto \mathbf{p}^{(a)}(t)$) of Eq. (8.49). More precisely, using Eq. (8.41) with Eq. (8.51), and expressing

$$\frac{d\mathbf{E}}{dt} = \sum_{\ell=1}^{2} \frac{\partial \mathbf{E}}{\partial B_\ell} \cdot \dot{B}_\ell, \tag{8.53}$$

we find

$$\Lambda_{\ell,\ell'}(\vec{B}) = \frac{\partial \mathbf{E}}{\partial B_\ell} \cdot \tilde{\mathbf{M}}^{-1}(\vec{B}) \cdot \frac{d\mathbf{p}^{(i)}}{\partial B_{\ell'}}, \quad \ell, \ell' = 1, 2. \tag{8.54}$$

We can see that these terms satisfy $\Lambda_{\ell,\ell'} = \Lambda_{\ell',\ell}$, as explicitly shown in Eq. (G.10). Hence they are components of the symmetric tensor $\Lambda^S_{\mu,\nu}$.

On the other hand, by using the fact that we can define a relation of the form $\dot{B}_\ell = g_\ell(\vec{B})\Omega$ for the protocol of Eq. (8.31), we can express the total work in terms of purely geometric quantities, by rewritting Eqs. (8.48) and (8.49) in terms of the vector potentials of Eqs. (8.19) and (8.20). In the present case, they read

$$\begin{aligned}
\vec{A}^A_3(\vec{B}) &= \left(\Lambda^A_{3,1}(\vec{B}), \Lambda^A_{3,2}(\vec{B})\right), \\
\vec{A}^S_\ell(\vec{B}) &= \left(\Lambda^S_{\ell,1}(\vec{B}), \Lambda^S_{\ell,2}(\vec{B})\right), \quad \ell = 1, 2, \\
\tilde{\vec{A}}(\vec{B}) &= \Omega \sum_{\ell=1}^{2} g_\ell(\vec{B}) \left(\Lambda^S_{\ell,1}(\vec{B}), \Lambda^S_{\ell,2}(\vec{B})\right),
\end{aligned} \tag{8.55}$$

We have highlighted the antisymmetric and symmetric character in each case. Notice that, according to the analysis of Sections 8.1.2 and 8.2, the symmetric component contributes purely to dissipation of energy and entropy production, while the antisymmetric one is related to useful work.

In order to characterize the performance of the heat engine and refrigerator as in Eqs. (8.23) and (8.24) we also need the heat transported in one period as a response to the thermal bias. It reads

$$Q_{\mathrm{tr},\Delta \mathrm{T}} = -\int_0^{2\pi/\Omega} dt\, J^{(\mathrm{th})}_{\mathrm{L}}(t) \tag{8.56}$$

with $J^{(\mathrm{th})}_{\mathrm{L}}(t)$ defined in Eq. (8.42). This component is not geometric and we recall that the total transported heat is $Q_{\mathrm{tr}} = Q_{\mathrm{tr,ac}} + Q_{\mathrm{tr},\Delta \mathrm{T}}$.

According to our conventions, the contribution to the contour integral of the first component of Eq. (8.22) is always positive and is the portion related to the net dissipated power and entropy production due to the ac driving. Instead, the second one, also defining $Q_{\mathrm{tr,ac}}$ in Eq. (8.21), can have any sign. In the case of a heat engine, $Q_{\mathrm{tr,ac}}$ and $Q_{\mathrm{tr},\Delta \mathrm{T}}$ have the same sign, i.e. the pumped heat flows in the same direction as the component induced by the temperature bias. As a consequence, it generates useful work that can be absorbed by the ac sources. Notice that in such a case, the second term of Eq. (8.22) has an opposite sign to the first. In the refrigerator, it is the opposite. Irrespectively of the sign of $Q_{\mathrm{tr,ac}}$, which determines that the system operates as a heat engine or a refrigerator, the crucial quantity to optimize is the integral of $\vec{A}^A(\vec{B})$ over a suitable chosen closed path in the parameter space.

8.3.1.3 *Results*

We present some results for specific parameters of the driving protocol defined in Eq. (8.31).

We start by analyzing the case with $\Delta T = 0$ and showing that a necessary condition for the heat currents to be finite is that the coupling to the left and right reservoirs are different, i. e. $\hat{\tau}_L \neq \hat{\tau}_R$. In fact, let us notice that these couplings determine the functions $\lambda_L(\vec{B})$ and $\lambda_R(\vec{B})$. If we assume symmetric couplings, we have $\lambda_L(\vec{B}) = \lambda_R(\vec{B})$ and $K_L = K_R$. Therefore, we get $\mathbf{M}_L(\vec{B}) = \mathbf{M}_R(\vec{B})$ in Eq. (8.33). After replacing the latter matrices in Eq. (8.42), we get $J_L^{(\mathrm{h}),\mathrm{a}}(t) = J_R^{(\mathrm{h}),\mathrm{a}}(t)$ at every time. This implies that the currents obtained by averaging over one period, i. e. $J_{\mathrm{L}}^{(\mathrm{h})}$ and $J_{\mathrm{R}}^{(\mathrm{h})} \equiv J^{(\mathrm{h}),\mathrm{a}}$, must be equal to zero in order to agree with Eq. (8.3). Interestingly, one can check by means of the explicit calculations that the adiabatically pumped current in one period $J^{(\mathrm{h}),\mathrm{a}}$ is zero even if one allows K_L and K_R to be different. Moreover, we verified that the magnitude of the pumped heat current depends on the chosen combinations of Pauli matrices (see Appendix G). The maximum pumping for the protocol of Eq. (8.31) corresponds to $\mathcal{H}_{\mathrm{c},\alpha}$ containing $\hat{\tau}_L = \hat{\sigma}_x$ and $\hat{\tau}_R = \hat{\sigma}_z$, as in Eq. (8.27). As a matter of fact, in the other two combinations ($\hat{\tau}_L = \hat{\sigma}_x$, $\hat{\tau}_R = \hat{\sigma}_y$, and $\hat{\tau}_L = \hat{\sigma}_y$, $\hat{\tau}_R = \hat{\sigma}_z$) one obtains half the magnitude.

We now turn to analyze the geometric properties, which can be fully characterized by the vector potentials $\vec{A}^A(\vec{B})$ and $\tilde{\vec{A}}^S(\vec{B})$, entering Eqs. (8.22) and (8.21). These vectors are represented with arrows in the parameters space in Fig. 8.3. In the Fig. 8.3 we show several paths, which are plotted in blue, corresponding to the protocol of Eq. (8.31) with different relative phases ϕ. This provides a visual representation of the magnitude of $Q_{\mathrm{tr,ac}}$ and the two types of geometric components of W. In all the cases we represent with red arrows the vector $\vec{A}^A(\vec{B})$ along the path while the green arrows represent the vector potential $\tilde{\vec{A}}^S(\vec{B})$ along the same protocol (note that $\tilde{\vec{A}}^S(\vec{B})$ is inherently associated with the protocol and cannot be defined outside it). The latter vectors follow the circulation of the path. Thus, they lead to a positive non-vanishing contribution to W for all the values of ϕ. Instead, the vectors $\vec{A}^A(\vec{B})$ are in general opposite to the circulation of the path along some pieces. In particular, for trajectories like the ones corresponding to $\phi = n\pi$, they are parallel to the circulation along half of the path and antiparallel in the other half, leading to a vanishing result of the integral.

In Fig. 8.4 we plot the adiabatically pumped heat current $Q_{\mathrm{tr,ac}}$, black curve, as a function of the phase lag ϕ in the weak pumping limit. The latter corresponds to considering values of $B_{x,1}$ and $B_{z,1}$ small enough so that $\oint \vec{A}_3^A \cdot d\vec{B}$ in Eqs. (8.22) and (8.21) is proportional to the area, in the parameter space, enclosed by the closed contour defining the protocol. Indeed, using the Green's theorem, these integrals can be written as a surface integral of the derivatives of $\vec{A}_3^A$ with respect to $\vec{B}$. When $B_{x,1}$ and $B_{z,1}$ are small, such derivatives do not depend on $\vec{B}$ and can be factorized outside the integral. Accordingly, as shown in Fig. 8.4, the pumped heat current (black curve) behaves as a sine function of ϕ, which vanishes at $\phi = 0$. In particular, we note that a heat current is extracted from the reservoir R when ϕ is between o and π and injected for $\pi < \phi < 2\pi$. The dependence of the total work W developed by the ac sources with respect to the phase lag ϕ is is also plotted in Fig. 8.4 (red curve) using the same parameters as for the heat current. We notice that W is finite in the whole range of values of ϕ, behaving like a cosine function with a vertical offset, hence, it is non-vanishing in any case.

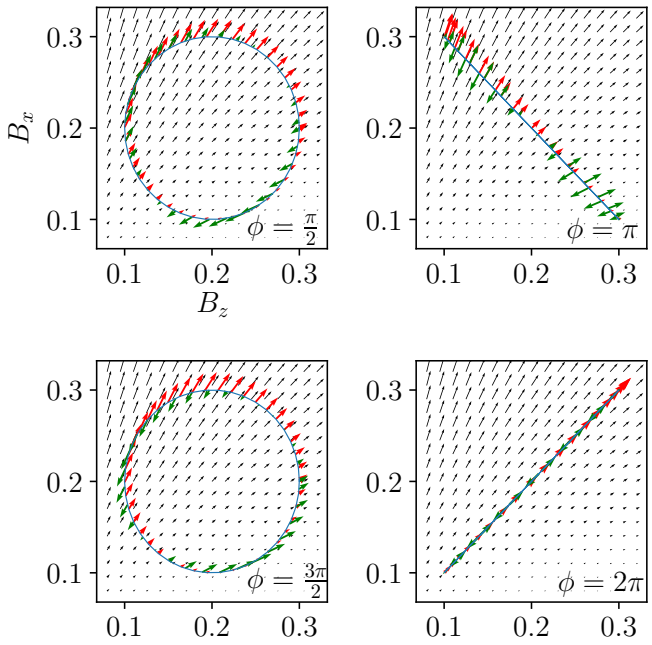

Figure 8.3: Vectors $\vec{A}^A$ and $\tilde{\vec{A}}^S$. Black and red arrows represent the vector $\vec{A}^A_3(\vec{B}) \equiv \left(\Lambda^A_{3,1}(\vec{B}), \Lambda^A_{3,2}(\vec{B})\right)$ in the parameter space, while the green arrows represent the vector $\tilde{\vec{A}}^S$ defined in Eq. (8.20). The blue line is the closed path corresponding to the driving protocol in Eq. (8.31) with $B_{x,0} = B_{z,0} = 0.2k_BT$, $B_{x,1} = B_{z,1} = 0.1k_BT$. The other parameters are $\pi K_L = \pi K_R = 0.2$ and $\epsilon_C = 100k_BT$ and define the spectral properties of the bosonic bath as indicated in Eq. (8.37).

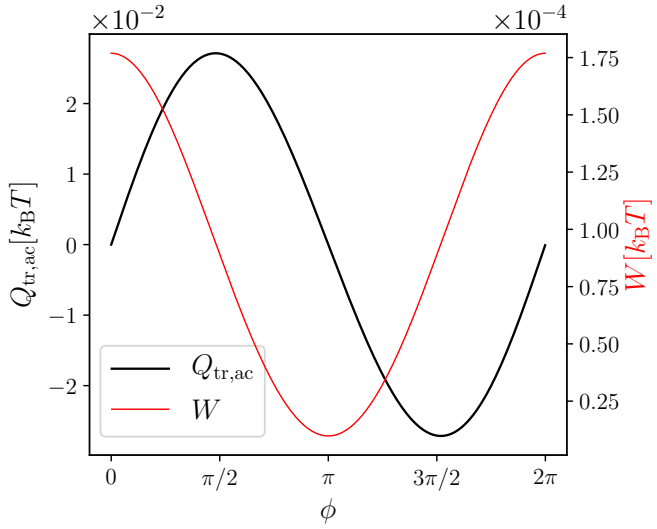

Figure 8.4: Adiabatically pumped heat Q_{ac} and total work W versus the phase lag ϕ in the weak pumping limit for $\Delta T = 0$. Same parameters as in Fig. 8.3.

In what follows, we show some results for the strong pumping regime corresponding to larger amplitudes of $B_{x,1}$ and $B_{z,1}$. In the top panel of Fig. 8.5, we plot the heat pumped and the work performed in a period by the ac source as functions of the phase lag ϕ. As in the case of weak pumping

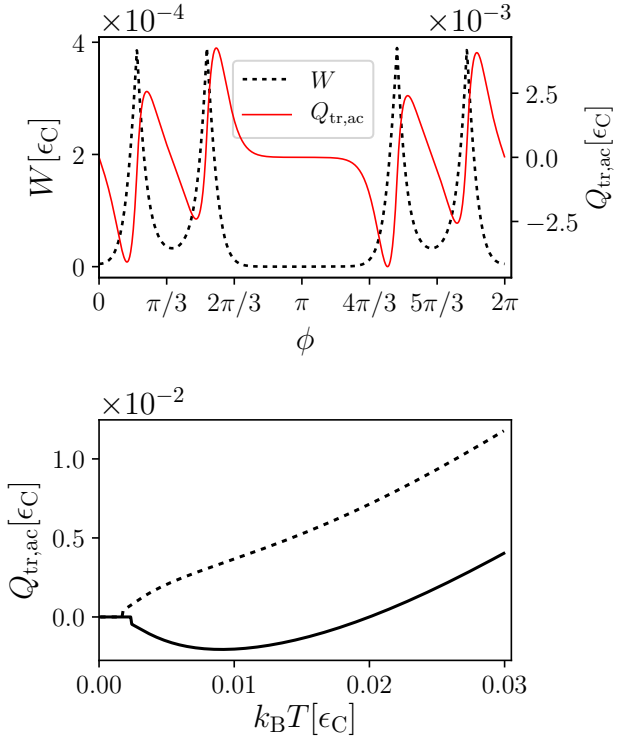

Figure 8.5: Top panel: Pumped heat and work versus the phase difference between adiabatically-driven system parameters for $k_B T = 0.01\epsilon_C$. Bottom panel: normalized pumped heat currents flowing in the left and right lead for $\phi = \pi/2$. We have used the following parameters: $\pi K_L = \pi K_R = 1/5$, $B_{z,0} = 0.06\epsilon_C$ ($B_{z,0} = 0.04\epsilon_C$ for the dashed lines in the bottom panel), $B_{x,0} = 0.03\epsilon_C$, $B_{x,1} = B_{z,1} = 0.07\epsilon_C$, and $\Delta T = 0$.

previously analyzed, the pumped heat as well as the work performed by the ac sources are equal to zero at $\phi = 0$ and π, since the contour has no area (see Fig. 8.3). For other parameters, it is difficult to make a simple argument to explain in which direction is the heat pumped. In fact, we see that $Q_{\text{tr,ac}}$ changes sign many times between $\phi = 0$ and $\phi = 2\pi$, whereas W shows multiple positive peaks. In the bottom panel of Fig. 8.5 we plot the pumped heat in the absence of thermal bias as a function of temperature. For a suitable choice of parameters (relative to the solid curves), the direction of the flow of adiabatic heat can be reversed just by increasing the temperature of the reservoirs. In the top panel of Fig. 8.6 we plot the variation of the heat pumped and the work performed by the ac source, namely $Q_{\text{tr,ac}}$ and W, as a function of the temperature T. We note that W is always positive, as expected, and is non monotonous (displaying a maximum). $Q_{\text{tr,ac}}$ are the same data as in Fig. 8.5 bottom, but plotted in a larger range of temperatures. $Q_{\text{tr,ac}}$ is non monotonous too and changes sign, going from negative values for small T to positive values at around $k_B T = 0.02\epsilon_C$. The inset of the top panel of Fig. 8.6 shows the efficiency $\eta^{(\text{pump})}$, defined in Eq. (8.25), of the system operated as a heat pump as a function of T. The non-monotonic behavior simply reflects the fact that, in the strong pumping regime, the heat currents change sign at around $k_B T = 0.02\epsilon_C$, as shown in Fig. 8.5.

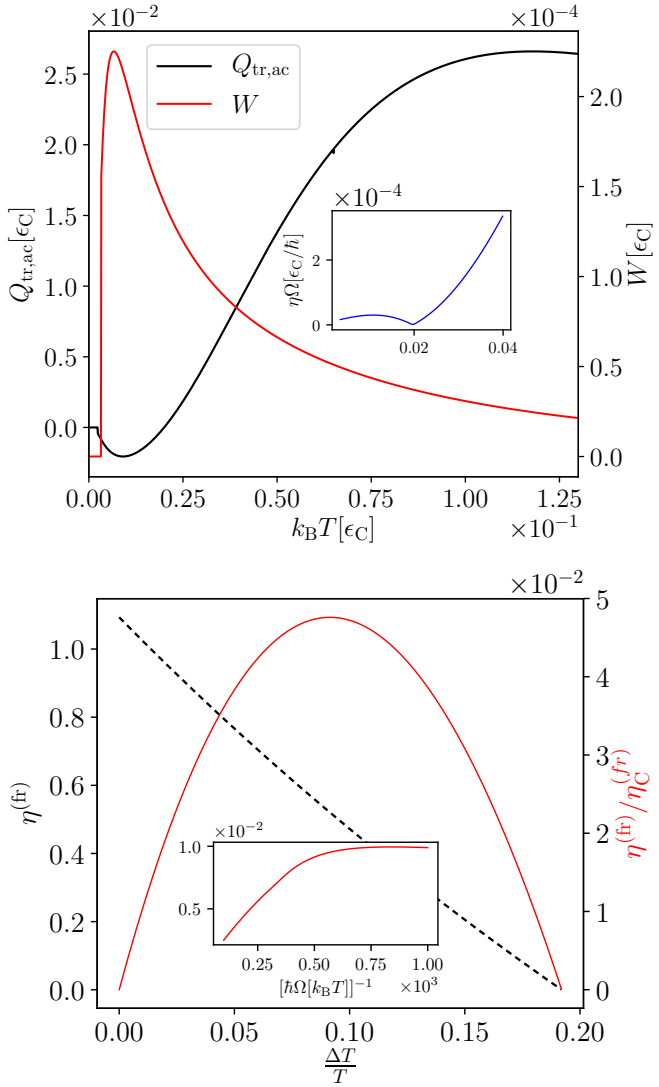

Figure 8.6: In the top panel: pumped heat and work versus reference temperature T. Inset: efficiency of a heat pump for $\Delta T = 0$ as a function of $k_B T$. Same parameters as in Fig. 8.5 for the solid curves. In the bottom panel: Coefficient of performance for refrigeration (black dashed curve for absolute value and red curve for normalized to the Carnot value) versus ΔT, for $\hbar\Omega = k_B T/100$ and versus Ω (in the inset), for $\Delta T = T/500$. We use the following parameters: $\pi K_L = \pi K_R = 0.2$, $B_{z,1} = 10 k_B T$, $B_{x,0} = 20 k_B T$, $B_{x,1} = 30 k_B T$, $B_{z,0} = 7 k_B T$, $\epsilon_C = 120 k_B T$, $\phi = \pi/2$.

Finally, in the bottom panel of Fig. 8.6 we assess the performance of the driven q-bit as a refrigerator which removes heat from the cold reservoir (R) even in the presence of a positive thermal bias ΔT, i. e. for $T_R < T_L$. Given this temperature bias, we focus on a protocol with $\phi = \pi/2$ and the same driving parameters as in Fig. 8.4, in which case, we already know from the analysis of this figure, that heat is pumped from the coldest reservoir and the heat current at zero bias is maximum.

We plot the COP $\eta^{(\mathrm{fr})}$ as a black dashed curve, defined in Eq. (8.24), and the normalized COP $\eta^{(\mathrm{fr})}/\eta_C^{(\mathrm{fr})}$ (red curve) as functions of ΔT, where $\eta_C^{(\mathrm{fr})} = T/\Delta T$ is the Carnot COP. Starting from $\Delta T = 0$, where $\eta^{(\mathrm{fr})}$ is roughly

equal to 1.1, the plot shows that $\eta^{(\mathrm{fr})}$ monotonously decreases with ΔT. This behavior can be understood by recalling that the refrigeration mode results from a competition between the heat induced by the temperature difference and the pumped heat against the thermal bias. In fact, Q_{tr} is made up of two components: i) the component $Q_{\Delta T} = 2\pi J^{(h),f}/\Omega$, which is the heat current flowing from the hot to the cold reservoir during one period, therefore entering the reservoir R ($Q_{\Delta T} > 0$). This component increases linearly with ΔT; ii) $Q_{\mathrm{tr,ac}}$, which is the pumped heat current extracted from the cold reservoir R ($Q_{\mathrm{tr,ac}} < 0$), which is independent of ΔT. Therefore Q_{tr} remains negative as long as $Q_{\Delta T}$ is not large enough to compensate $Q_{\mathrm{tr,ac}}$. This occurs at $\Delta T \simeq 0.19\ T$, where the total transported heat Q_{tr} vanishes, i. e. the thermal machine is no longer a refrigerator (a further increase of ΔT leads to a sign reversal of the heat current).

On the other hand, the ratio $\eta^{(\mathrm{fr})}/\eta_{\mathrm{C}}^{(\mathrm{fr})}$ (red curve) is bell-shaped, since this ratio becomes $\propto \Delta T$. In the inset of the bottom panel of Fig. 8.6, we plot the normalized COP as a function of the inverse of the driving frequency Ω. Since $Q_{\Delta T} \propto \Omega^{-1}$, increasing the frequency – within the adiabatic regime – favors the pumping component Q_{ac} relative to $Q_{\Delta T}$. Notice, however, that by increasing the frequency the dissipative component represented by $\tilde{\vec{A}}$ in Eq. (8.22) becomes more detrimental to the efficiency. There is, thus, a compromise between the two effects and an optimal frequency of operation.

8.3.2 *Driven quantum dot*

In this case, the configuration consists of a central quantum dot driven by a time-dependent magnetic field and coupled to electron reservoirs with different polarizations. For the quantum dot the Hamiltonian H_S reads

$$H_S(t) = \Psi_d^\dagger \left[V_g\, \hat{\sigma}_0 - \vec{B}(t) \cdot \hat{\vec{\sigma}} \right] \Psi_d, \tag{8.57}$$

where $\Psi_d^\dagger = (d_\uparrow^\dagger, d_\downarrow^\dagger)$ is a spinor related to the spin degrees of freedom of the electron in the quantum dot, while $d_\sigma^\dagger$ and d_σ are respectively the creation and annihilation fermionic operators for these particles. The quantum dot contains two levels as a consequence of the Zeeman splitting introduced by the magnetic field. $\hat{\vec{\sigma}} = (\hat{\sigma}_x, \hat{\sigma}_y, \hat{\sigma}_z)$ is composed of the 2×2 Pauli matrices and $\hat{\sigma}_0$ is the identity, while $\vec{B}(t) = (B_x(t), B_y(t), B_z(t))$ is the external time-periodic magnetic field and V_g is a gate voltage, which rigidly shifts the energies of the two levels.

The reservoirs are represented by systems of non-interacting fermions. The electrons in the α reservoir are spin-polarized along the magnetization $\vec{m}_\alpha$. The Hamiltonian H_α which describes the reservoir reads

$$H_\alpha = \sum_{k\alpha} \Psi_{k\alpha}^\dagger \left[\varepsilon_{k\alpha} - \vec{m}_\alpha \cdot \hat{\vec{\sigma}} \right] \Psi_{k\alpha}, \quad \alpha = L, R, \tag{8.58}$$

where $\Psi_{k\alpha}^\dagger = \left(c_{k\alpha,\uparrow}^\dagger, c_{k\alpha,\downarrow}^\dagger \right)$ are spinors composed by the fermionic creation/annihilation operators $c_{k\alpha,\sigma}^\dagger$ and $c_{k\alpha,\sigma}$. We assume that both reservoirs have chemical potential $\mu_L = \mu_R = 0$.

The coupling between the quantum dot and the reservoirs is represented by

$$\mathcal{H}_{c,\alpha} = \sum_{k\alpha,\sigma=\uparrow,\downarrow} V_{k\alpha,\sigma} \left(c_{k\alpha,\sigma}^\dagger d_\sigma + d_\sigma^\dagger c_{k\alpha,\sigma} \right). \tag{8.59}$$

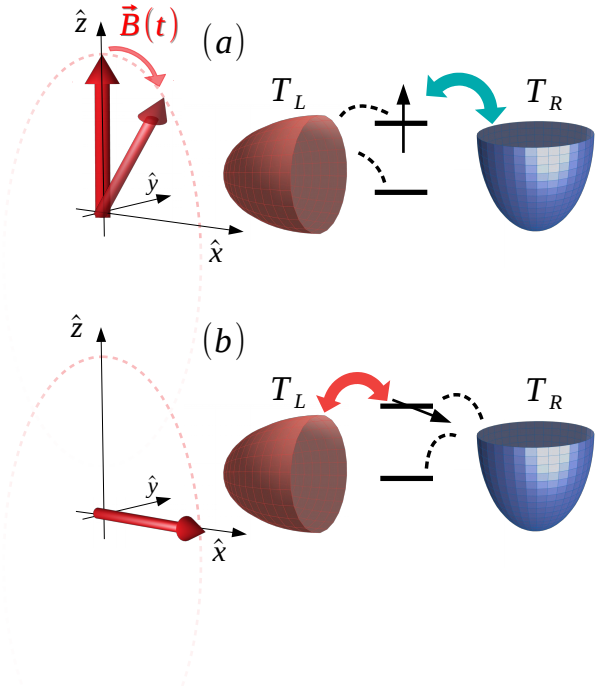

Figure 8.7: Illustration of the quantum dot driven by a magnetic field and connected to electron reservoirs with different polarizations, represented by different orientations of the paraboloids. The hybridization strength is modified according to the magnetic field's pointing direction. In (a) the electron hopping between the quantum dot and the right (z-polarized) reservoir is favored, as is denoted by the thick arrow. In (b) the pointing direction of the magnetic field has changed to x and now the quantum dot is stronger coupled to the left reservoir.

In order to solve the problem, it is convenient to change the basis of H_α to the one where the quantization axis for the spin coincides with the direction of $\vec{m}_\alpha$. This is accomplished by the transformation $\left(c^\dagger_{k\alpha,\uparrow}, c^\dagger_{k\alpha,\downarrow}\right) = \hat{U}^\alpha \left(c^\dagger_{k\alpha,+}, c^\dagger_{k\alpha,-}\right)$. In the new basis the Hamiltonians for the reservoirs and the couplings read

$$\mathcal{H}_\alpha = \sum_{k\alpha,s=\pm} c^\dagger_{k\alpha,s}\varepsilon_{k\alpha,s}c_{k\alpha,s}, \quad \alpha = L,R, \tag{8.60}$$

and

$$\mathcal{H}_{c,\alpha} = \sum_{k\alpha,s=\pm,\sigma=\uparrow,\downarrow} v_{k_\alpha s,\sigma}\left(c^\dagger_{k\alpha,s}d_\sigma + H.c.\right), \tag{8.61}$$

with $v_{k_\alpha s,\sigma} = U^\alpha_{s,\sigma}V_{k\alpha,\sigma}$.

As discussed in Section 8.1.2, in order to have a non-vanishing pumping component we need to break spatial symmetry. We achieve this by considering different polarizations in the reservoirs. For concreteness, we consider the L reservoir polarized along the positive x, and the R one polarized along the positive z direction. An illustration of the whole setup is sketched in Fig. 8.7.

This device bears resemblance to the driven q-bit discussed in Section 8.3.1. In fact, only the electrons with spins $z,\uparrow$ ($x,\uparrow$) can tunnel between the quantum dot and the R (L) reservoir. Therefore, when the magnetic field polarizes the quantum dot along the positive x direction, the tunneling of

the electrons between the quantum dot and the L reservoir is optimal, while the tunnel between the dot and the R reservoir is optimal when the electron in the dot is polarized along the positive z direction. The main difference between the present setup and the q-bit studied in Section 8.3.1 is the nature of the reservoirs, which is fermionic in the present case, while it is bosonic in the previous one. This difference is crucial from the technical point of view, because in the case of the quantum dot we will be able to solve the problem for arbitrary coupling between the driven system and the reservoirs. In addition, the quantum dot has a gate voltage, which moves its energy levels upwards or downwards in energy, thus tuning different parts of the spectrum of the quantum dot into the relevant transport window – $\sim k_B T$– around the chemical potential of the reservoirs. This ingredient can be used to improve the performance, as we will discuss in Section 8.3.2.2. Besides these differences, we expect the operation to be similar in both cases, at least within the regime where the coupling between the driven system and the reservoirs is very weak.

The heat-engine operational mode in the present case could be practically realized by implementing the time-dependent magnetic field by means of a rotating classical magnetic moment. The dynamics of the latter realizes the load of the heat engine. In such a case, a pumped heat $Q_{\mathrm{tr,ac}}$ flowing in the direction of the heat current induced by the thermal bias, will generate a torque and exert work on the magnetic moment, akin to the spin torque induced by an electrical bias [337, 338, 339, 320].

We will consider the same driving protocol as in the previous example, which is defined in Eq. (8.31), without focusing on the detailed mechanism generating the magnetic field. As in the previous example, we will show results for the heat pump and refrigerator modes.

8.3.2.1 *Green's function approach*

We can solve the problem exactly for arbitrary strength of the coupling between the quantum dot and the reservoirs by recourse to Green's functions. We will use the equilibrium finite-temperature formalism to evaluate the frozen susceptibilities and compute the response functions from Eq. (C.15). This problem could be also exactly solved by recourse to the non-equilibrium Schwinger - Keldysh formalism in the Floquet representation and afterwards consider the expansion in small $\hbar\Omega$ and ΔT as in Refs. [340, 314] arriving at the same results as the ones we present here. We briefly summarize the results below and show some details on the calculations in Appendix G,

$$\begin{aligned}
\Lambda^{A}_{3,\ell}(\vec{B}) &= -\frac{1}{h}\int d\varepsilon \frac{df(\varepsilon)}{d\varepsilon}\varepsilon \mathrm{Tr}\left[\hat{\Gamma}_R\hat{\rho}(\varepsilon)\hat{\sigma}_\ell\hat{\rho}(\varepsilon)\right],\ \ell=1,2\\
\Lambda^{S}_{\ell,\ell'}(\vec{B}) &= -\frac{1}{h}\int d\varepsilon \frac{df(\varepsilon)}{d\varepsilon} \mathrm{Tr}\left[\hat{\sigma}_\ell\hat{\rho}(\varepsilon)\hat{\sigma}_{\ell'}\hat{\rho}(\varepsilon)\right],\ \ell,\ell'=1,2\\
\Lambda^{S}_{3,3}(\vec{B}) &= -\frac{1}{h}\int d\varepsilon \frac{df(\varepsilon)}{d\varepsilon}\varepsilon^2 \mathrm{Tr}\left[\hat{\Gamma}_R\hat{G}_t(\varepsilon)\hat{\Gamma}_L\hat{G}_t^{\dagger}(\varepsilon)\right],
\end{aligned} \tag{8.62}$$

where $f(\varepsilon)=1/\left(e^{\varepsilon/(k_BT)}+1\right)$ is the Fermi-Dirac distribution function. We have also introduced the hybridization matrix $\hat{\Gamma}_\alpha$, with elements

$$(\hat{\Gamma}_\alpha)_{\sigma,\sigma'} = 2\pi\sum_{k\alpha,s=\pm} U^{\alpha}_{\sigma,s}U^{\alpha}_{\sigma',s}|V_{k\alpha}|^2\delta(\varepsilon-\varepsilon_{k\alpha,s}). \tag{8.63}$$

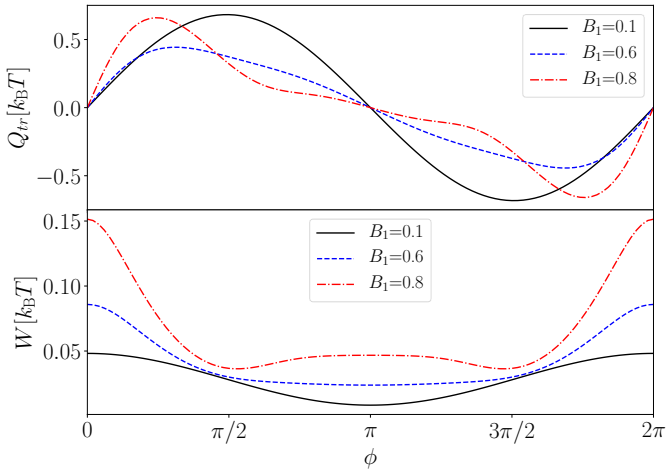

Figure 8.8: Pumped heat $Q_{\text{tr,ac}} = Q_{\text{tr}}$ (upper panel) and work done by the ac sources W (lower panel) for $\Delta T = 0$ as functions of the phase difference in the protocol defined by $B_x(t) = B_{x,0} + B_{x,1}\cos(\Omega t + \phi)$, $B_z(t) = B_{z,0} + B_{z,1}\cos(\Omega t)$ with $B_{x,0} = B_{z,0} = 0.4k_BT$ and $B_{x,1} = B_{z,1} = B_1 k_B T$. $\Gamma_L = \Gamma_R = 0.4k_BT$ and $\hbar\Omega = k_BT/800$. The plot with $B_1 = 0.1$ is multiplied by a factor 20 in order to be shown in the same scale.

We consider L (R) reservoirs fully polarized with spins along the positive x (z) directions and a constant density of states. Thus, $\Gamma_\alpha \simeq \sum_{k\alpha} |V_{k\alpha}|^2 \delta(\varepsilon - \varepsilon_{k\alpha,+})$ and $\hat{\Gamma}_\alpha \simeq \Gamma_\alpha \hat{\tau}_\alpha$, with

$$\hat{\tau}_L \equiv \frac{1}{2}(\hat{\sigma}_x + \hat{\sigma}_0)\,, \quad \hat{\tau}_R \equiv \frac{1}{2}(\hat{\sigma}_z + \hat{\sigma}_0)\,. \tag{8.64}$$

The local density of states is described by the matrix

$$\hat{\rho}(\varepsilon) = -2\text{Im}[\hat{G}_t(\vec{B},\varepsilon)] = \hat{G}_t(\vec{B},\varepsilon)\hat{\Gamma}\left[\hat{G}_t(\vec{B},\varepsilon)\right]^\dagger, \tag{8.65}$$

which depends on the frozen Green's function

$$\hat{G}_t(\vec{B},\varepsilon) = \left(\varepsilon - \vec{B}(t)\cdot\hat{\vec{\sigma}} + i\hat{\Gamma}/2\right)^{-1}, \tag{8.66}$$

with $\hat{\Gamma} = \hat{\Gamma}_L + \hat{\Gamma}_R$.

In Eqs. (8.62) we have highlighted the symmetric or antisymmetric nature of the components in each case. The fact that the components $\Lambda_{3,\ell}(\vec{B})$ are purely antisymmetric while $\Lambda_{\ell,\ell'}(\vec{B})$ are purely symmetric is a consequence of Onsager relations in combination with symmetry properties of the setup. These properties can be directly verified from the explicit calculations of Appendix G. The last component $\Lambda^S_{3,3}(\vec{B})$ is proportional to the thermal conductance. The symmetry properties of $\Lambda_{\mu,\nu}(\vec{B})$ are the same as in the q-bit example of Section 8.3.1. Thus, the definitions of the vector potentials in the present case are the same as in Eq. (8.55).

8.3.2.2 *Results*

We carry out a similar analysis to the one for the q-bit example given in Section 8.3.1. We consider the same two-parameter driving protocol as before, with $\vec{B}(t) = (B_x(t), 0, B_z(t))$ given by Eq. (8.31).

As mentioned before, for the case of $V_g = 0$ and weak coupling to the reservoirs, we expect a similar behavior to the case of the qubit. In Figure

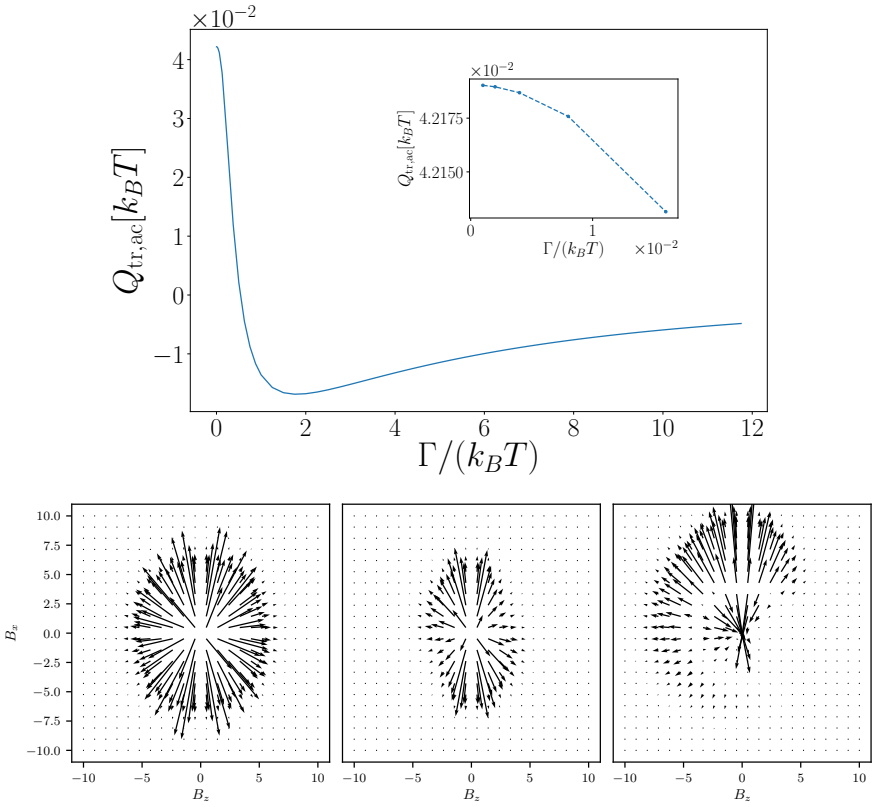

Figure 8.9: Pumped heat $Q_{\mathrm{tr,ac}} = Q_{\mathrm{tr}}$ for the quantum dot with the same parameters as the q-bit operating with the protocol of Eq. (8.31) shown in Fig. 8.4 with $\phi = \pi/2$ (upper panel). In the lower panel: vector fields $\vec{A}_3^A(\vec{B})$ for a driving protocol with $\vec{B}(t) = (B_x(t), 0, B_z(t))$, corresponding to a quantum dot coupled to reservoirs with different polarizations. R (L) reservoirs is polarized along positive z (x) direction. Left panel corresponds to $\Gamma_L = \Gamma_R$ and $V_g = 0$, middle correspond to $\Gamma_L = 0.1\Gamma_R$ and $V_g = 0$, while right panel corresponds to $\Gamma_L = 0.1\Gamma_R$ and $V_g = 2\Gamma_R$. The temperature of the reservoirs is $k_BT = 0.5\Gamma_R$.

8.8 we present the pumped heat $Q_{\mathrm{tr,ac}}(\phi)$ and the work developed by the ac sources W for $\Delta T = 0$, as function of the driving phase difference ϕ between the two ac components of the magnetic field. As in the qubit case analyzed in Section 8.3.1, for small amplitudes of the driving, $Q_{\mathrm{tr,ac}}$ is proportional to the area enclosed by the contour defined by the protocol. For this reason, the pumped heat behaves as $\propto \sin(\phi)$ and the generated work as $\propto \cos(\phi)$ plus a constant. These functions are the same as in the case of the driven qubit shown in Fig. 8.4. For larger values of the driving amplitude the pumped heat departs from this behavior. However, $Q_{\mathrm{tr,ac}}(\phi)$ vanishes for $\phi = 0, \pi$ for any value of $B_{x,1} = B_{z,1}$.

In the top panel of Fig. 8.9 we further explore the comparison between the driven quantum dot and the driven q-bit. In particular, we show the behavior of the pumped heat as a function of the coupling to the reservoirs, assuming $\Gamma_L = \Gamma_R = \Gamma$ and the same parameters and driving protocol of Fig. 8.4. We can verify that as the latter parameter approaches the limit $\Gamma \to 0$, the value of the pumped heat of the quantum dot approaches the one of the qubit case shown in Fig. 8.4. There is some quantitative difference, which can be traced back to the fact that the type of couplings are not exactly the same (notice the

matrix elements entering the couplings of the quantum dot are those of Eq. (8.64), while in the qubit we have considered $\hat{\sigma}_{x,z}$). We see that the strength of the coupling has a significant impact on the behavior of the pumped heat. For the present parameters, we observe an inversion in the direction of the pumped heat as the coupling increases and overcomes $\Gamma \sim |\vec{B}|$, at which the width of the levels of the quantum dot becomes comparable to the energy difference between them.

We now focus on the properties in the operation of the quantum-dot machine that are different from the weakly coupled driven q-bit. To this end, we further analyze the structure of the vector potentials $\vec{A}^{S/A}_{\mu}(\vec{B})$ and $\tilde{\vec{A}}^{S/A}(\vec{B})$ in Eq. (8.55) with the tensor $\Lambda_{\mu,\nu}(\vec{B})$ of Eq. (8.62). The vector map for $\vec{A}^{A}_{3}(\vec{B})$ in the parameter space for a given temperature T is shown in the bottom panel of Fig. 8.9. This representation is useful to visualize the symmetries of the setup and to select the driving protocol that maximizes the contour integral $\oint \vec{A}^{A}_{3}(\vec{B}) \cdot d\vec{B}$. In the left panel the quantum dot is contacted with the same strength to both reservoirs ($\Gamma_L = \Gamma_R$), L being polarized along positive x and R along positive z direction, as indicated in the sketch of Fig. 8.7. In the middle panel, the contact is stronger to L than to R ($\Gamma_R = 0.1\Gamma_L$). Consequently, we can visualize a higher intensity of the field $\vec{A}^{A}_{3}$ along the B_x than along the B_z direction. Both left and middle plots have $V_g = 0$, in which case the Hamiltonian of Eq. (8.57) is symmetric under the simultaneous transformations $\Psi^{\dagger}_{d} \to \Psi_{d}$ and $\vec{B} \to -\vec{B}$. The first one is a particle-hole transformation, under which the heat current changes the sign. Consequently, the field maps of the bottom panel of Fig. 8.9 present the symmetry $\vec{A}^{A}_{3}(\vec{B}) = -\vec{A}^{A}_{3}(-\vec{B})$. In the right panel, we can visualize that the breaking of the particle-hole symmetry by a gate voltage introduces a strong asymmetry in the vector field.

With the picture of the bottom panel of Fig. 8.9 in mind, we can readily design a closed trajectory that optimizes pumping. The latter corresponds to a path that goes parallel to the vector field within the region where its intensity is high, and closes antiparallel to the vector field in a very low-intensity region. An example of such a trajectory is shown in the top panel of Fig. 8.10. The corresponding vectors $\tilde{\vec{A}}^{S}(\vec{B})$ along the trajectory are also shown in cyan. Trajectories leading to high efficiencies of the machine would have as small dissipation as possible, in addition to high values of heat pumping. While the optimization of the pumping can be easily achieved by recourse to the vector field representation $\vec{A}^{A}_{3}(\vec{B})$, it is not easy to optimize a trajectory to decrease the integral over $\tilde{\vec{A}}^{S}(\vec{B})$. However, we know that this quantity can be reduced by decreasing the pumping frequency Ω.

In the bottom panel of Fig. 8.10 we illustrate the behavior of the COP of the driven quantum dot operating as a refrigerator. Overall, this quantity follows a similar behavior as a function of $\Delta T/T$ and Ω as the one of the qubit (see Fig. 8.6). Therefore, most of the comments and remarks presented in the analysis of Fig. 8.6 apply also here. However, it is several orders of magnitude higher in the present case, achieving values as large as 14 % $\eta^{\rm fr}_{C}$. The key for this improvement is the selection of an appropriate pumping protocol, taking advantage of the extra features introduced by the existence of the gate voltage V_g in the present problem.

We close this section by analyzing the geometric component of the first-order adiabatic reaction force defined in Eq. (8.18). In the present problem,

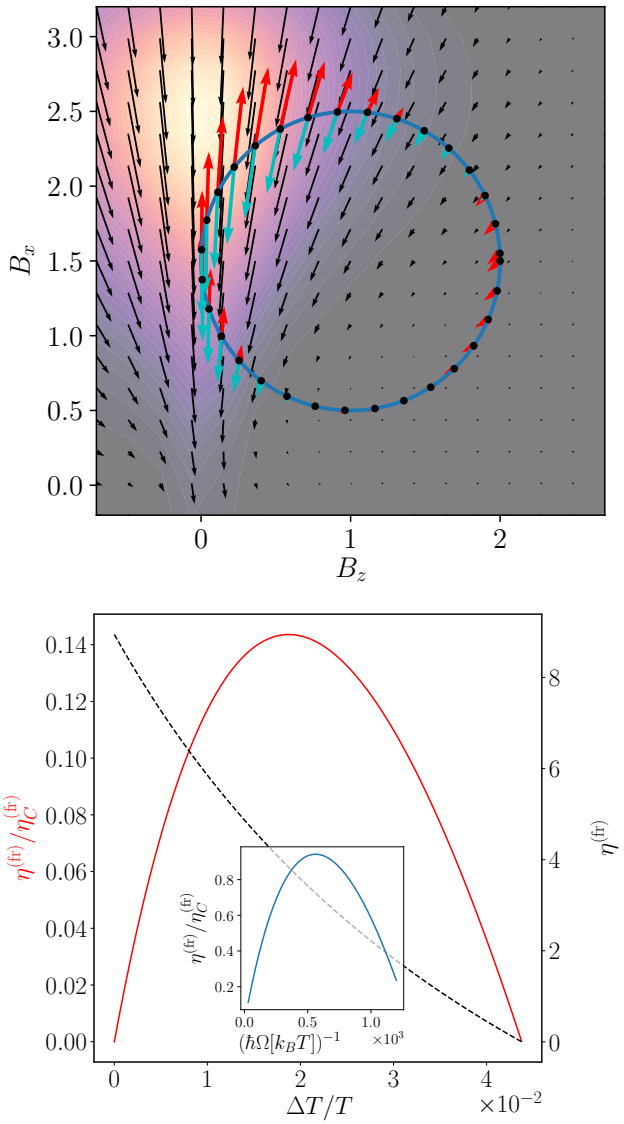

Figure 8.10: Top panel : Vector fields $\vec{A}_3^A(\vec{B})$ (cyan) and $\tilde{\vec{A}}^S(\vec{B})$ (red) over a closed path (solid blue curve) for the configuration shown in the lower panel of Fig. 8.9 ($\Gamma_R = 0.1\Gamma_L$). The driving protocol defining the path is $B_x(t) = B_{x,0} + B_{x,1}\cos(\Omega t + \phi)$, $B_z(t) = B_{z,0} + B_{z,1}\cos(\Omega t)$ with $B_{x,0} = 1.5\Gamma_R$, $B_{z,0} = \Gamma_R$, $B_{x,1} = B_{z,1} = \Gamma_R$, $\phi = \pi/2$. The black arrows represent $\vec{A}_3(\vec{B})$ outside the defined protocol. Bottom panel : Coefficient of performance for refrigeration (absolute in dashed black and normalized to the Carnot value in red) versus ΔT for the protocol of Fig. 8.10 for $\hbar\Omega = \Gamma_R/200$ Inset: Normalized coefficient of performance for refrigeration as a function of $\hbar\Omega$ for $\Delta T = T/150$.

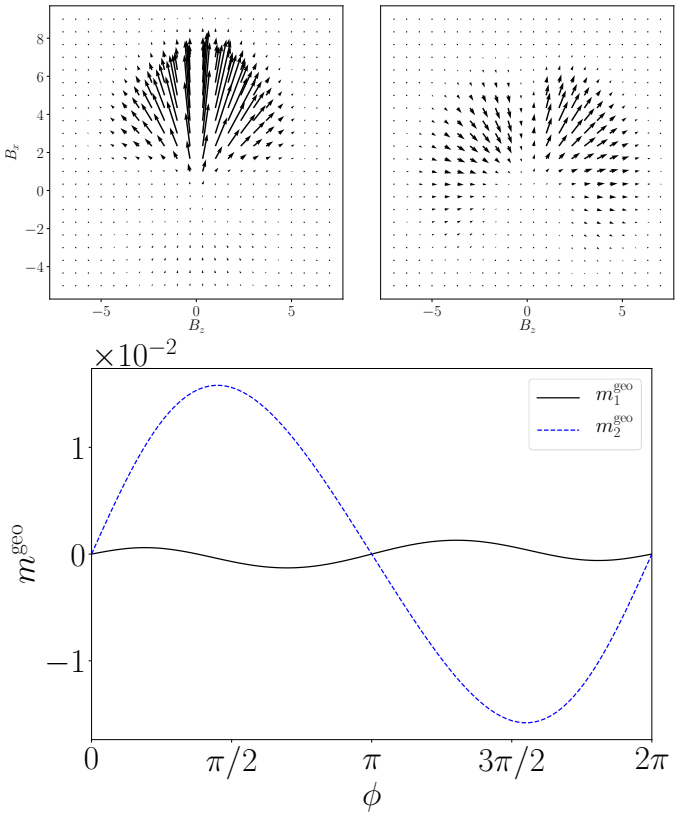

Figure 8.11: Vector fields $\vec{A}_1^S(\vec{B})$ (top panel) and $\vec{A}_2^S(\vec{B})$ (middle panel) following Eqs. (8.55) and (8.62), for the parameters of the rightmost panel of the bottom panel of Fig. 8.9. Right panel : Components of the geometric magnetization $m_{1,2}^{\rm geo}$, defined in Eq. (8.67) as functions of the phase-lag ϕ corresponding to paths of the form $B_x(t) = B_{x,0} + B_{x,1}\cos(\Omega t + \phi)$, $B_z(t) = B_{z,0} + B_{z,1}\cos(\Omega t)$ with $B_{x,0} = 1.5\Gamma_R$, $B_{z,0} = \Gamma_R$, $B_{x,1} = B_{z,1} = \Gamma_R$, on the vector fields of the top panel.

the latter coincides with the magnetic moment of the quantum dot. For $\Delta T = 0$, the magnetic moment of the quantum dot is given by

$$\begin{aligned} m_\ell &= \frac{\Omega}{2\pi}\int_0^{2\pi/\Omega} dt \langle \Psi_d^\dagger \hat{\sigma}_\ell \Psi_d \rangle(t) = m_\ell^{\rm BO} + m_\ell^{\rm geo}, \\ m_\ell^{\rm geo} &= \frac{\Omega}{2\pi}\oint \vec{A}_\ell^S(\vec{B})\cdot d\vec{B}, \end{aligned} \tag{8.67}$$

with $\hat{\sigma}_{x,y}$ for $\ell \equiv 1, 2$, respectively. Here, $m_\ell^{\rm BO}$ is the average over one period of the the instantaneous magnetization corresponding to the equilibrium frozen Hamiltonian, while $m_\ell^{\rm geo}$ is the geometric component, corresponding to the first-order adiabatic reaction force of Eq. (8.18). The vectors $\vec{A}_\ell^S(\vec{B})$ are calculated from Eq. (8.62) as defined in Eq. (8.55). Interestingly, the symmetric component of the thermal geometric tensor, which defines the dissipation, is directly related in the present problem to a local physical quantity, which is the quantum dot geometric magnetization [299]. The latter is experimentally accessible. In fact, notice that the component $m_\ell^{\rm BO}$ does not explicitly depend on the driving frequency, while the second term has an explicit linear dependence on Ω. Therefore, in a concrete experimental measurement of the quantum dot magnetization, both components should be distinguishable from one another.

The associated vector fields $\vec{A}^S_\ell(\vec{B})$ are shown in the top panel of Fig. 8.11 for configurations with stronger coupling to the L (x-polarized) reservoir than to the R (z-polarized) one and a finite gate voltage V_g, with the same values of the parameters as in the rightmost panel of the bottom panel of Fig. 8.9. In this representation, we can visualize higher intensity of the fields along $B_x, B_z > 0$ relative to $B_x, B_z < 0$, as a consequence of the polarization of the reservoirs along the positive x and z-axis. The amplitudes of $\vec{A}^S_1(\vec{B})$, shown in the left panel, are larger than those of $\vec{A}^S_2(\vec{B})$, shown in the right panel, due to the larger coupling to the reservoir polarized along x. The result of calculating the integrals over closed trajectories with different phase lags ϕ between the components B_x and B_z is shown in the bottom panel of Fig. 8.11. As in the case of the pumped heat, both components of the magnetization vanish at $\phi = 0, \pi$.

8.4 SUMMARY

We have presented a general description of the geometrical properties of quantum thermal machines under the effect of adiabatic periodic driving and a small thermal bias due to the contact to reservoirs at different temperatures. The cyclic time-dependence is introduced via classical variables, varying slowly in time, that enter the quantum Hamiltonian of the system. We show that the operation of the thermal machine, consisting of a few-level quantum system, is fully characterized by the thermal tensor $\Lambda_{\mu,\nu}$ defined in Section 8.2.1.

The formal derivation of this tensor is obtained by means of the adiabatic linear response theory complemented by Luttinger's representation of the thermal bias. The symmetric component of $\Lambda_{\mu,\nu}$ characterizes the total rate of entropy production, thus controlling the dissipation of all the sources involved in the operation of the machine. When the system is driven by two or more periodically-varying parameters, it is possible to obtain pumping of heat between reservoirs, even in the absence of a temperature bias. The heat pumped, the work performed on the system, and the dissipated power can be described by means of vector fields defined through the thermal tensor. In particular, the pumped heat by the driving and the work performed can be expressed in a purely geometric form as line integrals of those vector fields over the closed paths which represent the driving cycles in the parameter space. In the presence of a thermal bias, these two quantities allow the characterization of a thermal machine which realizes heat-work conversion.

We have illustrated these ideas using two paradigmatic quantum systems coupled to two thermal reservoirs. The first example consists of a qubit, whose energy levels and inter-level tunneling depend harmonically on time, attached to two bosonic reservoirs kept at different temperatures. The second example is a quantum dot coupled to electronic reservoirs and driven by a harmonically time-dependent and rotating magnetic field. The two examples are solved with different techniques, while two driving parameters are assumed. In the case of the qubit we rely on the master equation approach, valid for weak coupling to the reservoirs, while in the case of the quantum dot we solve the problem exactly for arbitrary coupling by recourse to linear response and Green's function formalisms. The two problems are very similar qualitatively and quantitatively when the driven system is weakly coupled to the reservoirs. In the two cases, we have calculated the vector fields responsible for the geometric characterization of the systems as thermal machines. We have computed the heat pumped and the work as functions of:

i) phase lag between the two driving parameters, ii) the reference temperature, and iii) the coupling between system and reservoir (for the second example). The efficiency of the thermal machines has been analyzed in terms of the temperature difference between reservoirs, the average temperature, and the frequency of the driving parameters in both cases. Finally, in the second example, we have shown how the representation of the pumped heat by means of vector fields can be used to identify the cycles that maximize it, thus improving the performance of a thermal machine.

9

QUANTUM COHERENT DYNAMICS OF ADIBATICALLY DRIVEN SYSTEMS

The study of heat transport and heat–work conversion in open quantum systems under the action of slow time-dependent protocols is a subject of active investigation for some time now. Examples are qubits [341, 342, 280, 306, 307, 343], harmonic oscillators [344, 236, 237, 343], and quantum dots [345, 346, 287, 233, 336, 340] under slow cyclic driving, as well as nanomechanical and nanomagnetic degrees of freedom in contact to bosonic or fermionic baths, eventually with a temperature bias.

In the context of open systems the concept "adiabatic dynamics" applies to the evolution where the typical time scale of the dynamics of the frozen Hamiltonian for the full setup, including the driven system along with the contact to the reservoirs and the reservoirs themselves is much faster than the characteristic time for the changes of this Hamiltonian. The type of formal approach used to calculate the relevant observables to describe this dynamics crucially depends on the strength of the coupling between the system and the reservoirs.

A typical framework to analyze the non-equilibrium dynamics in the weak-coupling limit is by means of master equations. A standard approach is the Lindblad formulation [347] which has been used to study the dynamics of different systems in the field of cold atoms, optics, quantum information and condensed matter [348, 349, 350, 351, 352, 353, 280, 306, 342, 290, 354]. The main strategy of this formulation is to employ the equation of motion for the reduced density matrix of the quantum system, with the degrees of freedom of the reservoirs traced away. An alternative route to the derivation of the master equation is to calculate the dynamics of the mean values of the

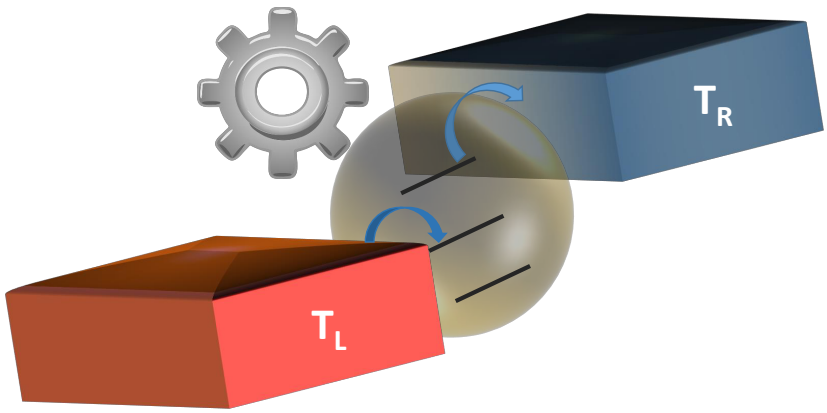

Figure 9.1: A N-level adiabatically driven system in contact with two reservoirs at different temperatures, $T_L = T + \Delta T$ and $T_R = T - \Delta T$.

matrix elements of the density matrix by treating the coupling between the system and the reservoirs in perturbation theory within Schwinger-Keldysh contour, which implies considering a contour that starts at a initial time t_0, evolves forwards and then backwards to t_0. This procedure was introduced in Ref. [355] for a metallic island and in Refs. [345, 346] for a single-level quantum dot in the stationary regime. A different derivation was more recently presented [356] and extended to time-dependent systems [357].

In the opposite limit, when the coupling between the reservoirs and the driven system is strong, a very general and powerful scheme is the non-equilibrium Green's function formalism, which is also based on Schwinger-Keldysh treatment of the time-evolution[358, 9, 359, 360], which enables the treatment of systems with many-body interactions as well as non-interacting systems. A very useful resource in this context is the the analytical continuation properties known as Langreth theorem [15, 361, 4]. For non-interacting systems scattering matrix is the other powerful formalism[318] and there is a one-to-one correspondence to the Green's function formalism[362]. Here, we show how to derive master equations in the adiabatic regime from the non-equilibrium Green's function formalism combined with suitable analytical continuations. As in Refs. [355, 345, 346] we start from the Schwinger-Keldysh treatment of the time evolution, treating the coupling between the system and the reservoir as a perturbation. We extend that derivation to the case of a time-dependent Hamiltonian for the driven system in which the adiabatic expansion is implemented in the evolution along the Keldysh contour.

Concretely, starting from non-equilibrium Green's function formalism, we derive a quantum master equation (which includes both diagonal and off-diagonal components of the density matrix) for an adiabatically-driven N-level system weakly coupled to thermal reservoirs with fixed temperature and chemical potential, see Fig. 9.1. The derived quantum master equation (QME) would be equivalent to the global Redfield master equation in the Lindblad formulation. As illustrations, we will study the steady state and adiabatic dynamics of charge and energy taking eigenstate coherence into account for two specific examples: (1) a driven qutrit system connected to two bosonic reservoirs, and (2) a driven double quantum dot system connected to fermionic reservoirs. We will carefully analyze in these examples the conditions of validity of the description based on the rate equation (RE), where only the diagonal elements of the density matrix are taken into account. In addition, we will study the effect of eigenstate coherence on thermal transport and refrigeration based on adiabatic driving. To further comprehend the significance of eigenstate coherence and adiabatic driving in thermal transport properties of quantum systems, we will study thermal rectification in the two examples mentioned above using QME and RE.

The chapter is organized as follows. In the next section we will present the model for a periodically-driven quantum heat engine. There we shall study the dynamics of density matrix and the currents. In section 9.2, we will perform an adiabatic expansion to obtain full adiabatic master equations as well as charge and energy currents. In order to illustrate the general formulation, in section 9.3 we put forward two different examples: in the first one we shall study a driven qutrit in contact with bosonic reservoirs, and in the second example we shall considfer a driven coupled quantum dot system attached to fermionic reservoirs. In section (9.3.3), we study the individual effect of quantum coherence and adiabatic driving on thermal rectification. Finally, conclusions and perspectives are drawn in Sec. 9.4.

9.1 GENERAL FORMALISM

We present here the derivation of the master equation from non-equilibrium Green's function formalism combined with Langreth theorem.

9.1.1 *Model*

We consider a driven quantum system which depends on time through a set of time dependent parameters $\mathbf{X}(t) = (X_1(t), \ldots, X_N(t))$, described by the Hamiltonian

$$H_{\rm S}(t) \equiv H_{\rm S}(\mathbf{X}(t)). \tag{9.1}$$

In general, the system Hamiltonian contains one or more subsystems with multiple degrees of freedom, expressed in a convenient basis, which expands the Hilbert state. For example, in Section IV we consider a qutrit, characterized by three levels $|s\rangle,\ s = 0, 1, 2$ with time-dependent energies and time dependent transitions between the different levels. We also consider two coupled quantum dots of spinless fermions with time-dependent gate voltages and tunneling elements and an inter-dot Coulomb interaction. In this case, each quantum dot defines a subsystem, and the degrees of freedom of each quantum dot, are determined by the charge. The corresponding states of the basis are four and read $|s\rangle \equiv |0,0\rangle,\ |1,0\rangle,\ |0,1\rangle,\ |1,1\rangle$.

The system is coupled to a set of N_r reservoirs described the Hamiltonian

$$H_{\rm B} = \sum_{\alpha=1}^{N_r} \sum_{k\alpha} \epsilon_{k\alpha} \hat{b}^\dagger_{k\alpha} \hat{b}_{k\alpha}, \tag{9.2}$$

where the operators $\hat{b}^\dagger_{k\alpha}, \hat{b}_{k\alpha}$ may satisfy bosonic or fermionic statistics. For the case of bosons, we focus on bosonic excitations, like phonons or photons. For the case of fermions we focus on electron systems with a finite chemical potential. The contact between the driven system and the baths is given by the Hamiltonian

$$\begin{aligned} H_{\rm C}^{\rm bos} &= \sum_{s,s'} \sum_{k,\alpha} V_{k\alpha} \hat{\pi}^\alpha_{s,s'} \left(\hat{b}^\dagger_{k\alpha} + \hat{b}_{k\alpha} \right), \\ H_{\rm C}^{\rm fer} &= \sum_{s,s'} \sum_{k,\alpha} \left(V_{k\alpha} \hat{b}^\dagger_{k\alpha} \hat{\pi}^\alpha_{s,s'} + H.c. \right), \end{aligned} \tag{9.3}$$

for the case of a bosonic and a fermionic baths, respectively, $V_{k\alpha}$ being the coupling strength between system and reservoir α. The operators $\hat{\pi}^\alpha_{s,s'} = \eta^\alpha_{s,s'} |s\rangle\langle s'|$ are defined on the basis $|s\rangle$ associated to the degrees of freedom of the central system and may be restricted by selection rules and the Pauli principle in the case of fermionic systems. For instance, in the case of the two coupled quantum dots of spinless fermions that we will analyze in Section IV, where each quantum dot is connected to one fermionic reservoir in the form of a tunneling process, these are $\hat{\pi}^{(1)}_{0,1} = \left[\hat{\pi}^{(1)}_{1,1}\right]^\dagger = \eta^{(1)}_{0,1} |0,\ell\rangle\langle 1,\ell|$ for the quantum dot (1) and $\hat{\pi}^{(2)}_{0,1} = \left[\hat{\pi}^{(2)}_{1,1}\right]^\dagger = \eta^{(2)}_{0,1} |\ell,0\rangle\langle \ell,1|$ for the quantum dot (2), with $\ell = 0, 1$.

The Hamiltonian for the system can be diagonalized at any time t by a unitary matrix $\hat{U}(t)$,

$$\tilde{\mathcal{H}}_{\rm S}(t) = \hat{U}(t) \mathcal{H}_{\rm S}(t) \hat{U}^\dagger(t) = \sum_l \varepsilon_l(t) \hat{\rho}_{ll}, \tag{9.4}$$

where $\hat{\rho}_{lj} = |l\rangle\langle j|$. We define $\hat{\pi}_\alpha = \sum_{s,s'} \hat{\pi}^\alpha_{s,s'}$ and we express the contact Hamiltonian in the diagonal basis as follows

$$\tilde{\mathcal{H}}_{\rm C}(t) = \sum_{k,\alpha}\sum_{l,j} V_{k\alpha}\left[\lambda_{\alpha,lj}(t)\hat{b}^\dagger_{k\alpha}\hat{\rho}_{lj} + \overline{\lambda}_{\alpha,lj}(t)\hat{\rho}_{lj}\hat{b}_{k\alpha}\right], \tag{9.5}$$

where, for the case of a bosonic bath,

$$\lambda_{\alpha,lj}(t) = \overline{\lambda}_{\alpha,lj}(t) = \left[\hat{U}(t)\hat{\pi}_\alpha\hat{U}^\dagger(t)\right]_{l,j}, \tag{9.6}$$

while for the case of a fermionic bath we have

$$\begin{aligned}\lambda_{\alpha,lj}(t) &= \left[\hat{U}(t)\hat{\pi}_\alpha\hat{U}^\dagger(t)\right]_{l,j},\\ \overline{\lambda}_{\alpha,lj}(t) &= \left[\hat{U}(t)\hat{\pi}^\dagger_\alpha\hat{U}^\dagger(t)\right]_{l,j}.\end{aligned} \tag{9.7}$$

9.1.2 *Dynamics of the density matrix*

In order to motivate our treatment, let us start by noticing that any observable $\mathcal{O}$, which depends on the degrees of freedom of the central system, can be expressed as follows

$$\mathcal{O}(t) = \sum_{l,j} O_{lj}(t)\hat{\rho}_{lj}, \tag{9.8}$$

where $O_{lj}(t) = \langle l|\mathcal{O}(t)|j\rangle$ are the matrix elements of the operator $\mathcal{O}(t)$ in the eigenstates basis. The expectation value of this observable at a given time t is

$$\langle\mathcal{O}\rangle(t) = {\rm Tr}\left[\hat{\rho}^{\rm tot}(t)\mathcal{O}(t)\right] = \sum_{lj} O_{lj}(t)\rho_{lj}(t), \tag{9.9}$$

where we define the density matrix as

$$\rho_{lj}(t) = {\rm Tr}\left[\hat{\rho}^{\rm tot}(t)\hat{\rho}_{lj}\right]. \tag{9.10}$$

In Eqs. (9.9) and (9.10) $\hat{\rho}^{\rm tot}(t)$ is the state of the full system coupled to the bath, which is described by the Hamiltonian $\mathcal{H}(t) = \tilde{\mathcal{H}}_S(t) + \mathcal{H}_{\rm B} + \tilde{\mathcal{H}}_{\rm C}(t)$. We see that the dynamics of Eq. (9.9) is determined by the evolution of the matrix elements of the operator in the basis of the instantaneous eigenstates of $\mathcal{H}_S(t)$ and the dynamics of the density matrix $\rho_{lj}(t)$. The latter depends on the full Hamiltonian $\mathcal{H}(t)$. Our aim is to derive the equation ruling the dynamics of this density matrix in the limit of weak coupling strength between the N-level system and the baths.

Changing to the Heisenberg representation, the matrix elements of Eq. (9.10) are

$$\rho_{lj}(t) = {\rm Tr}\left[\hat{\rho}_0\,\hat{\rho}^{\mathcal{H}}_{lj}(t)\right], \tag{9.11}$$

with $\hat{\rho}^{\rm tot}(t) = \mathcal{U}(t,t_0)\ \hat{\rho}_0\ \mathcal{U}^\dagger(t,t_0)$, $\hat{\rho}_0$ being the state at the initial time. $\mathcal{U}(t,t_0) = \hat{T}\left\{\exp^{-i\int_{t_0}^t dt'\mathcal{H}(t')}\right\}$ is the evolution operator, being $\hat{T}$ the time-order operator and we have introduced the Heisenberg representation with respect to $\mathcal{H}$, $\hat{\rho}^{\mathcal{H}}_{ij}(t) = \mathcal{U}^\dagger(t,t_0)\hat{\rho}_{ij}\mathcal{U}(t,t_0)$. We now introduce the definitions of the lesser Green's function

$$G^<_{k\alpha}(t,t') = \pm i\left\langle b^{\dagger\mathcal{H}}_{k\alpha}(t')b^{\mathcal{H}}_{k\alpha}(t)\right\rangle, \tag{9.12}$$

where the upper (lower) sign applies to a fermionic (bosonic) reservoir α, and

$$G^{<}_{lj,uv}(t,t') = \pm i \left\langle \hat{\rho}^{\mathcal{H}}_{uv}(t')\hat{\rho}^{\mathcal{H}}_{lj}(t) \right\rangle , \tag{9.13}$$

where the upper sign applies to many-body fermionic states such that $|l\rangle$, $|j\rangle$, as well as $|u\rangle$, $|v\rangle$, differ in odd number of particles and the lower sign is for bosonic systems. We also introduce mixed lesser Green's functions

$$\begin{aligned} G^{<}_{lj,k\alpha^{\dagger}}(t,t') &= \pm i \left\langle b^{\dagger\mathcal{H}}_{k\alpha}(t')\hat{\rho}^{\mathcal{H}}_{lj}(t) \right\rangle , \\ G^{<}_{k\alpha,lj}(t,t') &= \pm i \left\langle \hat{\rho}^{\mathcal{H}}_{lj}(t) b^{\mathcal{H}}_{k\alpha}(t') \right\rangle . \end{aligned} \tag{9.14}$$

Calculating the evolution of $\hat{\rho}^{\mathcal{H}}_{lj}(t)$, taking the mean value with respect to ρ_0 as in Eq. (9.11) and introducing the definitions of the lesser Green's functions given in Eqs. (9.12), (9.13) and (9.14), we get

$$\begin{aligned} \frac{d\rho_{lj}}{dt} = \frac{i}{\hbar}\left\langle [\tilde{\mathcal{H}}^{\mathcal{H}}_{\mathrm{S}}, \hat{\rho}^{\mathcal{H}}_{lj}] \right\rangle \pm \frac{1}{\hbar}\sum_{k,\alpha} V_{k\alpha}\Big[\sum_{m} \lambda_{\alpha,ml}(t) G^{<}_{mj,k\alpha^{\dagger}}(t,t) \\ - \sum_{n} \lambda_{\alpha,jn}(t) G^{<}_{ln,k\alpha^{\dagger}}(t,t) + \sum_{m} \overline{\lambda}_{\alpha,ml}(t) G^{<}_{k\alpha,mj}(t,t) - \sum_{n} \overline{\lambda}_{\alpha,jn}(t) G^{<}_{k\alpha,ln}(t,t) \Big], \end{aligned} \tag{9.15}$$

where $\pm$ corresponds to fermionic and bosonic reservoirs, respectively. We now proceed with the line of argument presented in Refs. [355, 345, 346] for static Hamiltonians. We will obtain the master equations from Eq. (9.15) based on the expansion of the coupling term, and extend the derivation presented in those references by introducing the adiabatic expansion in the time-devolution. In our case we find it convenient to define non-equilibrium Green's functions for the operators $\hat{\rho}_{l,j}$, in addition to the ones for the reservoirs and we proceed with the derivation of the Dyson equation at the lowest order in the couplings $V_{k\alpha}$ in combination with Langreth theorem. These steps are very close to those followed in the study of quantum transport for strong coupling between system and reservoirs [360, 15].

We now introduce the interaction representation with respect to the uncoupled Hamiltonian $h = \tilde{\mathcal{H}}_{\mathrm{S}}(t) + \mathcal{H}_{\mathrm{B}}$. Therefore

$$\hat{\rho}^{\mathcal{H}}_{ij}(t) = \hat{T}_K \left[\exp\left\{ -i \int_K dt' \tilde{\mathcal{H}}^{h}_{\mathrm{C}}(t') \right\} \hat{\rho}^{h}_{ij}(t) \right] , \tag{9.16}$$

where the superscript h denotes the interaction representation with respect to h and $\hat{T}_K$ denotes time-ordering along the Schwinger-Keldysh contour K, which starts at t_0, evolves to $+\infty$ (contour $+$) and returns to t_0 (contour $-$)[15, 363]. Furthermore, we consider $t_0 = -\infty$ and $\rho_0 = \rho_{\mathrm{S}} \otimes \rho_{\mathrm{B}}$, where ρ_{S}, ρ_{B} are the density operators of the uncoupled system and reservoirs, respectively.

The next step is to evaluate the Green's functions in Eq. (9.15), up to the first order of perturbation theory in $V_{k\alpha}$. Following the analytic continuation procedure known as "Langreth rule", [15, 363] we obtain the following expressions, at the first order of perturbation theory, for Green's functions entering Eq. (9.15)

$$\begin{aligned} G^{<}_{lj,k\alpha^{\dagger}}(t,t') \simeq \int_{-\infty}^{\infty} dt_1 V_{k\alpha} \sum_{u,v} \overline{\lambda}_{\alpha,uv}(t) \Big[g^{r}_{lj,uv}(t,t_1) g^{<}_{k\alpha}(t_1,t') \\ + g^{<}_{lj,uv}(t,t_1) g^{a}_{k\alpha}(t_1,t') \Big], \end{aligned} \tag{9.17}$$

$$G^{<}_{k\alpha,lj}(t,t') \simeq \int_{-\infty}^{\infty} dt_1 V_{k\alpha} \sum_{u,v} \lambda_{\alpha,uv}(t) \Big[g^{r}_{k\alpha}(t,t_1) g^{<}_{uv,lj}(t_1,t') + g^{<}_{k\alpha}(t,t_1) g^{a}_{uv,lj}(t_1,t') \Big]. \quad (9.18)$$

The above derivation is found to be consistent with the systematic procedure based on real-time Green's functions, [15, 363] as detailed in Appendix H. In the expressions above we have introduced the notation $g_{\nu,\nu'}(t,t')$ and $g_{k\alpha}(t,t')$ to denote the Green's functions evaluated with respect to the uncoupled Hamiltonian h instead of $\mathcal{H}$. In addition to the lesser Greens functions previously defined, we have also introduced the definitions of the retarded Green's functions

$$g^{r}_{\nu,\nu'}(t,t') = \theta(t-t') \left[g^{>}_{\nu,\nu'}(t,t') - g^{<}_{\nu,\nu'}(t,t') \right], \quad (9.19)$$

with $g^{>}_{\nu,\nu'}(t,t') = \mp \left[g^{<}_{\nu',\nu}(t',t) \right]^{*}$ and the advanced Green's function $g^{a}_{\nu,\nu'}(t,t') = \left[g^{a}_{\nu',\nu}(t',t) \right]^{*}$.

Using Eqs. (9.18), Eq. (9.15) can be written as

$$\frac{d\left\langle \hat{\rho}_{lj} \right\rangle}{dt} = \frac{i}{\hbar} \left[\varepsilon_l(t) - \varepsilon_j(t) \right] \left\langle \hat{\rho}_{lj} \right\rangle + \frac{1}{\hbar} \sum_{\alpha} \Big[\sum_{m} \lambda_{\alpha,ml}(t) \Lambda^{\alpha(0)}_{mj}(t) - \sum_{n} \lambda_{\alpha,jn}(t) \Lambda^{\alpha(0)}_{ln}(t) + \sum_{m} \overline{\lambda}_{\alpha,ml}(t) \overline{\Lambda}^{\alpha(0)}_{mj}(t) - \sum_{n} \overline{\lambda}_{\alpha,jn}(t) \overline{\Lambda}^{\alpha(0)}_{ln}(t) \Big] \quad (9.20)$$

This equation (9.20) is exact up to order $V^2_{k\alpha}$. We have introduced the definitions

$$\Lambda^{\alpha(\kappa)}_{mj}(t) = \pm \sum_{u,v} \overline{\lambda}_{\alpha,uv}(t) \int_{-\infty}^{\infty} dt_1 \Big(g^{r}_{mj,uv}(t,t_1) \Sigma^{<(\kappa)}_{\alpha}(t_1,t) + g^{<}_{mj,uv}(t,t_1) \Sigma^{a(\kappa)}_{\alpha}(t_1,t) \Big), \quad (9.21)$$

and

$$\overline{\Lambda}^{\alpha(\kappa)}_{mj}(t) = \pm \sum_{u,v} \lambda_{\alpha,uv}(t) \int_{-\infty}^{\infty} dt_1 \Big(\Sigma^{r(\kappa)}_{\alpha}(t,t_1) g^{<}_{uv,mj}(t_1,t) + \Sigma^{<(\kappa)}_{\alpha}(t,t_1) g^{a}_{uv,mj}(t_1,t) \Big), \quad (9.22)$$

which depend on the Green's functions of the isolated N-level system and on the following self-energies, which describe the coupling to the baths,

$$\Sigma^{r,a,<(\kappa)}_{\alpha}(t,t') = \int \frac{d\omega}{2\pi} e^{-i\omega(t-t')} \Sigma^{r,a,<(\kappa)}_{\alpha}(\omega). \quad (9.23)$$

In terms of the spectral function it can be written as follows,

$$\Gamma^{(\kappa)}_{\alpha}(\omega) = -2\mathrm{Im}\left[\Sigma^{r(\kappa)}_{\alpha}(\omega) \right] = 2\pi \sum_{k\alpha} |V_{k\alpha}|^2 \omega^{\kappa} \delta(\omega - \epsilon_{k\alpha}),$$
$$\Sigma^{<(\kappa)}_{\alpha}(\omega) = \pm i n_{\alpha}(\omega) \Gamma^{(\kappa)}_{\alpha}(\omega), \quad (9.24)$$

$n_{\alpha}(\omega)$ denotes the Fermi-Dirac or Bose-Einstein distribution function for the case of fermionic or bosonic bath, respectively. Importantly, the information on the temperature and chemical potential of a given reservoir α is only encoded in these functions. In the previous expressions, we have introduced the index κ to denote the different moments of the spectral function.

9.1.3 *Dynamics of the particle and energy current between system and baths*

The time-resolved density matrix $\rho_{ij}(t)$ fully characterizes the dynamics of the local properties of the system. Now we are interested in evaluating the charge current $J_\alpha^{(c)}(t)$ (in the case of the fermionic reservoirs) or in general the energy current $J_\alpha^{(E)}(t)$ flowing from the system to the reservoirs. These quantities can also be calculated by recourse to Green's functions as follows

$$\begin{aligned} J_\alpha^{(c)}(t) &= \frac{ie}{\hbar}\left\langle\left[\mathcal{H},\mathcal{N}_\alpha\right]\right\rangle \\ &= \mp\frac{e}{\hbar}\sum_k\sum_{m,n} V_{k\alpha}\left[\lambda_{\alpha,mn}(t)\,G^<_{mn,k\alpha^\dagger}(t,t) - \overline{\lambda}_{\alpha,mn}(t)\,G^<_{k\alpha,mn}(t,t)\right], \end{aligned} \tag{9.25}$$

$$\begin{aligned} J_\alpha^{(E)}(t) &= \frac{i}{\hbar}\left\langle\left[\mathcal{H},\mathcal{H}_\alpha\right]\right\rangle \\ &= \mp\frac{1}{\hbar}\sum_k\sum_{m,n} V_{k\alpha}\,\epsilon_{k\alpha}\left[\lambda_{\alpha,mn}(t)\,G^<_{mn,k\alpha^\dagger}(t,t) - \overline{\lambda}_{\alpha,mn}(t)\,G^<_{k\alpha,mn}(t,t)\right], \end{aligned} \tag{9.26}$$

where the upper sign is for fermionic and lower sign for bosonic reservoirs. Using Eqs. (9.18), we can evaluate these currents at the lowest order in the coupling strength. The result is

$$\begin{aligned} J_\alpha^{(c)} &= \frac{-1}{\hbar}\left[\sum_{m,n}\lambda_{\alpha,mn}(t)\Lambda^{\alpha(0)}_{mn}(t) - \sum_{m,n}\overline{\lambda}_{\alpha,mn}(t)\overline{\Lambda}^{\alpha(0)}_{mn}(t)\right] \\ J_\alpha^{(E)} &= \frac{-1}{\hbar}\left[\sum_{m,n}\lambda_{\alpha,mn}(t)\Lambda^{\alpha(1)}_{mn}(t) - \sum_{m,n}\overline{\lambda}_{\alpha,mn}(t)\overline{\Lambda}^{\alpha(1)}_{mn}(t)\right]. \end{aligned} \tag{9.27}$$

We see that the coefficients $\Lambda^{\alpha(0)}_{mn}(t)$ and $\overline{\Lambda}^{\alpha(0)}_{mn}(t)$ entering the equation of motion (9.20) for the density matrix also enter the expression for the charge currents. On the other hand, the heat currents are determined by the coefficients $\Lambda^{\alpha(1)}_{mn}(t)$ and $\overline{\Lambda}^{\alpha(1)}_{mn}(t)$ related to the first moment of the spectral function ($\kappa = 1$). Notice that the above expressions for the currents are exact up to order $V^2_{k\alpha}$.

9.1.4 *Power developed by the ac forces*

We express the Hamiltonian $\tilde{\mathcal{H}}_S$ in Eq. (9.4) as follows

$$\tilde{\mathcal{H}}_S(t) = -\hat{\mathbf{F}}\cdot\mathbf{X}(t), \tag{9.28}$$

where $\hat{\mathbf{F}} = -\partial\tilde{\mathcal{H}}_S/\partial\mathbf{X} = (\hat{\rho}_{11},\ldots,\hat{\rho}_{NN})$ and $\mathbf{X}(t) = (\varepsilon_1(t),\cdots\varepsilon_N(t))$. The power transferred to the system by the ac forces is

$$P^{\rm ac}(t) = \langle\dot{\tilde{\mathcal{H}}}_S(t)\rangle = \sum_{l=1}^N\langle\hat{\rho}_{ll}\rangle(t)\;\dot{X}_l(t). \tag{9.29}$$

In the absence of temperature and chemical potential differences at the reservoirs, this accounts for the total rate of heat and entropy production in the system.

9.2 ADIABATIC DYNAMICS

So far we have not introduced any assumptions regarding the nature of the time dependence. Here, we focus on slow (adiabatic) driving, where

the rate of change of the time-dependent parameters is small, which justifies treating the dynamics at different orders in these parameters. More precisely, adiabatic driving is the regime where the typical time-scale associated to the driving is much larger than any other time-scale associated to the dynamics of the system coupled to the baths. Here, we follow a treatment along the line of Ref. [340, 343]. We recall that the lesser Green's function $g^{<}_{lj,uv}(t_1,t_2) = \pm i \left\langle \hat{\rho}_{uv}(t_2)\hat{\rho}_{lj}(t_1) \right\rangle$ are evaluated with the operators expressed in the interaction picture with respect to $h = \tilde{\mathcal{H}}_{\rm S}(t) + \mathcal{H}_{\rm B}$, which for this particular function is equivalent to the Heisenberg picture with respect to $\tilde{\mathcal{H}}_{\rm S}(t)$.

We consider the expansion of $\tilde{\mathcal{H}}_{\rm S}(t')$ with respect to an "observational time" t,

$$\begin{aligned} \tilde{\mathcal{H}}_{\rm S}(t') &= \tilde{\mathcal{H}}^f_{\rm S} + \delta\tilde{\mathcal{H}}_{\rm S}(t'), \\ \delta\tilde{\mathcal{H}}_{\rm S}(t') &= \sum_{n=1}^{\infty} \frac{(t'-t)^n}{n!} \frac{\partial \tilde{\mathcal{H}}_{\rm S}}{\partial \mathbf{X}} \cdot \frac{d^n \mathbf{X}}{dt^n} = \sum_{k=1}^{N} \xi_k(t')\hat{\rho}_{kk}, \end{aligned} \tag{9.30}$$

where $\tilde{\mathcal{H}}^f_{\rm S}$ is the Hamiltonian with the time frozen at t and $\xi_k(t') = \sum_{n=1}^{\infty}(t'-t)^n/n! d^n X_k/dt^n$.

We then change to the interaction representation with respect to $\tilde{\mathcal{H}}^f_{\rm S}$ and consider the Green's function

$$g^{<}_{lj,uv}(t_1,t_2) = -i{\rm Tr}\left\{ \hat{\rho}_0 \hat{T}_K \left[e^{-i\int_K dt' \delta\tilde{\mathcal{H}}^f_{\rm S}(t')} \hat{\rho}^f_{lj}(t_1^+)\hat{\rho}^f_{uv}(t_2^-) \right] \right\}, \tag{9.31}$$

where t_1^+ and t_2^- indicates that the time t_1 is on the piece of the contour that starts in $-\infty$, while t_2 is on the piece of the contour that ends in $-\infty$. All the operators with the label f are calculated in the Heisenberg representation of the frozen Hamiltonian $\tilde{\mathcal{H}}^f_{\rm S}$. In particular,

$$\hat{\rho}^f_{lj}(t') = e^{\frac{i}{\hbar}t'\tilde{\mathcal{H}}^f_{\rm S}}\, \hat{\rho}_{lj}\, e^{-\frac{i}{\hbar}t'\tilde{\mathcal{H}}^f_{\rm S}} = e^{\frac{i}{\hbar}\epsilon_{lj}t'}\hat{\rho}_{lj} \tag{9.32}$$

with ϵ^f_j being the eigenenergies of $\tilde{\mathcal{H}}^f_{\rm S}$ and $\epsilon_{lj} = \epsilon^f_l - \epsilon^f_j$. Evaluating Eq. (H.9) up to linear order in the perturbation $\tilde{\mathcal{H}}^f_{\rm S}$ leads to

$$g^{<}_{lj,uv}(t_1,t_2) \simeq g^{<,f}_{lj,uv}(t_1,t_2) + \delta g^{<,f}_{lj,uv}(t_1,t_2), \tag{9.33}$$

where the first term is the frozen component and reads

$$\begin{aligned} g^{<,f}_{lj,uv}(t_1,t_2) &= \pm i\delta_{lv} \left\langle \hat{\rho}^f_{uj}(t_1) \right\rangle e^{i\epsilon_{uv}(t_2-t_1)} \\ &= \pm i\delta_{lv} \left\langle \hat{\rho}^f_{uj}(t_2) \right\rangle e^{i\epsilon_{jv}(t_2-t_1)}, \end{aligned} \tag{9.34}$$

while the second term is the correction up to linear order in $\delta\tilde{\mathcal{H}}^f_{\rm S}(t')$ (see calculation in Appendix (H)) and reads

$$\delta g^{<,f}_{lj,uv}(t_1,t_2) = -\frac{i}{\hbar} g^{<,f}_{lj,uv}(t_1,t_2) \left[\int_{-\infty}^{t_1} dt' \xi_j(t') + \int_{t_1}^{t_2} dt' \xi_v(t') - \int_{-\infty}^{t_2} dt' \xi_u(t') \right]. \tag{9.35}$$

The adiabatic approximation consists in keeping the terms $\propto \dot{\mathbf{X}}$ in $\delta g^{<,f}_{lj,uv}(t_1,t_2)$ under the assumption that the changes in $\mathbf{X}(t)$ take place within a time scale that is much larger than the typical time scale of the dynamics of the frozen system.

9.2.1 *Full adiabatic master equation*

Our aim is to calculate the matrix elements of the density matrix up to linear order in $\dot{\mathbf{X}}$. Hence, we split them as follows,

$$\langle \rho^f_{uv} \rangle(t) \equiv p_{uj}(t) = p^f_{uj}(t) + p^a_{uj}(t), \tag{9.36}$$

with p^f_{uj} being the solution of the frozen master equation and $p^a_{uj}(t)$ being the correction $\propto \dot{\mathbf{X}}$.

By substituting Eq. (H.9) into Eqs. (9.21) and (9.22), with Eq. (H.19) and the adiabatic approximation of Eq. (9.35), the master equation that includes both frozen and adiabatic contributions can be written as

$$\frac{dp_{lj}}{dt} = \frac{i}{\hbar}\left[\varepsilon_l(t) - \varepsilon_j(t)\right] p_{lj} + \frac{1}{2}\sum_{m,u}\Big[\Gamma^{(1)}_{ml,ju}(t)p_{mu} - \Gamma^{(2)}_{ml,uj}(t)p_{uj} - \Gamma^{(3)}_{jm,lu}(t)p_{lu} + \Gamma^{(4)}_{jm,ul}(t)p_{um}\Big], \tag{9.37}$$

where we introduced the transition rates

$$\Gamma^{(i)}_{ml,ju}(t) \quad = \quad \Gamma^{(i),f}_{ml,ju}(t) + \delta\Gamma^{(i)}_{ml,ju}(t). \tag{9.38}$$

The frozen rates are expressed as $\Gamma^{(i),f}_{ml,ju}(t) = \sum_\alpha \Gamma^{(i),f}_{ml,ju,\alpha}(t)$ with

$$\Gamma^{(1),f}_{ml,ju,\alpha}(t) \quad = \quad \lambda_{\alpha,ml}(t)\overline{\lambda}_{\alpha,ju}(t)\gamma^f_\alpha(\epsilon_{ju}) + \overline{\lambda}_{\alpha,ml}(t)\lambda_{\alpha,ju}(t)\tilde{\gamma}^f_\alpha(\epsilon_{uj}), \tag{9.39}$$

$$\Gamma^{(4),f}_{jm,ul,\alpha}(t) \quad = \quad \lambda_{\alpha,jm}(t)\overline{\lambda}_{\alpha,ul}(t)\tilde{\gamma}^f_\alpha(\epsilon_{ul}) + \overline{\lambda}_{\alpha,jm}(t)\lambda_{\alpha,ul}(t)\gamma^f_\alpha(\epsilon_{lu}), \tag{9.40}$$

$\Gamma^{(3),f}_{jm,lu,\alpha}(t) = \Gamma^{(1),f}_{jm,mu,\alpha}(t)$ and $\Gamma^{(2),f}_{ml,uj,\alpha}(t) = \Gamma^{(4),f}_{ml,um,\alpha}(t)$. The frozen contributions originating from Eq. (H.19) are expressed in terms of $\gamma^f_\alpha(\epsilon) = \hbar^{-1}n_\alpha(\epsilon)\Gamma^{(0)}_\alpha(\epsilon)$ and $\tilde{\gamma}^f_\alpha(\epsilon) = \hbar^{-1}(1 \mp n_\alpha(\epsilon))\Gamma^{(0)}_\alpha(\epsilon)$. On the other hand, the adiabatic corrections to the transition rates ($\delta\Gamma^{(i)}_{ml,ju}(t)$) which has its origin in Eq. (9.35) can be evaluated in a similar manner. The latter are $\propto \Gamma^{(0)}_\alpha \dot{\mathbf{X}}$ within the adiabatic approximation. In deriving Eq. (9.37), we have neglected the level renormalisation effects.

The diagonal and off-diagonal terms of p_{uj} are named, respectively, populations and coherences and are generally coupled. Splitting in this equation the density matrix elements and rates into their frozen and adiabatic components as in Eqs. (9.36) and (9.21), we can make use of the fact that the frozen component satisfies

$$0 = \frac{i}{\hbar}\left[\varepsilon_l(t) - \varepsilon_j(t)\right] p^f_{lj} + \frac{1}{2}\sum_{m,u}\Big[\Gamma^{(1),f}_{ml,ju}(t)p^f_{mu} - \Gamma^{(4),f}_{ml,um}(t)p^f_{uj} - \Gamma^{(1),f}_{jm,mu}(t)p^f_{lu} + \Gamma^{(4),f}_{jm,ul}(t)p^f_{um}\Big], \tag{9.41}$$

which leads to the following equation to be fulfilled by the adiabatic components (keeping only linear-order terms in $\dot{\mathbf{X}}$),

$$\frac{dp^f_{lj}}{dt} = \frac{1}{2}\sum_{m,u}\Big[\Gamma^{(1),f}_{ml,ju}(t)p^a_{mu} - \Gamma^{(4),f}_{ml,um}(t)p^a_{uj} - \Gamma^{(1),f}_{jm,mu}(t)p^a_{lu} + \Gamma^{(4),f}_{jm,ul}(t)p^a_{um}\Big] + \frac{1}{2}\sum_{m,u}\Big[\delta\Gamma^{(1)}_{ml,ju}(t)p^f_{mu} - \delta\Gamma^{(2)}_{ml,um}(t)p^f_{uj} - \delta\Gamma^{(3)}_{jm,mu}(t)p^f_{lu} + \delta\Gamma^{(4)}_{jm,ul}(t)p^f_{um}\Big]. \tag{9.42}$$

These equations must be supplemented by the normalization of the populations $\sum_l p_l = 1$. Furthermore, considering only the contribution of the frozen rates in the previous equation leads to $p^a_{lj} \sim \mathcal{O}(\dot{\mathbf{X}}/\Gamma^0_\alpha)$, while including also the terms in the second line of the equation will introduce a correction of $\mathcal{O}(\dot{\mathbf{X}})$, which can be neglected in comparison to the previous one. Notice that this reasoning is the same followed in Ref. [364, 233, 336].

Similarly, substituting Eqs. (9.21) in the definition of the energy currents, we get

$$J^{(E)}_\alpha(t) = \frac{1}{2\hbar}\sum_{m,n,u}\Big[\epsilon_{um}\,\Gamma^{(4),f}_{mn,um,\alpha}(t)p_{un}(t) - \epsilon_{nu}\,\Gamma^{(1),f}_{mn,nu,\alpha}(t)p_{mu}(t)\Big]. \tag{9.43}$$

Similarly, for the charge currents we obtain

$$J^{(c)}_\alpha(t) = \frac{1}{\hbar}\sum_{m,n,u}\Big[\Gamma^{(4),f}_{mn,um,\alpha}(t)p_{un}(t) - \Gamma^{(1),f}_{mn,nu,\alpha}(t)p_{mu}(t)\Big]. \tag{9.44}$$

Notice that the charge current has been defined only for the fermionic case.

Moreover, currents are made up of a frozen and an adiabatic contributions [$J^{(E),f}_\alpha(t)$ and $J^{(E),a}_\alpha(t)$, respectively, for energy currents] coming from the respective terms of the density matrix.

9.3 EXAMPLES

9.3.1 *Qutrit*

We now use the formalism presented in the previous sections to analyze the energy dynamics of a driven qutrit — a three-level system such as an atom with a ground state and two excited states — asymmetrically attached to two bosonic reservoirs. The latter could, for instance, represent two electromagnetic environments to which the atom is coupled. We consider the following Hamiltonian for the driven three-level system

$$H_{\rm S}(t) = \sum_{j=0}^{2}\varepsilon_j(t)\hat{\pi}_{jj} + w(t)\Big(\hat{\pi}_{12} + \hat{\pi}_{21}\Big), \tag{9.45}$$

where $\varepsilon_j(t)$, with $j = 0, 1, 2$, are the energy levels relative to the ground state (0) and the two excited states (1 and 2). The inter-level coupling parameter $w(t)$ denotes the amplitude for, possibly, time-dependent transitions between the two excited states. The bath Hamiltonian is given by Eq. (9.2) with $N_r = 2$, $\hat{b}_{k\alpha}$ being bosonic operators for reservoir $\alpha = L, R$. As shown in Fig. 9.1, we fix the temperature of the two baths as $T_{\rm L} = T + \Delta T$ and $T_{\rm R} = T - \Delta T$. Moreover, we will consider Ohmic baths with linear dissipation relation spectral density

$$\Gamma_\alpha(\epsilon) = \Gamma_\alpha\,\epsilon\,e^{-\epsilon/\epsilon_c}, \quad \text{with } \epsilon > 0, \tag{9.46}$$

where $\epsilon_c = \hbar\omega_c$, ω_c being the high frequency cut-off. We assume that the left bath is connected to the qutrit through energy level 1 and right bath is connected through energy level 2, so that the contact Hamiltonian is given by

$$\begin{aligned} H_{\rm C} = &\sum_k V_{kL}\left(\hat{\pi}_{10} + \hat{\pi}_{01}\right)\left(b^\dagger_{kL} + b_{kL}\right) \\ &+ \sum_k V_{kR}\left(\hat{\pi}_{02} + \hat{\pi}_{20}\right)\left(b^\dagger_{kR} + b_{kR}\right). \end{aligned} \tag{9.47}$$

As detailed in Sec. 9.1, we first diagonalize the system Hamiltonian with a suitable unitary transformation $\hat{U}(t)$ so that

$$\tilde{\mathcal{H}}_{\mathrm{S}}(t) = \sum_{q=\pm} \epsilon_q(t)\hat{\rho}_{qq} + \varepsilon_0(t)\hat{\rho}_{00}, \tag{9.48}$$

where

$$\epsilon_{\pm}(t) = \left(\frac{\varepsilon_1(t)+\varepsilon_2(t)}{2}\right) \pm \frac{1}{2}\sqrt{(\varepsilon_1(t)-\varepsilon_2(t))^2 + 4w(t)^2}. \tag{9.49}$$

Moreover, the contact Hamiltonian becomes

$$\tilde{\mathcal{H}}_{\mathrm{C}} = \sum_{k,\alpha}\sum_{q=\pm} V_{k\alpha}\left(\lambda_{\alpha,0q}(t)\,\hat{\rho}_{0q} + \lambda_{\alpha,q0}(t)\,\hat{\rho}_{q0}\right)\left(b_{k\alpha} + b^{\dagger}_{k\alpha}\right), \tag{9.50}$$

where $\lambda_{L,0+}(t) = -\lambda_{R,0-}(t) = \cos\theta(t)/2$ and $\lambda_{L,0-}(t) = \lambda_{R,0+}(t) = \sin\theta(t)/2$, $\theta(t) = \tan^{-1}\left(\frac{2w(t)}{\varepsilon_1(t)-\varepsilon_2(t)}\right)$ and $\lambda_{\alpha,0q}(t) = \lambda_{\alpha,q0}(t)$. The full adiabatic master equation for diagonal and off-diagonal terms of the density matrix can be obtained following Sec. 9.2.1 (detailed calculations are presented in App. H.4).

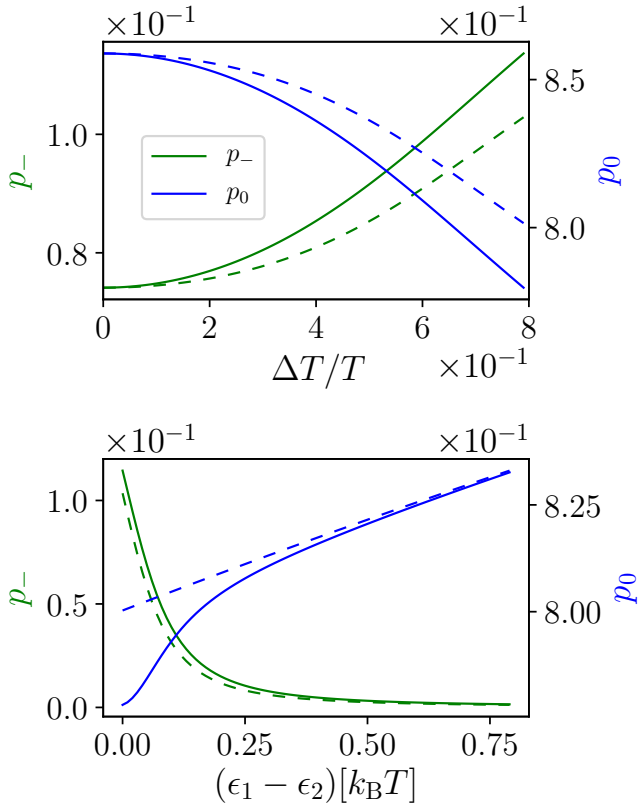

Figure 9.2: Population probabilities in the absence of driving as functions of ΔT for fixed level splitting $\varepsilon_1 - \varepsilon_2 = 0$ (top panel), and as functions of level splitting for $\Delta T = 0.8T$ (bottom panel). Green lines refers to p_- (with axis on the left) and blue lines refers to p_0 (with axis on the right). Solid (dashed) lines result from the solution of the RE (QME). Parameters values are: $\Gamma_L = \Gamma_R = 0.5$, $\epsilon_c = 100\ k_BT$, $w = 0.05\ k_BT$, $\varepsilon_1 + \varepsilon_2 = 5\ k_BT$, and $\varepsilon_0 = 0$.

We first consider the situation where the driving is absent (ε_j and w are time-independent) and study the effect of coherence by comparing the

outcomes of the QME and the RE. In particular, in Fig. 9.2 we plot the populations p_0 (blue lines) and p_- (green lines) of the states $|0\rangle$ and $|-\rangle$, respectively, as functions of ΔT (top panel) and energy level splitting ($\varepsilon_1 - \varepsilon_2$, bottom panel). Solid lines result from the solution of the RE, while dashed lines from the solution of the QME. The top plot in Fig. 9.2 shows that the effect of coherence on the populations is absent for $\Delta T = 0$ (where the overall system is at equilibrium) and gets important with large values of ΔT. The bottom plot in Fig. 9.2, instead, shows that coherence is significant as long as the level splitting is small (up to values of $\varepsilon_1 - \varepsilon_2 \simeq 0.5\ k_B T$). For this choice of parameters, indeed, the gap between bonding and anti-bonding energy level $\Delta = \epsilon_+ - \epsilon_- = \sqrt{(\varepsilon_1 - \varepsilon_2)^2 + 4w^2}$ is smaller than the energy scale $k_B \Delta T$ and coherent dynamics between the states $|0\rangle$ and $|1\rangle$ can take place. [352]

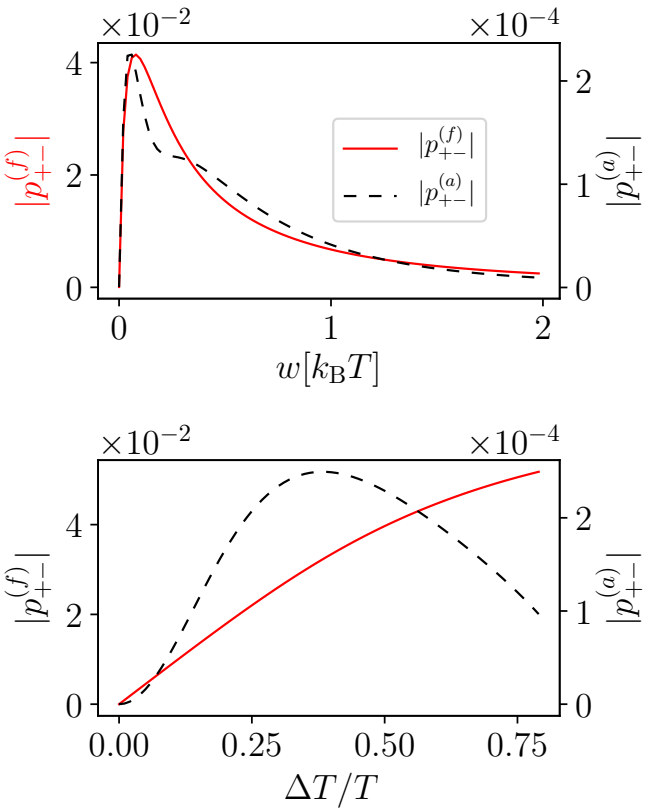

Figure 9.3: Frozen (f) and adiabatic (a) contributions to the coherence p_{+-} as functions of the inter-level coupling w for fixed $\Delta T = 0.5T$ (top panel), and as functions of ΔT for fixed $w = 0.05\ k_B T$ (bottom panel). Red solid lines refer to the absolute value of the frozen contribution (with axis on the left) and black dashed lines refers to the absolute value of the adiabatic contribution (with axis on the right). Parameters values are: $\Gamma_L = \Gamma_R = 0.5$, $\epsilon_c = 100\ k_B T$, $\varepsilon_{\rm rel} = 0$, $\varepsilon_{\rm av} = 20\ k_B T$, $\delta\varepsilon = 30\ k_B T$, $\delta\bar{\varepsilon} = 0.5\ k_B T$ and $\phi = \pi/2$.

Let us now assume that the system is driven by modulating the parameters according to the following scheme: $\varepsilon_1(t) + \varepsilon_2(t) = \varepsilon_{\rm av} + \delta\varepsilon \cos(\Omega t + \phi)$ and $\varepsilon_1(t) - \varepsilon_2(t) = \varepsilon_{\rm rel} + \delta\bar{\varepsilon} \cos(\Omega t)$, while w is time-independent. In Fig. (9.3) we plot the absolute value of the frozen and adiabatic contributions to the coherences ($p^{(f)}_{+-}$ and $p^{(a)}_{+-}$, respectively) as functions of w (top panel) and ΔT

(bottom panel). Red solid lines refer to the frozen contribution (with values on the left axis) and black dashed lines refer to the adiabatic contribution (with value on the right axis). The top panel of Fig. (9.3) shows that frozen and adiabatic components of the coherence display similar behavior as functions of inter-level coupling, although the absolute values differ by two order of magnitude. In particular, they are zero at $w = 0$, since no coupling is present, and are strongly suppressed at large w, since the gap Δ gets larger than the energy scale $k_B \Delta T$, thus presenting a maximum at about $w = 0.08\, k_B T$. The bottom panel of Fig. (9.3) shows that the coherence p_{+-} vanishes for $\Delta T = 0$, while both components increase with ΔT. Notably, while the frozen one increases monotonically, the adiabatic component shows a maximum at intermediate values of ΔT. To summarize, a necessary condition for obtaining a finite coherence is non-equilibrium dynamics: adiabatic driving alone does not produce any coherence effect in the absence of a thermal bias since the system is described by the Gibbs state at each instant of time.

9.3.2 *Coupled quantum dots*

In this section we analyze the effect of coherence in a fermionic driven system consisting of a pair of coupled quantum dots.[233] For simplicity, we focus on the case with infinite intra-dot Coulomb repulsion, which limits the occupation to at the most one electron per quantum dot, and we assume spinless fermions.

Concretely, we consider the following Hamiltonian for a pair of coupled single-level quantum dot

$$H_S(t) = \varepsilon_1(t)\, a_1^\dagger a_1 + \varepsilon_2(t)\, a_2^\dagger a_2 + w(t)\, (a_1^\dagger a_2 + a_2^\dagger a_1) + U \hat{n}_1 \hat{n}_2, \tag{9.51}$$

where a_j and $a_j^\dagger$ are, respectively, the annihilation and creation operators for the quantum dot $j = 1, 2$. The, possibly, time-dependent parameters are the QDs' energy levels $\varepsilon_1(t)$ and $\varepsilon_2(t)$, and the hopping element $w(t)$ between the two QDs, while U is the inter-dot Coulomb interaction with $n_j = a_j^\dagger a_j$. The bath Hamiltonian is given by Eq. (9.2) with $N_r = 2$, $b_{k\alpha}$ being fermionic operators for reservoir $\alpha = L, R$. Moreover, we assume a characterless spectral density, namely $\Gamma_\alpha(\epsilon) = \Gamma_\alpha$. The contact Hamiltonian is given by

$$H_C = \sum_k V_{kL} b_{kL}^\dagger a_1 + \sum_k V_{kR} b_{kR}^\dagger a_2 + h.c., \tag{9.52}$$

so that each QD is connected only to one reservoir.

The Hilbert space of the double-dot system is composed of the following four occupation states: $|0\rangle$ (empty), $|1\rangle = a_1^\dagger |0\rangle$ (single occupancy, left QD), $|2\rangle = a_2^\dagger |0\rangle$ (single occupancy, right QD) and $|d\rangle = a_1^\dagger a_2^\dagger |0\rangle$ (double occupancy). In the diagonalized basis the system Hamiltonian reads

$$\tilde{\mathcal{H}}_S(t) = \sum_{q=\pm,d} \epsilon_q(t) \hat{\rho}_{qq}, \tag{9.53}$$

where $\epsilon_\pm(t)$ are given by Eq. (9.49) and $\epsilon_d(t) = U + \varepsilon_1(t) + \varepsilon_2(t)$. The contact Hamiltonian becomes

$$\tilde{\mathcal{H}}_C = \sum_{k,\alpha} \sum_{q=\pm} V_{k\alpha} \left(\lambda_{\alpha,0q}\, b_{k\alpha}^\dagger \hat{\rho}_{0q} + \lambda_{\alpha,dq}\, b_{k\alpha}^\dagger \hat{\rho}_{qd} + h.c. \right), \tag{9.54}$$

where $\lambda_{L,0+}(t) = -\lambda_{R,0-}(t) = \lambda_{R,+d} = \lambda_{L,-d} = \cos\theta(t)/2$ and $\lambda_{L,0-}(t) = \lambda_{R,0+}(t) = \lambda_{R,-d} = -\lambda_{L,+d} = \sin\theta(t)/2$, $\theta(t) = \tan^{-1}\left(\frac{2w(t)}{\varepsilon_1(t) - \varepsilon_2(t)}\right)$. Notice

that $\lambda_{\alpha,0q} = \lambda^*_{\alpha,q0}$ and $\lambda_{\alpha,dq} = \lambda^*_{\alpha,qd}$. The full adiabatic master equation for diagonal and off-diagonal terms of the density matrix can be obtained following Sec. 9.2.1. We now examine the system when driven by modulating

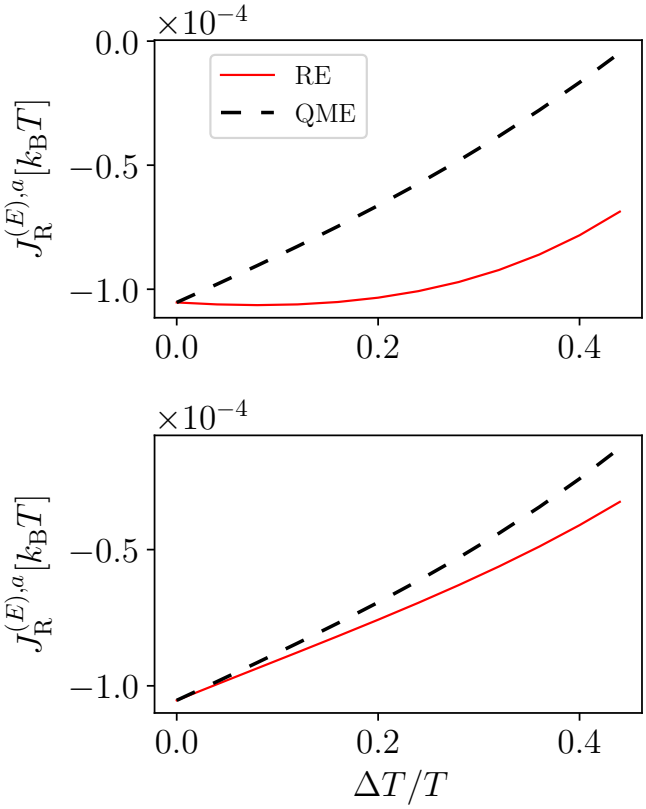

Figure 9.4: Adiabatically-pumped energy current in the right reservoir averaged over one period relative to the qutrit system (top panel) and to the coupled QD system (bottom panel) as a function of a ΔT. Solid red (dashed black) lines results from the solution of the RE (QME). Parameters values are: $\Gamma_L = \Gamma_R = 0.2$, $w = 0.05 k_{\mathrm{B}}T$, $\epsilon_{\mathrm{rel}} = 0.5 k_{\mathrm{B}}T$, $\epsilon_{\mathrm{av}} = 2 k_{\mathrm{B}}T$, $\delta\epsilon = 2 k_{\mathrm{B}}T$, $\delta\bar{\epsilon} = 0.5 k_{\mathrm{B}}T$, $\phi = \pi/2$; for qutrit $\Gamma_L = \Gamma_R = 0.2$ and for coupled quantum dots $\Gamma_L = \Gamma_R = 0.2 k_{\mathrm{B}}T$, $U = 0$.

in time the parameters $\varepsilon_1(t)$ and $\varepsilon_2(t)$ according to the scheme presented in Sec. 9.3.1, while taking w time-independent. Our aim is to calculate numerically, for both examples (bosonic qutrit and fermionic double QD) the energy currents flowing between the system and the reservoirs and the power developed by the ac forces. We notice that, in the adiabatic regime, asymmetric coupling (with respect to the reservoirs) is a necessary condition to obtain a net pumping of energy over a period. In both examples, this means coupling a given level to only one of the reservoirs. In Fig. 9.4 we plot the adiabatically-pumped energy current (averaged over a period) flowing into the right reservoir $J_R^{(E),a} = \Omega/(2\pi) \int_0^{2\pi/\Omega} dt\, J_R^{(E),a}(t)$ as a function of the ΔT for both systems (qutrit in the top panel and double QD in the bottom panel). The solid red lines result from the solution of the RE, in the absence of coherence effects, while the dashed black lines result from the solution of the QME. The fact that the value of $J_R^{(E),a}$ is negative means that the energy current is exiting the right, cold reservoir for all ΔT, so that the systems work as refrigerators. Interestingly, in both cases we find that the presence

of coherence always decrease the absolute value of the energy current, thus suppressing the refrigeration effect. The effect is more pronounced for the qutrit than for the double QD.

In Fig. 9.5 we plot the power transferred to the system by the ac source averaged over a period $P^{\mathrm{ac}} = \frac{\Omega}{2\pi}\int_0^{2\pi/\Omega} P^{\mathrm{ac}}(t)dt$ in the presence of thermal bias as a function of the hopping element w. The solid red lines represent the power calculated without taking into account the effect of coherence (using RE) whereas the dashed black lines are obtained in the presence of coherence (using QME). We observe that coherence produces a small correction (a slight increase) to the power transferred by the ac source (such correction is almost negligible in the case of coupled QDs). As a result, coherence decreases the amount of heat extracted from the cold reservoir while increasing the amount of power transferred by the ac source, thus deteriorating the performance of a refrigerator working in the adiabatic regime.

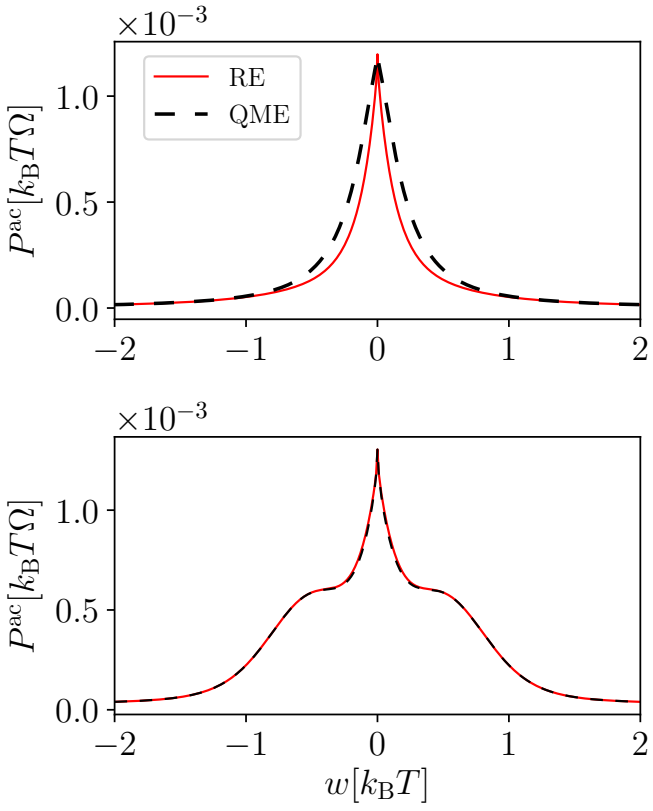

Figure 9.5: Power transferred by the ac source averaged over one period corresponding to the qutrit system (top panel) and to the coupled QD system (bottom panel) as a function of inter-level (dot) tunneling. Solid red (dashed black) lines results from the solution of the RE (QME). Parameters values are: $\Delta T = 0.8T$, $\epsilon_{\mathrm{rel}} = 0.5k_{\mathrm{B}}T$, $\epsilon_{\mathrm{av}} = 1k_{\mathrm{B}}T$, $\delta\epsilon = 0.5k_{\mathrm{B}}T$, $\delta\bar{\epsilon} = 0.5k_{\mathrm{B}}T$, $\phi = \pi/2$; for qutrit $\Gamma_L = \Gamma_R = 0.5$ and for coupled quantum dots $\Gamma_L = \Gamma_R = 0.5k_{\mathrm{B}}T$, $U = 0$.

9.3.3 *Thermal Rectification*

In this section we will examine the effect of adiabatic driving in determining thermal rectification of an adiabatically driven quantum coherent system. A

thermal rectifier is a device connected to two reservoirs that blocks the flow of heat current in one direction, and allows an optimal flow in the opposite direction. There are two necessary and sufficient conditions to obtain finite thermal rectification for quantum devices[124, 127, 45]: (i) presence of non-linearities, and (ii) asymmetric coupling to the baths. Multi-level systems possess intrinsic non-linearity and the asymmetric coupling to the baths can be established either by taking asymmetric coupling constants or by coupling different subsystems to different baths. Hence, thermal rectification is an expected phenomenon in these devices. In the following, we will study the effect of adiabatic driving (using the QME) on thermal rectification.

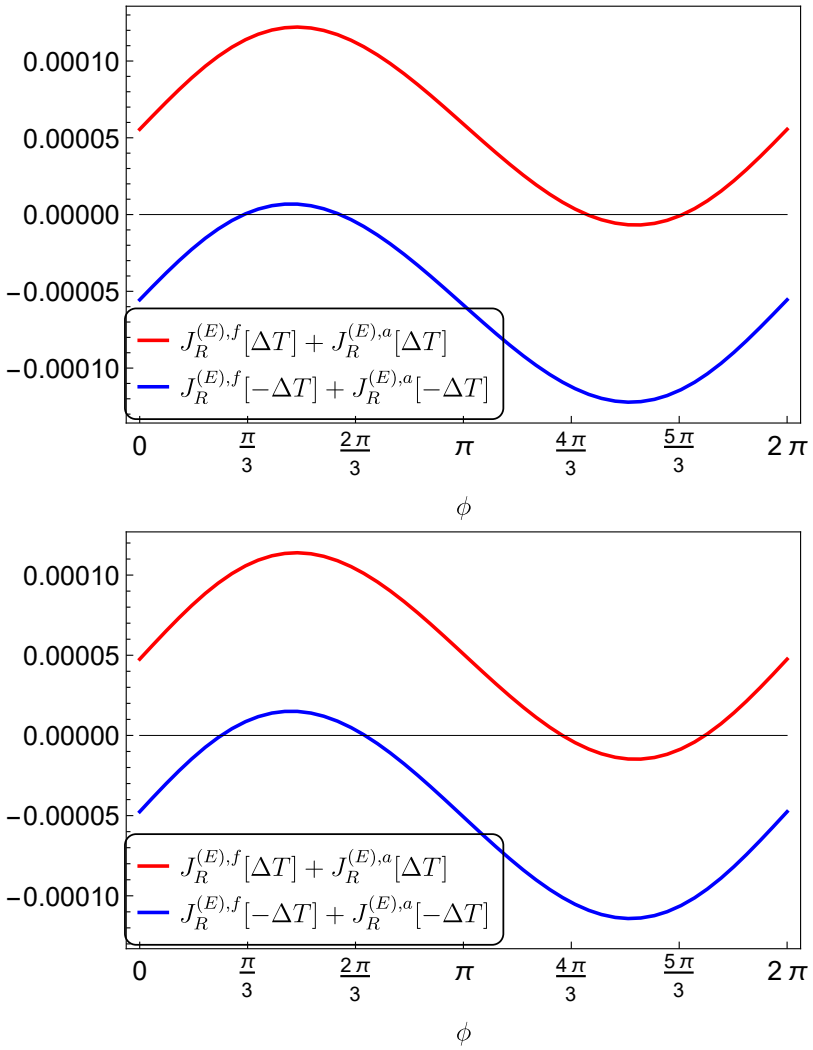

Figure 9.6: Total heat current averaged over the driving the period for forward (red line) and backward (blue line) bias condition as a function of phase lag ϕ in the driving for qutrit (upper panel) and for coupled quantum dot (lower panel) using QME. The heat current due to thermal bias is measured in units of $[k_B T]^2/\hbar$ and the adiabatically pumped heat in one cycle is measured in units of $k_B T$. Parameters: $\epsilon_{\rm rel} = 0.5 k_{\rm BT}$, $\epsilon_{\rm av} = 1 k_B T$, $\delta\epsilon = 2 k_B T$, $\delta\bar{\epsilon} = 0.5 k_B T$ for both systems. $\epsilon_c = 10 k_B T$, $\Gamma_L = 1/20$, $\Gamma_R = 1/5$, $\Delta T = T/1000$ for qutrit and for coupled quantum dots $\Gamma_L = k_B T/20$,$\Gamma_R = k_B T/5$, $U = 0$ and $\Delta T = 2T/1000$.

In the presence of adiabatic driving, the heat current has two components: the heat current due to thermal bias $J_\alpha^{(E),f}(t)$ and the adiabatically pumped heat current $J_\alpha^{(E),a}(t)$. The heat currents averaged over a period are given by $J_R^{(E),f} = \Omega/(2\pi)\int_0^{2\pi/\Omega} dt\, J_R^{(E),f}(t)$ and $J_R^{(E),a} = \Omega/(2\pi)\int_0^{2\pi/\Omega} dt\, J_R^{(E),a}(t)$. We define thermal rectification through the expression

$$R = \frac{\left|\bar{J}_R^{(E),f}[\Delta T] + J_R^{(E),a}[\Delta T]\right| - \left|J_R^{(E),f}[-\Delta T] + J_R^{(E),a}[-\Delta T]\right|}{\left|J_R^{(E),f}[\Delta T] + J_R^{(E),a}[\Delta T]\right| + \left|J_R^{(E),f}[-\Delta T] + J_R^{(E),a}[-\Delta T]\right|}, \tag{9.55}$$

where we consider $\Delta T > 0$. $R = 0$ implies no rectification, whereas $R = \pm 1$ mean perfect rectification. In Fig. 9.6, we study the linear response regime ($\Delta T \ll T$), where the adiabatically pumped heat current is independent of ΔT, namely $J_R^{(E),a}[\Delta T] \equiv J_R^{(E),a}[\Delta T = 0]$. We can therefore fix the driving such that the adibatically pumped heat current always flows from the left reservoir to the right reservoir irrespective of the thermal bias. However, the heat current due to thermal bias changes sign when the thermal bias is inverted. In the setting mentioned above, we have that $J_R^{(E),f}[\Delta T], J_R^{(E),a} > 0$ whereas $J_R^{(E),f}[-\Delta T] < 0$. Hence, as shown in Fig. 9.6, for a particular values of ϕ (for instance for $\phi \sim \phi/3$ in the backward direction (blue line) and for $\phi \sim 4\phi/3$ in the forward direction (red line)), the adiabatically pumped heat current exactly cancels the heat current due to $-\Delta T$ leading to perfect rectification, i.e. $R \to \pm 1$. Note that, the value of ΔT where we get perfect thermal rectification as well as the direction of thermal rectification depend on the details of the driving and system bath coupling.

9.4 SUMMARY

We have presented a formulation, based on Keldysh non-equilibrium Green's functions, to derive the quantum master equations for an adiabatically-driven quantum system for both the bosonic and fermionic cases. Our explicit calculations are performed up to first order in the coupling strength between system and baths and account for both the dissipative as well as level renormalization effects. We expect the extension at higher orders in the coupling strength to be straightforward. Expressions for charge and energy currents have also been derived. The general formulation has been complemented with two examples: a qutrit in contact with bosonic reservoirs and a system of two coupled quantum dots in contact with fermionic reservoirs. In particular, we have studied the effect of eigenstate coherence in the instantaneous as well as the adiabatic regime. We have observed that eigenstate coherence is enhanced in systems close to degeneracy and largely out of equilibrium. We have also noticed a significant effect of eigenstate coherence in thermodynamic quantities such as heat currents and power. Moreover, the effects of eigenstate coherence turns out to be more pronounced in the qutrit system compared to the coupled quantum dots one. In the refrigerator mode, eigenstate coherence tends to decrease the absolute value of the heat current extracted from the cold bath, while increases the power absorbed, thus decreasing the overall efficiency.

10

CONCLUSIONS

In conclusion, we studied different aspects of thermal transport and thermodynamics in static and driven nanoscale devices. We presented models and formulations to study thermal transport properties in nanoscale devices.

In the first three chapters, we presented a brief summary about the field of thermal transport and thermodynamics, mainly focusing on nanoscale devices. We discussed on thermal machines, transport theories, nanoscale devices, thermodynamics at nanoscale and experimental progress in realizing nanoscale devices based on thermal transport.

In Chapter IV, we studied the phenomena of thermal drag in metallic island and quantum dot based devices. A flow of heat current was observed in an unbiased system when it was coupled to a thermally or potentially biased system through Coulomb interactions. We observed that the direction of heat flow in the drag (unbiased) circuit depends on the energy dependence of transition rates. In addition, the presence or absence of energy dependent transition rates in the drive and the drag circuit also played a crucial role in determining the order dependence of the drag heat current on potential or thermal bias. In Chapter V, utilizing the filtering effect of energy dependent transition rates, we presented models based on quantum dots and metallic islands describing absorption refrigerators. In Chapter VI, we studied thermal rectification in a range of devices, including qubits, resonators and quantum dots. We studied the properties of thermal rectification in aforementioned devices in both the weak and strong coupling regime. We observed that the bounds established by thermal rectification in the weak coupling regime gets broken in the strong coupling regime. In addition, we observed that the monotonous behavior of thermal rectification as a function of coupling strength in the weak coupling regime does not hold in the strong coupling regime. In the case of Coulomb coupled quantum dots, we achieved perfect non-local thermal rectification by using energy dependent transition rates. In Chapter VII, we studied thermal transport in two different single electron devices using master equations. In the first setup, we theoretically matched the experimental results for non-linear thermovoltage in a single electron transistor. We observed that the co-tunneling rates play an important role in the low temperature regime. In the second setup, in a single electron transistor setup using master equations we theoretically reproduced the experimental results demonstrating a significant probability of extracting work arbitrarily bigger than the free energy difference in a single protocol realization.

In Chapter VIII, we studied the geometric properties of different thermodynamic quantities for an adiabatically driven system attached to thermal leads kept at slightly different temperatures. We observed that not only the heat currents but also other thermodynamics quantities such as power and efficiency have geometric nature. We observed that the symmetric com-

ponent of the thermal geometric tensor associated with power generation gives dissipation whereas the asymmetric component is non-dissipative in nature and has a Berry-type geometric origin. In addition, we noticed that the heat-work conversion exclusively relies on the geometric contributions to heat and work. In fact, we recovered the Carnot efficiency only in the limit in which transported heat and work were entirely geometric. Lastly in Chapter IX, we presented an alternative derivation of adiabatic quantum master equations using the Keldysh formulation for non-equilibrium Green's functions. We studied the effect of quantum coherence on the adiabatic dynamics of two different devices: 1) qutrit attached to bosonic reservoirs and 2) tunnel coupled quantum dots attached to fermionic reservoirs. In addition, we studied the effect of adiabatic driving and quantum coherence on heat currents, power and thermal rectification.

A

APPENDIX 1

A.1 QUANTUM MASTER EQUATIONS USING FERMI GOLDEN RULE

In this appendix, we will derive the master equation using the Fermi Golden rule. This is the most sought after approach when one needs to study the dynamics of mesoscopic systems where semi-classical Pauli master equation is sufficient and when higher order co-tunneling rates are required. The derivation of master equation in Chapter 9 works well for systems with discrete degrees of freedom, but fails to address the continuous degrees of freedom in the system Hamiltonian, for example metallic islands.

A.1.1 *Sequential tunneling rates*

In this subsection, we will derive sequential tunneling rates for metallic island in contact with fermionic baths as an example for the derivation of master equation using the Fermi golden rule. Similar techniques can be applied to obtain the semi-classical master equation for other discrete quantum systems. Using Fermi golden rule, the first order transition rate from initial state i to final state f is given by

$$\gamma_{i\to f} = \frac{2\pi}{\hbar} \left|\langle f \left| H_{\alpha,S} \right| i \rangle\right|^2 \delta(\epsilon_f - \epsilon_i), \tag{A.1}$$

where $H_{\alpha,S}$ is the coupling Hamiltonian between the bath α and the system S, ϵ_f / i gives the energy of the final/initial state of the device.

The electrostatic energy of the metallic island

$$E_U(n) = E_c n^2 + \kappa, \tag{A.2}$$

where κ does not depend on n. The electrostatic energy required to change the number of electrons from n to $n+1$ is given by:

$$\Delta E_U(n) = E_U(n+1) - E_U(n) = E_c(2n+1) \tag{A.3}$$

Next, we will study electron tunneling through a junction between metallic island and a fermionic bath. The transition rate of an electron from the reservoir (α) into the system (1) changing the number of electron in the island from n to $n+1$ is given by

$$\begin{aligned} \gamma_{kk'}(n) &= \frac{2\pi}{\hbar} \left|\langle k' | H_{\alpha,MD} | k \rangle\right|^2 \delta(\epsilon_{k'1} - \epsilon_{k\alpha} + \Delta E_U(n) - eV_\alpha) \\ &= \frac{2\pi}{\hbar} |t_{kk'}|^2 \delta(\epsilon_{k'1} - \epsilon_{k\alpha} + \Delta E_n), \end{aligned} \tag{A.4}$$

where k represents the state of the electron in the bath which tunnels into state k' in the island, $\Delta E_n = \Delta E_U(n) - eV$ is the total amount of energy an

electron has to overcome in order to tunneling across the junction and V_α is the potential of the bath α. The delta function represents the conservation of energy given by

$$\epsilon_{k\alpha} + eV_\alpha + E_U(n) = \epsilon_{k'1} + E_U(n+1). \tag{A.5}$$

The opposite process when an electron tunnels from the system to the bath, i.e. when the island charge state goes from $n+1 \to n$, has the same transition rate. The total transition rate can be obtained by summing over all possible states, taking into account the occupation of these states given by Fermi distribution. The total transition rate Γ for electron tunneling into and out of the metallic island

$$\begin{aligned} \Gamma_{n\,n+1,\alpha} &= \sum_{kk'} \gamma_{kk'}(n) f_\alpha(\epsilon_{k\alpha}) \left(1 - f_1(\epsilon_{k'1})\right) \\ \Gamma_{n+1\,n,\alpha} &= \sum_{kk'} \gamma_{k'k}(n+1) f_1(\epsilon_{k'1}) \left(1 - f_\alpha(\epsilon_{k\alpha})\right), \end{aligned} \tag{A.6}$$

where the fermi distribution

$$f_\alpha(\epsilon) = \left[1 + e^{\epsilon / k_B T_\alpha}\right]^{-1}. \tag{A.7}$$

We can change the sum over k, k' to an integral over the energy states of the bath and the island. Taking the density of states as well as transition probability to be energy independent (in the low temperature regime, all the processes happen in a narrow band of energy around fermi energy energy), we obtain

$$\begin{aligned} \Gamma_{n\,n+1,\alpha} &= \frac{1}{e^2 R_\alpha} \int d\epsilon f_\alpha(\epsilon) \left(1 - f_1(\epsilon - \Delta E_n)\right) \\ \Gamma_{n+1\,n,\alpha} &= \frac{1}{e^2 R_\alpha} \int d\epsilon f_\alpha(\epsilon) \left(1 - f_1(\epsilon + \Delta E_n)\right), \end{aligned} \tag{A.8}$$

where

$$\frac{1}{R_\alpha} = \frac{4\pi e^2 |t_{kk'}|^2 D_\alpha D_1}{\hbar} \tag{A.9}$$

gives the resistance provided by the tunnel junction, D_α and D_1 are the density of states of the bath and system respectively. Once the transition rates are known, probabilities can be easily calculated using semi-classical master equations. The energy tunneling rates are defined as

$$\begin{aligned} \Gamma^{(E)}_{n\,n+1,\alpha} &= \sum_{kk'} \epsilon_{k\alpha} \gamma_{kk'}(n) f_\alpha(\epsilon_{k\alpha}) \left(1 - f_1(\epsilon_{k'1})\right) \\ \Gamma^{(E)}_{n+1\,n,\alpha} &= \sum_{kk'} \epsilon_{k\alpha} \gamma_{k'k}(n+1) f_1(\epsilon_{k'1}) \left(1 - f_\alpha(\epsilon_{k\alpha})\right). \end{aligned} \tag{A.10}$$

Following similar line of argument as for charge tunneling rates, the energy tunneling rates can be reduced to a simpler form

$$\begin{aligned} \Gamma^{(E)}_{n\,n+1,\alpha} &= \frac{1}{e^2 R_\alpha} \int d\epsilon\, \epsilon f_\alpha(\epsilon) \left(1 - f_1(\epsilon - \Delta E_n)\right) \\ \Gamma^{(E)}_{n+1\,n,\alpha} &= -\frac{1}{e^2 R_\alpha} \int d\epsilon\, \epsilon f_\alpha(\epsilon) \left(1 - f_1(\epsilon + \Delta E_n)\right). \end{aligned} \tag{A.11}$$

A.1.2 *Cotunneling rates*

The co-tunneling process become dominant when the sequential tunneling process is suppressed. At low temperature, when the electrons do not have

enough energy to jump the energy barrier maintained by Coulomb blockade, co-tunneling becomes the dominant process. In other words, when the single electron processes are not energetically allowed, higher-order processes involving virtual state in the system can still be energetically possible. The cotunneling transition rate when an electron tunnels from the bath α to the bath β through the system

$$\gamma^{\text{cot}}_{i\to f} = \frac{2\pi}{\hbar}\sum_{\nu}\frac{\langle f|H_{\alpha,S}|\nu\rangle\langle\nu|H_{\beta,S}|i\rangle}{\epsilon_i-\epsilon_\nu+i\eta}, \tag{A.12}$$

where ν represents the intermediate state. In the cotunneling process, a charge can be transferred from one bath to another without changing the state of the system. The cotunneling process defined for the same bath do not transfer energy or particle, so we will not consider these processes. Summing over all possible states in the baths and system taking the respective distribution into account, the total cotunneling rate can be expressed as

$$\Gamma^{\text{cot}} = \frac{\hbar}{2\pi e^4 R_\alpha R_\beta}\int d\epsilon_{k\alpha}\, d\epsilon_{q1}\, d\epsilon_{q'1}\, d\epsilon_{k'\beta}\, f(\epsilon_{k\alpha})\left(1-f(\epsilon_{q1})\right)\left(1-f(\epsilon_{k'\beta})\right)$$
$$f(\epsilon_{q'1})\left|\frac{1}{\epsilon_{q1}+\delta E_\alpha-\epsilon_{k\alpha}}+\frac{1}{\epsilon_{k'\beta}+\delta\epsilon_\beta-\epsilon_{q'1}}\right|^2\delta(eV+\epsilon_{k\alpha}-\epsilon_{q1}+\epsilon_{q'1}-\epsilon_{k'\beta}), \tag{A.13}$$

where $\delta E_\alpha = E_U(n+1)-E_U(n)-eV_\alpha$ is the energy required to tunnel an electron from the bath α to the system, $\delta E_\beta = E_U(n)-E_U(n-1)+eV_\beta$ is the energy required to tunnel an electron from the system to the bath β, considering the system to be initially in the state n. We define, $eV = eV_\alpha - eV_\beta$. The energy rate when an electron goes from the bath α to the bath β is given by:

$$\Gamma^{\text{cot}} = \frac{\hbar}{2\pi e^4 R_\alpha R_\beta}\int d\epsilon_{k\alpha}\, d\epsilon_{q1}\, d\epsilon_{q'1}\, d\epsilon_{k'\beta}\, \epsilon_{k\alpha}\, f(\epsilon_{k\alpha})\left(1-f(\epsilon_{q1})\right)\left(1-f(\epsilon_{k'\beta})\right)$$
$$f(\epsilon_{q'1})\left|\frac{1}{\epsilon_{q1}+\delta E_\alpha-\epsilon_{k\alpha}}+\frac{1}{\epsilon_{k'\beta}+\delta\epsilon_\beta-\epsilon_{q'1}}\right|^2\delta(eV+\epsilon_{k\alpha}-\epsilon_{q1}+\epsilon_{q'1}-\epsilon_{k'\beta}). \tag{A.14}$$

Eqs. (A.1) and (A.12) can be used to obtain sequential and cotunneling rates for different systems. We will use them to obtain sequential and cotunneling rates for Coulomb coupled metallic islands and quantum dots (see App. for details). The probabilities and currents can be obtained as described in Chapter 9.

B

APPENDIX 2

B.1 KELDYSH-SCHWINGER FORMULATION BASED ON NON-EQUILIBRIUM GREEN'S FUNCTION

Master equations are better suited when the system-bath coupling is weak. When system-bath coupling becomes stronger, higher order terms such as co-tunneling become important. In this regime, Keldysh-Schwinger formulation based on non-equilibrium Green's function describes the dynamics better than the master equation formulation. This formalism has been the normal framework to investigate transport properties when the system is strongly coupled to the reservoirs. It is also very general and flexible and has been used to study electron[9, 359, 360], phonon[365], and spin[366] systems. Although, Keldysh-Schwinger formulation gives an exact result for linear systems, some approximations are required to obtain analytic results for non-linear systems, for example an interacting quantum dot in contact with fermionic baths. There are numerous methods, mostly numeric, to obtain exact results for non-linear systems. We shall start with the definition of heat current. The heat current from the system to the bath α is defined as

$$J_\alpha^{(E)}(t) = -i \left\langle [H_\alpha(t), H(t)] \right\rangle , \tag{B.1}$$

where $H_\alpha(t)$ is the Hamiltonian for bath α and H is the total Hamiltonian of the device. The bath Hamiltonian as well as the system Hamiltonian commutes with H_α. Hence, only the contact Hamiltonian survives. For linear coupling between the system (S) and the bath (as defined in subsection 2.1.3), the heat current can be written as:

$$J_\alpha^{(E)}(t) = \mp 2 \sum_k \epsilon_{k\alpha} V_{k\alpha} \mathrm{Re} \left[G^<_{S\alpha}(t,t) \right] , \tag{B.2}$$

where $G^<_{S\alpha}(t,t') = \pm i \left\langle \alpha^\dagger(t') S(t) \right\rangle$, $\alpha^\dagger$ is the bath creation operator ($c^\dagger_{k\alpha}$ for fermions and $b^\dagger_{k\alpha}$ for bosons) and S is the system operator of the contact Hamiltonian (spin operator in the case of qubit, a fermionic annihilation operator for quantum dot (metallic islands) and the sum of creation and annihilation operator for the resonator). The upper sign is for fermionic system and the lower sign for bosonic system and qubit. The general approach is to define time ordered Green's function in the Keldysh contour and use analytic continuation rules to obtain the lesser Green's function. First of all, we define the time ordered system-bath mixed Green's function as:

$$G^t_{S\alpha}(t,t') = -i \left\langle \mathcal{T} S(t) \alpha^\dagger(t') \right\rangle . \tag{B.3}$$

Using equation of motion, one can express the dynamics of the time ordered mixed Green's function as

$$-i\delta_{t'} G^t_{S\alpha}(t,t') = \epsilon_{k\alpha} G^t_{S\alpha}(t,t') + V_{k\alpha} G^t_{SS}(t,t'). \tag{B.4}$$

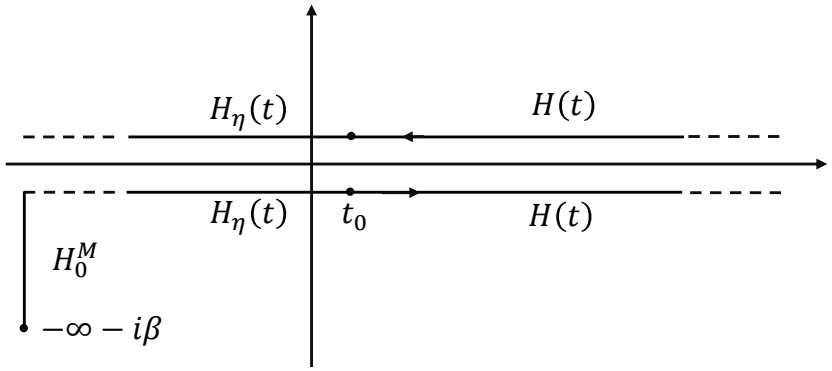

Figure B.1: Sketch of the Keldysh contour. Initially, in the vertical branch from $-\infty - i\beta$ to $-\infty$, the system and bath are allowed to attain a thermal equilibrium at the inverse temperature β. The Matsubara (M) formalism is applied to calculate the initial ensemble average when the baths are at thermal equilibrium. $H_0^M = H_{0,S} + H_B + H_C$, where $H_{0,S}$ is the quadratic part of the system Hamiltonian which can be studied exactly. Then, the interaction (if any present in the system) is switched on adiabatically, $H_\eta(t) = H_{0,S}(t) + H_B(t) + \eta H_{U,S}(t)$ where $H_{U,S}$ is the non-quadratic part of the system Hamiltonian and η is a small number which guarantees the adiabatic switching. The interaction is completely switched on at time t_0. In this thesis, we will study the steady state dynamics, i. e. the long time dynamics such that $t_0 << t$, where t is the observation time. In this limit, the initial statistics are usually washed out.

In a similar manner, the time ordered Green's function for the bath in the absence of system is given by

$$g^t_{k\alpha}(t,t') = \frac{\delta(t-t')}{-i\partial_{t'} - \epsilon_{k\alpha}} \tag{B.5}$$

Using Eq. (B.5) in Eq. (B.4) we obtain

$$G^t_{S\alpha}(t,t') = V_{k\alpha} \int dt_1 G^t_{SS}(t,t_1) g^t_{k\alpha}(t_1,t'). \tag{B.6}$$

Note that, in Eq. (B.6) we have effectively separated the bath and system degrees of freedom. However, the system Green's function has to be calculated with respect to the full Hamiltonian. Using analytic continuation, we obtain the expression for lesser Green's function

$$G^<_{S\alpha}(t,t') = V_{k\alpha} \int dt_1 \left[G^r_{SS}(t,t_1) g^<_{k\alpha}(t_1,t') + G^<_{SS}(t,t_1) g^a_{k\alpha}(t_1,t') \right]. \tag{B.7}$$

In writing Eq. (B.7), we assumed that interactions are coupled adiabatically as shown in Fig. B.1 and the contribution due to the $[t_0, t_0 - i\beta]$ piece vanishes. Note that the sign of lesser Green's function depends on the corresponding statistics. Substituting Eq. (B.7) in Eq. (B.2), the expression for the heat current reduces to

$$J^{(E)}_\alpha(t) = \mp 2 \sum_k \epsilon_{k\alpha} |V_{k\alpha}|^2 \int dt_1 \mathrm{Re} \left[G^r_{SS}(t,t_1) g^<_{k\alpha}(t_1,t) + G^<_{SS}(t,t_1) g^a_{k\alpha}(t_1,t) \right]. \tag{B.8}$$

The retarded/advanced Green's function can be evaluated using equation of motion technique. The expression for the retarded/advanced Green's

function depends on the specific system considered. However, a general relation for lesser Green's function can be obtained in terms of retarded and advanced Green's function using the Dyson equation. Perturbation expansion in term of system-bath coupling leads to following Dyson equation:

$$\hat{G}^t(t,t') = \hat{G}^{0,t}(t,t') + \int dt_1 \int dt_2 \hat{G}^t(t,t_1)\hat{\Sigma}^t(t_1,t_2)\hat{G}^{0,t}(t_2,t'), \tag{B.9}$$

where $\hat{G}^{0,t}$ is the free Green's function of the system and $\Sigma^t(t_1,t_2) = \sum_{k,\alpha} |V_{k\alpha}|^2 g^t_{k\alpha}(t_1,t_2)$ gives the self energy due to system bath coupling. Note that, the Green's functions are now matrices instead of numbers and it accounts for all the degrees of freedom of the system. The system Green's function in the expression for heat current which accounts for the degrees of freedom of the system in contact with the bath is a subset of $\hat{G}^t(t,t')$. We can use the analytic continuation rules to obtain following expression for lesser green's function

$$\hat{G}^<(t,t') = \int dt_1 \int dt_2 \hat{G}^r(t,t_1)\hat{\Sigma}^<(t_1,t_2)\hat{G}^a(t_2,t'). \tag{B.10}$$

Note that above relation for lesser Green's function holds only for long time response[367]. Since, we would be basically interested in the steady state dynamics, Eq. (B.10) would be enough.

B.1.1 *Static systems*

For static systems, the steady state dynamics can be straightforwardly obtained by applying Fourier transformation. For the time-independent case, we can use the relative time Fourier transformation given by:

$$G^t(\epsilon) = \int dt' G^t(t,t') e^{i\epsilon(t-t')}. \tag{B.11}$$

Applying the Fourier transform to Eq. (B.8) and Eq. (B.10), we obtain

$$J^{(E)}_\alpha = \mp 2 \int \frac{d\epsilon}{2\pi}\, \epsilon\, \mathrm{Re}\left[G^r_{SS}(\epsilon)\Sigma^<_\alpha(\epsilon) + G^<_{SS}(\epsilon)\Sigma^a_\alpha(\epsilon)\right], \tag{B.12}$$

for the heat current and

$$\hat{G}^<(\epsilon) = \hat{G}^r(\epsilon)\hat{\Sigma}^<(\epsilon)\hat{G}^a(\epsilon), \tag{B.13}$$

for the lesser Green's function. Using Eq. (B.13), the only unknown factor becomes the retarded Green's function which can be calculated using the equation of motion and is model specific.

B.1.2 *Driven systems*

In this subsection, we will discuss the dynamics of driven quantum system using Floquet formulation along with non-equilibrium Green's functions. We define the green's function for the baths as:

$$\begin{aligned} g^{<,1}_{k\alpha}(t,t') &= \mp i \int \frac{d\epsilon}{2\pi}\, n_\alpha(\epsilon)\rho_{k\alpha}(\epsilon) e^{-i\epsilon(t-t')}, \\ g^{a,1}_{k\alpha}(t,t') &= \int \frac{d\epsilon}{2\pi} \int \frac{d\epsilon'}{2\pi} \frac{\rho_{k\alpha}(\epsilon')}{\epsilon - \epsilon' - i\eta} e^{-i\epsilon(t-t')}, \end{aligned} \tag{B.14}$$

where upper sign is always for fermionic baths whereas the lower sign is for bosonic baths, $n_\alpha(\epsilon)$ represents the distribution of bath α. Considering

periodic driving with period Ω, we apply the Floquet fourier transform given by:

$$\hat{G}^r(t,\epsilon) = \int dt' \hat{G}^r(t,t') e^{i\epsilon(t-t')}$$
$$\hat{G}^r(n,\epsilon) = \frac{1}{\tau}\int_0^\tau \hat{G}^r(t,\epsilon) e^{in\Omega t}. \tag{B.15}$$

The heat current flowing in the lead α can be defined as (see Eq. (B.8)):

$$J_\alpha^{(E)} = J_{\alpha,1}^{(E)} + J_{\alpha,2}^{(E)}, \tag{B.16}$$

where

$$J_{\alpha,1}^{E} = 2\, Re\Big[\int dt_1 \int \frac{d\epsilon}{2\pi} e^{-i\epsilon(t_1-t)} G^r_{S,S}(t,t_1)(i)\epsilon n_\alpha(\epsilon)\Gamma_\alpha(\epsilon)\Big], \tag{B.17}$$

and

$$J_{\alpha,2}^{(E)} = \mp 2\, Re\Big[\int dt_1 \int \frac{d\epsilon}{2\pi} e^{-i\epsilon(t_1-t)} G^<_{S,S}(t,t_1) \int \frac{d\epsilon'}{2\pi} \frac{\epsilon'\Gamma_\alpha(\epsilon')}{\epsilon-\epsilon'-i\eta}\Big]. \tag{B.18}$$

We used the definition for advanced and lesser Green's function for the uncoupled baths (Eqs. (B.14)). Using the Floquet Fourier transformation, we obtain:

$$J_{\alpha,1}^{(E)} = \sum_l \int \frac{d\epsilon}{2\pi} \left[\hat{G}^r_{S,S}(l,\epsilon) - \hat{G}^{r*}_{S,S}(-l,\epsilon)\right] e^{-il\Omega t} \mathcal{Z}^E_\alpha(\epsilon). \tag{B.19}$$

where $\mathcal{Z}^E_\alpha(\epsilon) = -i\epsilon n_\alpha(\epsilon)\Gamma_\alpha(\epsilon)$. We use the relations (see Appendix B.1.2.2 for details),

$$\int \frac{d\epsilon}{2\pi} \mathcal{Z}_\alpha(\epsilon)\Big[G^r_{S,S}(l,\epsilon) - G^{r*}_{S,S}(-l,\epsilon)\Big] = \int \frac{d\epsilon}{2\pi}\Big[\mathcal{Z}^E_\alpha(\epsilon - l\Omega) - \mathcal{Z}^E_\alpha(\epsilon)\Big]$$
$$G^{r*}_{S,S}(-l,\epsilon) + \int \frac{d\epsilon}{2\pi} \mathcal{Z}^E_\alpha(\epsilon)\Big[G^r_{S,S}(l,\epsilon) - G^{r*}_{S,S}(-l,\epsilon+l\Omega)\Big], \tag{B.20}$$

and

$$G^r_{S,S}(l,\epsilon) - \hat{G}^{r*}_{S,S}(-l,\epsilon+l\Omega) = \Big[\sum_n \hat{G}^r(l+n,\epsilon-n\Omega)$$
$$\Big[\hat{\Sigma}^>(\epsilon) - \hat{\Sigma}^<(\epsilon)\Big]\hat{G}^{r*}(n,\epsilon-n\Omega)\Big]_{S,S}. \tag{B.21}$$

Using Eqs. (B.20) and (B.20), Eq. (B.19) reduces to

$$J_{\alpha,1}^{(E)}(t) = \sum_{ln}\int \frac{d\epsilon}{2\pi} e^{-il\Omega t}\Big\{\mathcal{Z}^E_\alpha(\epsilon)\Big[\hat{G}^r(l+n,\epsilon-n\Omega)\Big[\hat{\Sigma}^>(\epsilon-n\Omega)$$
$$-\hat{\Sigma}^<(\epsilon-n\Omega)\Big]\hat{G}^{r*}(n,\epsilon-n\Omega)\Big] + \Big(\mathcal{Z}^E_\alpha(\epsilon-l\Omega) - \mathcal{Z}^E_\alpha(\epsilon)\Big)\hat{G}^{r*}(-l,\epsilon)\Big\}_{S,S} \tag{B.22}$$

In a similar manner using Floquet Fourier transform in Eq. (B.18), one obtains:

$$J_{\alpha,2}^{(E)}(t) = \mp 2Re\Big[\sum_{ln}\int \frac{d\epsilon}{2\pi} e^{-il\Omega t}\hat{G}^r(n+l,\epsilon)\hat{\Sigma}^<(\epsilon)$$
$$\hat{G}^{r*}(n,\epsilon)\int \frac{d\epsilon'}{2\pi}\frac{\epsilon'\Gamma_\alpha(\epsilon')}{\epsilon-(\epsilon'-n\Omega)-i\eta}\Big]_{S,S}. \tag{B.23}$$

After some calculations,

$$J^{(E)}_{\alpha,2}(t) = \mp \sum_{ln} \int \frac{d\epsilon}{2\pi} e^{-il\Omega t} \Big\{ \hat{G}^r(l+n,\epsilon)\hat{\Sigma}^<(\epsilon) \hat{G}^{r^*}(n,\epsilon)\Big[\mathcal{Y}^E_\alpha(\epsilon+n\Omega) - \mathcal{Y}^{E^*}_\alpha(\epsilon+n\Omega+l\Omega)\Big]\Big\}_{S,S}, \quad \text{(B.24)}$$

where

$$\mathcal{Y}^E_\alpha(\epsilon) = \int \frac{d\epsilon'}{2\pi} \epsilon' \Gamma_\alpha(\epsilon') \left[\mathcal{P}\left\{\frac{1}{\epsilon-\epsilon'}\right\} + i\pi\delta(\epsilon-\epsilon')\right], \quad \text{(B.25)}$$

$\mathcal{P}$ represents the principal value. Summing Eq. (B.22) and Eq. (B.24), one obtains the final expression for energy current flowing in individual lead at time t. For driven systems, a finite amount of energy is stored in the contact region, however, on average this current goes to zero. The energy current stored in the contact between bath α and the system at time t

$$J^{(E)}_{\alpha,C}(t) = \frac{d}{dt}\langle H_{C,\alpha}\rangle = \pm 2 \sum_k V_{k\alpha}\, \mathrm{Im}\left[\frac{d}{dt} G^<_{S\alpha}(t,t)\right]. \quad \text{(B.26)}$$

From Eq. (B.26), we have:

$$J^{(E)}_{\alpha,C} = \pm 2 \sum_k |V_{k\alpha}|^2 \int dt_1\, \mathrm{Im}\Big[\frac{d}{dt}\Big(G^r_{S,S}(t,t_1) g^<_\alpha(t_1,t) + G^<_{S,S}(t,t_1) g^a_\alpha(t_1,t)\Big)\Big] \quad \text{(B.27)}$$

The second term in the right hand side goes to zero (the lesser Green's function is imaginary by definition and we neglect the Lamb shift component of the self energy for time being) giving:

$$J^{(E)}_{\alpha,C} = \mp i \sum_k |V_{k\alpha}|^2 \int \frac{d\epsilon}{2\pi} \frac{d}{dt}\Big(G^r_{S,S}(t,\epsilon) + G^{r^*}_{S,S}(t,\epsilon)\Big) g^<_\alpha(\epsilon). \quad \text{(B.28)}$$

After Fourier transformation, we obtain:

$$J^{(E)}_{\alpha,C} = \mp 2i\Omega \sum_k |V_{k\alpha}|^2 \int \frac{d\epsilon}{2\pi} \sum_l l\, \mathrm{Im}\left(G^r_{S,S}(l,\epsilon) e^{-il\Omega t}\right) g^<_\alpha(\epsilon). \quad \text{(B.29)}$$

B.1.2.1 *Adiabatic driving*

The adiabatic contribution can be obtained by expanding Eq. (2.34), upto first order in driving frequency.

$$\mathcal{Z}^h_\alpha(\epsilon+n\Omega) = \mathcal{Z}^h_\alpha(\epsilon) + n\Omega \frac{\partial \mathcal{Z}^h_\alpha(\epsilon)}{\partial\epsilon}$$
$$\mathcal{Y}^h_\alpha(\epsilon+n\Omega) = \mathcal{Y}^h_\alpha(\epsilon) + n\Omega \frac{\partial \mathcal{Y}^h_\alpha(\epsilon)}{\partial\epsilon}. \quad \text{(B.30)}$$

In order to calculate the adiabatic contribution, it is sufficient to take only the zeroth order contribution for the Green's functions[8], $G^r(n,\epsilon) \equiv G^{r,f}(n,\epsilon)$, where $G^{r,f}(n,\epsilon)$ is the Green's function which evolves with the instantaneous Hamiltonian.

B.1.2.2 *Derivation of Eq. (B.20)*

The retarded Green's function can be written in terms of lesser and greater Green's function:

$$\begin{aligned}\hat{G}^r(t,t') &= \theta(t-t')\left[\hat{G}^>(t,t') - \hat{G}^<(t,t')\right] \\ &= -i\theta(t-t')\int d\tau_1 d\tau_2 \hat{G}^r(t,\tau_1)\hat{\Gamma}(\tau_1,\tau_2)\left[\hat{G}^r(t',\tau_2)\right]^*, \quad \text{(B.31)}\end{aligned}$$

where $\hat{\Gamma}(\tau_1,\tau_2) = i\left[\hat{\tilde{\Sigma}}^>(\tau_1,\tau_2) - \hat{\tilde{\Sigma}}^<(\tau_1,\tau_2)\right]$. Taking Floquet Fourier transform, we obtain:

$$\begin{aligned}\hat{G}^r(t,t') = -i\theta(t-t')\sum_{k_1,k_3}\int \frac{d\epsilon}{2\pi}\hat{G}^r(k_1,\epsilon)\hat{\Gamma}(\epsilon) \\ \left[\hat{G}^r(k_3,\epsilon)\right]^* e^{-i(\epsilon(t-t')+\Omega(k_1 t - k_3 t'))}, \quad \text{(B.32)}\end{aligned}$$

and

$$\hat{G}^r(k,\epsilon) = \sum_l \int \frac{d\omega}{2\pi}\frac{\hat{G}^r(l,\omega)\hat{\Gamma}(\omega)\hat{G}^{r^*}(l,\omega)}{\epsilon - \omega - l\Omega + i\eta}. \quad \text{(B.33)}$$

Similarly, the Floquet Fourier transformed advanced Green's function can be written as:

$$\hat{G}^{r^*}(-k,\epsilon+k\Omega) = \sum_l \int \frac{d\omega}{2\pi}\frac{\hat{G}^r(l+k,\omega)\hat{\Gamma}(\omega)\hat{G}^{r^*}(l,\omega)}{\epsilon - \omega - l\Omega_0 - i\eta}. \quad \text{(B.34)}$$

Using Eqs. (B.33) and (B.34), we obtain:

$$\begin{aligned}\hat{G}^r_{\alpha\alpha}(l,\epsilon) - \hat{G}^{r^*}_{\alpha\alpha}(-l,\epsilon+l\Omega_0) = \sum_{\gamma\delta}\sum_n \hat{G}^r_{\alpha\gamma}(l+n,\epsilon-n\Omega_0) \\ \left[\hat{\tilde{\Sigma}}^>_{\gamma\delta}(\epsilon) - \hat{\tilde{\Sigma}}^<_{\gamma\delta}(\epsilon)\right]\hat{G}^{r^*}_{\alpha\delta}(n,\epsilon-n\Omega_0). \quad \text{(B.35)}\end{aligned}$$

C

APPENDIX 3

C.1 KUBO FORMULATION : LINEAR RESPONSE

In this appendix, we will study the linear response regime and define different thermoelectric as well as thermdodynamic parameters in terms of linear response coefficients. To analyze the performance of the adiabatic thermal machines, we need to compute the currents. This can be done by conventional many-body techniques, such as the non-equilibrium Green's function formalism, scattering matrix theory (for systems without many-body interactions), or master equations (for weak coupling between system and reservoirs). In this section, we shall employ a Hamiltonian representation for the temperature difference and a Kubo linear response framework for small ΔT to derive general results. This enables us to analyze the energy dynamics induced by the thermal driving on the same footing with that induced by the time-dependent driving. Here we follow Luttinger's approach [368] to thermal transport which introduces a "gravitational" potential whose gradients induce energy flows akin to the electrical currents induced by gradients of the electrochemical potential. Details of this approach are given in Appendix C.1.1.

We then reintroduce the total Hamiltonian H of Eq. (2.1) which can be expressed as

$$H(t) = H_S(t) + H_B + H_C + H_{th}(t). \tag{C.1}$$

The system Hamiltonian, $H_S(t)$ depends on time through the N slowly and periodically varying parameters (driving potentials) $\vec{X}(t) = \{X_\ell(t)\}$ with $\ell = 1, \ldots, N$, so that $H_S(t) \equiv H_S[\vec{X}(t)]$. The second term describes the two reservoirs $H_B = H_R + H_L$ at thermal equilibrium with a fixed temperature T, which are macroscopic systems of bosonic excitations or fermionic particles. In the latter case, they are held at the same chemical potential $\mu_L = \mu_R = \mu$ and should be described by the grand-canonical Hamiltonian, $H_\alpha \to H_\alpha - \mu N_\alpha$, where N_α denotes the number of particles in reservoir α. The last term in Eq. (C.1) accounts for the fact that the two reservoirs are held at different temperatures and derives from the Luttinger formulation of thermal transport.

C.1.1 *Luttinger theory of thermal transport*

The idea of expressing the thermal difference in a Hamiltonian language was originally introduced by Luttinger [368]. Here, we follow the revised version of Luttinger's theory presented by Tatara in Ref. [369], which we briefly review and adapt in order to deal with a Hamiltonian containing a tunneling contact between the central system and the reservoirs at which the thermal difference is applied. Luttinger's theory is formulated in the continuum starting from a Hamiltonian $H_E(t) = \int d\mathbf{r} h(\mathbf{r}) \psi(\mathbf{r}, t)$, where

$\psi(\mathbf{r},t)$ is a "gravitational" potential. Gradients of the latter induce energy flows $\mathbf{j}^E$ akin to the electrical currents induced by gradients of the electric potential. Such energy flows obey a continuity equation $\dot{h}(\mathbf{r}) = -\partial_{\mathbf{r}} \cdot \mathbf{j}^E(\mathbf{r})$ as a consequence of energy conservation, which motivates the definition

$$H_{\text{Lutt}}(t) = \int_{-\infty}^{t} \mathrm{d}t' \int \mathrm{d}\mathbf{r}\, \mathbf{j}^E(t') \cdot \partial_{\mathbf{r}} \psi(\mathbf{r},t), \tag{C.2}$$

with $\partial_{\mathbf{r}}\psi(\mathbf{r},t) = \partial_{\mathbf{r}} T/T$. Such formulation is consistent with the rate of change of the entropy production,

$$\dot{S} = -\int \mathrm{d}\mathbf{r} \frac{1}{T} \partial_{\mathbf{r}} \cdot \langle \mathbf{j}^E(t) \rangle = -\int \mathrm{d}\mathbf{r} \langle \mathbf{j}^E(t) \rangle \cdot \frac{\partial_{\mathbf{r}} T}{T^2}, \tag{C.3}$$

through the relation $\langle \mathcal{H}_{\text{Lutt}}(t) \rangle = TS$.

Ref. [369] considers the alternative Hamiltonian

$$H_{A_T}(t) = -\int d\mathbf{r}\, \mathbf{j}^E(t') \cdot \vec{A}_T(\mathbf{r},t). \tag{C.4}$$

The Hamiltonians of Eqs. (C.2) and (C.4) coincide in the long-time average. In fact, $\int_{-\infty}^{+\infty} \mathrm{d}t\, H_{\text{Lutt}}(t) = \int_{-\infty}^{+\infty} \mathrm{d}t\, H_{A_T}(t)$ with

$$\partial_t \vec{A}_T(\mathbf{r},t) = \partial_{\mathbf{r}} \psi(\mathbf{r},t) = \partial_{\mathbf{r}} T/T. \tag{C.5}$$

In this way, $\vec{A}_T(\mathbf{r},t)$ and $\psi(\mathbf{r},t)$ behave, respectively, in a similar way as the vector and scalar potentials of electromagnetism. Adapting the definition of Eq. (C.4) to the present case, we define

$$H_{\text{th}}(t) = -\sum_{\alpha=L,R} \mathcal{J}_\alpha^E(t) \xi_\alpha(t), \tag{C.6}$$

where $\xi_\alpha(t)$ plays the same role as the thermal vector potential and the operator representing the energy flux entering reservoir α is given by

$$\mathcal{J}_\alpha^E = \dot{H}_\alpha = -i\,[H_\alpha, H]\,/\hbar. \tag{C.7}$$

Here, H_α is the Hamiltonian of reservoir α. When the chemical potential is the same for all reservoirs, time averaging the mean value of this operator over one period $\tau = 2\pi/\Omega$ directly gives the heat current,

$$J_\alpha^Q = \frac{\Omega}{2\pi} \int_0^{2\pi/\Omega} \mathrm{d}t \langle \mathcal{J}_\alpha^E(t) \rangle. \tag{C.8}$$

The relation between the Luttinger field and the temperature bias, the counterpart of Eq. (C.5), reads

$$\dot{\xi}_\alpha(t) = \delta T_\alpha(t)/T. \tag{C.9}$$

C.1.2 *Adiabatic Response*

Our quantum machine operates in a regime in which both the driving parameters $\vec{X}(t)$ and the temperature bias δT_α (with the associated parameter $\xi_\alpha(t)$) vary in time. Adiabatic driving implies that the driving frequency Ω is small compared to any characteristic frequency of the system's degrees of freedom as well as the relevant relaxation times associated with the coupling to the reservoirs. We can then regard the velocities at which the parameters are changed and the temperature bias as sufficiently small so that

the currents can be computed in linear response in $\dot{\mathbf{X}}$. This procedure was previously introduced in Ref. [340] and it is similar to the one of Ref. [309] for closed driven systems. The adiabatic time evolution of any observable $\mathcal{O}$ is described by the Kubo-like formula

$$\langle \mathcal{O} \rangle(t) = \langle \mathcal{O} \rangle_t + \sum_{\ell=1}^{N} \chi_t^{\mathrm{ad}} \left[\mathcal{O}, \mathcal{F}_\ell \right] \dot{X}_\ell(t) + \sum_{\alpha=L,R} \chi_t^{\mathrm{ad}} \left[\mathcal{O}, \mathcal{J}_\alpha^E \right] \dot{\xi}_\alpha(t). \tag{C.10}$$

Here, the left-hand side denotes an average with respect to the nonequilibrium density matrix, while $\langle \mathcal{O} \rangle_t$ is an average with respect to the equilibrium density matrix of the frozen Hamiltonian $H_t = H_S(t) + H_B + H_C$, $\rho_t = \sum_m p_m |m\rangle\langle m|$, where $p_m = e^{-\beta \varepsilon_m}/Z_t$, $\beta = 1/k_B T$, and $\mathcal{H}_t |m\rangle = \varepsilon_m |m\rangle$. Notice that the instantaneous eigenvectors $|m\rangle$ and eigenenergies ε_m depend on the time t. Here we have introduced the operator

$$\mathcal{F}_\ell = -\frac{\partial H}{\partial X_\ell}, \quad \text{with } \ell = 1, \ldots, N \tag{C.11}$$

which has the interpretation of a force induced by the driving. The adiabatic response functions appearing in Eq. (C.10) take the form

$$\chi_t^{\mathrm{ad}} \left[\mathcal{O}_1, \mathcal{O}_2 \right] = -\frac{i}{\hbar} \int_{-\infty}^{t} \mathrm{d}t' (t - t') \langle \left[\mathcal{O}_1(t), \mathcal{O}_2(t') \right] \rangle_t. \tag{C.12}$$

We have also assumed that the perturbations are switched on at $t_0 = -\infty$.

Within this framework, we can evaluate the adiabatic evolution of any observable. We are particularly interested in the energy current flowing into the coldest reservoir and the induced forces. Similar to the definition in Eq. (8.1), we find it convenient to define the $N+1$-dimensional force vector

$$\mathcal{F} = (\vec{\mathcal{F}}, \mathcal{J}_R^E). \tag{C.13}$$

Using this notation, the adiabatic dynamics for the forces and the energy current into the coldest reservoir can be written as

$$\langle \mathcal{F} \rangle(t) = \langle \mathcal{F} \rangle_t + \underline{\underline{\mathbf{\Lambda}}}(\vec{X}) \cdot \dot{\mathbf{X}}. \tag{C.14}$$

As expected, the physical response depends on the two Luttinger parameters $\xi_L(t)$ and $\xi_R(t)$ only through the temperature bias $\dot{X}_{N+1}(t) = \Delta T(t)/T$, as can be seen using Eqs. (C.23) and (C.24). In Eq. (C.14), we introduce the response matrix $\underline{\underline{\mathbf{\Lambda}}}(\mathbf{X})$ with elements defined as

$$\Lambda_{\mu,\nu}(\vec{X}) = \begin{cases} \chi_t^{\mathrm{ad}} \left[\mathcal{F}_\mu, \mathcal{F}_\nu \right] & \mu \leq N \\ \sum_{\alpha=L,R} \chi_t^{\mathrm{ad}} \left[\mathcal{J}_\alpha^E, \mathcal{F}_\nu \right] & \mu = N+1 \end{cases} \tag{C.15}$$

Note that in deriving the linear response expression for the current, one should neglect the term H_t^{th}, which would lead to a "diamagnetic" component of the heat current [369]. The notation in Eq. (C.15) highlights the fact that the $\Lambda_{\mu,\nu}(\vec{X})$ depend on time only through the parameters $\vec{X}$.

As the coefficients of Eq. (C.15) are evaluated with respect to the frozen equilibrium density matrix, they obey the Onsager relations [340, 370]

$$\Lambda_{\mu,\nu}(\vec{X}, \vec{B}) \quad = \quad s_\mu s_\nu \Lambda_{\nu,\mu}(\vec{X}, -\vec{B}), \tag{C.16}$$

where $s_\nu = \pm$ for operators $\mathcal{F}_\nu$ which are even/odd under time reversal. In view of its relevance for time-reversal symmetry, we made a possible dependence on an applied magnetic field $\vec{B}$ explicit here, but will suppress it in the following unless necessary.

C.1.2.1 *Identities satisfied by the adiabatic susceptibilities*

In order to prove the identities of Eq. (C.23), satisfied by the adiabatic susceptibilities for the thermal driving corresponding to the frozen Hamiltonian H_t, we proceed by writing the following equation satisfied by the current operators,

$$\mathcal{J}_L^E(t) + \mathcal{J}_R^E(t) = \dot{H}_S(t), \tag{C.17}$$

where $\dot{H}_S$ encloses all the terms of H_t corresponding to the central system and contacts between system and reservoirs. All the operators are expressed in Heisenberg representation with respect to $\mathcal{H}_t$

$$\sum_{\alpha,\beta=L,R} \chi_t^{\rm ad}\left[\mathcal{J}_\alpha^E, \mathcal{J}_\beta^E\right] = \chi_t^{\rm ad}\left[\dot{H}_S, \dot{H}_S\right] = 0. \tag{C.18}$$

In order to prove that the right-hand side (rhs) of this equation is zero we start from the definition of the adiabatic susceptibility,

$$\chi_t^{\rm ad}\left[\dot{H}_S, \dot{H}_S\right] = -i \lim_{\omega\to 0} \partial_\omega \chi_{\dot{S},\dot{S}}(\omega) = \lim_{\omega\to 0} \frac{{\rm Im}[\chi_{\dot{S},\dot{S}}(\omega)]}{\omega}, \tag{C.19}$$

being $\chi_{\dot{S},\dot{S}}(\omega)$ the Fourier transform of the susceptibility $\chi_{\dot{S},\dot{S}}(t-t') = -i\theta(t-t')\langle\left[\dot{H}_S(t), \dot{H}_S(t')\right]\rangle_t$. Since all the mean values correspond to the equilibrium frozen Hamiltonian H_t, we have $\chi_{\dot{S},\dot{S}}(t-t') = \partial_t\partial_{t'}\chi_{S,S}(t-t')$, being $\chi_{S,S}(t-t') = -i\theta(t-t')\langle[H_S(t), H_S(t')]\rangle_t$. Hence,

$$\chi_{\dot{S},\dot{S}}(\omega) = -\omega^2 \chi_{S,S}(\omega). \tag{C.20}$$

For a system with a bounded spectrum, $\chi_t^{\rm ad}\left[\dot{H}_S, \dot{H}_S\right] = 0$ when the limit $\omega \to 0$ is evaluated in Eq. (C.19). In fact, introducing the Lehmann representation in $\chi_{S,S}(\omega)$ and using (C.20) and (C.19) we get

$$\begin{aligned}\chi_t^{\rm ad}\left[\dot{H}_S, \dot{H}_S\right] = \pi \lim_{\omega\to 0} \omega^2 \sum_{n,m} p_m |\langle m|H_S|n\rangle|^2 \\ \times \left[\delta(\omega - (\varepsilon_m - \varepsilon_n)) - \delta(\omega - (\varepsilon_n - \varepsilon_m))\right]\end{aligned} \tag{C.21}$$

with $H_t|m\rangle = \varepsilon_m|m\rangle$. In the latter equation $|\langle m|H_S|n\rangle|^2$ is finite for a system with a bounded spectrum, while $\sum_{n,m}\left[\delta(\omega - (\varepsilon_m - \varepsilon_n)) - \delta(\omega - (\varepsilon_n - \varepsilon_m))\right]$ is the density of states for the excitations of the full system. Typically, the latter function is gapped or has a power-law behavior $\sim |\omega|^\gamma$ with $\gamma > 0$, which proves the rhs of Eq. (C.18).

Using Eq. (C.18), we get the identities of Eq. (C.23). A similar argument can be elaborated for the identities related to the response functions combining energy currents and ac-driving forces. In that case, we can prove

$$\begin{aligned}\sum_{\alpha=L,R} \chi_t^{\rm ad}\left[\mathcal{J}_\alpha^E, \mathcal{F}_l\right] = \chi_t^{\rm ad}\left[\dot{H}_S, \mathcal{F}_l\right] = 0, \\ \sum_{\alpha=L,R} \chi_t^{\rm ad}\left[\mathcal{F}_l, \mathcal{J}_\alpha^E\right] = \chi_t^{\rm ad}\left[\mathcal{F}_l, \dot{H}_S\right] = 0,\end{aligned} \tag{C.22}$$

following similar reasoning as with Eq. (C.18).

Summarizing, the adiabatic response functions in which the energy current enters are

$$\begin{aligned}\chi_t^{\rm ad}\left[\mathcal{J}_\alpha^E, \mathcal{J}_\alpha^E\right] &= \chi_t^{\rm ad}\left[\mathcal{J}_{\bar{\alpha}}^E, \mathcal{J}_{\bar{\alpha}}^E\right] \\ \chi_t^{\rm ad}\left[\mathcal{J}_\alpha^E, \mathcal{J}_\alpha^E\right] &= -\chi_t^{\rm ad}\left[\mathcal{J}_\alpha^E, \mathcal{J}_{\bar{\alpha}}^E\right], \qquad \text{(C.23)} \\ \chi_t^{\rm ad}\left[\mathcal{F}_l, \mathcal{J}_\alpha^E\right] &= -\chi_t^{\rm ad}\left[\mathcal{F}_l, \mathcal{J}_{\bar{\alpha}}^E\right], \\ \chi_t^{\rm ad}\left[\mathcal{J}_\alpha^E, \mathcal{F}_l\right] &= -\chi_t^{\rm ad}\left[\mathcal{J}_{\bar{\alpha}}^E, \mathcal{F}_l\right], \qquad \text{(C.24)}\end{aligned}$$

up to some function that vanishes when averaging over one period. In the above equations $\bar{\alpha}$ denotes the reservoir opposite to α.

C.1.2.2 *Lehmann representation for the thermoadiabatic tensor*

Performing a Fourier transform in the adiabatic susceptibilities entering the of Eq. (C.15), we see that the elements of this tensor can be expressed as

$$\Lambda_{\mu,\nu}(\vec{X}) = -i\partial_\omega \chi_{\mu,\nu}(\omega)|_{\omega=0} = \lim_{\omega\to 0} \frac{\mathrm{Im}[\chi_{\mu,\nu}(\omega)]}{\omega}, \tag{C.25}$$

being $\chi_{\mu,\nu}(\omega)$ the Fourier transform of the susceptibility $\chi_{\mu,\nu}(t-t') = -i\theta(t-t')\langle\left[\mathcal{F}_\mu(t), \mathcal{F}_\nu(t')\right]\rangle_t$. Using the notation $\mathcal{F}_\mu = -\partial_\mu \mathcal{H}_t$ and expressing the susceptibility in the Lehmann representation we have

$$\begin{aligned}\chi_{\mu,\nu}(\omega) &= \hbar \sum_{n,m} p_m \left(\varepsilon_m - \varepsilon_n\right)^2 \left[\frac{\langle \partial_\mu m|n\rangle\langle n|\partial_\nu m\rangle}{\omega - (\varepsilon_m - \varepsilon_n) + i\eta}\right. \\ &\quad \left. - \frac{\langle \partial_\nu m|n\rangle\langle n|\partial_\mu m\rangle}{\omega - (\varepsilon_n - \varepsilon_m) + i\eta}\right],\end{aligned} \tag{C.26}$$

with $\eta = 0^+$. We have used the following identities calculated from $\mathcal{H}_t|n\rangle = \varepsilon_n|n\rangle$ and $\langle n|\partial_\mu\left(\mathcal{H}_t|m\rangle\right)$

$$\begin{aligned}\langle n|\partial_\mu \mathcal{H}_t|m\rangle &= \left(\varepsilon_m - \varepsilon_n\right)\langle n|\partial_\mu m\rangle + \delta_{n,m}\partial_\mu \varepsilon_m, \\ \langle m|\partial_\mu \mathcal{H}_t|n\rangle &= \left(\varepsilon_m - \varepsilon_n\right)\langle \partial_\mu m|n\rangle + \delta_{n,m}\partial_\mu \varepsilon_m,\end{aligned} \tag{C.27}$$

Calculating the derivative as indicated in Eq. (C.25), we have $\Lambda_{\mu,\nu}(\vec{X}) = \Lambda^A_{\mu,\nu}(\vec{X}) + \Lambda^S_{\mu,\nu}(\vec{X})$, with the antisymmetric and symmetric components given by

$$\begin{aligned}\Lambda^S_{\mu,\nu}(\vec{X}) = \quad & \hbar\pi \lim_{\omega\to 0} \sum_{n,m} p_m \frac{\left(\varepsilon_n - \varepsilon_m\right)^2}{\omega} \mathrm{Re}[\langle \partial_\mu m|n\rangle\langle n|\partial_\nu m\rangle] \\ & \times \left[\delta(\omega - (\varepsilon_m - \varepsilon_n)) - \delta(\omega - (\varepsilon_n - \varepsilon_m))\right] \\ & \Lambda^A_{\mu,\nu}(\vec{X}) = 2\hbar \sum_m p_m \,\mathrm{Im}\left[\langle \partial_\mu m|\partial_\nu m\rangle\right],\end{aligned} \tag{C.28}$$

D

APPENDIX 4

D.1 MASTER EQUATIONS FOR TWO CAPACITIVELY-COUPLED ISLANDS

The expressions for the master equations which involve all possible sequential and co-tunneling particle transition rates are

$$\mathbf{M}\cdot\begin{pmatrix} p_{n_1,n_2} \\ p_{n_1+1,n_2} \\ p_{n_1,n_2+1} \\ p_{n_1+1,n_2+1} \end{pmatrix} = \begin{pmatrix} 0 \\ 0 \\ 0 \\ 1 \end{pmatrix}, \tag{D.1}$$

where the columns of the transition matrix $\mathbf{M}$ are given by

$$\mathbf{M}[1] = \begin{pmatrix} -\sum_{\alpha\nu}\left[\Gamma^{(c)}_{\nu,1}(n_1,n_2)+\Gamma^{(c)}_{\alpha,2}(n_1,n_2)+\gamma^{(c)}_{\alpha\nu}(n_1,n_2)\right] \\ \sum_{\nu}\Gamma^{(c)}_{1,\nu}(n_1,n_2) \\ \sum_{\alpha}\Gamma^{(c)}_{2,\alpha}(n_1,n_2) \\ \sum_{\alpha\nu}\gamma^{(c)}_{\alpha\nu}(n_1+1,n_2+1) \end{pmatrix},$$

$$\mathbf{M}[2] = \begin{pmatrix} \sum_{\nu}\Gamma^{(c)}_{\nu,1}(n_1,n_2) \\ -\sum_{\alpha\nu}\left[\Gamma^{(c)}_{1,\nu}(n_1,n_2)+\Gamma^{(c)}_{\alpha,2}(n_1+1,n_2)+\gamma^{(c)}_{\alpha\nu}(n_1+1,n_2)\right] \\ \sum_{\alpha\nu}\gamma^{(c)}_{\alpha\nu}(n_1,n_2+1) \\ \sum_{\alpha}\Gamma^{(c)}_{2,\alpha}(n_1+1,n_2) \end{pmatrix},$$

$$\mathbf{M}[3] = \begin{pmatrix} \sum_{\alpha}\Gamma^{(c)}_{\alpha,2}(n_1,n_2) \\ \sum_{\alpha\nu}\gamma^{(c)}_{\alpha\nu}(n_1+1,n_2) \\ -\sum_{\alpha\nu}\left[\Gamma^{(c)}_{2,\alpha}(n_1,n_2)+\Gamma^{(c)}_{\nu,1}(n_1,n_2+1)+\gamma^{(c)}_{\alpha\nu}(n_1,n_2+1)\right] \\ \sum_{\nu}\Gamma^{(c)}_{1,\nu}(n_1,n_2+1) \end{pmatrix},$$

and

$$\mathbf{M}[4] = \begin{pmatrix} 1 \\ 1 \\ 1 \\ 1 \end{pmatrix}. \tag{D.2}$$

$p(n_i,n_j)$ gives the occupation probability for the states (n_i,n_j), $\alpha=\{\mathrm{L2},\mathrm{R2}\}$ and $\nu=\{\mathrm{L1},\mathrm{R1}\}$. The sequential tunneling rates $\Gamma^{(c)}_{\alpha,\nu}(n_1,n_2)$ are given by Eqs. (4.6) and (4.7) whereas the co-tunneling rates $\gamma^{(c)}_{\alpha\nu}(n_1,n_2)$ are given in Appendix D.2. From the conservation of probability, i.e.

$$p(n_1,n_2)+p(n_1+1,n_2)+p(n_1,n_2+1)+p(n_1+1,n_2+1)=1,$$

the master equations can be solved to obtain the probabilities in terms of transition rates.

D.2 CHARGE AND HEAT TRANSITION RATES FOR CO-TUNNELING

Assuming small biases and low temperature, only four states for the occupation of the islands need to be taken into account. When the initial state is (n_1, n_2), such transition rates are associated to an electron reaching island 2 from lead α =L2, R2 and another electron reaching island 1 from lead ν = L1, R1 and can be written as (see Appedix A)

$$\Gamma_{\alpha\nu}^{\mathrm{cot(c/h)}}(n_1, n_2) = \frac{1}{e^2\mathcal{R}_\alpha}\frac{1}{e^2\mathcal{R}_\nu} H_{n_1,n_2}^{(\mathrm{c/h})}\left(\delta U_2, \delta U_1 - eV_\nu, \delta U_1 + \delta U_2 + E_I - eV_\nu\right), \tag{D.3}$$

where,

$$H_{n_1,n_2}^{(\mathrm{c/h})}(E_1, E_2, E_3) = \frac{\hbar}{2\pi}\int_{-\infty}^{\infty} d\xi F_{\alpha 2}^{(\mathrm{c/h})}(-\xi) F_{\nu 1}^{(c)}(\xi + E_3) \left|\frac{1}{\xi + E_1 - i\eta} - \frac{1}{\xi + E_3 - E_2 - i\eta}\right|^2 \tag{D.4}$$

is a function whose first and second arguments represent the intermediate energy states due to tunneling in island 2 and island 1, respectively, while the third argument represents the total change in energy of the cotunnelling process. Similarly, when the initial state is $(n_1 + 1, n_2 + 1)$, the transition rates are associated to an electron reaching island 2 from lead α =L2, R2 and another electron reaching island 1 from lead ν =L1, R1 and can be written as

$$\Gamma_{\alpha\nu}^{\mathrm{cot(c/h)}}(n_1 + 1, n_2 + 1) = \frac{1}{e^2\mathcal{R}_\alpha}\frac{1}{e^2\mathcal{R}_\nu} H_{n_1+1,n_2+1}^{(\mathrm{c/h})}\left(-\delta U_2 - E_I, -\delta U_1 - E_I + eV_\nu, -\delta U_1 - \delta U_2 - E_I + eV_\nu\right). \tag{D.5}$$

$$H_{n_1+1,n_2+1}^{(\mathrm{c/h})}(E_1, E_2, E_3) = \frac{\hbar}{2\pi}\int_{-\infty}^{\infty} d\xi\, G_{2\alpha}^{(\mathrm{c/h})}(\xi) G_{1\nu}^{(c)}(-\xi - E_3) \left|\frac{1}{\xi + E_1 - i\eta} - \frac{1}{\xi + E_3 - E_2 - i\eta}\right|^2 \tag{D.6}$$

Analogously, the expressions relative the remaining initial states $(n_1 + 1, n_2)$ and $(n_1, n_2 + 1)$ can be written as

$$\Gamma_{\alpha\nu}^{\mathrm{cot(c/h)}}(n_1 + 1, n_2) = \frac{1}{e^2\mathcal{R}_\alpha}\frac{1}{e^2\mathcal{R}_\nu} H_{n_1+1,n_2}^{(\mathrm{c/h})}\left(\delta U_2 + E_I, -\delta U_1 + eV_\nu, -\delta U_1 + \delta U_2 + eV_\nu\right) \tag{D.7}$$

and

$$\Gamma_{\alpha\nu}^{\mathrm{cot(c/h)}}(n_1, n_2 + 1) = \frac{1}{e^2\mathcal{R}_\alpha}\frac{1}{e^2\mathcal{R}_\nu} H_{n_1,n_2+1}^{(\mathrm{c/h})}\left(-\delta U_2, \delta U_1 + E_I - eV_\nu, \delta U_1 - \delta U_2 - eV_\nu\right), \tag{D.8}$$

respectively, where

$$H_{n_1+1,n_2}^{(\mathrm{c/h})}(E_1, E_2, E_3) = \frac{\hbar}{2\pi}\int_{-\infty}^{\infty} d\xi F_{\alpha 2}^{(\mathrm{c/h})}(-\xi) G_{1\nu}^{(c)}(-\xi - E_3) \left|\frac{1}{\xi + E_1 - i\eta} - \frac{1}{\xi + E_3 - E_2 - i\eta}\right|^2. \tag{D.9}$$

$$H^{(c/h)}_{n_1,n_2+1}(E_1,E_2,E_3) = \frac{\hbar}{2\pi}\int_{-\infty}^{\infty} d\xi G^{(c/h)}_{2\alpha}(\xi) F^{(c)}_{\nu 1}(\xi+E_3) \left|\frac{1}{\xi+E_1-i\eta} - \frac{1}{\xi+E_3-E_2-i\eta}\right|^2. \quad \text{(D.10)}$$

We could compute the integrals in Eqs. (D.4) and (D.9) exactly at first order in ΔT and for arbitrary V using the standard approaches[177, 73, 58] (see App. D.3). Note, in particular, that the master equations are affected by the co-tunneling processes that involve electrodes on different circuites, since they change the occupations of the islands (see App. D.1).

D.2.1 *Derivation*

The co-tunneling rate in its most general form when one electron enters island 1 and another electron leaves island 2 can be written as:

$$\Gamma^{cot(c)}_{\alpha\nu} = \frac{\hbar}{2\pi e^4 R_\alpha R_\nu}\int dE_\alpha dE_\nu dE_{s_1} dE_{s_2} f_\nu(E_\nu)\left(1-f_\alpha(E_\alpha)\right) f_2(E_{s_2})\left(1-f_1(E_{s_1})\right) \left|\frac{1}{E^+ + E_{s_1} - E_\nu} + \frac{1}{E^- + E_\alpha - E_{s_2}}\right|^2 \delta\left(E_\alpha - E_\nu + E_{s_1} - E_{s_2} + \Delta E\right) = \frac{\hbar(2\pi)^{-1}}{e^4 R_\alpha R_\nu} \int d\xi_\alpha d\xi_\nu F^{(c)}_{\nu 1}(-\xi_\nu) G^{(c)}_{2\alpha}(\xi_\alpha) \left|\frac{1}{E^+ + \xi_\nu} + \frac{1}{E^- + \xi_\alpha}\right|^2 \delta\left(\xi_\alpha + \xi_\nu + \Delta E\right) \quad \text{(D.11)}$$

where, E_j, $j = \{\alpha, \nu, s_i\}$ refers to the energy states of the corresponding leads and islands; ΔE is the total energy change in the co-tunneling process which can be written in terms of change in electrostatic energy and potential bias. Since the temperature of both of the islands is same, the above expression for co-tunneling rate is equally applicable for co-tunneling involving only one island. Also, $G^{(c)}_{2\alpha}$ is the sequential tunneling rate corresponding to the α^{th} reservoir given by Eq. (4.9).

Case 1: $\mathbf{\Delta T = 0}$

When $\Delta T = 0$, we can use the following simplification;

$$G^{(c)}_{2\alpha}(-E) = F^{(c)}_{\nu 1}(E) = F(E)$$

On using above identity and applying delta function in one of the integral, Eq. (D.11) reduces to;

$$\Gamma^{cot(c)}_{\alpha\nu} = \frac{\hbar}{2\pi e^4 R_\alpha R_\nu}\int d\epsilon F(-\epsilon) F(\epsilon+\Delta E) \left|\frac{1}{\epsilon + E_1 - i\eta} - \frac{1}{\epsilon + E_2 - i\eta}\right|^2 \quad \text{(D.12)}$$

where, $E_1 = E^+$; $E_2 = -E^- + \Delta E$ and $\eta \to 0$ is applied to regularize the divergent integral in Eq. (D.11). All the co-tunneling rates involving either two islands or one island can be written in this form with corresponding E_1, E_2 and resistances involved. The regularization method, described in ref. [58, 177], involves the removal of divergent terms using the sequential transition rates.

Using $n(E) = 1/\left(e^{E/k_B T} - 1\right)$, we get

$$F(-\epsilon)F(\epsilon+\Delta E) = -\epsilon\left(\epsilon+\Delta E\right)\left[n(\epsilon+\Delta E) - n(\epsilon)\right] n(\Delta E),$$

$$n(E) = \frac{1}{e^{E/k_B T} - 1} = -\frac{1}{2}\left[1 - i\text{Cot}\left(\frac{iE}{2k_B T}\right)\right].$$

Using the identity,

$$\psi(1-z) - \psi(z) = \pi\text{Cot}(\pi z),$$

we obtain:

$$n(\epsilon + \Delta E) - n(\epsilon) = \frac{i}{2\pi}\left[\psi\left(1 - \left(\frac{i\beta(\epsilon + \Delta E)}{2\pi}\right)\right) - \psi\left(1 - \frac{i\beta\epsilon}{2\pi}\right) - \psi\left(\frac{i\beta(\epsilon + \Delta E)}{2\pi}\right) + \psi\left(\frac{i\beta\epsilon}{2\pi}\right)\right]. \quad \text{(D.13)}$$

Representing,

$$\psi^-(\epsilon') = \psi\left(1 - \frac{i\beta\epsilon'}{2\pi}\right)$$
$$\psi^+(\epsilon') = \psi\left(\frac{i\beta\epsilon'}{2\pi}\right),$$

we may write the co-tunneling rate in complex form as:

$$\Gamma_{\alpha\nu}^{\text{cot(c)}} = \kappa \int_{-\infty}^{\infty} dz\, g(z)\left[\psi^-(z + \Delta E) - \psi^-(z) + \psi^+(z) - \psi^+(z + \Delta E)\right] \left|\frac{1}{z + E_1 - i\eta} - \frac{1}{z + E_2 - i\eta}\right|^2 \quad \text{(D.14)}$$

where $g(z) = z(z + \Delta E)$ and $\kappa = \frac{-i\hbar n(\Delta E)}{4\pi^2 e^4 R_\alpha R_\nu}$. With,

$$I^-(E_1, E_2) = \kappa \int_{-\infty}^{\infty} dz\, g(z)\Delta\psi^-(z) \frac{(E_2 - E_1)^2}{\left[(z + E_1)^2 + \eta^2\right]\left[(z + E_2)^2 + \eta^2\right]} \quad \text{(D.15)}$$

and,

$$I^+(E_1, E_2) = \kappa \int_{-\infty}^{\infty} dz\, g(z)\Delta\psi^+(z) \frac{(E_2 - E_1)^2}{\left[(z + E_1)^2 + \eta^2\right]\left[(z + E_2)^2 + \eta^2\right]} \quad \text{(D.16)}$$

where,

$$\Delta\psi^\pm(-E_i) = \psi^\pm(\Delta E - E_i) - \psi^\pm(-E_i)$$

the co-tunneling rate can be written in compact form as;

$$\gamma_{\alpha\nu}^{(c)} = I^-(E_1, E_2) - I^+(E_1, E_2). \quad \text{(D.17)}$$

1. Calculation of the Residues

To solve the integral in Eq. (D.14), we break it into ψ^+ and ψ^- terms in Eq. (D.15) and Eq. (D.16) to have poles due to the digamma functions only either on upper half or lower half of complex plane. Now, to evaluate I^-, we close our contour in upper complex plane using an infinite radius semi-circle so that we have no poles from ψ^- inside the contour. Hence, the only pole enclosed by the contour is given by;

$$z = -E_i + i\eta$$

The residue for above poles can be calculated to obtain;

$$a_{-1}^{(i)}(I^-) = \frac{\alpha g(i\eta - E_i)\Delta\psi^-\left(-E_i + i\eta\right)\left(E_j - E_i\right)}{2i\eta\left(E_j - E_i + 2i\eta\right)} \tag{D.18}$$

Similarly, to evaluate I^+, we close our contour in the lower complex plane so that we have no poles from ψ^+ inside the contour. Hence, the only pole enclosed by the contour is given by;

$$z = -E_i - i\eta$$

The residue for above pole can be calculated to obtain;

$$a_{-1}^{(i)}(I^+) = \frac{\alpha g(i\eta - E_i)\Delta\psi^+\left(-E_i - i\eta\right)\left(E_j - E_i\right)}{-2i\eta\left(E_j - E_i - 2i\eta\right)} \tag{D.19}$$

2. Calculation of $I(E_1, E_2)$

The integral in Eq. (D.15) can be written as sum of residues as;

$$I^-(E_1, E_2) = \frac{\pi\kappa}{\eta}\sum_{ij}\left[\frac{g\left(-E_i + i\eta\right)\Delta\psi^-\left(-E_i + i\eta\right)\left(E_j - E_i\right)}{\left(E_j - E_i + 2i\eta\right)}\right] \tag{D.20}$$

We Taylor expand in η, the term inside the square bracket of Eq. (D.20). We keep only the first order term in η (which eventually is independent of η as observed from Eq. (D.20)) and we remove the zeroth order term which diverges when $\eta \to 0$. We get:

$$I^-\left(E_1, E_2\right) = 2\pi i\kappa\sum_{ij}\left[\frac{g(-E_i)}{E_i - E_j}\Delta\psi^-(-E_i) + \frac{1}{2}g'(-E_i)\Delta\psi^-(-E_i) - \frac{i\beta}{4\pi}g(-E_i)\Delta\psi_1^-(-E_i)\right] \tag{D.21}$$

where;

$$\Delta\psi_1^{\pm}(-E_i) = \psi_1^{\pm}(\Delta E - E_i) - \psi_1^{\pm}(-E_i)$$

and ψ_1 represents the first derivative of ψ. Next, we will solve integral (D.16) using similar approach. We obtain

$$I^+\left(E_1, E_2\right) = -2\pi i\kappa\sum_{ij}\left[\frac{g(-E_i)}{E_i - E_j}\Delta\psi^+(-E_i) + \frac{1}{2}g'(-E_i)\Delta\psi^+(-E_i) - \frac{i\beta}{4\pi}g(-E_i)\Delta\psi_1^+(-E_i)\right] \tag{D.22}$$

3. Contribution from the semi-circle arcs

To calculate the contribution form the semi-circle arcs, we consider the case for $z \to \infty$. We use following asymptotic expansion for the digamma function

$$\psi(z)\Big|_{z\to\infty} \approx \ln(z) - \frac{1}{2z} + O(z^{-2}). \tag{D.23}$$

Using Eq. (D.23), we obtain

$$\Delta\psi^+(\epsilon) = \psi^+(\epsilon + \Delta E) - \psi^+(\epsilon) = \psi\left(\frac{i\beta}{2\pi}(\epsilon + \Delta E)\right) - \psi\left(\frac{i\beta}{2\pi}\epsilon\right) \approx \frac{\Delta E}{\epsilon} + O(\epsilon^{-2}) \tag{D.24}$$

$$\Delta\psi^{-}(\epsilon) = \psi^{-}(\epsilon + \Delta E) - \psi^{-}(\epsilon) = \psi\left(1 - \frac{i\beta}{2\pi}(\epsilon + \Delta E)\right) - \psi\left(1 - \frac{i\beta}{2\pi}\epsilon\right)$$
$$\approx \frac{\Delta E}{\epsilon} + O(\epsilon^{-2}) \quad \text{(D.25)}$$

and,

$$\left|\frac{1}{z + E_1 - i\eta} - \frac{1}{z + E_2 - i\eta}\right|^2_{z\to\infty} \sim |z|^{-4}.$$

By simple power counting, we find

$$\Gamma^{\text{cot(c)}}_{\alpha\nu}(\text{arc}) \sim \int_{-\pi}^{\pi} d\theta R \cdot R^{-1} \cdot R^{-4} \cdot g(R) f(i\theta) \sim K R^{-4} g(R)$$

where, in this case $g(R) \sim R^2$ which implies the semi-circle arc does not contribute. In general, there is no contribution from the semi-circle arcs if $g(R) \sim R^n$ with $n < 4$.

Final solution for the co-tunneling rate ($\Delta T = 0$ case)

Including all the contributions the co-tunneling rate in the Eq. (D.11) can be written as;

$$\Gamma^{\text{cot(c)}}_{\alpha\nu} = 2\pi i\kappa \sum_{i,j=1,2} \left[\frac{-i\beta}{4\pi} g(-E_i)\left[\Delta\psi_1^{-}(-E_i) - \Delta\psi_1^{+}(-E_i)\right] + \left[\frac{1}{2}g'(-E_i) + \frac{g(-E_i)}{E_i - E_j}\right]\left[\Delta\psi^{+}(-E_i) + \Delta\psi^{-}(-E_i)\right]\right]. \quad \text{(D.26)}$$

2. CO-TUNNELING ENERGY RATES ($\Delta T = 0$ CASE)

The co-tunneling energy rate for a process when an electron tunnels from α into island 2 and at the same time an electron leaves island 1 is given below. In this process, energy flows out of the reservoir α.

$$\Gamma^{\text{cot(h)}}_{\alpha\nu}(out) = \frac{\hbar}{2\pi e^4 R_\alpha R_\nu} \int dE_\alpha dE_\nu dE_{s_1} dE_{s_2}\; E_\alpha\; f_\alpha(E_\alpha)\,(1 - f_\nu(E_\nu))\, f(E_{s_1})$$
$$(1 - f(E_{s_2})\left|\frac{1}{E^+ + E_{s_2} - E_\alpha} + \frac{1}{E^- + E_\nu - E_{s_1}}\right|^2 \delta\left(E_\nu - E_\alpha + E_{s_2} - E_{s_1} + \Delta E\right)$$
$$= \frac{\hbar}{2\pi e^4 R_\alpha R_\nu} \int d\xi_\alpha d\xi_\nu F^{(h)}_{\alpha 2}(-\xi_\alpha) G^{(c)}_{1\nu}(\xi_\nu) \left|\frac{1}{E^+ + \xi_\alpha} + \frac{1}{E^- + \xi_\nu}\right|^2$$
$$\delta\left(\xi_\nu + \xi_\alpha + \Delta E\right) \quad \text{(D.27)}$$

But, when $\Delta T = 0$, $F^{(\text{h})}_{\alpha i}(\Delta E) = \frac{1}{2}\Delta E\, F^{(\text{c})}_{\alpha i}(\Delta E)$. Doing some algebra, we obtain for the co-tunneling energy rates the same expression as for the co-tunneling charge rates (see Eq. (D.26)) with the function 'g' defined differently as,

$$\Gamma^{\text{cot(h)}}_{\alpha\nu}(out) = \Gamma^{\text{cot(c)}}_{\alpha\nu}\left[g(\epsilon) = -\frac{1}{2}\epsilon(\epsilon + \Delta E)\epsilon\right] \quad \text{(D.28)}$$

Similarly, lets define the co-tunneling energy rate for the electrons entering into the reservoir α;

$$\Gamma^{\mathrm{cot(h)}}_{\alpha\nu}(in) = \frac{\hbar}{2\pi e^4 R_\alpha R_\nu}\int dE_\alpha dE_\nu dE_{s_1} dE_{s_2}\;\; E_\alpha\; f_\nu(E_\nu)\,(1-f_\alpha(E_\alpha))\,f(E_{s_2})$$
$$(1-f(E_{s_1})\left|\frac{1}{E^+ + E_{s_1} - E_\nu} + \frac{1}{E^- + E_\alpha - E_{s_2}}\right|^2 \delta\left(E_\alpha - E_\nu + E_{s_1} - E_{s_2} + \Delta E\right) \tag{D.29}$$

We obtain similar co-tunneling rates as in Eq.(D.28) but with different expression for $g(\epsilon)$ given by

$$\Gamma^{\mathrm{cot(h)}}_{\alpha\nu}(in) = \Gamma^{\mathrm{cot(c)}}_{\alpha\nu}\left[g(\epsilon) = -\frac{1}{2}(\epsilon+\Delta E)(\epsilon+\Delta E)\epsilon\right] \tag{D.30}$$

All other co-tunneling energy rates can be written in the form of Eq. (D.28) and Eq. (D.30) with suitable modification for energy parameters and resistances involved.

Co-tunneling rates $\Delta T \neq 0$

In the presence of both thermal and potential bias, we cannot solve the integrals involved in the co-tunneling rates analytically. Although, we can still write the co-tunneling rates in the compact form using Eq. (D.4) and Eq. (D.9). In this section, we will suggest a proper regularization method for integrals in Eq. (D.4) and Eq. (D.9) and simplify it to a form which can be easily integrated numerically. We have;

$$H^{(\mathrm{c/h})}_{n_1,n_2}(E_1,E_2,E_3) = \frac{\hbar}{2\pi}\int_{-\infty}^{\infty} d\xi F^{(\mathrm{c/h})}_{\alpha 2}(-\xi)F^{(c)}_{\nu 1}(\xi+E_3)$$
$$\left|\frac{1}{\xi+E_1-i\eta} - \frac{1}{\xi+E_3-E_2-i\eta}\right|^2 \tag{D.31}$$

Simplifying the term in square modulus, we obtain:

$$H^{(\mathrm{c/h})}_{n_1,n_2}(E_1,E_2,E_3) = \frac{\hbar}{2\pi}\left[\int d\xi\,\frac{F^{(\mathrm{c/h})}_{\alpha 2}(-\xi)F^{(c)}_{\nu 1}(\xi+E_3)}{(\xi+E_1)^2+\eta^2}\right.$$
$$+\int d\xi\,\frac{F^{(\mathrm{c/h})}_{\alpha 2}(-\xi)F^{(c)}_{\nu 1}(\xi+E_3)}{(\xi+E_3-E_2)^2+\eta^2} - 2\int d\xi\, F^{(\mathrm{c/h})}_{\alpha 2}(-\xi)F^{(c)}_{\nu 1}(\xi+E_3)$$
$$\left.\frac{\left[(\xi+E_1)(\xi+E_3-E_2)+\eta^2\right]}{\left[(\xi+E_1)^2+\eta^2\right]\left[(\xi+E_3-E_2)^2+\eta^2\right]}\right] \tag{D.32}$$

Now, lets transform the first two terms in Eq. (D.32) such that $\xi \to z - E_1$ for the first term and $\xi \to z - E_3 + E_2$ for the second term.

$$H^{(\mathrm{c/h})}_{n_1,n_2}(E_1,E_2,E_3) = \frac{\hbar}{2\pi}\left[\int dz\,\frac{F^{(\mathrm{c/h})}_{\alpha 2}(-z+E_1)F^{(c)}_{\nu 1}(z+E_3-E_1)}{z^2+\eta^2}\right.$$
$$+\int d\xi\,\frac{F^{(\mathrm{c/h})}_{\alpha 2}(-z+E_3-E_2)F^{(c)}_{\nu 1}(z+E_2)}{z^2+\eta^2} - 2\int d\xi\, F^{(\mathrm{c/h})}_{\alpha 2}(-\xi)F^{(c)}_{\nu 1}(\xi+E_3)$$
$$\left.\frac{\left[(\xi+E_1)(\xi+E_3-E_2)+\eta^2\right]}{\left[(\xi+E_1)^2+\eta^2\right]\left[(\xi+E_3-E_2)^2+\eta^2\right]}\right] \tag{D.33}$$

We use the approach in reference [177] to regularize the integral, i.e.

$$\lim_{\eta\to 0}\int dz\,\frac{g(z-E_i)}{z^2+\eta^2}\longrightarrow\int dz\,\frac{g(z-E_i)-g(-E_i)}{z^2}.$$

So, when $\eta\to 0$,

$$\begin{aligned}H^{(\mathrm{c/h})}_{n_1,n_2}(E_1,E_2,E_3)=&\frac{\hbar}{2\pi}\\&\Bigg[\int dz\,\frac{F^{(\mathrm{c/h})}_{\alpha 2}(-z+E_1)F^{(c)}_{\nu 1}(z+E_3-E_1)-F^{(\mathrm{c/h})}_{\alpha 2}(E_1)F^{(c)}_{\nu 1}(E_3-E_1)}{z^2}\\&+\int dz\,\frac{F^{(\mathrm{c/h})}_{\alpha 2}(-z+E_3-E_2)F^{(c)}_{\nu 1}(z+E_2)-F^{(\mathrm{c/h})}_{\alpha 2}(E_3-E_2)F^{(c)}_{\nu 1}(E_2)}{z^2}\\&-2\int d\xi\,F^{(\mathrm{c/h})}_{\alpha 2}(-\xi)F^{(c)}_{\nu 1}(\xi+E_3)\,\frac{[(\xi+E_1)(\xi+E_3-E_2)]}{\left[(\xi+E_1)^2\right]\left[(\xi+E_3-E_2)^2\right]}\Bigg]\end{aligned}\tag{D.34}$$

The integrals in Eq. (D.34) are properly regularized and can be numerically evaluated for the case of both thermal and potential bias.

D.3 CHARGE AND HEAT CURRENT IN THE CO-TUNNELING REGIME

The expression for charge and heat currents flowing towards the right reservoir in contact with island 2 is given by

$$\begin{aligned}J^{(\mathrm{c/h})}_{\mathrm{R2}}=&Q^{(c/h)}\Bigg[\left[\Gamma^{\mathrm{cot(c/h)}}_{\mathrm{L1R2}}(n_1,n_2+1)+\Gamma^{\mathrm{cot}(c/h)}_{\mathrm{R1R2}}(n_1,n_2+1)+\Gamma^{(\mathrm{c/h})}_{\mathrm{2,R2}}(n_1,n_2)\right]\\&p(n_1,n_2+1)+\left[\Gamma^{\mathrm{cot(c/h)}}_{\mathrm{L1R2}}(n_1+1,n_2+1)+\Gamma^{\mathrm{cot(c/h)}}_{\mathrm{R1R2}}(n_1+1,n_2+1)\right.\\&\left.+\Gamma^{(\mathrm{c/h})}_{\mathrm{2,R2}}(n_1+1,n_2)\right]p(n_1+1,n_2+1)-\left[\Gamma^{\mathrm{cot(c/h)}}_{\mathrm{L1R2}}(n_1,n_2)+\Gamma^{\mathrm{cot(c/h)}}_{\mathrm{R1R2}}(n_1,n_2)\right.\\&\left.+\Gamma^{(\mathrm{c/h})}_{\mathrm{R2,2}}(n_1,n_2)\right]p(n_1,n_2)-\left[\Gamma^{\mathrm{cot(c/h)}}_{\mathrm{L1R2}}(n_1+1,n_2)+\Gamma^{\mathrm{cot(c/h)}}_{\mathrm{R1R2}}(n_1+1,n_2)\right.\\&\left.+\Gamma^{(\mathrm{c/h})}_{\mathrm{R2,2}}(n_1+1,n_2)\right]p(n_1+1,n_2)\Bigg],\end{aligned}\tag{D.35}$$

where $Q^{(\mathrm{c})}=e$ and $Q^{(h)}=1$. $J^{(\mathrm{c/h})}_{\mathrm{L2}}$ can be written anagously. Eq. (D.35) can be broken down into the one containing only sequential tunneling rates and another one containing only the co-tunneling rates.

E

APPENDIX 5

E.1 MASTER EQUATION

The probability p_{n_1,n_2} that the system is in a state with n_1 and n_2 electrons in QDs 1 and 2 is calculated by solving the following system of equations

$$\mathbf{M} \cdot \begin{pmatrix} p_{0,0} \\ p_{0,1} \\ p_{1,0} \\ p_{1,1} \end{pmatrix} = \begin{pmatrix} 0 \\ 0 \\ 0 \\ 1 \end{pmatrix}, \tag{E.1}$$

where the rows of the transition matrix $\mathbf{M}$ is given by

$$\mathbf{M}[1] = \begin{pmatrix} -\left[\Gamma_{L,1}(0) + \Gamma_{R,1}(0) + \Gamma_{C,2}(0)\right] \\ \Gamma_{2,C}(0) \\ \Gamma_{1,L}(0) + \Gamma_{1,R}(0) \\ 0 \end{pmatrix}^T,$$

$$\mathbf{M}[2] = \begin{pmatrix} 0 \\ \Gamma_{L,1}(1) + \Gamma_{R,1}(1) \\ \Gamma_{C,2}(1) \\ -\left[\Gamma_{1,L}(1) + \Gamma_{1,R}(1) + \Gamma_{2,C}(1)\right] \end{pmatrix}^T,$$

$$\mathbf{M}[3] = \begin{pmatrix} \Gamma_{C,2}(0) \\ -\left[\Gamma_{L,1}(1) + \Gamma_{R,1}(1) + \Gamma_{2,C}(0)\right] \\ 0 \\ \Gamma_{1,L}(1) + \Gamma_{1,R}(1) \end{pmatrix}^T ; \; \mathbf{M}[4] = \begin{pmatrix} 1 \\ 1 \\ 1 \\ 1 \end{pmatrix}^T$$

The first three equations correspond to the master equations where the time-derivatives $\dot{p}_{0,0}$, $\dot{p}_{1,1}$, and $\dot{p}_{0,1}$ are set to zero, while the last equation corresponds to the normalization requirement. The charge current is given by

$$J_L^{(c)} = e\left[p_{0,0}\Gamma_{L,1}(0) + p_{0,1}\Gamma_{L,1}(1) - p_{1,0}\Gamma_{1,L}(0) - p_{1,1}\Gamma_{1,L}(1)\right], \tag{E.2}$$

where e is the electron charge, and the heat current leaving reservoir α is given by

$$\begin{aligned} J_\alpha^{(h)} = {} & p_{0,0}\Gamma_{\alpha,1}(0)\Delta E_{U1}(0) - p_{1,1}\Gamma_{1,\alpha}(1)\Delta E_{U1}(1) \\ & + p_{0,1}\Gamma_{\alpha,1}(1)\Delta E_{U1}(1) - p_{1,0}\Gamma_{1,\alpha}(0)\Delta E_{U1}(0), \end{aligned} \tag{E.3}$$

for $\alpha = \mathrm{L,R}$, and

$$J_{\mathrm{C}}^{(\mathrm{h})} = P_{0,0}\Gamma_{\mathrm{C},2}(0)\Delta U_2(0) - P_{1,1}\Gamma_{2,\mathrm{C}}(1)\Delta U_2(1) + P_{1,0}\Gamma_{\mathrm{C},2}(1)\Delta U_2(1) - P_{0,1}\Gamma_{2,\mathrm{C}}(0)\Delta U_2(0). \quad \text{(E.4)}$$

Note that one can exploit the symmetry of the transitions energies with respect to the common chemical potential when $\theta_1 = \theta_2 = 1/2$ [see Eqs. (5.2) and Fig. 5.1(b)] to restrict the analysis to the range $\theta_1 \geq 1/2$, without loss of generality. In fact, the heat currents relative to the case $\theta_i = \bar{\theta}_i < 1/2$ are equal to the ones obtained with $\theta_i = 1 - \bar{\theta}_i (> 1/2)$, while the charge currents relative to the case $\theta_i = \bar{\theta}_i < 1/2$ are equal in amplitude but with opposite sign with respect to the ones obtained with $\theta_i = 1 - \bar{\theta}_i (> 1/2)$. This can be explicitly verified by substituting $\theta_i \to 1 - \theta_i$ and $\Gamma_{1,\alpha/\alpha,1}(n) \to \Gamma_{1,\alpha/\alpha,1}(1-n)$ in Eqs. (5.2), (E.1), (E.2), (E.3) and (E.4).

E.2 OPTIMAL RATES FOR COOLING POWER AND COP

By substituting the probability P_{n_1,n_2}, solution of Eq. (E.1), into the expression (E.4) for I_{C}^{h} and imposing the detailed balance condition (5.5), we find that $I_{\mathrm{C}}^{h} > 0$ if and only if

$$\begin{aligned} &\Gamma_{1,\mathrm{L}}(0)\Gamma_{\mathrm{R},1}(1)\left(e^{j\eta_{\mathrm{C}}^{\mathrm{h}}(\theta_1-1)} - 1\right) \\ &- \Gamma_{\mathrm{L},1}(1)\left[\Gamma_{1,\mathrm{L}}(0)\left(1 - e^{-j\eta_{\mathrm{C}}^{\mathrm{h}}}\right) + \Gamma_{1,\mathrm{R}}(0)\left(1 - e^{-j\eta_{\mathrm{C}}^{\mathrm{h}}\theta_1}\right)\right] \\ &- \left[\Gamma_{1,\mathrm{L}}(0) + \Gamma_{1,\mathrm{R}}(0)\right]\left[\Gamma_{\mathrm{L},1}(1) + \Gamma_{\mathrm{R},1}(1)\right]\left(e^{j/\eta_{\mathrm{C}}^{\mathrm{r}}} - 1\right) > 0. \end{aligned} \quad \text{(E.5)}$$

Interestingly, the condition (E.5) does not depend on the rates $\Gamma_{\mathrm{C}}^{(\mathrm{in/out})}$ relative to the cooled system, nor on θ_2. In Eq. (E.5), $\eta_{\mathrm{C}}^{\mathrm{h}} = 1 - T/T_{\mathrm{L}}$ is the Carnot efficiency of a heat engine operating between L and R, $\eta_{\mathrm{C}}^{\mathrm{r}} = T_{\mathrm{C}}/(T - T_{\mathrm{C}})$ is the Carnot COP of a refrigerator operating between R and C, and $j = E_{\mathrm{I}}/k_B T$. Restricting to the range $\theta_1 \geq 1/2$ (see App. E.1 for details), the first line of Eq. (E.5) is the only term that can be positive, so that a necessary non-trivial condition to satisfy Eq. (E.5) is that $\theta_1 > 1$.

When Eq. (E.5) is satisfied, at fixed E_{I}, θ_1 and θ_2, we find that I_{C}^{h} is a decreasing function of $\Gamma_{\mathrm{L},1}(1)$ and $\Gamma_{1,\mathrm{R}}(0)$, so that the optimal choice for such parameters is

$$\Gamma_{\mathrm{L},1}(1) = \Gamma_{1,\mathrm{R}}(0) = 0. \quad \text{(E.6)}$$

Now, assuming (E.6), $J_{\mathrm{C}}^{(\mathrm{h})}$ is an increasing function of the remaining rates $\Gamma_{1,\mathrm{L}}(0)$, $\Gamma_{\mathrm{R},1}(1)$, $\Gamma_{2,\mathrm{C}}(0)$, $\Gamma_{\mathrm{C},2}(1)$, so that the optimal choice is to take them as large as possible, compatibly with the validity of the sequential tunneling picture.

E.3 DERIVATION OF THE MASTER EQUATION FOR THE SYSTEM WITH THREE QDS

The Hamiltonian of the system with three QDs can be represented as

$$H_{\mathrm{sys}} = \sum_m \epsilon_m |m\rangle\langle m| + E_{\mathrm{I}}\left(|1,1,0\rangle\langle 1,1,0| + |1,1,1\rangle\langle 1,1,1|\right) + t\left(|1,0,0\rangle\langle 0,0,1| + |1,1,0\rangle\langle 0,1,1| + \mathrm{h.c.}\right), \quad \text{(E.7)}$$

where ϵ_m is the energy of state $|m\rangle$ in the absence of coupling, t is the hopping element between the two tunnel coupled QDs (3 and 1), and E_I represents the inter-dot charging energy between the capacitively-coupled QDs, 1 and 2. Under the assumption that the hopping element t is much smaller than the coupling energy between QDs and reservoirs, in Refs. [108, 109, 110, 111, 112] it was shown that the density matrix ρ (whose components are defined as $\rho_{mn} = \langle m|\rho|n\rangle$) satisfies a modified Liouville equation. In particular, the diagonal components ρ_{mm} satisfy[371]

$$\dot{\rho}_{mm} = -i[H_{\text{sys}}, \rho]_{mm} - \sum_{\alpha,l} \Gamma_{\alpha,ml}\rho_{mm} + \sum_{\alpha,k} \Gamma_{\alpha,km}\rho_{kk}, \tag{E.8}$$

while the off-diagonal components, resulting from coherent tunneling of electrons between QDS 3 and 1, satisfy

$$\dot{\rho}_{mn} = -i[H_{\text{sys}}, \rho]_{mn} - \frac{1}{2}\sum_{l} \left(\Gamma_{ml} + \Gamma_{nl}\right)\rho_{mn}. \tag{E.9}$$

In Eqs. (E.8) and (E.9), the first (Liouville) term contains the system Hamiltonian (E.7), while the other terms describe the coupling of the QDs with the reservoirs. In Eq. (E.9), $|m\rangle = |0,0,1\rangle$ and $|n\rangle = |1,0,0\rangle$ (and viceversa), or $|m\rangle = |0,1,1\rangle$ and $|n\rangle = |1,1,0\rangle$ (and viceversa), since the only non-zero off-diagonal terms are the ones related to electron tunneling between QDs 1 and 3 (with 2 either occupied or unoccupied). Note that Eqs. (E.8) and (E.9) depend explicitly only on the transition rate Γ_{ml}, from state $|m\rangle$ to state $|l\rangle$, which accounts for the transfer of electrons between a QD and the corresponding reservoir $\alpha = \alpha(m,l)$. In particular, the transition rates for tunnelling events between 1 and 3, such as $\Gamma_{\alpha,(0,0,1)(1,0,0)}$ and $\Gamma_{\alpha,(0,1,1)(1,1,0)}$, do not appear in Eqs. (E.8) and (E.9). The rates appearing in Eqs. (E.8) and (E.9) can be expressed as [58]

$$\Gamma_{\alpha,ml} = \hbar^{-1}\gamma_\alpha f_\alpha(\Delta\tilde{E}_{U,ml}), \tag{E.10}$$

where γ_α is the coupling energy between reservoir α and QD, $f_\alpha(\epsilon) = [1 + e^{\epsilon/(k_B T_\alpha)}]^{-1}$ is the reservoir Fermi distribution function, while $\Delta\tilde{E}_{U,ml} = \tilde{E}_U(l) - \tilde{E}_U(m)$ is the transition energy, where $\tilde{E}_U(m) = E_U(n_1, n_2, n_3)$ [see Eq. (5.11)] with the set of occupation numbers corresponding to the state $|m\rangle$.

In order to keep the notation compact, we assign an index to each set of occupation numbers as follows: $(0,0,0) \to 0$, $(1,0,0) \to 1$, $(0,1,0) \to 2$, $(0,0,1) \to 3$, $(1,1,0) \to 4$, $(0,1,1) \to 5$, $(1,0,1) \to 6$ and $(1,1,1) \to 7$. We will show now that the inter-dot tunneling rates, i. e. $\Gamma_{\alpha,31} =\equiv \Gamma_{\alpha,(0,0,1)(1,0,0)}$ and $\Gamma_{\alpha,54} \equiv \Gamma_{\alpha,(0,1,1)(1,1,0)}$, can be obtained by using Eqs. (E.8) and (E.9). [372] Let us consider the component (33) of Eq. (E.8), i. e.

$$\begin{aligned}\dot{\rho}_{33} = &-it\left(\rho_{13} - \rho_{31}\right) - \left(\Gamma_{30} + \Gamma_{35} + \Gamma_{36}\right)\rho_{33} \\ &+ \Gamma_{03}\,\rho_{00} + \Gamma_{53}\,\rho_{55} + \Gamma_{63}\,\rho_{66},\end{aligned} \tag{E.11}$$

where $\Gamma_{mn} \equiv \Gamma_{\alpha,mn}$ since only one reservoir is attached to each quantum dot and hence removing the bath index does not introduce any ambiguity. In the steady state ($\dot{\rho} = 0$), the components (31) and (54) of Eq. (E.9) can be written, respectively, as

$$\rho_{31} = \frac{t\left(\rho_{33} - \rho_{11}\right)}{\epsilon_3 - \epsilon_1 - i\frac{\tilde{\Gamma}^{(o)}}{2}} \tag{E.12}$$

and

$$\rho_{54} = \frac{t\,(\rho_{55} - \rho_{44})}{\epsilon_5 - \epsilon_4 - E_{\rm I} - i\frac{\tilde{\Gamma}^{(1)}}{2}}, \tag{E.13}$$

where $\tilde{\Gamma}^{(0)} = \Gamma_{36} + \Gamma_{35} + \Gamma_{30} + \Gamma_{16} + \Gamma_{14} + \Gamma_{10}$ accounts for all the processes which lead to the decay of the states $|3\rangle$ and $|1\rangle$, and $\tilde{\Gamma}^{(1)} = \Gamma_{53} + \Gamma_{52} + \Gamma_{57} + \Gamma_{41} + \Gamma_{42} + \Gamma_{47}$ accounts for all the processes which lead to the decay of the states $|0,1,1\rangle$ and $|1,1,0\rangle$. By substituting Eq. (E.12) into Eq. (E.11), with $\rho_{13} = \rho_{31}^*$, the latter equation will contain only diagonal elements of the density matrix, thus representing an ordinary master equation of the form

$$\dot{p}_3 = \sum_{l=0,5,6} (-\Gamma_{3l}\, p_3 + \Gamma_{l3}\, p_l) - \Gamma_{31} p_3 + \Gamma_{13} p_1, \tag{E.14}$$

where $p_m = \rho_m$ represents the probability for the state $|m\rangle$. In Eq. (E.14), the two terms (in Γ_{31} and Γ_{13}) accounting for the transitions between states $|0,0,1\rangle$ and $|1,0,0\rangle$, when QD 2 is unoccupied, now appear. The associated inter-dot tunneling rate takes the form

$$\Gamma_{31} = \frac{t^2 \tilde{\Gamma}^{(0)}}{(\epsilon_3 - \epsilon_1)^2 + \left(\frac{\tilde{\Gamma}^{(0)}}{2}\right)^2}. \tag{E.15}$$

Similarly, using Eq. (E.13) in the expression for $\dot{\rho}_{55}$ or $\dot{\rho}_{44}$, one obtains the inter-dot tunneling rate

$$\Gamma_{54} = \frac{t^2 \tilde{\Gamma}^{(1)}}{(\epsilon_3 - \epsilon_1 - E_{\rm I})^2 + \left(\frac{\tilde{\Gamma}^{(1)}}{2}\right)^2} \tag{E.16}$$

in the case where QD 2 is occupied. Note that both inter-dot tunneling rates have a Lorentzian profile.

The relevant heat currents can be written as

$$J_{\rm C}^{(\rm h)} = \sum_{m,l} \Delta\tilde{E}_{U,ml}\, (\Gamma_{ml}\, p_m - \Gamma_{lm}\, p_l)\,, \tag{E.17}$$

where the sum runs over the indices $(ml) = (02)$, (14), (35), (67) for the cooling power $J_{\rm C}^{(\rm h)}$, and over the values $(ml) = (03)$, (16), (25), (47) for the input heat $J_{\rm L}^{(\rm h)}$.

E.4 HEAT CURRENTS IN THE SYSTEM WITH METALLIC ISLANDS

Since MIs presents a continuum of states, the heat exchanged in a single electron transition is not fixed by the electrostatic energy difference as in Eq. (5.16), but it depends on the energy of the electron that is tunneling. We thus need to define the following heat rates [146]

$$\Gamma_{ml}^{h,\rm out} = \frac{1}{e^2 R_{\alpha\beta}} \int d\epsilon\, \epsilon\, \mathcal{N}_\alpha(\epsilon) \mathcal{N}_\beta(\epsilon - \Delta\tilde{E}_{U,lm}) f_\alpha(\epsilon)\, \left[1 - f_\beta(\epsilon - \Delta\tilde{E}_{U,lm})\right], \tag{E.18}$$

and

$$\Gamma_{ml}^{h,\rm in} = \frac{1}{e^2 R_{\alpha\beta}} \int d\epsilon\, (\epsilon - \Delta\tilde{E}_{U,lm}) \mathcal{N}_\alpha(\epsilon) \mathcal{N}_\beta(\epsilon - \Delta\tilde{E}_{U,lm}) f_\alpha(\epsilon) \left[1 - f_\beta(\epsilon - \Delta\tilde{E}_{U,lm})\right]. \tag{E.19}$$

$\Gamma^{h,\text{out}}_{ml}$ is to the heat rate extracted from $\alpha(m,l)$ (the reservoir or island from which the electron is tunneling) and $\Gamma^{h,\text{in}}_{ml}$ corresponds to the heat injected into $\beta(m,l)$ (the reservoir or island to which the electron is tunneling to) when the system undergoes a transition from m to l. We thus have that

$$J_{\text{C}}^{(\text{h})} = \sum_{ml} \left(\Gamma^{h,\text{out}}_{ml}\, p_m - \Gamma^{h,\text{in}}_{lm}\, p_l \right), \tag{E.20}$$

where, as in Eq. (E.17), the sum runs over the values $(ml) = (02)$, (14), (35), (67), for $J_{\text{C}}^{(\text{h})}$, and over $(ml) = (03)$, (16), (25), (47), for $J_{\text{L}}^{(\text{h})}$. The heat extracted from MI 2 can also be computed as in Eq. (E.20) by summing over the values $(ml) = (20)$, (41), (53), (76).

F

APPENDIX 6

F.1 MOST GENERIC SYSTEM-BATH COUPLING

In this appendix we prove that the system bath interaction described by Eq. (2.12) is indeed the most generic system-bath interaction.

The most generic Hermitian operator acting on the tensor product space between S=Q (a two-dimensional Hilbert space) and the baths (an arbitrary dimensional Hilbert space) can be expanded on the product basis of the two Hilbert spaces. We therefore consider a basis $\{\mathcal{B}_i\}_i$ of Hermitian operators acting on the space of the bath, and the specific basis $\vec{\sigma}_j \equiv \{\mathbb{1}, \sigma_x, \sigma_y, \sigma_z\}$ of Hermitian operators acting on the qubit space. This yields

$$H_{\alpha,\mathrm{Q}} = \sum_{i,j} a_{ij}\, \mathcal{B}_i \otimes \sigma_j = \sum_j B_j \otimes \sigma_j, \tag{F.1}$$

where $B_j = \sum_i a_{ij}\mathcal{B}_i$ is an Hermitian operator acting on the bath space. Using the relations

$$\begin{aligned} \sigma_x &= \sigma^+ + \sigma^- \\ \sigma_y &= i\sigma^+ - i\sigma^-, \end{aligned} \tag{F.2}$$

we obtain Eq. (2.12), where $B_\alpha = B_x + iB_y$.

F.2 RECTIFICATION IN THE WEAK COUPLING REGIME

We now compute the heat current flowing out of the leads in the weak coupling regime, valid when $H_{\alpha,\mathrm{Q}}$ is "small enough". As shown in Ref. [2], the evolution of the reduced density matrix ρ_Q of the qubit obeys a Lindblad master equation. Furthermore, when the qubit is not degenerate (i.e. when $\Delta \neq 0$), the Lindblad master equation can be cast in the form of a rate equation for the occupation probabilities of the qubit, defined by $p_1 = \mathrm{Tr}\{\rho_\mathrm{Q}\sigma^+\sigma^-\}$ and $p_0 = 1 - p_1$. Interestingly, only the terms in $H_{\alpha,\mathrm{Q}}$ proportional to σ^+ and σ^- contribute to the rate equation. Indeed, rewriting $H_{\alpha,\mathrm{Q}}$ as in Eq. (F.1), the rate equation only depends on the following matrix elements of the σ_j operators [2]:

$$\langle 0|\sigma_j|1\rangle\,, \tag{F.3}$$

where $\{|0\rangle\,, |1\rangle\}$ are the eigenstates of the qubit. In other words, only terms which can induce transitions in the qubit spectrum contribute to the master equation. Since $\langle 0|\sigma_j|1\rangle = 0$ for $\sigma_j = \mathbb{1}, \sigma_z$, the only terms that determine the populations are the ones proportional to σ_x and σ_y, and therefore to σ^+ and σ^-.

Neglecting for the moment the Lamb shift, the probabilities satisfy [2]

$$\frac{\partial}{\partial t}\begin{pmatrix} p_0 \\ p_1 \end{pmatrix} = \begin{pmatrix} -\gamma(\Delta) & \tilde{\gamma}(\Delta) \\ \gamma(\Delta) & -\tilde{\gamma}(\Delta) \end{pmatrix}\begin{pmatrix} p_0 \\ p_1 \end{pmatrix}, \tag{F.4}$$

where $\gamma(\Delta) = \gamma_L(\Delta, T_L) + \gamma_R(\Delta, T_R)$, and $\gamma_\alpha(\Delta, T_\alpha), \tilde{\gamma}_\alpha(\Delta, T_\alpha)$, for $\alpha = L, R$, are defined as in Sec. 6.3 (see App. F.3 for a derivation of the expression for the rates). Using Eq. (F.4) and $p_0 + p_1 = 1$, we can find the steady state populations

$$p_0 = \frac{\tilde{\gamma}(\Delta)}{\tilde{\gamma}(\Delta) + \gamma(\Delta)}, \qquad p_1 = \frac{\gamma(\Delta)}{\tilde{\gamma}(\Delta) + \gamma(\Delta)}. \tag{F.5}$$

The heat current flowing out of bath α at inverse temperature β_α can then be computed as

$$J_\alpha^{(h)}(\beta_\alpha) = \Delta \left(p_0 \gamma_\alpha(\Delta, T_\alpha) - p_1 \tilde{\gamma}_\alpha(\Delta, T_\alpha) \right). \tag{F.6}$$

Notice that also the steady-state heat current only depends on the rates, which in turn only depend on the terms in $H_{\alpha,Q}$ proportional to σ^+ and σ^-. Therefore, also the rectification coefficient, withing the weak-coupling regime, only depends on the terms proportional to σ^+ and σ^-. Since $\gamma_\alpha(\Delta, T_\alpha)$ and $\tilde{\gamma}_\alpha(\Delta, T_\alpha)$ are related by the detailed balance equation (see Sec. 6.3), we can express them as $\gamma_\alpha(\Delta, T_\alpha) = \gamma_\alpha^+(\Delta, T_\alpha) f(\Delta/(k_B T_\alpha))$ and $\tilde{\gamma}_\alpha(\Delta, T_\alpha) = \gamma_\alpha^+(\Delta, T_\alpha) f(-\Delta/(k_B T_\alpha))$, where $f(x) = (1 + e^x)^{-1}$ and where $\gamma_\alpha^+(\Delta, T_\alpha)$ is defined as in Sec. 6.3. Using Eqs. (F.5) and (F.6), and choosing as bath temperatures $T_L = T + \Delta T/2$ and $T_R = T - \Delta T/2$, we find that

$$J^{(h)}(\Delta T) = \Delta \frac{\gamma_L^+(\Delta, T_L)\gamma_R^+(\Delta, T_R)}{\gamma_L^+(\Delta, T_L) + \gamma_R^+(\Delta, T_R)} \left[f(\Delta/(k_B T_L)) - f(\Delta(k_B T_R)) \right]. \tag{F.7}$$

We now have a general expression for the heat current which only depends on the tunneling rates $\gamma_\alpha^+(\Delta, T_\alpha)$. In turn, given any bath and qubit-bath Hamiltonian, we are able to compute the rates as discussed in Sec. 6.3.

At last, we can find a general expression for R by plugging Eq. (F.7) into Eq. (6.3). This yields Eq. (6.4).

F.3 TUNNELING RATES

In this section we prove Eq. (6.6). In order to use the results of Ref. [2], we consider the system-bath Hamiltonian as written in Eq. (F.1), such that all operators are Hermitian. Furthermore, as argued in App. F.2, the term proportional to σ_z does not contribute to the heat current. Therefore we have that

$$H_{\alpha,Q} = B_x \otimes \sigma_x + B_y \otimes \sigma_y, \tag{F.8}$$

where

$$B_x = \frac{B^\dagger + B}{2}, \quad B_y = \frac{i(B^\dagger - B)}{2}. \tag{F.9}$$

Using results of Ref. [2] with $\mathcal{H}_{\alpha,Q}$ given by to Eq. (F.8), we find

$$\begin{aligned} \tilde{\gamma}_\alpha(\Delta, T_\alpha) &= \sum_{i,j=\{x,y\}} \gamma_{ij} \langle 1|\sigma_i|0\rangle \langle 0|\sigma_j|1\rangle = \\ &= \gamma_{xx} + \gamma_{yy} + i\gamma_{yx} - i\gamma_{xy} = \frac{1}{\hbar} \int_{-\infty}^{+\infty} dt\, e^{i\Delta t/\hbar} \langle B(s) B^\dagger(0) \rangle, \end{aligned} \tag{F.10}$$

where

$$\gamma_{ij} = \int_{-\infty}^{+\infty} dt\, e^{i\Delta t} \langle B_i^\dagger(t) B_j(0) \rangle, \tag{F.11}$$

and $B_i(t)$ is the time evolution of B_i in the interaction picture, i.e. $B_i(t)$ is the Heisenberg picture operator evolved solely according to Hamiltonian of the bath H_α. In the last step of Eq. (F.10) we used Eq. (F.9) to express B_x and B_y in terms of B and $B^\dagger$. This concludes the proof.

F.4 TUNNELING RATES IN SPECIFIC MODELS

In this section we derive the expression for $\gamma_\alpha^+(\Delta, T)$ in various models.

F.4.1 *Fermionic baths with linear (tunnel) couplings*

In this subsection we consider a fermionic bath $H_\alpha^{(\mathrm{F})}$, as defined in Eq. (2.7). Furthermore, we consider the case of equal chemical potentials, which can be treated by considering the energies $\epsilon_{\alpha k}$ in Eq. (2.7) as measured respect to the common chemical potential μ. Therefore, the energies $\epsilon_{\alpha k}$ are defined in the interval $[-\infty, +\infty]$. Plugging the linear coupling Hamiltonian, given in Eq. (2.12), into Eq. (6.6) yields

$$\tilde{\gamma}_\alpha(\Delta, T_\alpha) = \sum_{k,k'} V_{\alpha k} V^*_{\alpha k'} \int_{-\infty}^{+\infty} dt\, e^{i\Delta t} \left\langle c_{\alpha k}(t) c^\dagger_{\alpha k'} \right\rangle . \tag{F.12}$$

In the interaction picture, time-evolved bath operators $\hat{O}$ satisfy (with $\hbar = 1$)

$$\frac{d\hat{O}(t)}{dt} = i \left[H_\alpha, \hat{O}(t) \right] . \tag{F.13}$$

Using the fact that $[H_\alpha, c_{\alpha k}] = -\epsilon_{\alpha k} c_{\alpha k}$, we find

$$c_{\alpha k}(t) = e^{-i\epsilon_{\alpha k} t} c_{\alpha k}. \tag{F.14}$$

Plugging Eq. (F.14) into Eq. (F.12) yields

$$\tilde{\gamma}_\alpha(\Delta, T_\alpha) = 2\pi \sum_k |V_{\alpha k}|^2 \left\langle c_{\alpha k} c^\dagger_{\alpha k} \right\rangle \delta(\Delta - \epsilon_{\alpha k}) = 2\pi \sum_k |V_{\alpha k}|^2 [1 - f(\beta_\alpha \epsilon_{\alpha k})] \delta(\Delta - \epsilon_{\alpha k}), \tag{F.15}$$

where $f(x) = (\exp(x) + 1)^{-1}$. Recognizing the spectral function, defined in Eq. (2.14), we have that

$$\tilde{\gamma}_\alpha(\Delta, T_\alpha) = \Gamma_\alpha(\Delta)[1 - f(\Delta/(k_\mathrm{B} T_\alpha))], \tag{F.16}$$

where $V = V_k$ such that $\epsilon_k = \Delta$. Using the detailed balance condition, we find that

$$\gamma_\alpha^+(\Delta, T) = \Gamma_\alpha(\Delta), \tag{F.17}$$

which implies $g(\Delta, T) = 1$. This proves Eq. (6.11).

F.4.2 *Bosonic baths with linear (tunnel-like) coupling*

In this section we consider a bosonic bath $H_\alpha^{(\mathrm{B})}$, as defined in Eq. (2.6), and a linear coupling as in Eq. (2.12). As in the fermionic case, we have that $[H_\alpha^{(\mathrm{B})}, b_{\alpha k}] = -\epsilon_{\alpha k} b_{\alpha k}$, so also in this case we have that the interaction picture destruction operator is given by

$$b_{\alpha k}(t) = e^{-i\epsilon_{\alpha k} t} b_{\alpha k}. \tag{F.18}$$

Performing the same steps as in the fermionic case, we end up with Eq. (F.15) with $\langle b_{\alpha k} b^\dagger_{\alpha k} \rangle$ instead of $\langle c_{\alpha k} c^\dagger_{\alpha k} \rangle$, which leads to having $1 + n(\epsilon_{\alpha k}/(k_\mathrm{B} T_\alpha))$

instead of $1 - f(\epsilon_{\alpha k}/(k_B T_\alpha))$, where $n(x) \equiv (\exp(x) - 1)^{-1}$. We therefore find

$$\tilde{\gamma}_\alpha^-(\Delta, T_\alpha) = \Gamma_\alpha(\Delta)[1 + n(\Delta/(k_B T_\alpha))], \tag{F.19}$$

which, using the detailed balance condition, leads to

$$\gamma_\alpha^+(\Delta, T_\alpha) = \Gamma_\alpha(\Delta) \coth(\Delta/(2k_B T_\alpha)). \tag{F.20}$$

This proves Eq. (6.12).

F.4.3 *Arbitrary baths with different σ couplings*

In this subsection we consider arbitrary baths coupled to the qubit via Eq. (2.13). In fact, in this appendix we consider a more general case given by

$$H_{\alpha,Q} = \sum_{i=x,y,z} (\hat{n}_{\alpha,i}\sigma_i) \otimes (B_\alpha + B_\alpha^\dagger), \tag{F.21}$$

where $\hat{n}_\alpha = (\sin\theta_\alpha \cos\phi_\alpha, \sin\theta_\alpha \sin\phi_\alpha, \cos\theta_\alpha)$ is a unit vector, and B_α is an arbitrary bath operator. As discussed in Sec. 6.3, the term proportional to σ_z does not contribute to the heat current, so we can neglect it. The term that matters is

$$\hat{n}_{\alpha,x}\sigma_x + \hat{n}_{\alpha,y}\sigma_y = \sin\theta_\alpha \left(e^{i\phi_\alpha}\sigma^+ + e^{-i\phi_\alpha}\sigma^-\right). \tag{F.22}$$

Assuming that $B^\dagger$ produces excitations in the bath with positive energy, also the terms proportional to $B^\dagger\sigma^+$ and $B\sigma^-$ vanish. The relevant terms of the interacting Hamiltonian thus become

$$H_{\alpha,Q} = \sigma^+ \otimes \tilde{B}_\alpha + \sigma^- \otimes \tilde{B}_\alpha^\dagger, \tag{F.23}$$

where we define

$$\tilde{B}_\alpha = \sin\theta_\alpha e^{i\phi_\alpha} B_\alpha. \tag{F.24}$$

This interacting Hamiltonian is now of the form of Eq. (2.12). Therefore, the tunneling rates can be computed from Eq. (6.6), yielding

$$\tilde{\gamma}_\alpha(\Delta, T_\alpha) = \sin^2\theta_\alpha h(\Delta, T_\alpha), \tag{F.25}$$

where $h(\Delta, T_\alpha) = \int dt\, e^{i\Delta t} \langle B_\alpha(t) B_\alpha^\dagger(0)\rangle_\alpha$ only depends on the bath through the temperature, and it does not depend on θ_α nor ϕ_α. Using the detailed balance condition we find

$$\gamma_\alpha^+(\Delta, T_\alpha) = \sin^2\theta_\alpha h(\beta_\alpha)(1 + e^{-\beta_\alpha\Delta}). \tag{F.26}$$

This case is therefore described by the "similar bath" assumption [see Eq. (6.7)], where $\Gamma_\alpha(\Delta) = \sin^2\theta_\alpha$, and $g(\beta) = h(\beta)(1 + e^{-\beta\Delta})$.

F.5 THERMAL AVERAGES

In this section we show how to compute the expectation value $\langle n_{\alpha k}^2\rangle$ for the bosonic bath. Let us define the inverse temperature $\beta_\alpha = 1/(k_B T_\alpha)$ The partition function Z_α is given by

$$Z = \sum_{\{n_i\}=0}^{+\infty} p(\{n_i\}), \tag{F.27}$$

where the sum is over each n_i from 0 to $+\infty$, and where

$$p(\{n_i\}) = e^{-\beta_\alpha \sum_j n_j \epsilon_{\alpha j}} \tag{F.28}$$

is the canonical probability of finding the bath in a Fock state with occupation numbers $\{n_i\}$. Using these two definitions, and recalling that $\langle n_{\alpha k}^m \rangle \equiv \sum p(\{n_i\})\, n_k^m$, it is easy to prove that

$$-\frac{1}{\beta}\frac{\partial \ln Z}{\partial \epsilon_{\alpha k}} = \langle n_{\alpha k} \rangle , \tag{F.29}$$

$$\frac{1}{\beta^2}\frac{\partial^2 \ln Z}{\partial \epsilon_{\alpha k}^2} = \langle n_{\alpha k}^2 \rangle - \langle n_{\alpha k} \rangle^2 . \tag{F.30}$$

Plugging Eq. (F.28) into (F.27), and recognizing that we can perform all the sums as geometric series, we can express the logarithm of the bosonic partition function as

$$\ln Z = -\sum_j \ln\left(1 - e^{-\beta \epsilon_{\alpha j}}\right). \tag{F.31}$$

Plugging Eq. (F.31) into (F.29), we find the well know result that $\langle n_{\alpha k} \rangle = n(\beta_\alpha \epsilon_{\alpha k})$. Plugging Eq. (F.31) into (F.30), we find

$$\langle n_{\alpha k}^2 \rangle = 2n^2(\beta_\alpha \epsilon_{\alpha k}) + n(\beta \epsilon_{\alpha k}). \tag{F.32}$$

F.6 LAMB SHIFT

In this section we compute the Lamb shift of the qubit gap induced by the bath. In order to use the results of Ref. [2], we consider a coupling Hamiltonian as written in Eq. (F.8). As shown in Ref. [2], we have that

$$H_{\mathrm{LS}} = \sum_{\substack{\epsilon = \{0, \pm\Delta\} \\ i,j = \{x,y\}}} \delta\tilde{\Delta}_{xy}(\epsilon) \sigma_i^\dagger(\epsilon) \sigma_j(\epsilon), \tag{F.33}$$

where

$$\delta\tilde{\Delta}_{ij}(\epsilon) = \frac{1}{2\pi}\mathcal{P}\int_{-\infty}^{+\infty} \frac{\gamma_{ij}(\omega)}{\epsilon - \omega} d\omega \equiv \delta\tilde{\Delta}[\epsilon, \gamma_{ij}(\omega)], \tag{F.34}$$

with

$$\gamma_{ij}(\omega) = \int_{-\infty}^{+\infty} dt\, e^{i\omega t} \langle B_i^\dagger(t) B_j(0) \rangle \tag{F.35}$$

defined exactly as in Eq. (F.11), where Δ is replaced with ω, and where

$$\sigma_i(\epsilon) = \sum_{\epsilon' - \epsilon'' = \epsilon} |\epsilon''\rangle \langle \epsilon''| \sigma_i |\epsilon'\rangle \langle \epsilon'| . \tag{F.36}$$

Notice that the functional $\delta\tilde{\Delta}[\dots]$, defined in Eq. (F.34), is linear, and that ϵ'' and ϵ' run over the two eigenvalues of the qubit, $-\Delta/2, \Delta/2$. For ease of notation, we identify the excited state of the qubit with $|1\rangle = |\Delta/2\rangle$, and the ground state with $|0\rangle = |-\Delta/2\rangle$. Expanding the sum in Eq. (F.36), we have

$$\begin{aligned} \sigma_i(\Delta) &= \langle 0|\sigma_i|1\rangle \ |0\rangle \langle 1| , \\ \sigma_i(-\Delta) &= \langle 1|\sigma_i|0\rangle \ |1\rangle \langle 0| , \\ \sigma_i(0) &= \sum_{k=0,1} \langle k|\sigma_i|k\rangle \ |k\rangle \langle k| = 0, \end{aligned} \tag{F.37}$$

where we used the fact that both σ_x and σ_y have only zeros on the diagonal in the last equality. Therefore, the non-null elements are given by

$$\begin{aligned} \sigma_x(\Delta) &= \sigma^-, \qquad \sigma_x(-\Delta) = \sigma^+, \\ \sigma_y(\Delta) &= -i\sigma^-, \quad \sigma_y(-\Delta) = i\sigma^+. \end{aligned} \tag{F.38}$$

Plugging these results into Eq. (F.33), using the anti-commutation relation $\{\sigma^-, \sigma^+\} = \mathbb{1}$, and neglecting the terms proportional to the identity, we find

$$\begin{aligned} H_{\mathrm{LS}} = \sigma_z \left[\delta\tilde{\Delta}_{xx}(\Delta) + \delta\tilde{\Delta}_{yy}(\Delta) - i\delta\tilde{\Delta}_{xy}(\Delta) + i\delta\tilde{\Delta}_{yx}(\Delta)\right] \\ - \sigma_z \left[\delta\tilde{\Delta}_{xx}(-\Delta) + \delta\tilde{\Delta}_{yy}(-\Delta) + i\delta\tilde{\Delta}_{xy}(-\Delta) - i\delta\tilde{\Delta}_{yx}(-\Delta)\right]. \end{aligned} \tag{F.39}$$

Expressing $\delta\tilde{\Delta}_{ij}(\pm\Delta)$ in terms of the functional $\delta\tilde{\Delta}[Delta, \gamma_{ij}(omega)]$ yields

$$\begin{aligned} H_{\mathrm{LS}} = \sigma_z \delta\tilde{\Delta}\left[\Delta, \gamma_{xx}(\omega) + \gamma_{yy}(\omega) - i\gamma_{xy}(\omega) + i\gamma_{yx}(\omega)\right] \\ - \sigma_z \delta\tilde{\Delta}\left[-\Delta, \gamma_{xx}(\omega) + \gamma_{yy}(\omega) + i\gamma_{xy}(\omega) - i\gamma_{yx}(\omega)\right]. \end{aligned} \tag{F.40}$$

Using the definition of $\gamma_{ij}(\omega)$ in Eq. (F.35), and expressing B_x and B_y in terms of B and $B^\dagger$ through Eq. (F.9), it can be shown that

$$\begin{aligned} \gamma_{xx}(\omega) + \gamma_{yy}(\omega) - i\gamma_{xy}(\omega) + i\gamma_{yx}(\omega) = \tilde{\gamma}(\omega), \\ \gamma_{xx}(\omega) + \gamma_{yy}(\omega) + i\gamma_{xy}(\omega) - i\gamma_{yx}(\omega) = \gamma(-\omega), \end{aligned} \tag{F.41}$$

where $\tilde{\gamma}(\omega)$ and $\gamma(\omega)$ are the rates introduced in Eq. (F.4). Plugging Eq. (F.41) into Eq. (F.40) yields

$$H_{\mathrm{LS}} = \sigma_z \left(\delta\tilde{\Delta}\left[\Delta, \tilde{\gamma}(\omega)\right] - \delta\tilde{\Delta}\left[-\Delta, \gamma(-\omega)\right]\right) \tag{F.42}$$

Using Eq. (F.34), it can be shown that the operator $\delta\tilde{\Delta}[\Delta, \dots]$ satisfies the general property $\delta\tilde{\Delta}[-\Delta, f(-\omega)] = -\tilde{\Delta}[\Delta, f(\omega)]$. Therefore, we find

$$H_{\mathrm{LS}} = \sigma_z \tilde{\Delta}\left[\Delta, \tilde{\gamma}(\omega) + \gamma(\omega)\right]. \tag{F.43}$$

Finally, recalling that $\gamma(\omega) = \gamma_{\mathrm{L}}(\omega, T_{\mathrm{L}}) + \gamma_{\mathrm{R}}(\omega, T_{\mathrm{R}})$, we have that

$$\tilde{\gamma}(\omega) + \gamma(\omega) = \gamma_{\mathrm{L}}^{+}(\omega, T_{\mathrm{L}}) + \gamma_{\mathrm{R}}^{+}(\omega, T_{\mathrm{R}}). \tag{F.44}$$

Therefore, we find

$$H_{\mathrm{LS}} = \sigma_z \left(\delta\tilde{\Delta}\left[\Delta, \gamma_{\mathrm{L}}^{+}(\omega, T_{\mathrm{L}})\right] + \delta\tilde{\Delta}\left[\Delta, \gamma_{\mathrm{R}}^{+}(\omega, T_{\mathrm{R}})\right]\right), \tag{F.45}$$

which proves Eq. (6.15).

F.7 CO-TUNNELING CALCULATION

In this appendix we derive Eq. (6.20), i.e. the expression for the heat current adding co-tunneling rates to the ME calculation performed in the weak coupling regime (see Sec. 6.3). We will focus on the XX and YX coupling cases, defined in Sec. 6.4. For simplicity, in this appendix we express the system bath Hamiltonian $H_{\alpha,\mathrm{Q}}^{(\mathrm{sb})}$ as

$$\begin{aligned} H_{\mathrm{L,Q}}^{(\mathrm{sb})} = (q\sigma^+ + q^*\sigma^-) \otimes \sum_k V_{\alpha k}(b_{\alpha k} + b_{\alpha k}^\dagger), \\ H_{\mathrm{R,Q}}^{(\mathrm{sb})} = (\sigma^+ + \sigma^-) \otimes \sum_k V_{\alpha k}(b_{\alpha k} + b_{\alpha k}^\dagger), \end{aligned} \tag{F.46}$$

where q is a complex coefficient given by $q = 1$ in the XX case (since $\sigma_x = \sigma^+ + \sigma^-$) and by $q = i$ in the YX case (since $\sigma_y = i\sigma^+ - i\sigma^-$).

Co-tunneling is a second-order process where a state of the uncoupled system evolves into another state of the uncoupled system passing through a "virtual state" by interacting twice with $\mathcal{H}_{\alpha,\mathrm{Q}}^{(\mathrm{sb})}$. Since $\mathcal{H}_{\alpha,\mathrm{Q}}^{(\mathrm{sb})}$ contains the operators σ^+ and σ^-, and since co-tunneling rates are obtained by acting

twice with $\mathcal{H}^{(\mathrm{sb})}_{\alpha,\mathrm{Q}}$, the state of the qubit remain unaltered during a co-tunneling process. This property, which is denoted as "elastic co-tunneling", implies that co-tunneling rates do not enter the master equation for the probabilities.

We now consider all processes which transfer an excitation from the left to the right bath while the qubit is in the ground state. Let us denote with $|0\rangle$ and $|1\rangle$ the ground and excited state of the qubit, and with $|n_\alpha\rangle_k$ a Fock state with n_α excitations in mode k of bath α. The initial $|i\rangle$, final $|f\rangle$, and intermediate states $|\nu_i\rangle$ involved in the co-tunneling process are respectively given by

$$\begin{aligned} |i\rangle &= |0\rangle \otimes |n_{\mathrm{L}}\rangle_k \otimes |n_{\mathrm{R}}\rangle_{k'}\,, \\ |f\rangle &= |0\rangle \otimes |n_{\mathrm{L}}-1\rangle_k \otimes |n_{\mathrm{R}}+1\rangle_{k'}\,, \\ |\nu_1\rangle &= |1\rangle \otimes |n_{\mathrm{L}}-1\rangle_k \otimes |n_{\mathrm{R}}\rangle_{k'}\,, \\ |\nu_2\rangle &= |1\rangle \otimes |n_{\mathrm{L}}\rangle_k \otimes |n_{\mathrm{R}}+1\rangle_{k'}\,, \end{aligned} \tag{F.47}$$

for all choices of k and k'. Using the Fermi golden rule, the rate of transition from the initial state $|i\rangle$ to the final state $|f\rangle$ is given by

$$\mathrm{Y}_{i\to f} = \frac{2\pi}{\hbar}\left|A_{if}\right|^2 \delta(\epsilon_i - \epsilon_f), \tag{F.48}$$

where $\epsilon_{i/f}$ is the energy of the initial/final state in the absence of the system-bath interaction, and

$$A_{if} = \sum_j \frac{\langle f|\sum_\alpha H^{(\mathrm{sb})}_{\alpha,\mathrm{Q}}|\nu_j\rangle\langle\nu_j|\sum_\alpha H^{(\mathrm{sb})}_{\alpha,\mathrm{Q}}|i\rangle}{\epsilon_i - \epsilon_{\nu_j} + i\eta}, \tag{F.49}$$

η being an infinitesimal positive quantity and ϵ_{ν_j} the energy of $|\nu_j\rangle$. Using Eqs. (F.46) and (F.47), we have that the non-null matrix elements are

$$\begin{aligned} \langle f|H^{(\mathrm{sb})}_{\mathrm{R,Q}}|\nu_1\rangle &= \langle\nu_2|H^{(\mathrm{sb})}_{\mathrm{R,Q}}|i\rangle = V_{\mathrm{R}k_{\mathrm{R}}}\sqrt{n_{\mathrm{R}}+1}, \\ \langle\nu_1|H^{(\mathrm{sb})}_{\mathrm{L,Q}}|i\rangle &= \langle f|H^{(\mathrm{sb})}_{\mathrm{L,Q}}|\nu_2\rangle = q\,V_{\mathrm{L}k_{\mathrm{L}}}\sqrt{n_{\mathrm{L}}}. \end{aligned} \tag{F.50}$$

The total co-tunneling rate of energy $\Gamma^{\mathrm{cot(c)}}_{\mathrm{LR}}(0)$ that accounts for the transfer of an excitation from left to right, while the qubit is in state $|0\rangle$, is obtained by performing a weighed sum, according to the equilibrium probabilities, over all the initial and final states of the quantity $\mathrm{Y}_{i\to f}$ multiplied by the transferred energy. Combining Eqs. (F.50), (F.49) and (F.48), and using for simplicity $\epsilon_k = \epsilon_{\mathrm{L}k}$ and $\epsilon_{k'} = \epsilon_{\mathrm{R}k'}$, we have that

$$\begin{aligned} \Gamma^{\mathrm{cot(c)}}_{\mathrm{LR}}(0) = \frac{2\pi}{\hbar}\sum_{kk'} &\epsilon_k\,|V_{\mathrm{L}k}|^2|V_{\mathrm{R}k'}|^2 n_{\mathrm{L}}(\epsilon_{\mathrm{k}})[1+n_{\mathrm{R}}(\epsilon_{\mathrm{k}'})] \\ &\times\left|\frac{q^*}{\Delta+\epsilon_{\mathrm{k}}+i\eta}+\frac{q}{\Delta-\epsilon_{\mathrm{k}}+i\eta}\right|\delta(\epsilon_{\mathrm{k}}-\epsilon_{\mathrm{k}'}). \end{aligned} \tag{F.51}$$

As usual, we assume that the energies in the leads form a continuum, so we can replace the sum with an integral. Performing some calculations, and recalling that $|q|^2 = 1$ both in the XX and XY case, we have that

$$\begin{aligned} \Gamma^{\mathrm{cot(c)}}_{\mathrm{LR}}(0) = \int_0^{+\infty}\frac{d\epsilon}{2\pi\hbar}\,&\epsilon\,\Gamma_{\mathrm{L}}(\epsilon)\Gamma_{\mathrm{R}}(\epsilon)n_{\mathrm{L}}(\epsilon)[1+n_{\mathrm{R}}(\epsilon)] \\ &\times\left|\frac{1}{\Delta+\epsilon+i\eta}+\frac{q}{q^*}\frac{1}{\Delta-\epsilon+i\eta}\right|. \end{aligned} \tag{F.52}$$

Note that the term q/q^* is respectively 1 and -1 in the XX and YX cases.

The total cotunneling rate of energy $\Gamma^{\mathrm{cot(c)}}_{\mathrm{RL}}(0)$ transferring an excitation from right to left when the qubit is in the ground state is given by Eq. (F.52) exchanging $\mathrm{L} \leftrightarrow \mathrm{R}$. We thus find that the net energy rate $\Gamma^{\mathrm{cot(c)}}(0) \equiv \Gamma^{\mathrm{cot(c)}}_{\mathrm{LR}} - \Gamma^{\mathrm{cot(c)}}_{\mathrm{RL}}(0)$ is given by

$$\Gamma^{\mathrm{cot(c)}}(0) = \int_0^{+\infty} \frac{d\epsilon}{2\pi\hbar}\, \epsilon\, \Gamma_{\mathrm{L}}(\epsilon)\Gamma_{\mathrm{R}}(\epsilon)[n_{\mathrm{L}}(\epsilon) - n_{\mathrm{R}}(\epsilon)] \times \left| \frac{1}{\Delta + \epsilon + i\eta} + \frac{q}{q^*} \frac{1}{\Delta - \epsilon + i\eta} \right|. \quad \text{(F.53)}$$

Repeating the same derivation assuming that the qubit is in the excited state, it can be shown that the net rate $\Gamma^{\mathrm{cot(c)}}(1)$ is the same, i.e. $\Gamma^{\mathrm{cot(c)}}(0) = \Gamma^{\mathrm{cot(c)}}(1)$. Therefore, the heat current will be given by adding Eq. (F.53) to the ME expression, proving Eq. (6.20).

F.8 NON EQUILIBRIUM GREEN'S FUNCTION CALCULATION

In this appendix, we will consider a qubit in contact with bosonic baths. In all our calculations, we fix the coupling on the right hand side to have only the $\hat{\sigma}_x$ component, i. e. $n_{y,R} = n_{z,R} = 0$ and $n_{x,R} = 1$. The total Hamiltonian in terms of spin operators

$$H = \frac{\Delta}{2}\hat{\sigma}_z + \sum_{k,\alpha} \epsilon_{\alpha k} \hat{b}^\dagger_{\alpha k} \hat{b}_{\alpha k} + \sum_j n_{j,\mathrm{L}} \hat{\sigma}_j \hat{B}_{\mathrm{L}} + \hat{\sigma}_x \hat{B}_{\mathrm{R}}. \quad \text{(F.54)}$$

Spin operators do not satisfy the usual Wick's theorem. The usual Feynman diagram techniques applied to obtain Dyson equations can't be used. In order to overcome this difficulty, one can undergo Majorana fermion transformation of spin operators using the following relations [373, 147]:

$$\hat{\sigma}_x = -i\hat{\eta}_y\eta_z;\ \hat{\sigma}_y = -i\hat{\eta}_z\hat{\eta}_x;\ \hat{\sigma}_z = -i\hat{\eta}_x\eta_y. \quad \text{(F.55)}$$

The total Hamiltonian in terms of Majorana fermions

$$H = -\frac{i\Delta}{2}\hat{\eta}_x\hat{\eta}_y + \sum_{k,\alpha} \epsilon_{\alpha k} b^\dagger_{\alpha k} b_{\alpha k} - i\Big[n_{x,\mathrm{L}}\hat{\eta}_y\hat{\eta}_z\hat{B}_{\mathrm{L}} + n_{y,\mathrm{L}}\hat{\eta}_z\hat{\eta}_x\hat{B}_{\mathrm{L}} + n_{z,\mathrm{L}}\hat{\eta}_x\hat{\eta}_y\hat{B}_{\mathrm{L}}\Big] - i\hat{\eta}_y\hat{\eta}_z\hat{B}_{\mathrm{R}}. \quad \text{(F.56)}$$

We write the Green's function for spin operators as:

$$\begin{aligned} \hat{G}^{<}_{l,l'}(t,t') &= -i\langle \hat{\sigma}_{l'}(t')\hat{\sigma}_l(t)\rangle, \\ \hat{G}^{r}_{l,l'}(t,t') &= -i\Theta(t-t')\langle [\hat{\sigma}_l(t), \hat{\sigma}_{l'}(t')]\rangle. \end{aligned} \quad \text{(F.57)}$$

The relations between the Green's function in the Majorana representation and the Green's function in spin representation are given by[373, 147],

$$\begin{aligned} &\hat{G}^{</>}_{l,l'}(t,t') = \mp i\hat{\Pi}^{</>}_{l,l'}(t,t') \\ &\hat{G}^{r}(t,t') = \theta(t-t')\left[\hat{\Pi}^{>}(t,t') + \hat{\Pi}^{<}(t,t')\right], \end{aligned} \quad \text{(F.58)}$$

where $\hat{\Pi}^{</>}_{l,l'}(t,t') = \pm i\langle \hat{\eta}_{l'}(t')\hat{\eta}_l(t)\rangle$ are the lesser/greater Green's functions for Majorana operators. The heat current flowing from the lead R to the system is given by

$$J^{(h)}_{\mathrm{L}}(t) = i\,\langle [H_{\mathrm{L}}(t), H(t)]\rangle = -2\sum_k \epsilon_{Lk} V_{Lk} \mathrm{Re}\left[G^{<}_{x,Lk}(t,t)\right], \quad \text{(F.59)}$$

where $G^{<}_{x,Lk}(t,t') = -i\left\langle \hat{b}^{\dagger}_{Lk}(t')\hat{\sigma}_x(t)\right\rangle$. Following standard Keldysh NEGF treatment using Langreth theorem, the steady state heat current as defined in Eq. (6.2) can be written as:

$$J^{(\mathrm{h})}(\Delta T) = 2\int d\epsilon\, \epsilon\, \mathrm{Re}\left[G^{r}_{xx}(\epsilon)D^{<}_{L}(\epsilon) + G^{<}_{xx}(\epsilon)D^{q}_{L}(\epsilon)\right], \tag{F.60}$$

where $D_{\alpha}(\epsilon) = \sum_k |V_{Rk}|^2 g_{Rk}(\epsilon)$ is the self energy of the bath R and $g_{Rk}(\epsilon)$ is the Green's function for the uncoupled bath R. Applying the relations of Eq. (F.58), the heat current can be computed as

$$J^{(E)}_{\alpha} = \int_0^{\infty} \frac{d\epsilon}{2\pi}\epsilon\left[\Pi^{>}_{xx}(\epsilon)D^{<}_{R}(\epsilon) + \Pi^{<}_{xx}(\epsilon)D^{>}_{R}(\epsilon)\right], \tag{F.61}$$

where the self energies due to system bath coupling, $D^{<}_{R}(\epsilon) = -in_R(\epsilon)\Gamma_R(\epsilon)$ and $D^{>}_{R}(\epsilon) = -i(1+n_R(\epsilon))\Gamma_R(\epsilon)$. In order to evaluate the heat currents, one needs to calculate the lesser and greater components of Majorana Green's function.

F.8.1 *Derivation of Green's function*

In this section, we will derive the Green's functions in Majorana representation. Normal ordering for Majorana fermions is not defined. It is useful to write the Majorana operators in terms of Dirac operators[373, 147]

$$\hat{\eta}_x = \hat{f} + \hat{f}^{\dagger};\;\; \hat{\eta}_y = i(\hat{f}^{\dagger} - \hat{f});\;\; \hat{\eta}_z = \hat{g} + \hat{g}^{\dagger}. \tag{F.62}$$

The fermionic nature of $\hat{f}$ is consistent with,

$$\hat{f} = \frac{\hat{\eta}_x + i\hat{\eta}_y}{2};\;\; \hat{f}^2 = 0;\;\; \hat{f}^{\dagger 2} = 0;\;\; \left\{\hat{f}, \hat{f}^{\dagger}\right\} = 1, \tag{F.63}$$

and should hold for g as well. The Majorana representation does not suffer from vertex problem([373]) and the constraints on spins are naturally imposed on Majorana operators[147]. The Hamiltonian for the qubit gets transformed to

$$H_{\mathrm{Q}} = \frac{\Delta}{2}(1 - 2\hat{f}^{\dagger}\hat{f}), \tag{F.64}$$

whereas the contact Hamiltonian

$$H_{\mathrm{LQ}} = \left[n_{x,\mathrm{L}}\,(f^{\dagger} - f)\hat{\eta}_z - in_{y,\mathrm{L}}\,\hat{\eta}_z(f + f^{\dagger}) + n_{z,\mathrm{L}}(1 - 2f^{\dagger}f)\right]\hat{B}_L, \tag{F.65}$$

and

$$H_{\mathrm{RQ}} = (\hat{f}^{\dagger} - \hat{f})\hat{\eta}_z\hat{B}_{\mathrm{R}}. \tag{F.66}$$

Note that we consider general spin coupling in the left lead whereas a fixed σ_x coupling in the right. The contour ordered Green's function for the Majorana operators can be written as:

$$\hat{\Pi}_{xx}(\tau,\tau') = \begin{bmatrix} \hat{\Pi}^{t}_{xx}(t,t') & \hat{\Pi}^{<}_{xx}(t,t') \\ \hat{\Pi}^{>}_{xx}(t,t') & \hat{\Pi}^{\bar{t}}_{xx}(t,t') \end{bmatrix} \tag{F.67}$$

We also define the Green's function for Dirac f - fermions in the Bogolyubov-Nambu representation, $\hat{\psi} \equiv (\hat{f}, \hat{f}^\dagger)^T$ and $\hat{\psi}^\dagger \equiv (\hat{f}^\dagger, \hat{f})$, such that $\hat{G}_\psi(\tau, \tau') = -i \langle \mathcal{T} \hat{\psi}(\tau) \hat{\psi}(\tau') \rangle$. On expansion in the Keldysh contour,

$$\hat{G}_\psi(\tau, \tau') = \begin{bmatrix} G^t_{ff^\dagger}(t,t') & G^t_{ff}(t,t') & G^<_{ff^\dagger}(t,t') & G^<_{ff}(t,t') \\ G^t_{f^\dagger f^\dagger}(t,t') & G^t_{f^\dagger f}(t,t') & G^<_{f^\dagger f^\dagger}(t,t') & G^<_{f^\dagger f}(t,t') \\ G^>_{ff^\dagger}(t,t') & G^>_{ff}(t,t') & G^{\bar{t}}_{ff^\dagger}(t,t') & G^{\bar{t}}_{ff}(t,t') \\ G^>_{f^\dagger f^\dagger}(t,t') & G^>_{f^\dagger f}(t,t') & G^{\bar{t}}_{f^\dagger f^\dagger}(t,t') & G^{\bar{t}}_{f^\dagger f}(t,t') \end{bmatrix}, \tag{F.68}$$

where for instance, $G_{ff^\dagger}(\tau, \tau') = -i \left\langle \mathcal{T} \hat{f}(\tau) \hat{f}^\dagger(\tau') \right\rangle$. For more clarification, see Eqs. (A2) and (A3) in Ref.[125]. The lesser and greater Green's function in Majorana representation,

$$\begin{aligned} \Pi^{<,>}_{xx}(t,t') &= \begin{bmatrix} 1 & 1 \end{bmatrix} \hat{G}^{<,>}_\psi(t,t') \begin{bmatrix} 1 \\ 1 \end{bmatrix} \\ \Pi^{<,>}_{yy}(t,t') &= \begin{bmatrix} 1 & -1 \end{bmatrix} \hat{G}^{<,>}_\psi(t,t') \begin{bmatrix} 1 \\ -1 \end{bmatrix} \end{aligned} \tag{F.69}$$

F.8.2 *Calculation of Dyson equation*

In order to obtain a Dyson equation for ψ, we need to do perturbation expansion in terms of the contact Hamiltonian for Dirac f-fermions.

$$\begin{aligned} G_{ff^\dagger}(\tau, \tau') &= G^0_{ff^\dagger}(\tau, \tau') \\ &\quad + \frac{i}{2} \sum_\alpha \int d\tau_1 d\tau_2 \left\langle \mathcal{T} \left[\hat{H}_{\alpha Q}(\tau_1) \hat{H}_{\alpha Q}(\tau_2) \hat{\bar{f}}(\tau) \hat{\bar{f}}^\dagger(\tau') \right] \right\rangle + \cdots \end{aligned} \tag{F.70}$$

After a long but straightforward calculation, we obtain

$$\hat{G}_\psi(\tau, \tau') = \hat{G}^0_\psi(\tau, \tau') + \int d\tau_1 d\tau_2 \, \hat{G}_\psi(\tau, \tau_1) \hat{\Sigma}_\psi(\tau_1, \tau_2) \hat{G}^0_\psi(\tau_2, \tau'), \tag{F.71}$$

where $\hat{\Sigma}_\psi = \hat{\Sigma}_{\psi,\mathrm{L}} + \hat{\Sigma}_{\psi,\mathrm{R}}$,

$$\begin{aligned} \hat{\Sigma}_{\psi,\mathrm{L}}(\tau_1, \tau_2) &= i\Sigma_L(\tau_1, \tau_2) \Big(n^2_{x,\mathrm{L}} \Pi^0_{z,z}(\tau_1, \tau_2) \hat{\lambda} \\ &\quad + n^2_{y,\mathrm{L}} \Pi^0_{z,z}(\tau_1, \tau_2) \hat{1} + 4 n^2_{z,\mathrm{L}} \begin{bmatrix} G^0_{ff^\dagger}(\tau_1, \tau_2) & 0 \\ 0 & G^0_{f^\dagger f}(\tau_1, \tau_2) \end{bmatrix} \Big), \end{aligned} \tag{F.72}$$

and

$$\hat{\Sigma}_{\psi,\mathrm{R}}(\tau_1, \tau_2) = i\Sigma_R(\tau_1, \tau_2) \Pi^0_{z,z}(\tau_1, \tau_2) \hat{\lambda}, \tag{F.73}$$

where $\hat{1}$ is the matrix of ones, the embedded self energy $\Sigma_\alpha(\tau_1, \tau_2) = -i \langle \mathcal{T} [B_{k\alpha}(\tau_1) B_{k\alpha}(\tau_2)] \rangle$, and

$$\hat{\lambda} = \begin{bmatrix} 1 & -1 \\ -1 & 1 \end{bmatrix}.$$

Writing the equation of motion for $\hat{G}^0_\psi$, we get:

$$\hat{G}^0_\psi(\tau,\tau')(-i\overleftarrow{\partial}_{\tau'}+\Delta\hat{\sigma}_z)=\delta(\tau-\tau')\hat{\mathbb{1}}, \tag{F.74}$$

where $\hat{\mathbb{1}}$ is a unit matrix. The retarded and advanced self energies due to coupling to the bath are given by:

$$\begin{aligned}\Sigma^{r/a}_\alpha(\epsilon)&=\sum_k|V_{\alpha k}|^2\left(\frac{1}{\epsilon-\epsilon_{\alpha k}\pm i\eta}-\frac{1}{\epsilon+\epsilon_{\alpha k}\pm i\eta}\right)\\&=\frac{\delta\tilde{\Delta}_\alpha(\epsilon)}{2}\mp\frac{i}{2}\left(\Gamma_\alpha(\epsilon)-\Gamma_\alpha(-\epsilon)\right),\end{aligned} \tag{F.75}$$

where $\delta\tilde{\Delta}_\alpha(\epsilon)$ is the lamb shift defined as:

$$\delta\tilde{\Delta}_\alpha(\epsilon)=\mathcal{P}\int_{-\infty}^{\infty}\frac{d\epsilon'}{\pi}\left(\frac{\Gamma_\alpha(\epsilon')}{\epsilon-\epsilon'}-\frac{\Gamma_\alpha(\epsilon')}{\epsilon+\epsilon'}\right), \tag{F.76}$$

The lesser and greater components of self energy take the form

$$\begin{aligned}\Sigma^<_\alpha(\epsilon)&=-in_\alpha(\epsilon)\left(\Gamma_\alpha(\epsilon)-\Gamma_\alpha(-\epsilon)\right),\\\Sigma^>_\alpha(\epsilon)&=-i(1+n_\alpha(\epsilon))\left(\Gamma_\alpha(\epsilon)-\Gamma_\alpha(-\epsilon)\right).\end{aligned} \tag{F.77}$$

The integration for the Lamb shift can be simplified to

$$\delta\tilde{\Delta}_\alpha(\epsilon)=\frac{\Gamma_\alpha}{\pi}\left(\epsilon\,e^{-\epsilon/\epsilon_C}\mathcal{E}\left[\frac{\epsilon}{\epsilon_C}\right]-\epsilon\,e^{\epsilon/\epsilon_C}\mathcal{E}\left[\frac{-\epsilon}{\epsilon_C}\right]-2\epsilon_C\right), \tag{F.78}$$

where

$$\mathcal{E}[\epsilon]=-\mathcal{P}\int_{-\epsilon}^{\infty}e^{-t}/t\;dt \tag{F.79}$$

is a well known exponential integral function. Note that, we used $\Gamma_\alpha(\epsilon)=0$ for $\epsilon<0$. Moreover, we have

$$\begin{aligned}\hat{\Sigma}_{\psi,\mathrm{L}}(\epsilon)=i\int\frac{d\epsilon'}{2\pi}\Sigma_L(\epsilon-\epsilon')\Big(&n^2_{x,\mathrm{L}}\Pi^0_{z,z}(\epsilon')\hat{\lambda}\\&+n^2_{y,\mathrm{L}}\Pi^0_{z,z}(\epsilon')\hat{1}+4n^2_{z,\mathrm{L}}\begin{bmatrix}G^0_{ff^\dagger}(\epsilon')&0\\0&G^0_{f^\dagger f}(\epsilon')\end{bmatrix}\Big),\end{aligned} \tag{F.80}$$

$$\hat{\Sigma}_{\psi,\mathrm{R}}(\epsilon)=i\int\frac{d\epsilon'}{2\pi}\Sigma_R(\epsilon-\epsilon')\Pi^0_{z,z}(\epsilon')\hat{\lambda}. \tag{F.81}$$

Following Ref. [15] for

$$\Sigma(\tau_1,\tau_2)=A(\tau_1,\tau_2)B(\tau_1,\tau_2) \tag{F.82}$$

the Langreth rules are given by

$$\begin{aligned}\Sigma^<(\tau_1,\tau_2)&=A^<(\tau_1,\tau_2)B^<(\tau_1,\tau_2),\\\Sigma^r(\tau_1,\tau_2)&=A^<(\tau_1,\tau_2)B^r(\tau_1,\tau_2)+A^r(\tau_1,\tau_2)B^<(\tau_1,\tau_2)\\&\quad+A^r(\tau_1,\tau_2)B^r(\tau_1,\tau_2)\end{aligned} \tag{F.83}$$

Since both Eqs. (F.72) and (F.73) have the form of Eq. (F.82), one can obtain the lesser ($\Sigma^<_\psi$), greater ($\Sigma^>_\psi$), retarded (Σ^r_ψ) and advanced (Σ^a_ψ) self energies in

terms of different components of embedded self energy and the free Green's function for the system using Eq. (F.83). For instance,

$$\hat{\Sigma}^{<}_{\psi,\mathrm{L}}(\epsilon) = i\int \frac{d\epsilon'}{2\pi}\Sigma^{<}_{L}(\epsilon-\epsilon')\Big(n^2_{x,\mathrm{L}}\Pi^{0,<}_{z,z}(\epsilon')\hat{\lambda} + n^2_{y,\mathrm{L}}\Pi^{0,<}_{z,z}(\epsilon')\hat{1} + 4n^2_{z,\mathrm{L}}\begin{bmatrix} G^{0,<}_{ff^\dagger}(\epsilon') & 0 \\ 0 & G^{0,<}_{f^\dagger f}(\epsilon')\end{bmatrix}\Big), \tag{F.84}$$

$$\hat{\Sigma}^{<}_{\psi,\mathrm{R}}(\epsilon) = i\int \frac{d\epsilon'}{2\pi}\Sigma^{<}_{R}(\epsilon-\epsilon')\Pi^{0,<}_{z,z}(\epsilon')\hat{\lambda}. \tag{F.85}$$

Eqs. (F.75) and (F.77) give all the components of the embedded self energies of the baths. The only unknowns are the free Green's functions of the system which we will discuss below. The free dynamics of the system Hamiltonian can be easily computed to obtain

$$\begin{aligned} G^{0,r}_{ff^\dagger}(\epsilon) &= \mathcal{P}\left\{\frac{1}{\epsilon+\Delta}\right\} - i\pi\delta(\epsilon+\Delta), \\ G^{0,r}_{f^\dagger f}(\epsilon) &= \mathcal{P}\left\{\frac{1}{\epsilon-\Delta}\right\} - i\pi\delta(\epsilon-\Delta). \end{aligned} \tag{F.86}$$

We can use the relation, $G^r - G^a = G^> - G^<$ to write

$$\begin{aligned} G^{0,>}_{f^\dagger f}(\epsilon) - G^{0,<}_{f^\dagger f}(\epsilon) &= -2i\pi\delta(\epsilon-\Delta), \\ G^{0,>}_{ff^\dagger}(\epsilon) - G^{0,<}_{ff^\dagger}(\epsilon) &= -2i\pi\delta(\epsilon+\Delta). \end{aligned} \tag{F.87}$$

Using the fluctuation dissipation relation[15], $G^{0,<}(\epsilon) = -f(\epsilon)\left(G^{0,>}(\epsilon) - G^{0,<}(\epsilon)\right)$ and $G^{0,>}(\epsilon) = (1-f(\epsilon))\left(G^{0,>}(\epsilon) - G^{0,<}(\epsilon)\right)$ where $f(\epsilon)$ is the Fermi distribution of the system defined at average temperature of the two baths, we can write

$$\begin{aligned} G^{0,</>}_{f^\dagger f}(\epsilon) &= \pm 2i\pi f(\pm\epsilon)\delta(\epsilon-\Delta), \\ G^{0,</>}_{ff^\dagger}(\epsilon) &= \pm 2i\pi f(\pm\epsilon)\delta(\epsilon+\Delta). \end{aligned} \tag{F.88}$$

The retarded and advanced Green's function for the system in the Majorana notation

$$\Pi^{0,r/a}_{z,z}(\omega) = \frac{2}{\omega \pm i\eta}, \tag{F.89}$$

such that

$$\Pi^{0,r}_{z,z}(\omega) - \Pi^{0,a}(\omega) = \Pi^{0,>}_{z,z}(\omega) - \Pi^{0,<}_{z,z}(\omega) = -4i\pi\delta(\omega). \tag{F.90}$$

If we take the effective temperature of the Majorana fermions to be given by $\beta_{\mathrm{eff}}(\beta_L, \beta_R)$, we have from the fluctuation-dissipation theorem for the ordinary fermionic system in equilibrium[15]:

$$\Pi^{0,>}_{z,z}(\omega) + \Pi^{0,<}_{z,z}(\omega) = \left(\Pi^{0,r}_{z,z}(\omega) - \Pi^{0,a}_{z,z}(\omega)\right)\tanh\left(\frac{\beta_{\mathrm{eff}}\omega}{2}\right) \tag{F.91}$$

Using Eqs. (F.90) and (F.91), one can find the lesser and greater Green's function for the Majorana operators.

Similarly, the time ordered and anti-time ordered self energies are obtained from

$$\begin{aligned} \hat{\Sigma}^{t}_{\psi}(\epsilon) + \hat{\Sigma}^{\bar{t}}_{\psi}(\epsilon) &= \hat{\Sigma}^{>}_{\psi}(\epsilon) + \hat{\Sigma}^{<}_{\psi}(\epsilon), \\ \hat{\Sigma}^{t}_{\psi}(\epsilon) - \hat{\Sigma}^{\bar{t}}_{\psi}(\epsilon) &= \hat{\Sigma}^{a}_{\psi}(\epsilon) + \hat{\Sigma}^{r}_{\psi}(\epsilon). \end{aligned} \tag{F.92}$$

Substituting Eq. (F.68) in Eq. (F.71) and undergoing Fourier transform, we obtain:

$$\hat{G}_{\psi}^{-1}(\epsilon) = \hat{G}_{\psi}^{0^{-1}}(\epsilon) - \hat{\Sigma}_{\psi}(\epsilon), \tag{F.93}$$

where the bare system Green's function,

$$\hat{G}_{\psi}^{0,t^{-1}}(\epsilon) = -\hat{G}_{\psi}^{0,\bar{t}^{-1}}(\epsilon) = \epsilon\hat{\mathbb{1}} + \Delta\hat{\sigma}_z, \tag{F.94}$$

such that

$$\hat{\sigma}_k\hat{G}_{\psi}(\epsilon) = \begin{bmatrix} \epsilon^+ - [\Sigma_{\psi}^t(\epsilon)]_{11} & -[\Sigma_{\psi}^t(\epsilon)]_{12} & -[\Sigma_{\psi}^<(\epsilon)]_{11} & -[\Sigma_{\psi}^<(\epsilon)]_{12} \\ -[\Sigma_{\psi}^t(\epsilon)]_{21} & \epsilon^- - [\Sigma_{\psi}^t(\epsilon)]_{22} & -[\Sigma_{\psi}^<(\epsilon)]_{21} & -[\Sigma_{\psi}^<(\epsilon)]_{22} \\ [\Sigma_{\psi}^>(\epsilon)]_{11} & [\Sigma_{\psi}^>(\epsilon)]_{12} & \epsilon^+ + [\Sigma_{\psi}^{\bar{t}}(\epsilon)]_{11} & [\Sigma_{\psi}^{\bar{t}}(\epsilon)]_{12} \\ [\Sigma_{\psi}^>(\epsilon)]_{21} & [\Sigma_{\psi}^>(\epsilon)]_{22} & [\Sigma_{\psi}^{\bar{t}}(\epsilon)]_{21} & \epsilon^- + [\Sigma_{\psi}^{\bar{t}}(\epsilon)]_{22} \end{bmatrix}^{-1}, \tag{F.95}$$

where $\epsilon^{\pm} = \epsilon \pm \Delta$ and $\hat{\sigma}_k = \text{diag}(1, 1, -1, -1)$ is introduced to keep the appropriate sign for two different branches of the Keldysh contour[125]. Using Eq. (F.69) along with Eq. (F.95), one can obtain the lesser and greater Green's function in the Majorana representation. Substituting the Majorana Green's functions in Eq. (F.61), we obtain the final expression for current with general spin coupling in the left lead and a fixed spin coupling $\hat{\sigma}_x$ in the right lead.

F.8.3 *Calculation of Currents for simple models*

F.8.3.1 *The XX and YX case*

The current for $\sigma_{L/R} = \sigma_{y/x}$ system-bath coupling can be calculated from Eq. (F.61) after calculating the Green's functions from Eq. (F.95). Note that one has to properly choose $n_{j,\text{L}}$s to obtain the XX and XY case. Considering the zero dimensionality of the spin system and the conservation of energy current, $J_L + J_R = 0$, we arrive at the following expression for the heat current

$$J_{YX}(\Delta T) = \int \frac{d\epsilon}{2\pi}\mathcal{T}_{R,xy}(n_L(\epsilon) - n_R(\epsilon)), \tag{F.96}$$

where

$$\mathcal{T}_{\text{YX}} = \frac{4\,\epsilon^3\,\Gamma_{\text{L}}(\epsilon)\Gamma_{\text{R}}(\epsilon)}{\left(\epsilon^2 - \mathcal{X}(\epsilon) - \Delta^2\right)^2 + \mathcal{Y}^2(\epsilon)}, \tag{F.97}$$

where

$$\mathcal{X}(\epsilon) = \epsilon\left(\delta\tilde{\Delta}_{\text{L}}(\epsilon) + \delta\tilde{\Delta}_{\text{R}}(\epsilon)\right) + (1 + 2n_{\text{L}}(\epsilon))\,(1 + 2n_{\text{R}}(\epsilon))\,\Gamma_{\text{L}}(\epsilon)\Gamma_{\text{R}}(\epsilon) - \delta\tilde{\Delta}_{\text{L}}(\epsilon)\delta\tilde{\Delta}_{\text{R}}(\epsilon), \tag{F.98}$$

and

$$\mathcal{Y}(\epsilon) = \left(\delta\tilde{\Delta}_{\text{L}}(\epsilon) - e\right)(1 + 2n_{\text{R}}(\epsilon))\,\Gamma_{\text{R}}(\epsilon) \;+\; \text{L} \leftrightarrow \text{R}. \tag{F.99}$$

In Eq. (F.97), when the lamb shift term is neglected, the transmission probability has a Lorentzian form, whose width is determined by $\Gamma_{\alpha}(\epsilon)$. When the coupling is very weak, i.e. $\Gamma_{\alpha}(\epsilon) \ll \Delta \ll k_{\text{B}}T_{\alpha}$, the Lorentzian effectively

becomes a delta function peaked around Δ. In this limit, one can write $\epsilon \approx \Delta$ giving:

$$\mathcal{T}_{R,xy} \approx \frac{4\Delta^3 \Gamma_L(\Delta)\Gamma_R(\Delta)}{\xi^2(\Delta)}. \tag{F.100}$$

The above result corresponds to the one obtained using master equation in the sequential tunneling limit. One can obtain the heat current for $\sigma_L = \sigma_R = \sigma_x$ following a similar calculation

$$J_{XX}(\Delta T) = \int_0^\infty \frac{d\epsilon}{2\pi} \mathcal{T}_{R,xx}(\epsilon, B_z, T_L, T_R)\Big(n_L(\epsilon) - n_R(\epsilon)\Big), \tag{F.101}$$

where the transmission probability $\mathcal{T}_{R,xx}$ is given by:

$$\mathcal{T}_{R,xx}(\epsilon) = \frac{4\,\epsilon\Delta^2 \Gamma_L(\epsilon)\Gamma_R(\epsilon)}{\left(\epsilon^2 - \epsilon\left(\delta\tilde{\Delta}_L(\epsilon) + \delta\tilde{\Delta}_R(\epsilon)\right) - \Delta^2\right)^2 + \xi^2(\epsilon)}, \tag{F.102}$$

where $\xi(\epsilon) = \epsilon \sum_\alpha \Gamma_\alpha(\epsilon)\Big(1 + 2n_\alpha(\epsilon)\Big)$. We will consider Ohmic spectral density for both baths with high frequency cut off given by ϵ_C. At low temperature under weak coupling, when the coupling is of the order of thermal energy, the first order processes (sequential) are generally suppressed and the dominant contribution comes from second order co-tunneling processes. We have, $\epsilon \ll \Delta$ and

$$J_{XX}(\Delta T) \approx \int_0^\infty \frac{d\epsilon}{2\pi} \frac{4\epsilon\,\Gamma_L(\epsilon)\Gamma_R(\epsilon)}{\Delta^2}\Big(n_L(\epsilon) - n_R(\epsilon)\Big). \tag{F.103}$$

The above result corresponds to the co-tunneling contribution and matches with Eq. (6.20) for $\epsilon \ll \Delta$. Eq. (F.102) becomes Eq. (F.100) in the sequential tunneling limit.

F.8.4 *Exact calculation*

In this Section we derive the formal exact expressions for the dynamical susceptibility

$$\chi(t) = \frac{i}{\hbar}\Theta(t)\langle[\sigma_x(t), \sigma_x(0)]\rangle \tag{F.104}$$

within the path-integral approach to the spin-boson model [7]. To deal with a correlated initial state at time $t = 0$ we assume that the system starts at a preparation time $t_p < 0$ in a factorized state (Feynman Vernon)

$$W_{tot} = \hat{\rho}_{\rm L}(T_{\rm L}) \otimes \hat{\rho}_{\rm R}(T_{\rm R}) \otimes \hat{\rho}(t_p) \tag{F.105}$$

where each bath is in the thermal equilibrium state described by the density matrix $\hat{\rho}_\alpha(T_\alpha)$ and $\hat{\rho}(t_p)$ is a general state of the qubit at the preparation time. Assuming that the system is ergodic, the response funtion will not depend on the chosen initial state when $t_p \to -\infty$. For the sake of simplicity, we assume that the qubit starts in a diagonal state of σ_x, $|\eta_p\rangle$, with $\eta_p = 1$. We introduce the conditional propagating function

$$J(\zeta, t; \zeta_0, 0; \zeta_p, t_p) \tag{F.106}$$

to find the qubit in the state ζ at time t, conditioned to having measured the system in state ζ_0 at time $t = 0$ and having prepared it in state ζ_p at time t_p. Here ζ labels the four states of the density matrix, denoted in the following with the greek letter $\eta = \pm 1$ for diagonal states and $\xi = \pm 1$ for off-diagonal states.

The conditional propagating function can be written as real time path integral

$$\int \mathcal{D}\sigma(\cdot)\mathcal{D}\sigma'(\cdot)\mathcal{A}[\sigma(\cdot)]\mathcal{A}^*[\sigma'(\cdot)]\,\mathcal{F}[\sigma(\cdot),\sigma'(\cdot)] \tag{F.107}$$

where the functional $\mathcal{A}[\sigma(\cdot)]$ is the probability amplitude for the free qubit to follow the path $\sigma(t)$ (each path can only take values ∓ 1 of the "coordinate" corresponding to the operator σ_x), and $\mathcal{F}[\sigma(\cdot),\sigma'(\cdot)]$ is the real-time influence functional including the effects of the two baths. It is usual to express the paths in terms of the symmetric and anti-symmetric paths $\zeta(t)$ and $\xi(t)$:

$$\eta(t) = \frac{1}{2}[\sigma(t)+\sigma'(t)]\,,\ \xi(t) = \frac{1}{2}[\sigma(t)-\sigma'(t)]\,. \tag{F.108}$$

When $\eta = \pm 1$ the qubit is in one of the two diagonal states of the density matrix expressed in the σ_x basis. It is usually said that the system is in a sojourn. Instead when $\xi(t) = \pm 1$ the system is in an off-diagonal state of the density matrix, or in a blip state. The double path integral in Eq. (F.107) can be visualized as a single path over the four states of the density matrix. During a sojourn of duration τ it is $\xi(\tau) = 0$ and vice-versa during a blip lasting τ it is $\eta(\tau) = 0$.

The influence functional in the presence of two baths coupled to the qubit via σ_x takes the simple form

$$\mathcal{F}[\sigma,\sigma';t_0] = \exp\left\{\int_{t_0}^{t} dt' \int_{t_0}^{t'} dt'' \sum_{\nu}\Big[\dot{\xi}(t')\right.$$
$$\left.\mathrm{Re}\left[Q_\alpha(t'-t'')\right]\dot{\xi}(t'') + i\dot{\xi}(t')\mathrm{Im}\left[Q_\alpha(t'-t'')\right]\dot{\eta}(t'')\Big]\right\} \tag{F.109}$$

where $Q_\alpha(t) = \mathrm{Re}[Q_\alpha(t)] + i\mathrm{Im}[Q_\alpha(t)]$ is the complex bath-α correlation function

$$Q_\alpha(t) = \int_0^\infty \frac{d\omega}{\pi\hbar}\frac{2\Gamma_\alpha(\hbar\omega)}{\omega^2}\Big[\coth\left(\frac{\hbar\omega}{2k_B T_\alpha}\right)(1-\cos(\omega t)) + i\sin(\omega t)\Big]\,. \tag{F.110}$$

In terms of conditional propagating functions the dynamical susceptibility, Eq. (F.104) is given by

$$\chi(t) = \frac{i}{\hbar}\Theta(t)\lim_{t_p\to-\infty}\sum_{\eta=\pm1}\sum_{\xi_0=\pm1}\eta\xi_0 J(\eta,t;\xi_0,0;\eta_p,t_p)\,. \tag{F.111}$$

Here Eq. (F.106) is evaluated for a path staring in a sojourn η_p at t_p, in a blip ξ_0 at time zero and again in a sojourn at time t. We find

$$J(\eta,t;\xi_0,0;\eta_p,t_p) = \eta\eta_p\sum_{m,n=1}^{\infty}\Big(-\frac{\Delta^2}{4\hbar^2}\Big)^{m+n-1}\int_{t_p}^{t}\mathcal{D}_{2m-1,2n-1}\{t_j\}$$
$$\sum_{\{\xi_j=\pm1\}'} G^L_{n+m-1}G^R_{n+m-1}\sum_{\{\eta=\pm1\}'} H^L_{n+m-1}H^R_{n+m-1}$$

where the the symbol $\{\}'$ reminds that the sum is over all sequences of blips and sojourns in accordance with the constraints indicated in the argument. Paths consist of $2n-1$ transitions for $t_p < t' < 0$ and $2m-1$ transitions

for $0 < t' < t$. The blip-sojourn interactions enter the H_is, whereas the G_js include the blip-blip interactions and are given by

$$H^{\alpha}_{n+m-1} = \exp\left\{ i \sum_{k=0}^{m+n-2} \sum_{j=0}^{m+n-1} \xi_j X^{\alpha}_{j,k} \eta_k \right\}, \tag{F.112}$$

$$G^{\alpha}_{n+m-1} = \exp\left\{ -\sum_{j=1}^{n+m} \mathrm{Re}\left[Q^{\alpha}_{2j,2j-1} \right] \right\} \exp\left\{ -i \sum_{j=2}^{m+n} \sum_{k=1}^{j-1} \xi_j \xi_k \Lambda^{\alpha}_{j,k} \right\} \tag{F.113}$$

$$\begin{aligned} X^{\alpha}_{j,k} &= \mathrm{Im}\left[Q^{\alpha}_{2j,2k+1} + Q^{\alpha}_{2j-1,2k} - Q^{\alpha}_{2j,2k} - Q^{\alpha}_{2j-1,2k+1} \right], \\ \Lambda^{\alpha}_{j,k} &= \mathrm{Re}\left[Q^{\alpha}_{2j,2k-1} + Q^{\alpha}_{2j-1,2k} - Q^{\alpha}_{2j,2k} - Q^{\alpha}_{2j-1,2k-1} \right]. \end{aligned} \tag{F.114}$$

Inserting the conditional propagating function Eq. (F.106) in the susceptibility Eq. (F.111) it is possible to perform the sum over the sojourns leading to

$$\chi(t) = \frac{2}{\hbar} \lim_{t_p \to -\infty} \sum_{m=1}^{\infty} \sum_{n=1}^{\infty} \left(-\frac{\Delta^2}{2\hbar^2} \right)^{m+n-1} \int_{t_p}^{t} \mathcal{D}_{2m-1,2n-1}\{t_j\} \sum_{\{\xi_j = \pm 1\}} \xi_n G^{L}_{n+m-1} \\ G^{R}_{n+m-1} \sin\left(\phi^{L}_{0,n+m-1} + \phi^{R}_{0,n+m-1} \right) \Pi_{k=1}^{m+n-2} \cos\left(\phi^{L}_{k,n+m-1} + \phi^{R}_{k,n+m-1} \right) \tag{F.115}$$

where

$$\phi^{\alpha}_{k,m} = \sum_{j=k+1}^{m} \xi_j X^{\alpha}_{j,k} \,. \tag{F.116}$$

Eq. (F.115) is the formal exact expression for the susceptibility for a qubit simultaneously coupled to two harmonic baths at different temperatures for general spectral densities and temperatures.

F.8.4.1 *Ohmic baths and the case $K_L + K_R = 1/2$*

We now specialize to the case of two baths with Ohmic damping defined in Eq. (2.15) where we assume identical dependence on the energies included in $I(\epsilon)$. The bath correlation functions take the form

$$Q_{\alpha}(t) = 2K_{\alpha} \ln\left\{ \left(\frac{\epsilon_C}{\pi k_B T_{\alpha}} \right) \sinh\left(\frac{\pi k_B T_{\alpha} |t|}{\hbar \beta_{\alpha}} \right) \right\} + i\pi K_{\alpha} \mathrm{sgn}(t) \,. \tag{F.117}$$

The blip-sojourn interactions and the phases $\phi^{\nu}_{k,m}$, Eq (F.116) simplify, taking the form

$$\begin{aligned} &X^{\alpha}_{j,k} = \pi K_{\alpha} \,, \text{ for } j = k+1 \qquad X^{\alpha}_{j,k} = 0 \,, \text{ for } j \neq k+1 \\ &\phi^{\alpha}_{k,n+m} = \xi_{k+1} \pi K_{\alpha} \,. \end{aligned} \tag{F.118}$$

The susceptibility F.115 becomes

$$\chi(t) = \frac{2}{\hbar} \lim_{t_p \to -\infty} \sum_{m=1}^{\infty} \sum_{n=1}^{\infty} \left(-\frac{\Delta^2}{2\hbar^2} \right)^{m+n-1} \int_{t_p}^{t} \mathcal{D}_{2m-1,2n-1}\{t_j\} \\ \sum_{\{\xi_j = \pm 1\}} \xi_1 \xi_n G^{L}_{n+m-1} G^{R}_{n+m-1} \sin(\pi(K_L + K_R)) \cos(\pi(K_L + K_R))^{n+m-2} \tag{F.119}$$

We observe that dependence from the damping strenghts K_α coming from the blip-sojourn interactions $X_{i,j}$, is in the simple form $K_L + K_R$. Thus we expect that in the case of two Ohmic baths coupled to the qubit with strengths $K_L + K_R = 1/2$ these interactions can be treated analogously to the standard spin-boson model for a qubit coupled to a single bath at $K = 1/2$. We remark that in Eq. (F.119) the coupling strengths enter non linearly the blip-blip interactions, $G^L_{n+m-1} G^R_{n+m-1}$, which include the temperatures of the two baths. Therefore, the two baths at $K_L + K_R = 1/2$ are not simply equivalent to a single bath at $K = 1/2$ with an "effective" temperature.

We proceed with the evaluation of Eq. (F.119) for $K_L + K_R = 1/2$. We observe that all the terms in the sum, except for the first one $m = n = 1$, have $n + m - 2$ zeros from $\cos(\pi(K_L + K_R))^{n+m-2}$. They give a non-vanishing contribution if a proper divergency comes from the interaction terms between the system's transitions included in the $G^L_{n+m-1} G^R_{n+m-1}$. This is the typical case of a bath at $K = 1/2$. Finite contributions arise whenever a "pair"-interaction can be cast in the following form, written in Laplace space

$$\lim_{K\to 1/2} \Delta^2 \cos(\pi K) \int_0^\infty d\tau e^{-\lambda\tau} e^{-\mathrm{Re}[Q(\tau)]} = \frac{\pi}{2}\frac{\Delta^2}{\epsilon_C} \equiv \hbar\gamma\,. \tag{F.120}$$

The divergency of the integral comes from the $\tau \to 0$ behavior of the pair interaction for $K = 1/2$

$$e^{-\mathrm{Re}[Q(\tau)]} = \left(\frac{\epsilon_C}{\pi k_B T} \sinh\left(\frac{\pi k_B T |t|}{\hbar}\right)\right)^{-2K} \to \left(\frac{\hbar}{\epsilon_C \tau}\right)^{2K}. \tag{F.121}$$

The zero is compensated by the short distance singularity of the attractive interaction between nearest neighbor transitions, which can be thought of as opposite charges of a dipole. In the case of two baths with $K_L + K_R = 1/2$ we have

$$\begin{aligned} e^{-\sum_\alpha \mathrm{Re}[Q_\alpha(\tau)]} &= \prod_\alpha \left(\frac{\epsilon_C}{\pi k_B T_\alpha} \sinh\left(\frac{\pi k_B T_\alpha |t|}{\hbar}\right)\right)^{-2K_\alpha} \\ &\to \left(\frac{\hbar}{\epsilon_C \tau}\right)^{2K_L} \left(\frac{\hbar}{\epsilon_C \tau}\right)^{2K_R} = \frac{\hbar}{\epsilon_C \tau}\,. \end{aligned} \tag{F.122}$$

The $\tau \to 0$ behavior does not depend on the temperatures and we get diverging factors which exactly cancel the zero of the $\cos(\pi(K_L + K_R))$, as for a single bath at $K = 1/2$

$$\lim_{K_L+K_R\to 1/2} \Delta^2 \cos(\pi(K_L + K_R)) \int_0^\infty d\tau e^{-\lambda\tau} e^{-\sum_\alpha \mathrm{Re}[Q_\alpha(\tau)]} = \frac{\pi}{2}\frac{\Delta^2}{\epsilon_C} \equiv \hbar\gamma\,. \tag{F.123}$$

Such an integral describes a collapsed dipole which does not interact with any other dipole, having effectively a zero dipole moment. This mechanism allows to sum the different terms of the sum in Eq. (F.119), leading to

$$\chi(t) = \frac{4}{\hbar^3}\frac{\Delta^2}{2\gamma}\Theta(t)\, e^{-\gamma t/2} \int_0^\infty d\tau \; e^{-\sum_\alpha \mathrm{Re}[Q_\alpha(\tau)]} \left[e^{-\gamma|t-\tau|/2} - e^{-\gamma(t+\tau)/2}\right]. \tag{F.124}$$

Performing its Fourier transform and inserting it in the Meir Wingreen formula we can get the heat current between two harmonic baths under the "strong" coupling condition $K_L + K_R = 1/2$.

F.9 QUANTUM NON-LINEAR CIRCUIT

The Hamiltonian for the non-linear resonator system as presented in Sec. 9.1.1 is given by

$$H_S = \epsilon_0 \hat{b}^\dagger \hat{b} + \frac{U}{2} \hat{b}^\dagger \hat{b}^\dagger \hat{b} \hat{b}. \tag{F.125}$$

The equation of motion for retarded Green's function of the systm ($G^r_{b;b} = -i\theta(t-t') \left\langle \left[\hat{b}(t), \hat{b}^\dagger(t') \right] \right\rangle$) can be written as:

$$i\partial_t G^r_{b;b}(t,t') = \delta(t-t') + \epsilon_0 G^r_{b;b}(t,t') + U G^r_{n,b;b}(t,t') + \sum_{k,\alpha} V_{k\alpha} G^r_{k\alpha;b}(t,t') \tag{F.126}$$

We can further apply the equation of motion to $G_{k\alpha;b}(t,t')$ to obtain:

$$\left(\epsilon - \epsilon_0 - \Sigma^{(0)}(\epsilon)\right) G_{b;b}(\epsilon) = 1 + U G_{n,b;b}(\epsilon), \tag{F.127}$$

where $\Sigma^{(0)}(\epsilon)$ is the usual self energy due to system-bath coupling defined as:

$$\Sigma^{(0)}(\epsilon) = \sum_\alpha \Sigma^{(0)}_\alpha(\epsilon) = \sum_{k,\alpha} |V_{k\alpha}|^2 g_{k\alpha;k\alpha}(\epsilon), \tag{F.128}$$

where $g_{k\alpha;k\alpha}$ is the retarded Green's function for the free bath. In order to evaluate Eq. (F.126), we need to evaluate $G_{n,b;b}(\epsilon)$ in terms of $G_{b;b}(\epsilon)$. Using equation of motion, we find:

$$\begin{aligned}(\epsilon - \epsilon_0)\, G_{n,b;b}(\epsilon) = 2\langle n \rangle + U G_{n,n,b;b}(\epsilon) \\ + \sum_{k,\alpha} V_{k\alpha} \left[2G_{n,k\alpha;b}(\epsilon) - G_{b,b,k\alpha^\dagger;b}(\epsilon) \right]\end{aligned} \tag{F.129}$$

We truncate Eq. (F.129) by approximating, $G_{n,n,b;b}(\epsilon) = \langle n \rangle\, G_{n,b;b}(\epsilon)$ such that:

$$\begin{aligned}(\epsilon - \epsilon_0 - U\langle n \rangle)\, G_{n,b;b}(\epsilon) = 2\langle n \rangle \\ + \sum_{k\alpha} V_{k\alpha} \left[2G_{n,k\alpha;b}(\epsilon) - G_{b,b,k\alpha^\dagger;b}(\epsilon) \right]\end{aligned} \tag{F.130}$$

We can again use equation of motion to evaluate $G_{n,k\alpha;b}(\epsilon)$. We obtain

$$\begin{aligned}(\epsilon - \epsilon_{k\alpha}) G_{n,k\alpha;b}(\epsilon) = V_{k\alpha} \Big(G_{n,b;b} - n_\alpha(\epsilon_{k\alpha}) G_{b;b}(\epsilon) \\ + \left\langle b^\dagger b_{k\alpha} \right\rangle G_{k\alpha;b}(\epsilon) \Big) + \left\langle b^\dagger b_{k\alpha} \right\rangle,\end{aligned} \tag{F.131}$$

and

$$\begin{aligned}(\epsilon + \epsilon_{k\alpha} - 2\epsilon_0 - 2U\langle n \rangle)\, G_{b,b,k\alpha^\dagger;b}(\epsilon) = 2\left\langle b b^\dagger_{k\alpha} \right\rangle \\ - V_{k\alpha} G_{n,b;b}(\epsilon) + 2V_{k\alpha} n_\alpha(\epsilon_{k\alpha}) G_{b;b}(\epsilon)\end{aligned} \tag{F.132}$$

We don't take into account the terms involving correlation between the leads and the system, such that $\left\langle b^\dagger b_{k\alpha} \right\rangle = \left\langle b b^\dagger_{k\alpha} \right\rangle = 0$ (Cite meir wingreen). Substituting Eq. (F.131) and Eq. (F.132) into Eq. (F.130),

$$G_{n,b;b} = \frac{2I(\epsilon)\langle n \rangle}{U} - \frac{2\left(\Sigma^{(2)}(\epsilon) + \Sigma^{(3)}(\epsilon)\right) I(\epsilon)}{U} G_{b;b} \tag{F.133}$$

where

$$I(\epsilon)/U = \left(\epsilon - \epsilon_0 - U\langle n\rangle - \left(2\Sigma^{(0)}(\epsilon) + \Sigma^{(1)}(\epsilon)\right)\right)^{-1}, \tag{F.134}$$

$\Sigma^{(0)}(\epsilon) = \sum_{k,\alpha} |V_{k\alpha}|^2 (\epsilon - \epsilon_{k\alpha} + i\eta)^{-1}$, $\Sigma^{(1)}(\epsilon) = \sum_{k,\alpha} |V_{k\alpha}|^2 (\epsilon + \epsilon_{k\alpha} - 2\epsilon_0 - 2U\langle n\rangle + i\eta)^{-1}$, $\Sigma^{(2)}(\epsilon) = \sum_{k,\alpha} |V_{k\alpha}|^2 n_\alpha(\epsilon_{k\alpha}) (\epsilon - \epsilon_{k\alpha} + i\eta)^{-1}$ and $\Sigma^{(3)}(\epsilon) = \sum_{k,\alpha} |V_{k\alpha}|^2 n_\alpha(\epsilon_{k\alpha}) (\epsilon + \epsilon_{k\alpha} - 2\epsilon_0 - 2U\langle n\rangle + i\eta)^{-1}$. Substituting Eq. (F.133) in Eq. (F.126), we find the final expression for $G_{b;b}$. Note that, one would have to evaluate $\langle n\rangle$ self-consistently.

$$G_{b;b}(\epsilon) = \frac{1 + 2I(\epsilon)\langle n\rangle}{\epsilon - \epsilon_0 - \frac{U}{2} - \Sigma^{(0)}(\epsilon) + 2I(\epsilon)\left(\Sigma^{(2)}(\epsilon) + \Sigma^{(3)}(\epsilon)\right)}. \tag{F.135}$$

The self energies are given by:

$$\begin{aligned}
\Sigma_\alpha^{(0)}(\epsilon) &= \int \frac{d\omega}{2\pi}\left[\frac{\Gamma_\alpha(\omega)}{\epsilon - \omega + i\eta}\right], \\
\Sigma^{(1)}(\epsilon) &= \sum_\alpha \int \frac{d\omega}{2\pi}\left[\frac{\Gamma_\alpha(\omega)}{\epsilon + \omega - 2\epsilon_0 - 2U\langle n\rangle + i\eta}\right], \\
\Sigma^{(2)}(\epsilon) &= \sum_\alpha \int \frac{d\omega}{2\pi}\left[\frac{n_\alpha(\omega)\Gamma_\alpha(\omega)}{\epsilon - \omega + i\eta}\right], \\
\Sigma^{(3)}(\epsilon) &= \sum_\alpha \int \frac{d\omega}{2\pi}\left[\frac{\Gamma_\alpha(\omega) n_\alpha(\omega)}{\epsilon + \omega - 2\epsilon_0 - 2U\langle n\rangle + i\eta}\right].
\end{aligned}$$

For any function g

$$\int d\omega \frac{g(\omega)}{x - \omega + i\eta} = \mathcal{P}\int d\omega \left\{\frac{g(\omega)}{x - \omega}\right\} - \frac{i}{2} g(x), \tag{F.136}$$

where the first term is the Cauchy-Hadamard principal value distribution.

G

APPENDIX 7

G.1 DRIVEN QUBIT: CALCULATION OF CURRENTS AND POWER FOR DIFFERENT SPIN COUPLINGS

G.1.1 *Coupling:* $\hat{\tau}_L = \hat{\sigma}_x$ *and* $\hat{\tau}_R = \hat{\sigma}_z$

The different components of $\mathbf{p}(t)$ for the driving protocol of Eq. (8.31) with $\hat{\tau}_L = \hat{\sigma}_x$ and $\hat{\tau}_R = \hat{\sigma}_z$ can be calculated by solving Eqs. (8.39) and (8.40). They read

$$\begin{aligned}
p_1^{(\mathrm{i})} &= \frac{1}{1+e^{-\delta E/k_{\mathrm{B}}T}},\\
p_{1,\Delta T}^{(\mathrm{i})} &= \frac{\delta E\Big(-B_z^2K_L+B_x^2K_R\Big)\,\mathrm{sech}^2\left(\frac{\delta E}{2k_{\mathrm{B}}T}\right)}{4k_{\mathrm{B}}\Big(B_z^2K_L+B_x^2K_R\Big)}\frac{\Delta T}{T^2},\\
p_1^{(\mathrm{a})} &= -\frac{dp_1^{(\mathrm{i})}}{dt}\frac{\delta E\tanh\left(\frac{\delta E}{2k_{\mathrm{B}}T}\right)e^{\delta E/\epsilon_{\mathrm{C}}}}{4\pi\Big(B_z^2K_L+B_x^2K_R\Big)},\\
p_2^{(\mathrm{i})} &= 1-p_1^{(\mathrm{i})},\quad p_{2,\Delta T}^{(\mathrm{i})} = -p_{1,\Delta T}^{(\mathrm{i})},\quad p_2^{(\mathrm{a})} = -p_1^{(\mathrm{a})}.
\end{aligned} \tag{G.1}$$

The heat currents are

$$\begin{aligned}
J_L^{(\mathrm{h}),a}(t) &= \frac{dp_1^{(\mathrm{i})}}{dt}\frac{\delta E\,B_z^2\,K_L}{B_z^2K_L+B_x^2K_R},\\
J_R^{(\mathrm{h}),a}(t) &= \frac{dp_1^{(\mathrm{i})}}{dt}\frac{\delta E\,B_x^2\,K_L}{B_z^2K_L+B_x^2K_R}.
\end{aligned} \tag{G.2}$$

G.1.2 *Coupling:* $\hat{\tau}_L = \hat{\sigma}_x$ *and* $\hat{\tau}_R = \hat{\sigma}_y$

In this case the adiabatic probabilities can be written as

$$\begin{aligned}
p_1^{(\mathrm{a})} &= -\frac{dp_1^{(\mathrm{i})}}{dt}\frac{\delta E e^{\delta E/\epsilon_{\mathrm{C}}}\tanh\left(\delta E/k_{\mathrm{B}}T\right)}{4\pi B_z^2K_L+\pi\delta E^2K_R},\\
p_2^{(\mathrm{a})} &= -p_1^{(\mathrm{a})}.
\end{aligned} \tag{G.3}$$

In the absence of a bias, the instantaneous contribution to the current vanishes, and the only contributions come from adiabatic corrections. The adiabatic heat current flowing in the left and right lead are given by

$$\begin{aligned}
J_{\mathrm{L}}^{(\mathrm{h}),a}(t) &= \frac{dp_1^{(\mathrm{i})}}{dt}\frac{4\delta E B_z^2\,K_L}{4B_z^2K_L+\delta E^2K_R},\\
J_{\mathrm{R}}^{(\mathrm{h}),a}(t) &= \frac{dp_1^{(\mathrm{i})}}{dt}\frac{\delta E^3K_R}{4B_z^2K_L+\delta E^2K_R}.
\end{aligned} \tag{G.4}$$

Using the modulation in Eq. (8.31) with $\phi = \frac{\pi}{2}$, we obtain

$$\frac{dp_1^{(\mathrm{i})}}{dt} = \frac{-\Omega \operatorname{sech}^2(\delta E/k_{\mathrm{BT}})}{2k_{\mathrm{B}}T\delta E}\Big[2B_{z,0}B_{z,1}\sin(\Omega t) + 2B_{x,0}B_{x,1}\cos(\Omega t) + \left(B_{z,1}^2 - B_{x,1}^2\right)\sin(2\Omega t)\Big]. \tag{G.5}$$

Plugging Eq. (G.5) into Eqs. (G.4), the time averaged adiabatic heat currents can be written as a function of different parameters

$$J_{\mathrm{L}}^{(\mathrm{h})} = \frac{1}{\tau}\int_0^\tau J_{\mathrm{L}}^{(\mathrm{a})}(t) = \frac{k_{\mathrm{B}}T\Omega}{2\pi}\int_0^{2\pi} dx f\Big[\frac{\epsilon_0}{k_{\mathrm{B}}T}, \frac{\epsilon_1}{k_{\mathrm{B}}T}, \frac{\Delta_0}{k_{\mathrm{B}}T}, \frac{\Delta_1}{k_{\mathrm{B}}T}, \frac{K_\alpha}{k_{\mathrm{B}}T}, x\Big], \tag{G.6}$$

where f is a dimensionless function which depends on all the parameters of the driving modulation and on the coupling strengths with the leads. Similar expression can be obtained for the heat current flowing in the right contact. In particular, the adiabatic heat currents are linear in the driving frequency as observed in Eq. (G.6).

G.1.3 *Symmetry properties of* $\Lambda_{\ell,\ell'}$

For $\Delta T = 0$, we can rewrite the work W as

$$W = \int_0^{2\pi/\Omega} dt\Big[\frac{dE_1}{dt}p_1^{(\mathrm{a})} + \frac{dE_2}{dt}p_2^{(\mathrm{a})}\Big] \tag{G.7}$$

and, by using the normalization condition $\sum_j p_j^{(\mathrm{a})} = 0$ and the fact that $E_1(t) = -E_2(t)$, we find

$$W = 2\sum_j \int_0^{2\pi/\Omega} dt\, \frac{dE_2}{dX_j}\dot{X}_j p_2^{(a)}, \tag{G.8}$$

where $X_1(t)$ and $X_2(t)$ are the two driving parameters of the q-bit. Moreover, applying the fact that $\delta E = 2E_2$, we find

$$\begin{aligned} W &= \int_0^{2\pi/\Omega} dt\, \zeta(\mathbf{B})\sum_{j,k}\frac{d\delta E}{dX_j}\frac{dp_2^{(\mathrm{i})}}{dX_k}\dot{X}_j\dot{X}_k \\ &= \int_0^{2\pi/\Omega} dt\, \zeta(\mathbf{B})\sum_{j,k}\frac{d\delta E}{dX_j}\frac{dp_2^{(\mathrm{i})}}{d\delta E}\frac{d\delta E}{dX_k}\dot{X}_j\dot{X}_k \end{aligned} \tag{G.9}$$

where $\zeta(\mathbf{B})$ is defined by the relation $p_2^{(\mathrm{a})} = \zeta(\mathbf{B})\frac{dp_2^{(\mathrm{i})}}{dt}$ (see Eq. (G.1)), which is a consequence of Eq. (8.41). Comparing Eq. (G.9) with Eq. (8.16), we obtain:

$$\Lambda_{12}(\mathbf{B}) = \Lambda_{21}(\mathbf{B}) = \zeta(\mathbf{B})\frac{d\delta E}{dX_1}\frac{dp_2^{(\mathrm{i})}}{d\delta E}\frac{d\delta E}{dX_2}. \tag{G.10}$$

Eq. (G.10) and Eq. (8.54) have the same form.

G.2 DRIVEN QUANTUM DOT - CALCULATION OF THE THERMAL GEOMETRIC TENSOR

We need to calculate the following coefficients

$$\begin{aligned} \Lambda_{\mu,\nu}(t) &= \frac{1}{\hbar}\int_{-\infty}^{-\infty} dt'(t-t')\chi_{\mu,\nu}(t-t') \\ &= -\lim_{\omega\to 0}\frac{\mathrm{Im}\left[\chi_{\mu,\nu}(\omega)\right]}{\hbar\omega}, \quad \mu,\nu = 1,2,3 \end{aligned} \tag{G.11}$$

with

$$\chi_{\mu,\nu}(t-t') = -i\theta(t-t')\langle\left[\mathcal{F}_\mu(t),\mathcal{F}_\nu(t')\right]\rangle, \tag{G.12}$$

being $\mathcal{F}_{1,2} = \Psi_d^\dagger\ \hat{\sigma}_{x,z}\Psi_d$, and $\mathcal{F}_3 = \mathcal{J}_{Q,R} = -i\sum_{k_R,s,\sigma}\varepsilon_{k_R,s}v_{k_R,s,\sigma}c_{k_R,s}^\dagger d_\sigma + H.c.$. We can calculate (G.11) following standard procedures based on the formalism of imaginary-time Green's functions. We can define $\hat{\mathcal{G}}(\tau) = -\langle T_\tau\left[\Psi_d(\tau)\Psi_d^\dagger(0)\right]\rangle$ and $\hat{\mathcal{G}}_{k_R,d}(\tau) = -\langle T_\tau\left[\Psi_{k_R}(\tau)\Psi_d^\dagger(0)\right]\rangle$, where T_τ denotes ordering along the imaginary axis. In terms of this, it is possible to write

$$\begin{aligned}
\chi_{\ell,\ell'}(iq_n) &= \frac{1}{\beta}\sum_{ik_n}\mathrm{Tr}\left[\hat{\sigma}_\ell\hat{\mathcal{G}}(ik_n+iq_n)\hat{\sigma}_{\ell'}\hat{\mathcal{G}}(ik_n)\right],\\
\chi_{3,\ell}(iq_n) &= \frac{1}{\beta}\sum_{ik_n}\sum_{k_R}\mathrm{Tr}\left\{\hat{\varepsilon}_{k_R}\hat{v}_R\left[i\hat{\mathcal{G}}(ik_n+iq_n)\hat{\sigma}_\ell\right.\right.\\
&\quad\left.\left.\times\hat{\mathcal{G}}_{d,k_R}(ik_n) - i\hat{\mathcal{G}}_{k_R,d}(ik_n)\hat{\sigma}_\ell\hat{\mathcal{G}}(ik_n-iq_n)\right]\right\}\\
&= -\chi_{\ell,3}(iq_n), \qquad \ell,\ell' = 1,2,\\
\chi_{3,3}(iq_n) &= -\frac{1}{\beta}\sum_{ik_n}\sum_{k_R,k_L'}\\
&\quad\mathrm{Tr}\left\{\hat{\varepsilon}_{k_R}\hat{v}_R\hat{\mathcal{G}}_{k_R,d}(ik_n+iq_n)\hat{\varepsilon}_{k_R'}\hat{v}_L\hat{\mathcal{G}}_{k_L',d}(ik_n)\right.\\
&\quad\left.+\hat{\mathcal{G}}_{d,k_R}(ik_n+iq_n)\hat{\varepsilon}_{k_R}\hat{v}_R\hat{\mathcal{G}}_{d,k_L'}(ik_n)\hat{\varepsilon}_{k_L'}\hat{v}_L\right\}
\end{aligned} \tag{G.13}$$

with $\varepsilon_{k_\alpha,s,s'} = \varepsilon_{k_\alpha,s}\delta_{s,s'}$, $\alpha = L,R$, $q_n = 2\pi n/\beta$ and $k_n = (2n+1)\pi/\beta$.

It is convenient to introduce the spectral representation

$$\begin{aligned}
\hat{\mathcal{G}}(ik_n) &= \int\frac{d\varepsilon}{2\pi}\frac{\hat{\rho}_t(\varepsilon)}{ik_n-\varepsilon},\\
\hat{\mathcal{G}}_{k_\alpha,d}(ik_n) &= \int\frac{d\varepsilon}{2\pi}\frac{\hat{\rho}_{k_\alpha,d}(\varepsilon)}{ik_n-\varepsilon}
\end{aligned} \tag{G.14}$$

with

$$\hat{\rho}_t(\varepsilon) = -2\mathrm{Im}\left[\hat{G}_t(\varepsilon)\right] = \hat{G}_t(\varepsilon)\hat{\Gamma}\left[\hat{G}_t(\varepsilon)\right]^\dagger, \tag{G.15}$$

$$\hat{\rho}_{k_\alpha,d}(\varepsilon) = \hat{\rho}_{k_\alpha}^0(\varepsilon)\hat{v}_\alpha\hat{\rho}_t(\varepsilon) + \hat{\rho}_{k_\alpha}^0(\varepsilon)\hat{v}_\alpha\hat{\rho}_t(\varepsilon), \tag{G.16}$$

where $\rho_{k_\alpha,s,s'}^0(\varepsilon) = 2\pi\delta_{s,s'}\delta(\varepsilon-\varepsilon_{k_\alpha,s})$ and $G_{k_\alpha,s,s'}^0(\varepsilon) = \delta_{s,s'}\left(\varepsilon+i\eta-\varepsilon_{k_\alpha,s}\right)^{-1}$. The retarded frozen Green's function of the quantum dot in contact to the reservoirs is given in Eq. (8.66), while $\hat{\Gamma} = -2\mathrm{Im}\left[\hat{G}_t(\varepsilon)^{-1}\right] = \sum_\alpha\hat{\Gamma}_\alpha$ is the hybridization matrix accounting for the contact between the quantum dot and the reservoirs, being $\hat{\Gamma}_\alpha = \sum_{k_\alpha}\hat{v}_{k_\alpha}\hat{\rho}_{k_\alpha}^0\hat{v}_{k_\alpha}$.

Using Eq. (G.14) into Eq. (G.13), after some algebra and performing the analytic continuation to the real axis we get

$$\begin{aligned}
\Lambda_{\ell,\ell'}(t) &= -\frac{1}{h}\int d\varepsilon\frac{df(\varepsilon)}{d\varepsilon}\mathrm{Tr}\left[\hat{\sigma}_\ell\hat{\rho}_t(\varepsilon)\hat{\sigma}_{\ell'}\hat{\rho}_t(\varepsilon)\right],\ \ell,\ell' = 1,2\\
\Lambda_{3,\ell}(t) &= -\frac{1}{h}\int d\varepsilon\ \varepsilon\frac{df(\varepsilon)}{d\varepsilon}\mathrm{Tr}\left[\hat{\Gamma}_R\hat{\rho}_t(\varepsilon)\hat{\sigma}_\ell\hat{\rho}_t(\varepsilon)\right],\\
&= -\Lambda_{\ell,3}(t) \qquad \ell = 1,2,\\
\Lambda_{3,3}(t) &= -\frac{1}{h}\int d\varepsilon\ \varepsilon^2\frac{df(\varepsilon)}{d\varepsilon}\mathrm{Tr}\left[\hat{\Gamma}_R\hat{G}_t(\varepsilon)\hat{\Gamma}_L\hat{G}_t^\dagger(\varepsilon)\right],
\end{aligned} \tag{G.17}$$

H

APPENDIX 8

H.1 EVALUATION OF THE MEAN VALUES

In this section we will evaluate the mean values entering in Eq. (9.15). The mean values will be calculated perturbatively up to first order in the coupling strength $V_{k\alpha}$, starting with the time-ordered correlator

$$\begin{aligned} & i\left\langle T_K \hat{b}^\dagger_{k\alpha}(t')\hat{\rho}_{mj}(t)\right\rangle \\ & \approx \int_K dt_1 \left\langle T_K\left[\tilde{\mathcal{H}}^H_C(t_1)\hat{b}^\dagger_{k\alpha}(t')\hat{\rho}_{mj}(t)\right]\right\rangle \\ & = V_{k\alpha}\sum_{uv}\overline{\lambda}_{\alpha,uv}\int_K dt_1 \left\langle T_K\left[\hat{\rho}_{mj}(t)\hat{\rho}_{uv}(t_1)\right]\right\rangle \left\langle T_K\left[\hat{b}^\dagger_{k\alpha}(t')\hat{b}_{k\alpha}(t_1)\right]\right\rangle . \end{aligned} \tag{H.1}$$

We can deform the contour K into a pair of contours such that K_1 goes from $-\infty$ to ∞ and K_2 from ∞ to $-\infty$. If t lies in K_1 and t' lies in K_2, one can write:

$$\int_{K_1} = \int_{-\infty}^{t} + \int_{t}^{\infty}; \quad \int_{K_2} = \int_{-\infty}^{t'} + \int_{t'}^{\infty}, \tag{H.2}$$

such that

$$\begin{aligned} & i\left\langle \hat{b}^\dagger_{k\alpha}(t')\hat{\rho}_{mj}(t)\right\rangle \approx V_{k\alpha}\sum_{uv}\overline{\lambda}_{\alpha,uv}\Bigg[\left[\int_{-\infty}^{t} + \int_{t}^{\infty}\right] dt_1 \left\langle\left[\hat{\rho}_{mj}(t)\hat{\rho}_{uv}(t_1)\right]\right\rangle \\ & \left\langle\left[\hat{b}^\dagger_{k\alpha}(t')\hat{b}_{k\alpha}(t_1)\right]\right\rangle + \left[\int_{\infty}^{t'} + \int_{t'}^{-\infty}\right] dt_1 \left\langle\left[\hat{\rho}_{mj}(t)\hat{\rho}_{uv}(t_1)\right]\right\rangle \left\langle\left[\hat{b}^\dagger_{k\alpha}(t')\hat{b}_{k\alpha}(t_1)\right]\right\rangle\Bigg]. \end{aligned} \tag{H.3}$$

For the mixed lesser Green's function defined in Eq. (9.14), Eq. (H.3) can be re-written as:

$$\begin{aligned} G^<_{mj,k\alpha^\dagger}(t,t') \approx \int_{-\infty}^{\infty} dt_1 V_{k\alpha}\sum_{uv}\overline{\lambda}_{\alpha,uv}(t)\Big[& g^r_{mj,uv}(t,t_1)g^<_{k\alpha}(t_1,t') \\ & + g^<_{mj,uv}(t,t_1)g^a_{k\alpha}(t_1,t')\Big], \end{aligned} \tag{H.4}$$

where the definition for Green's functions are given in Eqs. (9.12), (9.13) and (9.14).

H.2 CALCULATION OF COEFFICIENTS OF THE FROZEN MASTER EQUATION

Using Eqs. (H.19) and substituting in the first term of Eq. (9.21) we have terms of the type

$$i\int dt_1 \mathrm{Im}\left[g^{r,f}_{mj,uv}(t,t_1)\right]\Sigma^{<(0)}_{\alpha}(t_1,t) = \pm\frac{\Gamma_\alpha(\Delta\epsilon_{uv})}{2} n_\alpha(\Delta\epsilon_{uv})\left(\left\langle\hat{\rho}^f_{mv}\right\rangle_t \delta_{ju} \pm \left\langle\hat{\rho}^f_{uj}\right\rangle_t \delta_{mv}\right), \quad \text{(H.5)}$$

which are referred to as dissipation-type terms[347]. Similarly, there are also terms of the type,

$$\int dt_1 \mathrm{Re}\left[g^{r,f}_{mj,uv}(t,t_1)\right]\Sigma^{<(0)}_{\alpha}(t_1,t) = -i\left\langle\left(\hat{\rho}^f_{mv}\right\rangle_t \delta_{ju} \pm \left\langle\hat{\rho}^f_{uj}\right\rangle_t \delta_{mv}\right)\mathcal{P}\int\frac{d\epsilon}{2\pi}\frac{n_\alpha(\epsilon)\Gamma_\alpha(\epsilon)}{\epsilon-\Delta\epsilon_{uv}}, \quad \text{(H.6)}$$

which lead to level renormalization. For some specific spectral functions the above integral can be calculated explicitly[352]. Moreover, substituting Eq. (H.19) in the first term of Eq. (9.22), the imaginary part is given by:

$$i\int dt_1 \mathrm{Im}\left[g^{r,f}_{mj,uv}(t,t_1)\right]\Sigma^{<(1)}_{\alpha}(t_1,t) = \pm\Delta\epsilon_{uv}\frac{\Gamma_\alpha(\Delta\epsilon_{uv})}{2} n_\alpha(\Delta\epsilon_{uv})\left(\left\langle\hat{\rho}^f_{mv}\right\rangle_t \delta_{ju} \pm \left\langle\hat{\rho}^f_{uj}\right\rangle_t \delta_{mv}\right). \quad \text{(H.7)}$$

Similarly, the real part becomes:

$$\int dt_1 \mathrm{Re}\left[g^{r,f}_{mj,uv}(t,t_1)\right]\Sigma^{<(1)}_{\alpha}(t_1,t) = -i\left\langle\left(\hat{\rho}^f_{mv}\right\rangle_t \delta_{ju} \pm \left\langle\hat{\rho}^f_{uj}\right\rangle_t \delta_{mv}\right)\mathcal{P}\int\frac{d\epsilon}{2\pi}\frac{\epsilon\, n_\alpha(\epsilon)\Gamma_\alpha(\epsilon)}{\epsilon-\Delta\epsilon_{uv}}. \quad \text{(H.8)}$$

H.3 ADIABATIC DYNAMICS

H.3.1 *Lesser Green's function*

We now introduce the interaction representation with respect to $\tilde{\mathcal{H}}^f_{\mathrm{S}}$ and consider the Green's function

$$g^{<}_{lj,uv}(t_1,t_2) = \pm i\mathrm{Tr}\left\{\hat{\rho}_0\hat{T}_K\left[e^{-i\int_K dt'\delta\tilde{\mathcal{H}}^f_{\mathrm{S}}(t')}\hat{\rho}^f_{lj}(t_1^+)\hat{\rho}^f_{uv}(t_2^-)\right]\right\}, \quad \text{(H.9)}$$

where t_1^+ and t_2^- indicates that the time t_1 is on the piece of the contour that starts in $-\infty$, while t_2 is on the piece of the contour that ends in $-\infty$. All the operators with the label f are calculated in the Heisenberg representation of the frozen Hamiltonian $\tilde{\mathcal{H}}^f_{\mathrm{S}}$. In particular,

$$\hat{\rho}^f_{lj}(t') = e^{\frac{i}{\hbar}t'\tilde{\mathcal{H}}^f_{\mathrm{S}}}\hat{\rho}_{lj}\, e^{-\frac{i}{\hbar}t'\tilde{\mathcal{H}}^f_{\mathrm{S}}} = e^{\frac{i}{\hbar}\epsilon_{lj}t'}\hat{\rho}_{lj} \quad \text{(H.10)}$$

with ϵ^f_j being the eigenenergies of $\tilde{\mathcal{H}}^f_{\mathrm{S}}$ and $\epsilon_{lj} = \epsilon^f_l - \epsilon^f_j$.

Evaluating Eq. (H.9) up to linear order in the perturbation $\tilde{\mathcal{H}}^f_{\mathrm{S}}$ leads to

$$g^{<}_{lj,uv}(t_1,t_2) \simeq g^{<,f}_{lj,uv}(t_1,t_2) + \delta g^{<,f}_{lj,uv}(t_1,t_2), \quad \text{(H.11)}$$

where the first term is the frozen component and reads

$$\begin{aligned} g^{<,f}_{lj,uv}(t_1,t_2) &= \pm i\delta_{lv}\left\langle \hat{\rho}^{f}_{uj}(t_1)\right\rangle e^{i\Delta\epsilon_{uv}(t_2-t_1)} \\ &= \pm i\delta_{lv}\left\langle \hat{\rho}^{f}_{uj}(t_2)\right\rangle e^{i\Delta\epsilon_{jv}(t_2-t_1)}, \end{aligned} \tag{H.12}$$

and the second term

$$\begin{aligned} &\delta g^{<,f}_{lj,uv}(t_1,t_2) \\ &= \pm\frac{1}{\hbar}\,\delta_{lv}\left\langle \hat{\rho}^{(f)}_{uj}(t_1)\right\rangle e^{i\Delta\epsilon_{uv}(t_2-t_1)}\left[\int_{t_0}^{t_1}dt'\xi_j(t')+\int_{t_1}^{t_2}dt'\xi_v(t')+\int_{t_2}^{t_0}dt'\xi_u(t')\right] \\ &= \pm\frac{1}{\hbar}\,\delta_{lv}\left\langle \hat{\rho}^{(f)}_{uj}(t_2)\right\rangle e^{i\Delta\epsilon_{jv}(t_2-t_1)}\left[\int_{t_0}^{t_1}dt'\xi_j(t')+\int_{t_1}^{t_2}dt'\xi_v(t')+\int_{t_2}^{t_0}dt'\xi_u(t')\right]. \end{aligned} \tag{H.13}$$

In terms of Heaviside function

$$\begin{aligned} \delta g^{<,f}_{lj,uv}(t_1,t_2) = \pm\frac{1}{\hbar}\,\delta_{lv}\left\langle \hat{\rho}^{(f)}_{uj}(t_1)\right\rangle e^{i\Delta\epsilon_{uv}(t_2-t_1)}\int_{-\infty}^{\infty}dt'\Big[\theta(t_1-t')\xi_j(t') \\ +\theta(t'-t_1)\xi_v(t')-\theta(t'-t_2)\xi_v(t')-\theta(t_2-t')\xi_u(t')\Big]. \end{aligned} \tag{H.14}$$

The adiabatic approximation consists in keeping the terms $\propto \dot{\mathbf{X}}$ in $\delta g^{<,f}_{lj,uv}(t_1,t_2)$ under the assumption that the changes in $\mathbf{X}(t)$ take place within a time scale that is much larger than the typical time scale of the dynamics of the frozen system. Under the adiabatic approximation:

$$\begin{aligned} \delta g^{<,f}_{lj,uv}(t,t_1) = \pm\frac{1}{\hbar}\,\delta_{lv}\left\langle \hat{\rho}^{(f)}_{uj}(t)\right\rangle e^{i\Delta\epsilon_{uv}(t_1-t)}\int_{-\infty}^{\infty}dt'(t'-t)\Big[\theta(t-t')\dot{X}_j(t) \\ +\theta(t'-t)\dot{X}_v(t)-\theta(t'-t_1)\dot{X}_v(t)-\theta(t_1-t')\dot{X}_u(t)\Big], \end{aligned} \tag{H.15}$$

and

$$\begin{aligned} \delta g^{<,f}_{lj,uv}(t_1,t) = \pm\frac{1}{\hbar}\,\delta_{lv}\left\langle \hat{\rho}^{(f)}_{uj}(t)\right\rangle e^{i\Delta\epsilon_{jv}(t-t_1)}\int_{-\infty}^{\infty}dt'(t'-t)\Big[\theta(t_1-t')\dot{X}_j(t) \\ +\theta(t'-t_1)\dot{X}_v(t)-\theta(t'-t)\dot{X}_v(t)-\theta(t-t')\dot{X}_u(t)\Big]. \end{aligned} \tag{H.16}$$

H.3.2 *Greater Green's function*

We have,

$$g^{>}_{uv,lj}(t_1,t_2) = -i\left\langle \hat{\rho}_{uv}(t_1)\hat{\rho}_{lj}(t_2)\right\rangle \tag{H.17}$$

Evaluating the expression for greater Green's function up to linear order in the perturbation $\tilde{\mathcal{H}}^{f}_{\mathrm{S}}$ leads to

$$g^{>}_{uv,lj}(t_1,t_2) \simeq g^{>,f}_{uv,lj}(t_1,t_2)+\delta g^{>,f}_{uv,lj}(t_1,t_2), \tag{H.18}$$

where the first term is the frozen component and reads

$$\begin{aligned} g^{>,f}_{uv,lj}(t_1,t_2) &= -i\delta_{lv}\left\langle \hat{\rho}^{f}_{uj}(t_1)\right\rangle e^{i\Delta\epsilon_{jv}(t_1-t_2)} \\ &= -i\delta_{lv}\left\langle \hat{\rho}^{f}_{uj}(t_2)\right\rangle e^{i\Delta\epsilon_{uv}(t_1-t_2)}, \end{aligned} \tag{H.19}$$

and the second term

$$\begin{aligned}
&\delta g^{>,f}_{uv,lj}(t_1,t_2)\\
&= -\frac{1}{\hbar}\,\delta_{lv}\left\langle \hat{\rho}^{(f)}_{uj}(t_1)\right\rangle e^{i\Delta\epsilon_{jv}(t_1-t_2)}\left[\int_{t_0}^{t_2}dt'\xi_j(t')+\int_{t_2}^{t_1}dt'\xi_v(t')+\int_{t_1}^{t_0}dt'\xi_u(t')\right]\\
&= -\frac{1}{\hbar}\,\delta_{lv}\left\langle \hat{\rho}^{(f)}_{uj}(t_2)\right\rangle e^{i\Delta\epsilon_{uv}(t_1-t_2)}\left[\int_{t_0}^{t_2}dt'\xi_j(t')+\int_{t_2}^{t_1}dt'\xi_v(t')+\int_{t_1}^{t_0}dt'\xi_u(t')\right]
\end{aligned} \tag{H.20}$$

In terms of Heaviside function

$$\begin{aligned}
\delta g^{>,f}_{uv,lj}(t_1,t_2) = -\frac{1}{\hbar}\,\delta_{lv}\left\langle \hat{\rho}^{(f)}_{uj}(t_1)\right\rangle e^{i\Delta\epsilon_{jv}(t_1-t_2)}\int_{-\infty}^{\infty}dt'\Big[&\theta(t_2-t')\xi_j(t')\\
&+\theta(t'-t_2)\xi_v(t')-\theta(t'-t_1)\xi_v(t')-\theta(t_1-t')\xi_u(t')\Big].
\end{aligned} \tag{H.21}$$

Under the adiabatic approximation:

$$\begin{aligned}
\delta g^{>,f}_{uv,lj}(t,t_1) = -\frac{1}{\hbar}\,\delta_{lv}\left\langle \hat{\rho}^{(f)}_{uj}(t)\right\rangle e^{i\Delta\epsilon_{jv}(t-t_1)}\int_{-\infty}^{\infty}dt'(t'-t)\Big[&\theta(t_1-t')\dot{X}_j(t)\\
&+\theta(t'-t_1)\dot{X}_v(t)-\theta(t'-t)\dot{X}_v(t)-\theta(t-t')\dot{X}_u(t)\Big],
\end{aligned} \tag{H.22}$$

and

$$\begin{aligned}
\delta g^{>,f}_{uv,lj}(t_1,t) = -\frac{1}{\hbar}\,\delta_{lv}\left\langle \hat{\rho}^{(f)}_{uj}(t)\right\rangle e^{i\Delta\epsilon_{uv}(t_1-t)}\int_{-\infty}^{\infty}dt'(t'-t)\Big[&\theta(t-t')\dot{X}_j(t)\\
&+\theta(t'-t)\dot{X}_v(t)-\theta(t'-t_1)\dot{X}_v(t)-\theta(t_1-t')\dot{X}_u(t)\Big].
\end{aligned} \tag{H.23}$$

Using Eqs. (H.15), (H.16), (H.22) and (H.23) the adiabatic contribution to Eqs. (9.21) and (9.22) can be obtained in similar fashion as in Appendix (H.2).

H.4 CALCULATION OF MASTER EQUATIONS FOR A QUTRIT

We start with the case of qutrit. The rate equation for the diagonal terms of the density matrix is given by,

$$\frac{dp_{qq}}{dt} = -\sum_{\alpha}\left[\lambda_{\alpha,0q}\Lambda^{\alpha(0)}_{0q}-\lambda_{\alpha,0q}\Lambda^{\alpha(0)}_{q0}+\lambda_{\alpha,0q}\bar{\Lambda}^{\alpha(0)}_{0q}-\lambda_{\alpha,0q}\bar{\Lambda}^{\alpha(0)}_{q0}\right], \tag{H.24}$$

where $q=(+,-)$. Similarly, the off-diagonal terms are given by:

$$\begin{aligned}
\frac{dp_{q\bar{q}}}{dt} = \frac{i}{\hbar}\left\langle\left[\mathcal{H}_S,\hat{\rho}_{q\bar{q}}\right]\right\rangle - \sum_{\alpha}\Big[&\lambda_{\alpha,0q}\Lambda^{\alpha(0)}_{0\bar{q}}-\lambda_{\alpha,0\bar{q}}\Lambda^{\alpha(0)}_{q0}\\
&+\lambda_{\alpha,0q}\bar{\Lambda}^{\alpha(0)}_{0\bar{q}}-\lambda_{\alpha,0\bar{q}}\bar{\Lambda}^{\alpha(0)}_{q0}\Big],
\end{aligned} \tag{H.25}$$

where, when $q=+$, $\bar{q}=-$ and vice-versa. We have for one of the terms in Eq. (H.25),

$$\begin{aligned}
\Lambda^{\alpha(0)}_{0q} = \int dt_1\Big[&\lambda_{\alpha,0q}\left[g^{r}_{0q,q0}\Sigma^{<,(0)}_{\alpha}+g^{<}_{0q,q0}\Sigma^{a(0)}_{\alpha}\right]\\
&+\lambda_{\alpha,0\bar{q}}\left[g^{r}_{0q,\bar{q}0}\Sigma^{<(0)}_{\alpha}+g^{<}_{0q,\bar{q}0}\Sigma^{a(0)}_{\alpha}\right]\Big].
\end{aligned} \tag{H.26}$$

We can expand all other terms in Eq. (H.25) in a similar manner. Upto first order in lead coupling strength:

$$\Lambda_{0q}^{\alpha(0)} = \frac{\lambda_{\alpha,0q}}{2}\left[-\gamma_\alpha(\Delta\epsilon_{q0})p_{00} + \tilde{\gamma}_\alpha(\Delta\epsilon_{q0})p_{qq}\right] + \frac{\lambda_{\alpha,0\bar{q}}}{2}\tilde{\gamma}_\alpha(\Delta\epsilon_{\bar{q}0})p_{\bar{q}q}. \quad \text{(H.27)}$$

We find that the diagonal and off-diagonal terms of the density matrix are coupled to each other. Substituting Eqs. (H.27) in the rate equation for diagonal and off-diagonal terms of density matrix (Eq. (H.24) and Eq. (H.25) respectively), we obtain:

$$\frac{dp_{qq}}{dt} = -\sum_\alpha \Bigg[\lambda_{\alpha,0q}^2\Big[-\gamma_\alpha(\Delta\epsilon_{q0})p_{00} + \tilde{\gamma}_\alpha(\Delta\epsilon_{q0})p_{qq} + \gamma_\alpha(\Delta\epsilon_{0q})p_{qq} - \tilde{\gamma}_\alpha(\Delta\epsilon_{0q})p_{00}\Big] + \frac{1}{2}\lambda_{\alpha,0q}\,\lambda_{\alpha,0\bar{q}}\left[\tilde{\gamma}_\alpha(\Delta\epsilon_{\bar{q}0}) + \gamma_\alpha(\Delta\epsilon_{0\bar{q}})\right]\left(p_{\bar{q}q} + p_{q\bar{q}}\right)\Bigg] \quad \text{(H.28)}$$

and

$$\frac{dp_{q\bar{q}}}{dt} = \frac{i}{\hbar}(\epsilon_q - \epsilon_{\bar{q}})p_{q\bar{q}} - \frac{1}{2}\sum_\alpha \Bigg[\lambda_{\alpha,0q}\,\lambda_{\alpha,0\bar{q}}\Big[-\gamma_\alpha(\Delta\epsilon_{\bar{q}0})p_{00} + \tilde{\gamma}_\alpha(\Delta\epsilon_{\bar{q}0})p_{\bar{q}\bar{q}} + \gamma_\alpha(\Delta\epsilon_{0q})p_{qq} - \tilde{\gamma}_\alpha(\Delta\epsilon_{0q})p_{00} + \gamma_\alpha(\Delta\epsilon_{0\bar{q}})p_{\bar{q}\bar{q}} - \tilde{\gamma}_\alpha(\Delta\epsilon_{0\bar{q}})p_{00} - \gamma_\alpha(\Delta\epsilon_{q0})p_{00} + \tilde{\gamma}_\alpha(\Delta\epsilon_{q0})p_{qq}\Big] + \lambda_{\alpha,0q}^2\Big[\tilde{\gamma}_\alpha(\Delta\epsilon_{q0})p_{q\bar{q}} + \gamma_\alpha(\Delta\epsilon_{0q})p_{q\bar{q}}\Big] + \lambda_{\alpha,0\bar{q}}^2\Big[\gamma_\alpha(\Delta\epsilon_{0\bar{q}})p_{q\bar{q}} + \tilde{\gamma}_\alpha(\Delta\epsilon_{\bar{q}0})p_{q\bar{q}}\Big]\Bigg] \quad \text{(H.29)}$$

In simplified representation using,

$$\begin{aligned}
\Gamma^0 &= \frac{1}{2}\sum_\alpha \lambda_{\alpha,0q}\lambda_{\alpha,0\bar{q}}\Big[\gamma_\alpha(\Delta\epsilon_{\bar{q}0}) + \tilde{\gamma}_\alpha(\Delta\epsilon_{0q}) + \gamma_\alpha(\Delta\epsilon_{q0}) + \tilde{\gamma}_\alpha(\Delta\epsilon_{0\bar{q}})\Big],\\
\Gamma^q &= \frac{1}{2}\sum_\alpha \lambda_{\alpha,0q}\lambda_{\alpha,0\bar{q}}\left[\gamma_\alpha(\Delta\epsilon_{0q}) + \tilde{\gamma}_\alpha(\Delta\epsilon_{q0})\right],\\
\Gamma^{\bar{q}} &= \frac{1}{2}\sum_\alpha \lambda_{\alpha,0q}\lambda_{\alpha,0\bar{q}}\left[\gamma_\alpha(\Delta\epsilon_{0\bar{q}}) + \tilde{\gamma}_\alpha(\Delta\epsilon_{\bar{q}0})\right],\\
\Gamma^{q\bar{q}} &= \frac{1}{2}\sum_\alpha \Big[\lambda_{\alpha,0q}^2\left[\tilde{\gamma}_\alpha(\Delta\epsilon_{q0}) + \gamma_\alpha(\Delta\epsilon_{0q})\right] + \lambda_{\alpha,0\bar{q}}^2\left[\gamma_\alpha(\Delta\epsilon_{0\bar{q}}) + \tilde{\gamma}_\alpha(\Delta\epsilon_{\bar{q}0})\right]\Big],
\end{aligned} \quad \text{(H.30)}$$

Eq. (H.29) becomes:

$$\frac{dp_{q\bar{q}}}{dt} = \frac{i}{\hbar}(\epsilon_q - \epsilon_{\bar{q}})p_{q\bar{q}} + \Gamma^0 p_{00} - \Gamma^q p_{qq} - \Gamma^{\bar{q}} p_{\bar{q}\bar{q}} - \Gamma^{q\bar{q}} p_{q\bar{q}}. \quad \text{(H.31)}$$

In the steady state, $\frac{dp_{q\bar{q}}}{dt} = 0$ and one can write:

$$p_{q\bar{q}} = \frac{-\Gamma^0 p_{00} + \Gamma^q p_{qq} + \Gamma^{\bar{q}} p_{\bar{q}\bar{q}}}{i\hbar^{-1}\Delta\epsilon_{q\bar{q}} - \Gamma^{q\bar{q}}}, \quad \text{(H.32)}$$

and since $p_{q\bar{q}} = p_{\bar{q}q}^\dagger$,

$$p_{q\bar{q}} + p_{\bar{q}q} = \frac{2\Gamma^{q\bar{q}}\left(\Gamma^0 p_{00} - \Gamma^q p_{qq} - \Gamma^{\bar{q}} p_{\bar{q}\bar{q}}\right)}{\hbar^{-2}\Delta\epsilon_{q\bar{q}}^2 + \left(\Gamma^{q\bar{q}}\right)^2}. \quad \text{(H.33)}$$

Substituting Eq. (H.33) in Eq. (H.28), one obtains the rate equations for the population in terms of only the diagonal terms of the density matrix.

$$\frac{dp_{qq}}{dt} = \sum_{\alpha} \Big[\Gamma^{\alpha}_{0q} p_{00} - \Gamma^{\alpha}_{q0} p_{qq} - \frac{1}{2} \lambda_{\alpha,0q}(t)\, \lambda_{\alpha,0\bar{q}}(t) \Big[\tilde{\gamma}_{\alpha}(\Delta\epsilon_{\bar{q}0}) + \gamma_{\alpha}(\Delta\epsilon_{0\bar{q}}) \Big] \left(p_{\bar{q}q} + p_{q\bar{q}} \right) \Big], \quad \text{(H.34)}$$

and

$$\frac{dp_{q\bar{q}}}{dt} = \frac{i}{\hbar}(\epsilon_q - \epsilon_{\bar{q}}) p_{q\bar{q}} + \Gamma^0 p_{00} - \Gamma^q p_{qq} - \Gamma^{\bar{q}} p_{\bar{q}\bar{q}} - \Gamma^{q\bar{q}} p_{q\bar{q}}, \quad \text{(H.35)}$$

where $q = \pm$ and $\bar{q} = -q$. In Appendix (H.4) we present the explicit definitions of $\Gamma^0, \Gamma^q, \Gamma^{\bar{q}}$ and $\Gamma^{q\bar{q}}$. We can write the master equation for both diagonal and off-diagonal terms at different orders of driving. We first study the frozen component of the dynamics.

H.4.1 *Frozen Dynamics*

Using $p^{(f)}_{q\bar{q}} = p^{(f)^{\dagger}}_{\bar{q}q}$ along with $\frac{dp^{(f)}_{qq}}{dt} = 0$ in Eq. (H.35), one obtains:

$$p^{(f)}_{q\bar{q}} + p^{(f)}_{\bar{q}q} = \frac{2\Gamma^{q\bar{q}} \left(\Gamma^0 p^{(f)}_{00} - \Gamma^q p^{(f)}_{qq} - \Gamma^{\bar{q}} p^{(f)}_{\bar{q}\bar{q}} \right)}{\hbar^{-2} \Delta\epsilon^2_{q\bar{q}} + \left(\Gamma^{q\bar{q}} \right)^2}. \quad \text{(H.36)}$$

Substituting Eq. (H.36) in Eq. (H.34), taking into account $\frac{dp^{(f)}_{qq}}{dt} = 0$ and $\sum_q p^{(f)}_{qq} + p^{(f)}_{00} = 1$, one can solve the set of rate equation to obtain the probabilities in terms of the transition rates. The energy current in the frozen basis is given by

$$J^{(E,f)}_{\alpha} = \sum_{q} \Big[\Delta\epsilon_{0q} \left[-\Gamma^{\alpha}_{q0} p^{(f)}_{qq} + \Gamma^{\alpha}_{0q} p^{(f)}_{00} \right] - \frac{1}{2} \Delta\epsilon_{0\bar{q}} \lambda_{\alpha,0q} \lambda_{\alpha,0\bar{q}} \left[\tilde{\gamma}_{\alpha}(\Delta\epsilon_{\bar{q}0}) + \gamma_{\alpha}(\Delta\epsilon_{0\bar{q}}) \right] \left(p^{(f)}_{q\bar{q}} + p^{(f)}_{\bar{q}q} \right) \Big]. \quad \text{(H.37)}$$

When one neglects the off-diagonal terms, the rate equations take a simple form given by:

$$\mathbf{W}(t) \mathbf{p}^{(f)}(t) = 0, \quad \text{(H.38)}$$

where

$$\mathbf{W}(t) = \begin{bmatrix} -\left(\Gamma^{\alpha}_{0+} + \Gamma^{\alpha}_{0-} \right) & \Gamma^{\alpha}_{+0} & \Gamma^{\alpha}_{-0} \\ \Gamma^{\alpha}_{0+} & -\Gamma^{\alpha}_{+0} & 0 \\ \Gamma^{\alpha}_{0-} & 0 & -\Gamma^{\alpha}_{-0} \end{bmatrix}, \quad \text{(H.39)}$$

and

$$\mathbf{p}^{(f)} = \begin{bmatrix} p^{(f)}_0 \\ p^{(f)}_+ \\ p^{(f)}_- \end{bmatrix}. \quad \text{(H.40)}$$

The energy current is given by:

$$J^{(E,f)}_{\alpha} = \sum_{q} \Delta\epsilon_{0q} \left[-\Gamma^{\alpha}_{q0} p^{(f)}_{qq} + \Gamma^{\alpha}_{0q} p^{(f)}_{00} \right] \quad \text{(H.41)}$$

H.4.2 *Adiabatic dynamics*

Once the frozen components of diagonal and off-diagonal probabilities are obtained, one can use those probabilities to write the rate equation up to first order in driving (adiabatic correction). In the adiabatic limit, Eq. (H.35) takes the form:

$$\frac{dp^{(f)}_{q\bar{q}}}{dt} = \frac{i}{\hbar}(\epsilon_q - \epsilon_{\bar{q}})p^{(a)}_{q\bar{q}} + \Gamma^0 p^{(a)}_{00} - \Gamma^q p^{(a)}_{qq} - \Gamma^{\bar{q}} p^{(a)}_{\bar{q}\bar{q}} - \Gamma^{q\bar{q}} p^{(a)}_{q\bar{q}}. \tag{H.42}$$

Applying $p_{q\bar{q}} = p^{\dagger}_{\bar{q}q}$, we obtain:

$$p^{(a)}_{q\bar{q}} + p^{(a)}_{\bar{q}q} = \frac{2\Gamma^{q\bar{q}}\left(\Gamma^0 p^{(a)}_{00} - \Gamma^q p^{(a)}_{qq} - \Gamma^{\bar{q}} p^{(a)}_{\bar{q}\bar{q}}\right)}{\hbar^{-2}\Delta\epsilon^2_{\bar{q}\bar{q}} + (\Gamma^{q\bar{q}})^2} + \frac{1}{i\Delta\epsilon_{q\bar{q}} - \Gamma^{q\bar{q}}}\frac{dp^{(f)}_{q\bar{q}}}{dt} - \frac{1}{i\Delta\epsilon_{q\bar{q}} + \Gamma^{q\bar{q}}}\frac{dp^{(f)}_{\bar{q}q}}{dt}. \tag{H.43}$$

The adiabatic component of Eq. (H.34) is given by:

$$\frac{dp^{(f)}_{qq}}{dt} = \sum_{\alpha}\Big[\Gamma^{\alpha}_{0q}p^{(a)}_{00} - \Gamma^{\alpha}_{q0}p^{(a)}_{qq} - \frac{1}{2}\lambda^{t}_{\alpha,0q}\lambda^{t}_{\alpha,0\bar{q}} \left[\tilde{\gamma}_{\alpha}(\Delta\epsilon_{\bar{q}0}) + \gamma_{\alpha}(\Delta\epsilon_{0\bar{q}})\right]\left(p^{(a)}_{\bar{q}\bar{q}} + p^{(a)}_{q\bar{q}}\right)\Big]. \tag{H.44}$$

Substituting Eq. (H.43) in Eq. (H.44) and solving the master equations along with the normalization condition $\sum_q p^{(a)}_{qq} + p^{(a)}_{00} = 0$ gives the adiabatic contribution to the probabilities. The energy currents can be evaluated accordingly (see Appendix (H.4) for details):

$$J^{(E,a)}_{\alpha} = \sum_{q}\Big[\Delta\epsilon_{0q}\left[-\Gamma^{\alpha}_{q0}p^{(a)}_{qq} + \Gamma^{\alpha}_{0q}p^{(a)}_{00}\right] - \frac{1}{2}\Delta\epsilon_{0\bar{q}}\lambda_{\alpha,0q} \lambda_{\alpha,0\bar{q}}\left[\tilde{\gamma}_{\alpha}(\Delta\epsilon_{\bar{q}0}) + \gamma_{\alpha}(\Delta\epsilon_{0\bar{q}})\right]\left(p^{(a)}_{q\bar{q}} + p^{(a)}_{\bar{q}q}\right)\Big]. \tag{H.45}$$

In the absence of eigenstate coherence, the rate equations become,

$$\mathbf{W}(t)\mathbf{p}^{(a)}(t) = 0, \tag{H.46}$$

where

$$\mathbf{p}^{(a)} = \begin{bmatrix} p^{(a)}_0 \\ p^{(a)}_+ \\ p^{(a)}_- \end{bmatrix}. \tag{H.47}$$

The energy current is given by:

$$J^{(E,a)}_{\alpha} = \sum_{q}\Delta\epsilon_{0q}\left[-\Gamma^{\alpha}_{q0}p^{(a)}_{qq} + \Gamma^{\alpha}_{0q}p^{(a)}_{00}\right]. \tag{H.48}$$

H.5 CALCULATIONS OF ENERGY CURRENT IN THE CASE OF QUTRIT

In this section, we will derive the expressions for charge and heat currents in the presence of off-diagonal elements of the reduced density matrix. As in the previous section, we start with the case of qutrit:

$$J_\alpha^{(E)} = \frac{1}{\hbar}\sum_q \Big[\lambda_{\alpha,q0}\Lambda_{q0}^{\alpha(1)}(t) + \lambda_{\alpha,0q}\Lambda_{0q}^{\alpha(1)}(t) - \overline{\lambda}_{\alpha,0q}\bar{\Lambda}_{0q}^{\alpha(1)}(t) - \overline{\lambda}_{\alpha,q0}\bar{\Lambda}_{q0}^{\alpha(1)}(t)\Big]. \quad \text{(H.49)}$$

We have,

$$\Lambda_{0q}^{\alpha(1)} = \int dt_1 \Big[\overline{\lambda}_{\alpha,q0}\left[G^r_{0q,q0}\Sigma_\alpha^{<,(1)} + G^<_{0q,q0}\Sigma_\alpha^{a(1)}\right] + \overline{\lambda}_{\alpha,\bar{q}0}\left[G^r_{0q,\bar{q}0}\Sigma_\alpha^{<(1)} + G^<_{0q,\bar{q}0}\Sigma_\alpha^{a(1)}\right]\Big]. \quad \text{(H.50)}$$

Upto first order in lead coupling strength:

$$\Lambda_{0q}^{\alpha(1)} = \frac{\overline{\lambda}_{\alpha,q0}}{2}\Delta\epsilon_{q0}\left[-\gamma_\alpha(\Delta\epsilon_{q0})p_{00} + \tilde{\gamma}_\alpha(\Delta\epsilon_{q0})p_{qq}\right] + \frac{\overline{\lambda}_{\alpha,\bar{q}0}}{2}\Delta\epsilon_{\bar{q}0}\,\tilde{\gamma}_\alpha(\Delta\epsilon_{\bar{q}0})p_{\bar{q}q}. \quad \text{(H.51)}$$

Using Eqs. (H.51) in the expression for energy current in Eq. (H.49), we obtain:

$$\begin{aligned} J_\alpha^{(E)} = \frac{1}{\hbar}\sum_q \Big[&\lambda_{\alpha,q0}\,\overline{\lambda}_{\alpha,0q}\Delta\epsilon_{0q}\Big[-\gamma_\alpha(\Delta\epsilon_{0q})p_{qq} + \tilde{\gamma}_\alpha(\Delta\epsilon_{0q})p_{00}\Big] + \lambda_{\alpha,0q}\,\overline{\lambda}_{\alpha,q0}\\ &\Delta\epsilon_{q0}\Big[-\gamma_\alpha(\Delta\epsilon_{q0})p_{00} + \tilde{\gamma}_\alpha(\Delta\epsilon_{q0})p_{qq}\Big] + \frac{1}{2}\Big[\lambda_{\alpha,0q}\,\overline{\lambda}_{\alpha,\bar{q}0}\Delta\epsilon_{\bar{q}0}\tilde{\gamma}_\alpha(\Delta\epsilon_{\bar{q}0})p_{\bar{q}q}\\ &- \lambda_{\alpha,q0}\,\overline{\lambda}_{\alpha,0\bar{q}}\Delta\epsilon_{0\bar{q}}\gamma_\alpha(\Delta\epsilon_{0\bar{q}})p_{q\bar{q}} - \overline{\lambda}_{\alpha,0q}\,\lambda_{\alpha,\bar{q}0}\Delta\epsilon_{0\bar{q}}\gamma_\alpha(\Delta\epsilon_{0\bar{q}})p_{\bar{q}q}\\ &+ \overline{\lambda}_{\alpha,q0}\,\lambda_{\alpha,0\bar{q}}\Delta\epsilon_{\bar{q}0}\tilde{\gamma}_\alpha(\Delta\epsilon_{\bar{q}0})p_{q\bar{q}}\Big]\Big]. \end{aligned} \quad \text{(H.52)}$$

H.6 THE LINDBLAD FORM

In this section, we will show that the master equations obtained using non-equilibrium Green's function has the Lindblad form and it corresponds to Redfield equations obtained using Lindblad formulation. For the sake of simplicity, we will consider the case of qutrit. The Hamiltonian for the qutrit

$$\tilde{H}_S = (\epsilon_+\hat{\rho}_{++} + \epsilon_-\hat{\rho}_{--} + \epsilon_0\hat{\rho}_{00}) \otimes \hat{1}_B, \quad \text{(H.53)}$$

the Hamiltonian for the baths

$$\tilde{H}_B = \hat{1}_S \otimes \sum_{k,\alpha}\epsilon_{k\alpha}\hat{b}^\dagger_{k\alpha}\hat{b}_{k\alpha}, \quad \text{(H.54)}$$

and the Hamiltonian for the contacts

$$H_{C,ff} = \sum_{q=\pm}\lambda_{\alpha,0q}\hat{\rho}_{0q} \otimes \sum_k V_{k\alpha}\left(\hat{b}_{k\alpha} + \hat{b}^\dagger_{k\alpha}\right) + \sum_{q=\pm}\lambda_{\alpha,q0}\hat{\rho}_{q0} \otimes \sum_k V_{k\alpha}\left(\hat{b}_{k\alpha} + \hat{b}^\dagger_{k\alpha}\right). \quad \text{(H.55)}$$

If the contact Hamiltonian is written as

$$H_C = A_n \otimes B_n, \tag{H.56}$$

where A represents the system degree of freedom and B represents the bath degree of freedom and

$$\begin{aligned}
A_1 &= \lambda_{L,0+}\hat{\rho}_{0+} \quad & B_1 &= \sum_k V_{kL}\left(\hat{b}_{kL} + \hat{b}_{kL}^\dagger\right) \\
A_2 &= \lambda_{L,0-}\hat{\rho}_{0-} \quad & B_2 &= \sum_k V_{kL}\left(\hat{b}_{kL} + \hat{b}_{kL}^\dagger\right) \\
A_3 &= \lambda_{L,+0}\hat{\rho}_{+0} \quad & B_3 &= \sum_k V_{kL}\left(\hat{b}_{kL} + \hat{b}_{kL}^\dagger\right) \\
A_4 &= \lambda_{L,-0}\hat{\rho}_{-0} \quad & B_4 &= \sum_k V_{kL}\left(\hat{b}_{kL} + \hat{b}_{kL}^\dagger\right),
\end{aligned} \tag{H.57}$$

and

$$\begin{aligned}
A_5 &= \lambda_{R,0+}\hat{\rho}_{0+} \quad & B_5 &= \sum_k V_{kR}\left(\hat{b}_{kR} + \hat{b}_{kR}^\dagger\right) \\
A_6 &= \lambda_{R,0-}\hat{\rho}_{0-} \quad & B_6 &= \sum_k V_{kR}\left(\hat{b}_{kR} + \hat{b}_{kR}^\dagger\right) \\
A_7 &= \lambda_{R,+0}\hat{\rho}_{+0} \quad & B_7 &= \sum_k V_{kR}\left(\hat{b}_{kR} + \hat{b}_{kR}^\dagger\right) \\
A_8 &= \lambda_{R,-0}\hat{\rho}_{-0} \quad & B_8 &= \sum_k V_{kR}\left(\hat{b}_{kR} + \hat{b}_{kR}^\dagger\right).
\end{aligned} \tag{H.58}$$

The baths correlation function

$$\Upsilon_{mn}(\epsilon) = \int_{-\infty}^{\infty} d\tau \, \langle B_m(\tau) B_n(0)\rangle \, e^{i\epsilon\tau}. \tag{H.59}$$

Since for all m, n and a fixed bath α, $B_m = B_n$, we obtain

$$\Upsilon_{mn}(\epsilon) \equiv \Upsilon_\alpha(\epsilon) = \Gamma_\alpha(\epsilon)(1 + n_\alpha(\epsilon)) + \Gamma_\alpha(-\epsilon) n_\alpha(-\epsilon). \tag{H.60}$$

We define the reduced density matrix of the system

$$\hat{\rho}_S = \begin{bmatrix} \rho_{++} & \rho_{+-} & 0 \\ \rho_{-+} & \rho_{--} & 0 \\ 0 & 0 & \rho_{00} \end{bmatrix}. \tag{H.61}$$

The Redfield equation for the time evolution of the reduced density matrix in the wide band limit is given by:

$$\begin{aligned}
\frac{d\hat{\rho}_S^I}{dt} = \frac{1}{2}\sum_{mn}\sum_{a,b,c,d} \Upsilon_{mn}(\epsilon_b - \epsilon_a) e^{-i(\epsilon_b - \epsilon_a - \epsilon_d + \epsilon_c)t} A_n^{ab} \left(A_m^{cd}\right)^* \Big\{ \hat{L}_{ab}\hat{\rho}_S^I(t)\hat{L}_{cd}^\dagger \\
- L_{cd}^\dagger L_{ab}\hat{\rho}_S^I(t)\Big\} + \frac{1}{2}\sum_{mn}\sum_{a,b,c,d} \Upsilon_{mn}(\epsilon_b - \epsilon_a) e^{i(\epsilon_b - \epsilon_a - \epsilon_d + \epsilon_c)t} \left(A_n^{ab}\right)^* A_m^{cd} \\
\Big\{ \hat{L}_{cd}\hat{\rho}_S^I(t)\hat{L}_{ab}^\dagger - \hat{\rho}_S^I(t) L_{ab}^\dagger L_{cd}\Big\},
\end{aligned} \tag{H.62}$$

where the density matrix was expressed in the interaction (I) picture. a, b, c, d represent different eigenstates $0, +, -$ of the system Hamiltonian, m, n can

be from 1 to 8 as shown in Eqs. (H.57) and (H.58) and $\hat{L}_{ab} = |a\rangle\langle b|$. The time evolution of ρ_{-+} can be obtained from

$$\langle -|\frac{d\hat{\rho}_S^I}{dt}|+\rangle = \frac{1}{2}\sum_{mn}\sum_{a,b,c,d}\Big[\gamma_{mn}(\epsilon_b-\epsilon_a)e^{-i(\epsilon_b-\epsilon_a-\epsilon_d+\epsilon_c)t}A_n^{ab}\,(A_m^c d)^* \Big\{\delta_{-a}\rho^I_{bd}\delta_{c+}-\delta_{-d}\delta_{ca}\rho^I_{b+}\Big\} + \gamma_{mn}(\epsilon_b-\epsilon_a)e^{i(\epsilon_b-\epsilon_a-\epsilon_d+\epsilon_c)t}\left(A_n^{ab}\right)^* A_m^{cd} \Big\{\delta_{c-}\rho^I_{db}\delta_{a+}-\rho^I_{-b}\delta_{ac}\delta_{d+}\Big\}\Big] \quad \text{(H.63)}$$

After some straightforward calculation, the master equation in the Schrödinger picture takes the form:

$$\frac{d\rho_{-+}}{dt} = -i\,\langle -|[H_S,\hat{\rho}_S]|+\rangle + \frac{1}{2}\sum_\alpha\Big[\lambda_{\alpha,0+}\lambda_{\alpha,0-}\gamma_\alpha(\epsilon_0-\epsilon_-)\rho_{00} - \lambda_{\alpha,0+}\lambda_{\alpha,-0}\gamma_\alpha(\epsilon_+-\epsilon_0)\rho_{++} - \lambda_{\alpha,0-}\lambda_{\alpha,-0}\gamma_\alpha(\epsilon_- -\epsilon_0)\rho_{-+} + \lambda_{\alpha,0+}\lambda_{\alpha,-0}\gamma_\alpha(\epsilon_0-\epsilon_+)\rho_{00} - \lambda_{\alpha,+0}\lambda_{\alpha,0+}\gamma_\alpha(\epsilon_+-\epsilon_0)\rho_{-+} - \lambda_{\alpha,-0}\lambda_{\alpha,0+}\gamma_\alpha(\epsilon_- -\epsilon_0)\rho_{--}\Big], \quad \text{(H.64)}$$

which is exactly the same as the master equation obtained through non-equilibrium Green's function. So, the master equation we obtained using non equilibrium Green's function corresponds to the Redfield equation in the Lindblad formalism.

BIBLIOGRAPHY

[1] G. Schaller. Open Quantum Systems Far from Equilibrium, volume 881. Springer International Publishing, 2014.

[2] H. P. Breuer and F. Petruccione. The Theory of Open Quantum Systems. Oxford University Press, Oxford, 2002.

[3] H. Haug and A. P. Jauho. Quantum Kinetics in Transport and Optics f Semiconductors. Springer-Verlag Berlin Heidelberg, 2008.

[4] G. Stefanucci and R. van Leeuwen. Nonequilibrium many-body theory of quantum systems. Cambridge University Press, 2013.

[5] Ryogo Kubo. Statistical-mechanical theory of irreversible processes. i. general theory and simple applications to magnetic and conduction problems. Journal of the Physical Society of Japan, 12(6):570–586, 1957.

[6] Ryogo Kubo, Mario Yokota, and Sadao Nakajima. Statistical-mechanical theory of irreversible processes. ii. response to thermal disturbance. Journal of the Physical Society of Japan, 12(11):1203–1211, 1957.

[7] U. Weiss. Quantum Dissipative Systems. World Scientific, 2012.

[8] María Florencia Ludovico, Michael Moskalets, David Sánchez, and Liliana Arrachea. Dynamics of energy transport and entropy production in ac-driven quantum electron systems. Phys. Rev. B, 94:035436, Jul 2016.

[9] Yigal Meir and Ned S. Wingreen. Landauer formula for the current through an interacting electron region. Phys. Rev. Lett., 68:2512–2515, Apr 1992.

[10] Teemu Ojanen and Antti-Pekka Jauho. Mesoscopic photon heat transistor. Phys. Rev. Lett., 100:155902, Apr 2008.

[11] Kirill A. Velizhanin, Michael Thoss, and Haobin Wang. Meir-wingreen formula for heat transport in a spin-boson nanojunction model. The Journal of Chemical Physics, 133(8):084503, 2010.

[12] Jian-Sheng Wang, Jian Wang, and Nan Zeng. Nonequilibrium green's function approach to mesoscopic thermal transport. Phys. Rev. B, 74:033408, Jul 2006.

[13] Keiji Saito. Energy dissipation and fluctuation response in driven quantum langevin dynamics. EPL (Europhysics Letters), 83(5):50006, sep 2008.

[14] Dvira Segal. Heat transfer in the spin-boson model: A comparative study in the incoherent tunneling regime. Phys. Rev. E, 90:012148, Jul 2014.

[15] Hartmut Haug and Antti-Pekka Jauho. Quantum kinetics in transport and optics of semiconductors, volume 2. Springer, 2008.

[16] Walter Hough. Fire-making apparatus in the United States National museum, volume 73. US Government Printing Office, 1890.

[17] R Boyle. 1662,'a defence of the doctrine touching the spring and weight of the air'. The works of Robert Boyle (1999–2000), 3:3–107, 1965.

[18] Edme Mariotte. Essays de phisique, ou, Memoires pour servir à la science des choses naturelles I [-IV]. Chez Estienne Michallet.

[19] H. T. Quan, Yu-xi Liu, C. P. Sun, and Franco Nori. Quantum thermodynamic cycles and quantum heat engines. Phys. Rev. E, 76:031105, Sep 2007.

[20] Kerson Huang. Statistical mechanics, john wily & sons. New York, 1963.

[21] J. B. Johnson. Thermal agitation of electricity in conductors. Phys. Rev., 32:97–109, Jul 1928.

[22] H. Nyquist. Thermal agitation of electric charge in conductors. Phys. Rev., 32:110–113, Jul 1928.

[23] R. A. Webb, S. Washburn, C. P. Umbach, and R. B. Laibowitz. Observation of $\frac{h}{e}$ aharonov-bohm oscillations in normal-metal rings. Phys. Rev. Lett., 54:2696–2699, Jun 1985.

[24] Jerry Moy Chow. Quantum information processing with superconducting qubits. Yale University, 2010.

[25] Charles H Bennett, François Bessette, Gilles Brassard, Louis Salvail, and John Smolin. Experimental quantum cryptography. Journal of cryptology, 5(1):3–28, 1992.

[26] Nicolas Gisin, Grégoire Ribordy, Wolfgang Tittel, and Hugo Zbinden. Quantum cryptography. Reviews of modern physics, 74(1):145, 2002.

[27] Jonne V. Koski, Ville F. Maisi, Jukka P. Pekola, and Dmitri V. Averin. Experimental realization of a szilard engine with a single electron. Proceedings of the National Academy of Sciences, 111(38):13786–13789, 2014.

[28] Olivier Maillet, Paolo A. Erdman, Vasco Cavina, Bibek Bhandari, Elsa T. Mannila, Joonas T. Peltonen, Andrea Mari, Fabio Taddei, Christopher Jarzynski, Vittorio Giovannetti, and Jukka P. Pekola. Optimal probabilistic work extraction beyond the free energy difference with a single-electron device. Phys. Rev. Lett., 122:150604, Apr 2019.

[29] John M Ziman. Principles of the Theory of Solids. Cambridge university press, 1972.

[30] R. Landauer. IBM J. Res. Dev., 1:223, 1957.

[31] R. Landauer M. Büttiker, Y. Imry and S. Pinhas. Phys. Rev. B, 31:6207, 1985.

[32] P. A. Erdman, J. T. Peltonen, B. Bhandari, B. Dutta, H. Courtois, R. Fazio, F. Taddei, and J. P. Pekola. Nonlinear thermovoltage in a single-electron transistor. Phys. Rev. B, 99:165405, Apr 2019.

[33] G. Benenti, K. Saito, and G. Casati. Thermodynamic bounds on efficiency for systems with broken time-reversal symmetry. Phys. Rev. Lett., 106:230602, Jun 2011.

[34] Gianmichele Blasi, Fabio Taddei, Liliana Arrachea, Matteo Carrega, and Alessandro Braggio. Nonlocal thermoelectricity in a superconductor–topological-insulator–superconductor junction in contact with a normal-metal probe: Evidence for helical edge states. Phys. Rev. Lett., 124:227701, Jun 2020.

[35] G. Benenti, G. Casati, K. Saito, and R. S. Whitney. Fundamental aspects of steady-state conversion of heat to work at the nanoscale. Physics Reports, 694:1 – 124, 2017. Fundamental aspects of steady-state conversion of heat to work at the nanoscale.

[36] J B Pendry. Quantum limits to the flow of information and entropy. Journal of Physics A: Mathematical and General, 16(10):2161–2171, jul 1983.

[37] Keith Schwab, EA Henriksen, JM Worlock, and Michael L Roukes. Measurement of the quantum of thermal conductance. Nature, 404(6781):974–977, 2000.

[38] Matthias Meschke, Wiebke Guichard, and Jukka P Pekola. Single-mode heat conduction by photons. Nature, 444(7116):187–190, 2006.

[39] B. Dutta, J. T. Peltonen, D. S. Antonenko, M. Meschke, M. A. Skvortsov, B. Kubala, J. König, C. B. Winkelmann, H. Courtois, and J. P. Pekola. Thermal conductance of a single-electron transistor. Phys. Rev. Lett., 119:077701, Aug 2017.

[40] A. V. Feshchenko, L. Casparis, I. M. Khaymovich, D. Maradan, O.-P. Saira, M. Palma, M. Meschke, J. P. Pekola, and D. M. Zumbühl. Tunnel-junction thermometry down to millikelvin temperatures. Phys. Rev. Applied, 4:034001, Sep 2015.

[41] JV Koski, T Sagawa, OP Saira, Y Yoon, A Kutvonen, P Solinas, M Möttönen, T Ala-Nissila, and JP Pekola. Distribution of entropy production in a single-electron box. Nature Physics, 9(10):644–648, 2013.

[42] Martin Josefsson, Artis Svilans, Adam M Burke, Eric A Hoffmann, Sofia Fahlvik, Claes Thelander, Martin Leijnse, and Heiner Linke. A quantum-dot heat engine operating close to the thermodynamic efficiency limits. Nature nanotechnology, 13(10):920–924, 2018.

[43] Shilpi Singh, Édgar Roldán, Izaak Neri, Ivan M. Khaymovich, Dmitry S. Golubev, Ville F. Maisi, Joonas T. Peltonen, Frank Jülicher, and Jukka P. Pekola. Extreme reductions of entropy in an electronic double dot. Phys. Rev. B, 99:115422, Mar 2019.

[44] J. V. Koski, V. F. Maisi, T. Sagawa, and J. P. Pekola. Experimental observation of the role of mutual information in the nonequilibrium dynamics of a maxwell demon. Phys. Rev. Lett., 113:030601, Jul 2014.

[45] J. Senior, A. Gubaydullin, B. Karimi, and et al. Heat rectification via a superconducting artificial atom. Commun Phys, 3:40, 2020.

[46] A. Ronzani, B. Karimi, J. Senior, and et al. Tunable photonic heat transport in a quantum heat valve. Nature Phys, 14:991–995, 2018.

[47] Jean-Philippe Brantut, Charles Grenier, Jakob Meineke, David Stadler, Sebastian Krinner, Corinna Kollath, Tilman Esslinger, and Antoine Georges. A thermoelectric heat engine with ultracold atoms. Science, 342(6159):713–715, 2013.

[48] Valentin Blickle and Clemens Bechinger. Realization of a micrometre-sized stochastic heat engine. Nature Physics, 8(2):143–146, 2012.

[49] Ignacio A Martínez, Édgar Roldán, Luis Dinis, Dmitri Petrov, Juan MR Parrondo, and Raúl A Rica. Brownian carnot engine. Nature physics, 12(1):67–70, 2016.

[50] Thorsten Hugel, Nolan B Holland, Anna Cattani, Luis Moroder, Markus Seitz, and Hermann E Gaub. Single-molecule optomechanical cycle. Science, 296(5570):1103–1106, 2002.

[51] Johannes Roßnagel, Samuel T Dawkins, Karl N Tolazzi, Obinna Abah, Eric Lutz, Ferdinand Schmidt-Kaler, and Kilian Singer. A single-atom heat engine. Science, 352(6283):325–329, 2016.

[52] G. Maslennikov, S. Ding, R. Hablützel, and et al. Quantum absorption refrigerator with trapped ions. Nat Commun, 10:202, 2019.

[53] Holger Thierschmann, Rafael Sánchez, Björn Sothmann, Fabian Arnold, Christian Heyn, Wolfgang Hansen, Hartmut Buhmann, and Laurens W Molenkamp. Three-terminal energy harvester with coupled quantum dots. Nature nanotechnology, 10(10):854–858, 2015.

[54] M.B Pogrebinskii. Mutual drag of charge carriers in the semiconductor-dielectric- semiconductor system. Fiz. Tekh. Poluprovodn., 11:637, 1997.

[55] B. N. Narozhny and A. Levchenko. Coulomb drag. Rev. Mod. Phys., 88:025003, May 2016.

[56] V. Moldoveanu and B. Tanatar. Coulomb drag in parallel quantum dots. EPL (Europhysics Letters), 86(6):67004, jun 2009.

[57] Rafael Sánchez, Rosa López, David Sánchez, and Markus Büttiker. Mesoscopic coulomb drag, broken detailed balance, and fluctuation relations. Phys. Rev. Lett., 104:076801, Feb 2010.

[58] Kristen Kaasbjerg and Antti-Pekka Jauho. Correlated coulomb drag in capacitively coupled quantum-dot structures. Phys. Rev. Lett., 116:196801, May 2016.

[59] Jong Soo Lim, David Sánchez, and Rosa López. Engineering drag currents in coulomb coupled quantum dots. New Journal of Physics, 20(2):023038, feb 2018.

[60] A. J. Keller, J. S. Lim, David Sánchez, Rosa López, S. Amasha, J. A. Katine, Hadas Shtrikman, and D. Goldhaber-Gordon. Cotunneling drag effect in coulomb-coupled quantum dots. Phys. Rev. Lett., 117:066602, Aug 2016.

[61] D. Bischoff, M. Eich, O. Zilberberg, C. Rössler, T. Ihn, and K. Ensslin. Measurement back-action in stacked graphene quantum dots. Nano Letters, 15(9):6003–6008, 2015. PMID: 26280388.

[62] Christian Volk, Stephan Engels, Christoph Neumann, and Christoph Stampfer. Back action of graphene charge detectors on graphene and carbon nanotube quantum dots. physica status solidi (b), 252(11):2461–2465, 2015.

[63] Gou Shinkai, Toshiaki Hayashi, Takeshi Ota, Koji Muraki, and Toshimasa Fujisawa. Bidirectional current drag induced by two-electron cotunneling in coupled double quantum dots. Applied Physics Express, 2:081101, jul 2009.

[64] Rafael Sánchez and Markus Büttiker. Optimal energy quanta to current conversion. Phys. Rev. B, 83:085428, Feb 2011.

[65] Rafael Sánchez, BjÃ¶rn Sothmann, Andrew N Jordan, and Markus BÃŒttiker. Correlations of heat and charge currents in quantum-dot thermoelectric engines. New Journal of Physics, 15(12):125001, dec 2013.

[66] Björn Sothmann, Rafael Sánchez, Andrew N. Jordan, and Markus Büttiker. Rectification of thermal fluctuations in a chaotic cavity heat engine. Phys. Rev. B, 85:205301, May 2012.

[67] A.-M. Daré and P. Lombardo. Powerful coulomb-drag thermoelectric engine. Phys. Rev. B, 96:115414, Sep 2017.

[68] F. Hartmann, P. Pfeffer, S. Höfling, M. Kamp, and L. Worschech. Voltage fluctuation to current converter with coulomb-coupled quantum dots. Phys. Rev. Lett., 114:146805, Apr 2015.

[69] B. Sothmann F. Arnold C. Heyn W. Hansen H. Buhmann H. Thierschmann, R. Sánchez and L. W. Molenkamp. Three terminal energy harvester with coupled quantum dots. Nat. Nanotechnol., 10:854, 2015.

[70] H. Thierschmann, F. Arnold, M. Mittermüller, L. Maier, C. Heyn, W. Hansen, H. Buhmann, and L. W. Molenkamp. Thermal gating of charge currents with coulomb coupled quantum dots. New Journal of Physics, 17(11):113003, oct 2015.

[71] H. Thierschmann, R. Sánchez, B. Sothmann, H. Buhmann, and L. W. Molenkamp. Thermoelectrics with coulomb-coupled quantum dots. Comptes Rendus Physique, 17(10):1109 – 1122, 2016. Mesoscopic thermoelectric phenomena / Phénoménes thermoélectriques mésoscopiques.

[72] Robert S. Whitney, Rafael Sánchez, Federica Haupt, and Janine Splettstoesser. Thermoelectricity without absorbing energy from the heat sources. Physica E: Low-dimensional Systems and Nanostructures, 75:257 – 265, 2016.

[73] Tomi Ruokola and Teemu Ojanen. Single-electron heat diode: Asymmetric heat transport between electronic reservoirs through coulomb islands. Phys. Rev. B, 83:241404, Jun 2011.

[74] Davide Venturelli, Rosario Fazio, and Vittorio Giovannetti. Minimal self-contained quantum refrigeration machine based on four quantum dots. Phys. Rev. Lett., 110:256801, Jun 2013.

[75] Yanchao Zhang, Guoxing Lin, and Jincan Chen. Three-terminal quantum-dot refrigerators. Phys. Rev. E, 91:052118, May 2015.

[76] J. V. Koski, A. Kutvonen, I. M. Khaymovich, T. Ala-Nissila, and J. P. Pekola. On-chip maxwell's demon as an information-powered refrigerator. Phys. Rev. Lett., 115:260602, Dec 2015.

[77] Rafael SÃ¡nchez. Correlation-induced refrigeration with superconducting single-electron transistors. Applied Physics Letters, 111(22):223103, 2017.

[78] Nicklas Walldorf, Antti-Pekka Jauho, and Kristen Kaasbjerg. Thermoelectrics in coulomb-coupled quantum dots: Cotunneling and energy-dependent lead couplings. Phys. Rev. B, 96:115415, Sep 2017.

[79] Thomas Dittrich, Peter Hänggi, Gert-Ludwig Ingold, Bernhard Kramer, Gerd Schön, and Wilhelm Zwerger. Quantum transport and dissipation, volume 3. Wiley-Vch Weinheim, 1998.

[80] Paolo Andrea Erdman, Bibek Bhandari, Rosario Fazio, Jukka P. Pekola, and Fabio Taddei. Absorption refrigerators based on coulomb-coupled single-electron systems. Phys. Rev. B, 98:045433, Jul 2018.

[81] Rafael Sánchez, Holger Thierschmann, and Laurens W Molenkamp. Single-electron thermal devices coupled to a mesoscopic gate. New Journal of Physics, 19(11):113040, nov 2017.

[82] J. P. Pekola and F. W. J. Hekking. Normal-metal-superconductor tunnel junction as a brownian refrigerator. Phys. Rev. Lett., 98:210604, May 2007.

[83] Noah Linden, Sandu Popescu, and Paul Skrzypczyk. How small can thermal machines be? the smallest possible refrigerator. Phys. Rev. Lett., 105:130401, Sep 2010.

[84] Paul Skrzypczyk, Nicolas Brunner, Noah Linden, and Sandu Popescu. The smallest refrigerators can reach maximal efficiency. Journal of Physics A: Mathematical and Theoretical, 44(49):492002, nov 2011.

[85] Nicolas Brunner, Noah Linden, Sandu Popescu, and Paul Skrzypczyk. Virtual qubits, virtual temperatures, and the foundations of thermodynamics. Phys. Rev. E, 85:051117, May 2012.

[86] B. Cleuren, B. Rutten, and C. Van den Broeck. Cooling by heating: Refrigeration powered by photons. Phys. Rev. Lett., 108:120603, Mar 2012.

[87] Ronnie Kosloff and Amikam Levy. Quantum heat engines and refrigerators: Continuous devices. Annual Review of Physical Chemistry, 65(1):365–393, 2014. PMID: 24689798.

[88] Nicolas Brunner, Marcus Huber, Noah Linden, Sandu Popescu, Ralph Silva, and Paul Skrzypczyk. Entanglement enhances cooling in microscopic quantum refrigerators. Phys. Rev. E, 89:032115, Mar 2014.

[89] Luis A. Correa, José P. Palao, Gerardo Adesso, and Daniel Alonso. Optimal performance of endoreversible quantum refrigerators. Phys. Rev. E, 90:062124, Dec 2014.

[90] Luis A. Correa. Multistage quantum absorption heat pumps. Phys. Rev. E, 89:042128, Apr 2014.

[91] Luis A. Correa, José P. Palao, Gerardo Adesso, and Daniel Alonso. Optimal performance of endoreversible quantum refrigerators. Phys. Rev. E, 90:062124, Dec 2014.

[92] D. Gelbwaser-Klimovsky and G. Kurizki. Heat-machine control by quantum-state preparation: From quantum engines to refrigerators. Phys. Rev. E, 90:022102, Aug 2014.

[93] Jonatan Bohr Brask and Nicolas Brunner. Small quantum absorption refrigerator in the transient regime: Time scales, enhanced cooling, and entanglement. Phys. Rev. E, 92:062101, Dec 2015.

[94] Mark T Mitchison, Mischa P Woods, Javier Prior, and Marcus Huber. Coherence-assisted single-shot cooling by quantum absorption refrigerators. New Journal of Physics, 17(11):115013, nov 2015.

[95] Ralph Silva, Paul Skrzypczyk, and Nicolas Brunner. Small quantum absorption refrigerator with reversed couplings. Phys. Rev. E, 92:012136, Jul 2015.

[96] Pierre Doyeux, Bruno Leggio, Riccardo Messina, and Mauro Antezza. Quantum thermal machine acting on a many-body quantum system: Role of correlations in thermodynamic tasks. Phys. Rev. E, 93:022134, Feb 2016.

[97] Ralph Silva, Gonzalo Manzano, Paul Skrzypczyk, and Nicolas Brunner. Performance of autonomous quantum thermal machines: Hilbert space dimension as a thermodynamical resource. Phys. Rev. E, 94:032120, Sep 2016.

[98] Zi-chen He, Xin-yun Huang, and Chang-shui Yu. Enabling the self-contained refrigerator to work beyond its limits by filtering the reservoirs. Phys. Rev. E, 96:052126, Nov 2017.

[99] G. Marchegiani, P. Virtanen, and F. Giazotto. On-chip cooling by heating with superconducting tunnel junctions. EPL (Europhysics Letters), 124(4):48005, dec 2018.

[100] Yi-Xin Chen and Sheng-Wen Li. Quantum refrigerator driven by current noise. EPL (Europhysics Letters), 97(4):40003, feb 2012.

[101] A. Mari and J. Eisert. Cooling by heating: Very hot thermal light can significantly cool quantum systems. Phys. Rev. Lett., 108:120602, Mar 2012.

[102] Bruno Leggio, Bruno Bellomo, and Mauro Antezza. Quantum thermal machines with single nonequilibrium environments. Phys. Rev. A, 91:012117, Jan 2015.

[103] Patrick P. Hofer, Martí Perarnau-Llobet, Jonatan Bohr Brask, Ralph Silva, Marcus Huber, and Nicolas Brunner. Autonomous quantum refrigerator in a circuit qed architecture based on a josephson junction. Phys. Rev. B, 94:235420, Dec 2016.

[104] Mark T Mitchison, Marcus Huber, Javier Prior, Mischa P Woods, and Martin B Plenio. Realising a quantum absorption refrigerator with an atom-cavity system. Quantum Science and Technology, 1(1):015001, mar 2016.

[105] D. T. McClure, L. DiCarlo, Y. Zhang, H.-A. Engel, C. M. Marcus, M. P. Hanson, and A. C. Gossard. Tunable noise cross correlations in a double quantum dot. Phys. Rev. Lett., 98:056801, Jan 2007.

[106] Gou Shinkai, Toshiaki Hayashi, Takeshi Ota, and Toshimasa Fujisawa. Correlated coherent oscillations in coupled semiconductor charge qubits. Phys. Rev. Lett., 103:056802, Jul 2009.

[107] Rafael Sánchez and Markus Büttiker. Optimal energy quanta to current conversion. Phys. Rev. B, 83:085428, Feb 2011.

[108] S. A. Gurvitz. Rate equations for quantum transport in multidot systems. Phys. Rev. B, 57:6602–6611, Mar 1998.

[109] B. L. Hazelzet, M. R. Wegewijs, T. H. Stoof, and Yu. V. Nazarov. Coherent and incoherent pumping of electrons in double quantum dots. Phys. Rev. B, 63:165313, Apr 2001.

[110] D. Sztenkiel and R. Świrkowicz. Electron transport through parallel double quantum dots with interdot correlations. physica status solidi (b), 244(7):2543–2548, 2007.

[111] Bing Dong, H. L. Cui, and X. L. Lei. Quantum rate equations for electron transport through an interacting system in the sequential tunneling regime. Phys. Rev. B, 69:035324, Jan 2004.

[112] Bing Dong, X. L. Lei, and Norman J. M. Horing. First-order coherent resonant tunneling through an interacting coupled-quantum-dot interferometer: Generic quantum rate equations and current noise. Phys. Rev. B, 77:085309, Feb 2008.

[113] R. C. Dynes, V. Narayanamurti, and J. P. Garno. Direct measurement of quasiparticle-lifetime broadening in a strong-coupled superconductor. Phys. Rev. Lett., 41:1509–1512, Nov 1978.

[114] J. P. Pekola, V. F. Maisi, S. Kafanov, N. Chekurov, A. Kemppinen, Yu. A. Pashkin, O.-P. Saira, M. Möttönen, and J. S. Tsai. Environment-assisted tunneling as an origin of the dynes density of states. Phys. Rev. Lett., 105:026803, Jul 2010.

[115] Francesco Giazotto, Tero T. Heikkilä, Arttu Luukanen, Alexander M. Savin, and Jukka P. Pekola. Opportunities for mesoscopics in thermometry and refrigeration: Physics and applications. Rev. Mod. Phys., 78:217–274, Mar 2006.

[116] F. Giazotto and M. Martínez-Pérez. The josephson heat interferometer. Nature, 492:401–405, 2012.

[117] J. Pekola. Towards quantum thermodynamics in electronic circuits. Nature Phys, 11:118–123, 2015.

[118] Olivier Maillet, Diego A. Subero Rengel, Joonas T. Peltonen, Dmitry S. Golubev, and Jukka P. Pekola. Electric field control of radiative heat transfer in a superconducting circuit, 2020.

[119] Chauncey Starr. The copper oxide rectifier. Physics, 7(1):15–19, 1936.

[120] David M.-T. Kuo and Yia-chung Chang. Thermoelectric and thermal rectification properties of quantum dot junctions. Phys. Rev. B, 81:205321, May 2010.

[121] Alejandro Marcos-Vicioso, Carmen López-Jurado, Miguel Ruiz-Garcia, and Rafael Sánchez. Thermal rectification with interacting electronic channels: Exploiting degeneracy, quantum superpositions, and interference. Phys. Rev. B, 98:035414, Jul 2018.

[122] Jian-Hua Jiang, Manas Kulkarni, Dvira Segal, and Yoseph Imry. Phonon thermoelectric transistors and rectifiers. Phys. Rev. B, 92:045309, Jul 2015.

[123] Dvira Segal and Abraham Nitzan. Spin-boson thermal rectifier. Phys. Rev. Lett., 94:034301, Jan 2005.

[124] Lian-Ao Wu, Claire X. Yu, and Dvira Segal. Nonlinear quantum heat transfer in hybrid structures: Sufficient conditions for thermal rectification. Phys. Rev. E, 80:041103, Oct 2009.

[125] Bijay Kumar Agarwalla and Dvira Segal. Energy current and its statistics in the nonequilibrium spin-boson model: Majorana fermion representation. New Journal of Physics, 19(4):043030, apr 2017.

[126] Tomi Ruokola, Teemu Ojanen, and Antti-Pekka Jauho. Thermal rectification in nonlinear quantum circuits. Phys. Rev. B, 79:144306, Apr 2009.

[127] Lian-Ao Wu and Dvira Segal. Sufficient conditions for thermal rectification in hybrid quantum structures. Phys. Rev. Lett., 102:095503, Mar 2009.

[128] Nan Zeng and Jian-Sheng Wang. Mechanisms causing thermal rectification: The influence of phonon frequency, asymmetry, and nonlinear interactions. Phys. Rev. B, 78:024305, Jul 2008.

[129] M. Terraneo, M. Peyrard, and G. Casati. Controlling the energy flow in nonlinear lattices: A model for a thermal rectifier. Phys. Rev. Lett., 88:094302, Feb 2002.

[130] Baowen Li, Lei Wang, and Giulio Casati. Thermal diode: Rectification of heat flux. Phys. Rev. Lett., 93:184301, Oct 2004.

[131] Yue-Yang Liu, Wu-Xing Zhou, Li-Ming Tang, and Ke-Qiu Chen. An important mechanism for thermal rectification in graded nanowires. Applied Physics Letters, 105(20):203111, 2014.

[132] K. G. S. H. Gunawardana, Kieran Mullen, Jiuning Hu, Yong P. Chen, and Xiulin Ruan. Tunable thermal transport and thermal rectification in strained graphene nanoribbons. Phys. Rev. B, 85:245417, Jun 2012.

[133] Gabriel T. Landi, E. Novais, Mário J. de Oliveira, and Dragi Karevski. Flux rectification in the quantum xxz chain. Phys. Rev. E, 90:042142, Oct 2014.

[134] Jean-Pierre Eckmann and Carlos Mejía-Monasterio. Thermal rectification in billiardlike systems. Phys. Rev. Lett., 97:094301, Aug 2006.

[135] Karl Joulain, Jérémie Drevillon, Younès Ezzahri, and Jose Ordonez-Miranda. Quantum thermal transistor. Phys. Rev. Lett., 116:200601, May 2016.

[136] M. J. Martínez-Pérez and F. Giazotto. Efficient phase-tunable josephson thermal rectifier. Applied Physics Letters, 102(18):182602, 2013.

[137] Teemu Ojanen. Selection-rule blockade and rectification in quantum heat transport. Phys. Rev. B, 80:180301, Nov 2009.

[138] Clayton R. Otey, Wah Tung Lau, and Shanhui Fan. Thermal rectification through vacuum. Phys. Rev. Lett., 104:154301, Apr 2010.

[139] Rafael Sánchez, BjÃ¶rn Sothmann, and Andrew N Jordan. Heat diode and engine based on quantum hall edge states. New Journal of Physics, 17(7):075006, jul 2015.

[140] C. W. Chang, D. Okawa, A. Majumdar, and A. Zettl. Solid-state thermal rectifier. Science, 314(5802):1121–1124, 2006.

[141] R Scheibner, M KÃ¶nig, D Reuter, A D Wieck, C Gould, H Buhmann, and L W Molenkamp. Quantum dot as thermal rectifier. New Journal of Physics, 10(8):083016, aug 2008.

[142] Markus Schmotz, Judith Maier, Elke Scheer, and Paul Leiderer. A thermal diode using phonon rectification. New Journal of Physics, 13(11):113027, nov 2011.

[143] M. Martínez-Pérez, A. Fornieri, and F. Giazotto. Rectification of electronic heat current by a hybrid thermal diode. Nature Nanotech, 10:303–307, 2015.

[144] Andreu Riera-Campeny, Mohammad Mehboudi, Marisa Pons, and Anna Sanpera. Dynamically induced heat rectification in quantum systems. Phys. Rev. E, 99:032126, Mar 2019.

[145] M. Turek and K. A. Matveev. Cotunneling thermopower of single electron transistors. Phys. Rev. B, 65:115332, Mar 2002.

[146] Bibek Bhandari, Giuliano Chiriacò, Paolo A. Erdman, Rosario Fazio, and Fabio Taddei. Thermal drag in electronic conductors. Phys. Rev. B, 98:035415, Jul 2018.

[147] Pablo Schad, Alexander Shnirman, and Yuriy Makhlin. Using majorana spin-$\frac{1}{2}$ representation for the spin-boson model. Phys. Rev. B, 93:174420, May 2016.

[148] Maura Sassetti and Ulrich Weiss. Correlation functions for dissipative two-state systems: Effects of the initial preparation. Phys. Rev. A, 41:5383–5393, May 1990.

[149] MH Devoret, Steven Girvin, and Robert Schoelkopf. Circuit-qed: How strong can the coupling between a josephson junction atom and a transmission line resonator be? Annalen der Physik, 16(10-11):767–779, 2007.

[150] J Bourassa, F Beaudoin, Jay M Gambetta, and A Blais. Josephson-junction-embedded transmission-line resonators: From kerr medium to in-line transmon. Physical Review A, 86(1):013814, 2012.

[151] Leong Chuan Kwek. Strong light-matter coupling: from atoms to solid-state systems. World Scientific, 2013.

[152] Yigal Meir, Ned S. Wingreen, and Patrick A. Lee. Transport through a strongly interacting electron system: Theory of periodic conductance oscillations. Phys. Rev. Lett., 66:3048–3051, Jun 1991.

[153] L. W. Molenkamp, Th. Gravier, H. van Houten, O. J. A. Buijk, M. A. A. Mabesoone, and C. T. Foxon. Peltier coefficient and thermal conductance of a quantum point contact. Phys. Rev. Lett., 68:3765–3768, Jun 1992.

[154] O. Chiatti, J. T. Nicholls, Y. Y. Proskuryakov, N. Lumpkin, I. Farrer, and D. A. Ritchie. Quantum thermal conductance of electrons in a one-dimensional wire. Phys. Rev. Lett., 97:056601, Aug 2006.

[155] Eric A. Hoffmann, Henrik A. Nilsson, Jason E. Matthews, Natthapon Nakpathomkun, Ann I. Persson, Lars Samuelson, and Heiner Linke. Measuring temperature gradients over nanometer length scales. Nano Letters, 9(2):779–783, 2009. PMID: 19159269.

[156] S. Jezouin, F. D. Parmentier, A. Anthore, U. Gennser, A. Cavanna, Y. Jin, and F. Pierre. Quantum limit of heat flow across a single electronic channel. Science, 342(6158):601–604, 2013.

[157] Heiblum M. Rosenblatt A. et al. Banerjee, M. Observed quantization of anyonic heat flow. Nature, 545:75, 2017.

[158] Longji Cui, Wonho Jeong, Sunghoon Hur, Manuel Matt, Jan C. Klöckner, Fabian Pauly, Peter Nielaba, Juan Carlos Cuevas, Edgar Meyhofer, and Pramod Reddy. Quantized thermal transport in single-atom junctions. Science, 355(6330):1192–1195, 2017.

[159] Drechsler U. Menges F. et al. Mosso, N. Heat transport through atomic contacts. Nature Nanotech, 12:430, 2017.

[160] Stefano Roddaro, Daniele Ercolani, Mian Akif Safeen, Soile Suomalainen, Francesco Rossella, Francesco Giazotto, Lucia Sorba, and Fabio Beltram. Giant thermovoltage in single inas nanowire field-effect transistors. Nano Letters, 13(8):3638–3642, 2013. PMID: 23869467.

[161] Phillip M. Wu, Johannes Gooth, Xanthippi Zianni, Sofia Fahlvik Svensson, Jan GÃ¶ran Gluschke, Kimberly A. Dick, Claes Thelander, Kornelius Nielsch, and Heiner Linke. Large thermoelectric power factor enhancement observed in inas nanowires. Nano Letters, 13(9):4080–4086, 2013. PMID: 23919739.

[162] A.S. Dzurak, C.G. Smith, M. Pepper, D.A. Ritchie, J.E.F. Frost, G.A.C. Jones, and D.G. Hasko. Observation of coulomb blockade oscillations in the thermopower of a quantum dot. Solid State Communications, 87(12):1145 – 1149, 1993.

[163] A. A. M Staring, L. W Molenkamp, B. W Alphenaar, H. van Houten, O. J. A Buyk, M. A. A Mabesoone, C. W. J Beenakker, and C. T Foxon. Coulomb-blockade oscillations in the thermopower of a quantum dot. Europhysics Letters (EPL), 22(1):57–62, apr 1993.

[164] L Molenkamp, A A M Staring, B W Alphenaar, H van Houten, and C W J Beenakker. Sawtooth-like thermopower oscillations of a quantum dot in the coulomb blockade regime. Semiconductor Science and Technology, 9(5S):903–906, may 1994.

[165] A. S. Dzurak, C. G. Smith, C. H. W. Barnes, M. Pepper, L. Martín-Moreno, C. T. Liang, D. A. Ritchie, and G. A. C. Jones. Thermoelectric signature of the excitation spectrum of a quantum dot. Phys. Rev. B, 55:R10197–R10200, Apr 1997.

[166] S. Möller, H. Buhmann, S. F. Godijn, and L. W. Molenkamp. Charging energy of a chaotic quantum dot. Phys. Rev. Lett., 81:5197–5200, Dec 1998.

[167] S. F. Godijn, S. Möller, H. Buhmann, L. W. Molenkamp, and S. A. van Langen. Thermopower of a chaotic quantum dot. Phys. Rev. Lett., 82:2927–2930, Apr 1999.

[168] M. C. Llaguno, J. E. Fischer, A. T. Johnson, and J. Hone. Observation of thermopower oscillations in the coulomb blockade regime in a semiconducting carbon nanotube. Nano Letters, 4(1):45, 2004.

[169] R. Scheibner, H. Buhmann, D. Reuter, M. N. Kiselev, and L. W. Molenkamp. Thermopower of a kondo spin-correlated quantum dot. Phys. Rev. Lett., 95:176602, Oct 2005.

[170] Budantsev M.V. Lavrov R.A. et al. Pogosov, A.G. Coulomb blockade and the thermopower of a suspended quantum dot. Jetp Lett., 83:122, 2006.

[171] R. Scheibner, E. G. Novik, T. Borzenko, M. König, D. Reuter, A. D. Wieck, H. Buhmann, and L. W. Molenkamp. Sequential and cotunneling behavior in the temperature-dependent thermopower of few-electron quantum dots. Phys. Rev. B, 75:041301, Jan 2007.

[172] S Fahlvik Svensson, A I Persson, E A Hoffmann, N Nakpathomkun, H A Nilsson, H Q Xu, L Samuelson, and H Linke. Lineshape of the thermopower of quantum dots. New Journal of Physics, 14(3):033041, mar 2012.

[173] S Fahlvik Svensson, E A Hoffmann, N Nakpathomkun, P M Wu, H Q Xu, H A Nilsson, D Sánchez, V Kashcheyevs, and H Linke. Nonlinear thermovoltage and thermocurrent in quantum dots. New Journal of Physics, 15(10):105011, oct 2013.

[174] Bivas Dutta, Danial Majidi, Alvaro GarcÃa Corral, Paolo A. Erdman, Serge Florens, Theo A. Costi, HervÃ© Courtois, and Clemens B. Winkelmann. Direct probe of the seebeck coefficient in a kondo-correlated single-quantum-dot transistor. Nano Letters, 19(1):506–511, 2019.

[175] C. W. J. Beenakker and A. A. M. Staring. Theory of the thermopower of a quantum dot. Phys. Rev. B, 46:9667–9676, Oct 1992.

[176] A. V. Andreev and K. A. Matveev. Coulomb blockade oscillations in the thermopower of open quantum dots. Phys. Rev. Lett., 86:280–283, Jan 2001.

[177] M. Turek and K. A. Matveev. Cotunneling thermopower of single electron transistors. Phys. Rev. B, 65:115332, Mar 2002.

[178] Jens Koch, Felix von Oppen, Yuval Oreg, and Eran Sela. Thermopower of single-molecule devices. Phys. Rev. B, 70:195107, Nov 2004.

[179] Björn Kubala and Jürgen König. Quantum-fluctuation effects on the thermopower of a single-electron transistor. Phys. Rev. B, 73:195316, May 2006.

[180] Björn Kubala, Jürgen König, and Jukka Pekola. Violation of the wiedemann-franz law in a single-electron transistor. Phys. Rev. Lett., 100:066801, Feb 2008.

[181] A. S. Vasenko, D. M. Basko, and F. W. J. Hekking. Giant mesoscopic fluctuations of the elastic cotunneling thermopower of a single-electron transistor. Phys. Rev. B, 91:085310, Feb 2015.

[182] D Boese and R Fazio. Thermoelectric effects in kondo-correlated quantum dots. Europhysics Letters (EPL), 56(4):576–582, nov 2001.

[183] R. Świrkowicz, M. Wierzbicki, and J. Barnaś. Thermoelectric effects in transport through quantum dots attached to ferromagnetic leads with noncollinear magnetic moments. Phys. Rev. B, 80:195409, Nov 2009.

[184] Rosa López and David Sánchez. Nonlinear heat transport in mesoscopic conductors: Rectification, peltier effect, and wiedemann-franz law. Phys. Rev. B, 88:045129, Jul 2013.

[185] Prasenjit Dutt and Karyn Le Hur. Strongly correlated thermoelectric transport beyond linear response. Phys. Rev. B, 88:235133, Dec 2013.

[186] Rafael Sánchez, BjÃ¶rn Sothmann, Andrew N Jordan, and Markus BÃŒttiker. Correlations of heat and charge currents in quantum-dot thermoelectric engines. New Journal of Physics, 15(12):125001, dec 2013.

[187] Miguel A. Sierra and David Sánchez. Strongly nonlinear thermovoltage and heat dissipation in interacting quantum dots. Phys. Rev. B, 90:115313, Sep 2014.

[188] Natalya A. Zimbovskaya. The effect of coulomb interactions on nonlinear thermovoltage and thermocurrent in quantum dots. The Journal of Chemical Physics, 142(24):244310, 2015.

[189] Paolo Andrea Erdman, Francesco Mazza, Riccardo Bosisio, Giuliano Benenti, Rosario Fazio, and Fabio Taddei. Thermoelectric properties of an interacting quantum dot based heat engine. Phys. Rev. B, 95:245432, Jun 2017.

[190] Diego Pérez Daroca, Pablo Roura-Bas, and Armando A. Aligia. Enhancing the nonlinear thermoelectric response of a correlated quantum dot in the kondo regime by asymmetrical coupling to the leads. Phys. Rev. B, 97:165433, Apr 2018.

[191] C. Jarzynski. Nonequilibrium Equality for Free Energy Differences. Phys. Rev. Lett., 78:2690–2693, 1997.

[192] Gavin E. Crooks. Entropy production fluctuation theorem and the nonequilibrium work relation for free energy differences. Phys. Rev. E, 60:2721–2726, 1999.

[193] Emil Mittag Debra J. Searles G. M. Wang, E. M. Sevick and Denis J. Evans. Experimental Demonstration of Violations of the Second Law of Thermodynamics for Small Systems and Short Time Scales. Phys. Rev. Lett., 89:050601, 2002.

[194] Artyom Petrosyan Sergio Ciliberto Raoul Dillenschneider Antoine Bérut, Artak Arakelyan and Eric Lutz. Experimental verification of Landauer's principle linking information and thermodynamics. Nature, 483:187–189, March 2012.

[195] C. Jarzynski S. B. Smith I. Tinoco Jr D. Collin, F. Ritort and C. Bustamante. Verification of the Crooks fluctuation theorem and recovery of RNA folding free energies. Nature, 437:231–234, September 2005.

[196] Udo Seifert. Stochastic thermodynamics, fluctuation theorems and molecular machines. Rep. Prog. Phys., 75:126001, 2012.

[197] J. M. R. Parrondo É Roldán, I. A. Martínez and D. Petrov. Universal features in the energetics of symmetry breaking. Nature Physics, 10:457–461, June 2014.

[198] T. Tanttu M. Möttönen D. V. Averin O.-P. Saira, Y. Yoon and J. P. Pekola. Test of the Jarzynski and Crooks Fluctuation Relations in an Electronic System. Phys. Rev. Lett., 109:180601, October 2012.

[199]

[200] R. S. Sarthour I. S. Oliveira M. Paternostro E. Lutz T. B. Batalhão, A. M. Souza and R. M. Serra. Irreversibility and the Arrow of Time in a Quenched QuantumSystem. Phys. Rev. Lett., 115:190601, November 2015.

[201] Landry Bretheau Philippe Campagne-Ibarcq Quentin Ficheux Janet Anders Alexia Auffèves Rémi Azouit Pierre Rouchon Nathanaël Cottet, Sébastien Jezouin and Benjamin Huard. Observing a quantum Maxwell demon at work. PNAS, 114:7561–7564, July 2017.

[202] A. Romito E. Lutz M. Naghiloo, J. J. Alonso and K. W. Murch. Information Gain and Loss for a Quantum Maxwell's Demon. Phys. Rev. Lett., 121:030604, July 2018.

[203] R Renner D Egloff, O C O Dahlsten and V Vedral. A measure of majorization emerging from single-shot statistical mechanics. New Journal of Physics, 17:073001, july 2015.

[204] Oscar C O Dahlsten Nicole Yunger Halpern, Andrew J P Garner and Vlatko Vedral. Introducing one-shot work into fluctuation relations. New Journal of Physics, 17:095003, sep 2015.

[205] Tim Schmiedl and Udo Seifert. Optimal finite-time processes in stochastic thermodynamics. Phys. Rev. Lett., 98:108301, Mar 2007.

[206] Alexandre P. Solon and Jordan M. Horowitz. Phase transition in protocols minimizing work fluctuations. Phys. Rev. Lett., page 180605, May 2018.

[207] Andrea Mari Vasco Cavina and Vittorio Giovannetti. Optimal processes for probabilistic work extraction beyond the second law. Scientific Reports, 6:29282, July 2016.

[208] Gert-Ludwig Ingold and Yu. V. Nazarov. Charge Tunneling Rates in Ultrasmall Junctions. NATO ASI Series. Springer US, Boston, 1992.

[209] Jukka P. Pekola Jonne V. Koski, Ville F. Maisi and Dmitri V. Averin. Experimental realization of a Szilard engine with a single electron. PNAS, 111:13786–13789, September 2014.

[210] Takahiro Sagawa and Masahito Ueda. Generalized Jarzynski Equality under Nonequilibrium FeedbackControl. Phys. Rev. Lett., 104:090602, March 2010.

[211] H. E. D. Scovil and E. O. Schulz-DuBois. Three-level masers as heat engines. Phys. Rev. Lett., 2:262–263, Mar 1959.

[212] J. E. Geusic, E. O. Schulz-DuBios, and H. E. D. Scovil. Quantum equivalent of the Carnot cycle. Phys. Rev., 156:343–351, Apr 1967.

[213] E. Geva and R. Kosloff. On the classical limit of quantum thermodynamics in finite time. The Journal of Chemical Physics, 97(6):4398–4412, 1992.

[214] A. E. Allahverdyan and Th. M. Nieuwenhuizen. Extraction of work from a single thermal bath in the quantum regime. Phys. Rev. Lett., 85:1799–1802, Aug 2000.

[215] P. Hänggi and F. Marchesoni. Artificial brownian motors: Controlling transport on the nanoscale. Rev. Mod. Phys., 81:387–442, Mar 2009.

[216] J. Gemmer, M. Michel, and G. Mahler. Quantum Thermodynamics, volume 784. Springer-Verlag Berlin Heidelberg, 2009.

[217] M. Horodecki and J. Oppenheim. Fundamental limitations for quantum and nanoscale thermodynamics. Nature Communications, 4:2059, Jun 2013.

[218] F. Binder, L. A. Correa, C. Gogolin, J. Anders, and G. Adesso. Thermodynamics in the Quantum Regime, volume 195. Springer International Publishing, 2018.

[219] R. Alicki. The quantum open system as a model of the heat engine. Journal of Physics A: Mathematical and General, 12(5):L103–L107, may 1979.

[220] E. Geva and R. Kosloff. A quantum-mechanical heat engine operating in finite time. a model consisting of spin-1/2 systems as the working fluid. The Journal of Chemical Physics, 96(4):3054–3067, 1992.

[221] M. Wiedmann, J. T. Stockburger, and J. Ankerhold. Out-of-equilibrium operation of a quantum heat engine: The cost of thermal coupling control.

[222] R. Dann and R. Kosloff. Quantum signatures in the quantum carnot cycle.

[223] T. Villazon, A. Polkovnikov, and A. Chandran. Swift heat transfer by fast-forward driving in open quantum systems. Phys. Rev. A, 100:012126, Jul 2019.

[224] A. Tobalina, A. Lizuain, and J. G. Muga. Vanishing efficiency of a speeded-up ion-in-paul-trap otto engine. EPL (Europhysics Letters), 127(2):20005, aug 2019.

[225] K. Funo, N. Lambert, B. Karimi, J. P. Pekola, Y. Masuyama, and F. Nori. Speeding up a quantum refrigerator via counterdiabatic driving. Phys. Rev. B, 100:035407, Jul 2019.

[226] P. A. Erdman, V. Cavina, R. Fazio, F. Taddei, and V. Giovannetti. Maximum power and corresponding efficiency for two-level heat engines and refrigerators: optimality of fast cycles. New Journal of Physics, 21(10):103049, oct 2019.

[227] R. Biele, C. A. Rodríguez-Rosario, T. Frauenheim, and A. Rubio. Controlling heat and particle currents in nanodevices by quantum observation. npj Quantum Materials, 2(1):38, Jul 2017.

[228] C. Elouard, D. Herrera-Martí, B. Huard, and A. Auffèves. Extracting work from quantum measurement in maxwell's demon engines. Phys. Rev. Lett., 118:260603, Jun 2017.

[229] C. Elouard and A. N. Jordan. Efficient quantum measurement engines. Phys. Rev. Lett., 120:260601, Jun 2018.

[230] L. Buffoni, A. Solfanelli, P. Verrucchi, A. Cuccoli, and M. Campisi. Quantum measurement cooling. Phys. Rev. Lett., 122:070603, Feb 2019.

[231] P. Murphy, S. Mukerjee, and J. Moore. Optimal thermoelectric figure of merit of a molecular junction. Phys. Rev. B, 78:161406(R), Oct 2008.

[232] M. Esposito, K. Lindenberg, and C. Van den Broeck. Thermoelectric efficiency at maximum power in a quantum dot. EPL (Europhysics Letters), 85(6):60010, mar 2009.

[233] S. Juergens, F. Haupt, M. Moskalets, and J. Splettstoesser. Thermoelectric performance of a driven double quantum dot. Phys. Rev. B, 87:245423, Jun 2013.

[234] D. Gelbwaser-Klimovsky, R. Alicki, and G. Kurizki. Minimal universal quantum heat machine. Phys. Rev. E, 87:012140, Jan 2013.

[235] B. Sothmann, R. Sánchez, and A. N. Jordan. Thermoelectric energy harvesting with quantum dots. Nanotechnology, 26(3):032001, dec 2014.

[236] C. Chamon, E. R. Mucciolo, L. Arrachea, and R. B. Capaz. Heat pumping in nanomechanical systems. Phys. Rev. Lett., 106:135504, Apr 2011.

[237] L. Arrachea, E. R. Mucciolo, C. Chamon, and R. B. Capaz. Microscopic model of a phononic refrigerator. Phys. Rev. B, 86:125424, Sep 2012.

[238] J. P. S. Peterson, T. B. Batalhão, M. Herrera, A. M. Souza, R. S. Sarthour, I. S. Oliveira, and R. M. Serra. Experimental characterization of a spin quantum heat engine. Phys. Rev. Lett., 123:240601, Dec 2019.

[239] B. Roche, R.-P. Riwar, B. Voisin, E. Dupont-Ferrier, R. Wacquez, M. Vinet, M. Sanquer, J. Splettstoesser, and X. Jehl. A two-atom electron pump. Nature Communications, 4(1):1581, 2013.

[240] H. Pothier, P. Lafarge, C. Urbina, D. Esteve, and M. H. Devoret. Single-electron pump based on charging effects. Europhysics Letters (EPL), 17(3):249–254, jan 1992.

[241] M. Campisi, J. Pekola, and R. Fazio. Nonequilibrium fluctuations in quantum heat engines: theory, example, and possible solid state experiments. New Journal of Physics, 17(3):035012, mar 2015.

[242] H. Thierschmann, R. Sánchez, B. Sothmann, F. Arnold, C. Heyn, W. Hansen, H. Buhmann, and L. W. Molenkamp. Three-terminal energy harvester with coupled quantum dots. Nature Nanotechnology, 10(10):854–858, 2015.

[243] J. P. Pekola and I. M. Khaymovich. Thermodynamics in single-electron circuits and superconducting qubits. Annual Review of Condensed Matter Physics, 10(1):193–212, 2019.

[244] A. Dechant, N. Kiesel, and E. Lutz. All-optical nanomechanical heat engine. Phys. Rev. Lett., 114:183602, May 2015.

[245] A. D. O'Connell, M. Hofheinz, M. Ansmann, R. C. Bialczak, M. Lenander, E. Lucero, M. Neeley, D. Sank, H. Wang, M. Weides, J. Wenner, J. M. Martinis, and A. N. Cleland. Quantum ground state and single-phonon control of a mechanical resonator. Nature, 464(7289):697–703, 2010.

[246] L. Arrachea, N. Bode, and F. von Oppen. Vibrational cooling and thermoelectric response of nanoelectromechanical systems. Phys. Rev. B, 90:125450, Sep 2014.

[247] P. Stadler, W. Belzig, and G. Rastelli. Ground-state cooling of a mechanical oscillator by interference in andreev reflection. Phys. Rev. Lett, 117:197202, Feb 2016.

[248] C. Urgell, W. Yang, S. L. De Bonis, C. Samanta, M. J. Esplandiu, Q. Dong, Y. Jin, and A. Bachtold. Cooling and self-oscillation in a nanotube electromechanical resonator. Nature Physics, 16:32, Jan 2020.

[249] J. P. Brantut, C. Grenier, J. Meineke, D. Stadler, S. Krinner, C. Kollath, T. Esslinger, and A. Georges. A thermoelectric heat engine with ultracold atoms. Science, 342(6159):713–715, 2013.

[250] O. Abah, J. Roßnagel, G. Jacob, S. Deffner, F. Schmidt-Kaler, K. Singer, and E. Lutz. Single-ion heat engine at maximum power. Phys. Rev. Lett., 109:203006, Nov 2012.

[251] S. Deng, A. Chenu, P. Diao, F. Li, S. Yu, I. Coulamy, A. del Campo, and H. Wu. Superadiabatic quantum friction suppression in finite-time thermodynamics. Science Advances, 4(4), 2018.

[252] Rogério J. de Assis, T. M. de Mendonca, Celso J. Villas-Boas, Alexandre M. de Souza, Roberto S. Sarthour, Ivan S. Oliveira, and Norton G. de Almeida. Phys. Rev. Lett., 122:240602, Jun 2019.

[253] R. Kosloff. A quantum mechanical open system as a model of a heat engine. The Journal of Chemical Physics, 80(4):1625, 1984.

[254] T. Feldmann and R. Kosloff. Performance of discrete heat engines and heat pumps in finite time. Phys. Rev. E, 61:4774–4790, May 2000.

[255] M. O. Scully. Quantum afterburner: Improving the efficiency of an ideal heat engine. Phys. Rev. Lett., 88:050602, Jan 2002.

[256] B. Lin and J. Chen. Performance analysis of an irreversible quantum heat engine working with harmonic oscillators. Phys. Rev. E, 67:046105, Apr 2003.

[257] T. D. Kieu. The second law, maxwell's demon, and work derivable from quantum heat engines. Phys. Rev. Lett., 93:140403, Sep 2004.

[258] Y. Rezek and R. Kosloff. Irreversible performance of a quantum harmonic heat engine. New Journal of Physics, 8(5):83–83, may 2006.

[259] H. T. Quan, Yu-xi Liu, C. P. Sun, and F. Nori. Quantum thermodynamic cycles and quantum heat engines. Phys. Rev. E, 76:031105, Sep 2007.

[260] M. J. Henrich, F. Rempp, and G. Mahler. Quantum thermodynamic otto machines: A spin-system approach. The European Physical Journal Special Topics, 151(1):157–165, 2007.

[261] The performance characteristics of an irreversible quantum otto harmonic refrigeration cycle. Science in China Series G: Physics, Mechanics and Astronomy, 52(9):1317–1323, 2009.

[262] O. Abah, J. Roßnagel, G. Jacob, S. Deffner, F. Schmidt-Kaler, K. Singer, and E. Lutz. Single-ion heat engine at maximum power. Phys. Rev. Lett., 109:203006, Nov 2012.

[263] A. del Campo, J. Goold, and M. Paternostro. More bang for your buck: Super-adiabatic quantum engines. Scientific Reports, 4(1):6208, 2014.

[264] A. Alecce, F. Galve, N. Lo Gullo, L. Dell'Anna, F. Plastina, and R. Zambrini. Quantum otto cycle with inner friction: finite-time and disorder effects. New Journal of Physics, 17(7):075007, jul 2015.

[265] B. Leggio and M. Antezza. Otto engine beyond its standard quantum limit. Phys. Rev. E, 93:022122, Feb 2016.

[266] B. Karimi and J. P. Pekola. Otto refrigerator based on a superconducting qubit: Classical and quantum performance. Phys. Rev. B, 94:184503, Nov 2016.

[267] R. Kosloff and Y. Rezek. The quantum harmonic otto cycle. Entropy, 19(4):136, Mar 2017.

[268] G. Watanabe, B. P. Venkatesh, P. Talkner, and A. del Campo. Quantum performance of thermal machines over many cycles. Phys. Rev. Lett., 118:050601, Feb 2017.

[269] M. Campisi and R. Fazio. The power of a critical heat engine. Nature Communications, 7:11895, Jun 2016.

[270] A. Solfanelli, M. Falsetti, and M. Campisi. Nonadiabatic single-qubit quantum otto engine.

[271] J.-M. Park, S. Lee, H.-M. Chun, and J. D. Noh. Quantum mechanical bound for efficiency of quantum otto heat engine. Phys. Rev. E, 100:012148, Jul 2019.

[272] R. Gallego, A. Riera, and J. Eisert. Thermal machines beyond the weak coupling regime. New Journal of Physics, 16(12):125009, dec 2014.

[273] S. Vinjanampathy and J. Anders. Quantum thermodynamics. Contemporary Physics, 57(4):545–579, 2016.

[274] T. D. Kieu. The second law, maxwell's demon, and work derivable from quantum heat engines. Phys. Rev. Lett., 93:140403, Sep 2004.

[275] R. Uzdin, A. Levy, and R. Kosloff. Equivalence of quantum heat machines, and quantum-thermodynamic signatures. Phys. Rev. X, 5:031044, Sep 2015.

[276] Kay Brandner, Keiji Saito, and Udo Seifert. Thermodynamics of micro- and nano-systems driven by periodic temperature variations. Phys. Rev. X, 5:031019, Aug 2015.

[277] J. O. González, J. P. Palao, D. Alonso, and L. A. Correa. Classical emulation of quantum-coherent thermal machines. Phys. Rev. E, 99:062102, Jun 2019.

[278] Francesco Campaioli, Felix A. Pollock, Felix C. Binder, Lucas Céleri, John Goold, Sai Vinjanampathy, and Kavan Modi. Enhancing the charging power of quantum batteries. Phys. Rev. Lett., 118:150601, Apr 2017.

[279] Felipe Barra. Dissipative charging of a quantum battery. Phys. Rev. Lett., 122:210601, May 2019.

[280] V. Cavina, A. Mari, and V. Giovannetti. Slow dynamics and thermodynamics of open quantum systems. Phys. Rev. Lett., 119:050601, Aug 2017.

[281] K. Brandner and K. Saito. Thermodynamic geometry of microscopic heat engines.

[282] Y. Aharonov and D. Bohm. Significance of electromagnetic potentials in the quantum theory. Phys. Rev., 115:485–491, Aug 1959.

[283] M. V. Berry. Quantal phase factors accompanying adiabatic changes. Proc. R. Soc. Lond. A, 392:392, Mar 1984.

[284] P. W. Brouwer. Scattering approach to parametric pumping. Phys. Rev. B, 58:R10135–R10138, Oct 1998.

[285] T. A. Shutenko, I. L. Aleiner, and B. L. Altshuler. Mesoscopic fluctuations of adiabatic charge pumping in quantum dots. Phys. Rev. B, 61:10366–10375, Apr 2000.

[286] J. E. Avron, A. Elgart, G. M. Graf, and L. Sadun. Optimal quantum pumps. Phys. Rev. Lett., 87:236601, Nov 2001.

[287] H. L. Calvo, L. Classen, J. Splettstoesser, and M. R. Wegewijs. Interaction-induced charge and spin pumping through a quantum dot at finite bias. Phys. Rev. B, 86:245308, Dec 2012.

[288] M. Hasegawa and T. Kato. Temperature-driven and electrochemical-potential-driven adiabatic pumping via a quantum dot. Journal of the Physical Society of Japan, 86(2):024710, 2017.

[289] M. Hasegawa and T. Kato. Effect of interaction on reservoir-parameter-driven adiabatic charge pumping via a single-level quantum dot system. Journal of the Physical Society of Japan, 87(4):044709, 2018.

[290] Jie Ren, Peter Hänggi, and Baowen Li. Berry-phase-induced heat pumping and its impact on the fluctuation theorem. Phys. Rev. Lett., 104:170601, Apr 2010.

[291] M. V. Berry and P. Shukla. High-order classical adiabatic reaction forces: slow manifold for a spin model. Journal of Physics A: Mathematical and Theoretical, 43(4):045102, jan 2010.

[292] M. Campisi, P. Talkner, and P. Hänggi. Fluctuation theorem for arbitrary open quantum systems. Phys. Rev. Lett., 102:210401, May 2009.

[293] N. Bode, S. V. Kusminskiy, R. Egger, and F. von Oppen. Scattering theory of current-induced forces in mesoscopic systems. Phys. Rev. Lett., 107:036804, Jul 2011.

[294] N. Bode, S. V. Kusminskiy, R. Egger, and F. von Oppen. Current-induced forces in mesoscopic systems: A scattering-matrix approach. Beilstein J. Nanotechnol., 3:144–162, Feb 2012.

[295] Mark Thomas, Torsten Karzig, Silvia Viola Kusminskiy, Gergely Zaránd, and Felix von Oppen. Scattering theory of adiabatic reaction forces due to out-of-equilibrium quantum environments. Phys. Rev. B, 86:195419, Nov 2012.

[296] L. J. Fernández-Alcázar, R. A. Bustos-Marún, and H. M. Pastawski. Decoherence in current induced forces: Application to adiabatic quantum motors. Phys. Rev. B, 92:075406, Aug 2015.

[297] H. L. Calvo, F. D. Ribetto, and R. A. Bustos-Marún. Real-time diagrammatic approach to current-induced forces: Application to quantum-dot based nanomotors. Phys. Rev. B, 96:165309, Oct 2017.

[298] L. J. Fernández-Alcázar, H. M. Pastawski, and R. A. Bustos-Marún. Nonequilibrium current-induced forces caused by quantum localization: Anderson adiabatic quantum motors. Phys. Rev. B, 99:045403, Jan 2019.

[299] P. Terrén Alonso, J. Romero, and L. Arrachea. Work exchange, geometric magnetization, and fluctuation-dissipation relations in a quantum dot under adiabatic magnetoelectric driving. Phys. Rev. B, 99:115424, Mar 2019.

[300] M. Berry and J. Robbins. Chaotic classical and half-classical adiabatic reactions: Geometric magnetism and deterministic friction. Proceedings of The Royal Society A: Mathematical, Physical and Engineering Sciences, 442:659–672, 09 1993.

[301] M. Campisi, S. Denisov, and P. Hänggi. Geometric magnetism in open quantum systems. Phys. Rev. A, 86:032114, Sep 2012.

[302] J. Thingna, P. Hänggi, R. Fazio, and M. Campisi. Geometric quantum pumping in the presence of dissipation. Phys. Rev. B, 90:094517, Sep 2014.

[303] A. T. Rezakhani, W.-J. Kuo, A. Hamma, D. A. Lidar, and P. Zanardi. Quantum adiabatic brachistochrone. Phys. Rev. Lett., 103:080502, Aug 2009.

[304] D. A. Sivak and G. E. Crooks. Thermodynamic metrics and optimal paths. Phys. Rev. Lett., 108:190602, May 2012.

[305] S. Deffner and E. Lutz. Nonequilibrium entropy production for open quantum systems. Phys. Rev. Lett., 107:140404, Sep 2011.

[306] M. Scandi and M. Perarnau-Llobet. Thermodynamic length in open quantum systems. Quantum, 3:197, October 2019.

[307] H. J. D. Miller, M. Scandi, J. Anders, and M. Perarnau-Llobet. Work fluctuations in slow processes: Quantum signatures and optimal control. Phys. Rev. Lett., 123:230603, Dec 2019.

[308] P. Abiuso and M. Perarnau-Llobet. Optimal cycles for low-dissipation heat engines.

[309] M. Tomka, T. Souza, S. Rosenberg, and A. Polkovnikov. Geodesic paths for quantum many-body systems.

[310] P. Weinberg, M. Bukov, L. D'Alessio, A. Polkovnikov, S. Vajna, and M. Kolodrubetz. Adiabatic perturbation theory and geometry of periodically-driven systems. Physics Reports, 688:1, May 2017.

[311] M. Kolodrubetz, V. Gritsev, and A. Polkovnikov. Classifying and measuring geometry of a quantum ground state manifold. Phys. Rev. B, 88:064304, Aug 2013.

[312] Jan Carl Budich and Sebastian Diehl. Topology of density matrices. Phys. Rev. B, 91:165140, Apr 2015.

[313] Charles-Edouard Bardyn, Lukas Wawer, Alexander Altland, Michael Fleischhauer, and Sebastian Diehl. Probing the topology of density matrices. Phys. Rev. X, 8:011035, Feb 2018.

[314] L. Arrachea, M. Moskalets, and L. Martin-Moreno. Heat production and energy balance in nanoscale engines driven by time-dependent fields. Phys. Rev. B, 75:245420, Jun 2007.

[315] D. J. Thouless. Quantization of particle transport. Phys. Rev. B, 27:6083–6087, May 1983.

[316] J. Avron, D. Osadchy, and R. Seiler. A topological look at the quantum hall effect. Physics Today, 56:38, 2003.

[317] D. Xiao, M.-C. Chang, and Q. Niu. Berry phase effects on electronic properties. Rev. Mod. Phys., 82:1959–2007, Jul 2010.

[318] M. Moskalets and M. Büttiker. Floquet scattering theory for current and heat noise in large amplitude adiabatic pumps. Phys. Rev. B, 70:245305, Dec 2004.

[319] R. Bustos-Marún, G. Refael, and F. von Oppen. Adiabatic quantum motors. Phys. Rev. Lett., 111:060802, Aug 2013.

[320] L. Arrachea and F. von Oppen. Nanomagnet coupled to quantum spin hall edge: An adiabatic quantum motor. Physica E: Low-dimensional Systems and Nanostructures, 74:596 – 602, 2015.

[321] L. J. Fernández-Alcázar, H. M. Pastawski, and R. A. Bustos-Marún. Dynamics and decoherence in nonideal thouless quantum motors. Phys. Rev. B, 95:155410, Apr 2017.

[322] M. F. Ludovico and M. Capone. Enhanced performance of a quantum-dot-based nanomotor due to coulomb interactions. Phys. Rev. B, 98:235409, Dec 2018.

[323] A. Bruch, S. V. Kusminskiy, G. Refael, and F. von Oppen. Interacting adiabatic quantum motor. Phys. Rev. B, 97:195411, May 2018.

[324] A. O. Caldeira and A. J. Leggett. Quantum tunnelling in a dissipative system. Annals of Physics, 149(2):374 – 456, 1983.

[325] A. J. Leggett, S. Chakravarty, A. T. Dorsey, M. P. A. Fisher, A. Garg, and W. Zwerger. Dynamics of the dissipative two-state system. Rev. Mod. Phys., 59:1–85, Jan 1987.

[326] Robert S. Whitney and Yuval Gefen. Berry phase in a nonisolated system. Phys. Rev. Lett., 90:190402, May 2003.

[327] Robert S. Whitney, Yuriy Makhlin, Alexander Shnirman, and Yuval Gefen. Geometric nature of the environment-induced berry phase and geometric dephasing. Phys. Rev. Lett., 94:070407, Feb 2005.

[328] G. De Chiara and G. M. Palma. Berry phase for a spin 1/2 particle in a classical fluctuating field. Phys. Rev. Lett., 91:090404, Aug 2003.

[329] D. Segal and A. Nitzan. Molecular heat pump. Phys. Rev. E, 73:026109, Feb 2006.

[330] Fernando C. Lombardo and Paula I. Villar. Correction to the geometric phase by structured environments: The onset of non-markovian effects. Phys. Rev. A, 91:042111, Apr 2015.

[331] R. Schmidt, M. F. Carusela, J. P. Pekola, S. Suomela, and J. Ankerhold. Work and heat for two-level systems in dissipative environments: Strong driving and non-markovian dynamics. Phys. Rev. B, 91:224303, Jun 2015.

[332] Junjie Liu, Hui Xu, Baowen Li, and Changqin Wu. Energy transfer in the nonequilibrium spin-boson model: From weak to strong coupling. Phys. Rev. E, 96:012135, Jul 2017.

[333] C. Wang, X.-M. Chen, K.-W. Sun, and J. Ren. Heat amplification and negative differential thermal conductance in a strongly coupled nonequilibrium spin-boson system. Phys. Rev. A, 97:052112, May 2018.

[334] T. Yamamoto, M. Kato, T. Kato, and K. Saito. Heat transport via a local two-state system near thermal equilibrium. New Journal of Physics, 20(9):093014, sep 2018.

[335] D. Newman, F. Mintert, and A. Nazir. A quantum limit to non-equilibrium heat engine performance imposed by strong system-reservoir coupling.

[336] R. P. Riwar and J. Splettstoesser. Charge and spin pumping through a double quantum dot. Phys. Rev. B, 82:205308, Nov 2010.

[337] X.-L. Qi, T. L. Hughes, and S.-C. Zhang. Fractional charge and quantized current in the quantum spin hall state. Nature Physics, 4(4):273–276, 2008.

[338] N. Bode, L. Arrachea, G. S. Lozano, T. S. Nunner, and F. von Oppen. Current-induced switching in transport through anisotropic magnetic molecules. Phys. Rev. B, 85:115440, Mar 2012.

[339] Q. Meng, S. Vishveshwara, and T. L. Hughes. Spin-transfer torque and electric current in helical edge states in quantum spin hall devices. Phys. Rev. B, 90:205403, Nov 2014.

[340] María Florencia Ludovico, Francesca Battista, Felix von Oppen, and Liliana Arrachea. Adiabatic response and quantum thermoelectrics for ac-driven quantum systems. Phys. Rev. B, 93:075136, Feb 2016.

[341] J. Ren, P. Hänggi, and B. Li. Berry-phase-induced heat pumping and its impact on the fluctuation theorem. Phys. Rev. Lett., 104:170601, Apr 2010.

[342] Patrick R. Zulkowski and Michael R. DeWeese. Optimal protocols for slowly driven quantum systems. Phys. Rev. E, 92:032113, Sep 2015.

[343] Bibek Bhandari, Pablo Terrén Alonso, Fabio Taddei, Felix von Oppen, Rosario Fazio, and Liliana Arrachea. Geometric properties of adiabatic quantum thermal machines. arXiv preprint arXiv:2002.02225, 2020.

[344] Michele Campisi, Peter Talkner, and Peter Hänggi. Fluctuation theorem for arbitrary open quantum systems. Phys. Rev. Lett., 102:210401, May 2009.

[345] Jürgen König, Herbert Schoeller, and Gerd Schön. Zero-bias anomalies and boson-assisted tunneling through quantum dots. Phys. Rev. Lett., 76:1715–1718, Mar 1996.

[346] Jürgen König, Jörg Schmid, Herbert Schoeller, and Gerd Schön. Resonant tunneling through ultrasmall quantum dots: Zero-bias anomalies, magnetic-field dependence, and boson-assisted transport. Phys. Rev. B, 54:16820–16837, Dec 1996.

[347] G. Lindblad. On the generators of quantum dynamical semigroups. Comm. Math. Phys., 48(2):119–130, 1976.

[348] Roie Dann, Amikam Levy, and Ronnie Kosloff. Time-dependent markovian quantum master equation. Phys. Rev. A, 98:052129, Nov 2018.

[349] Esteban A. Martinez and Juan Pablo Paz. Dynamics and thermodynamics of linear quantum open systems. Phys. Rev. Lett., 110:130406, Mar 2013.

[350] Nahuel Freitas and Juan Pablo Paz. Analytic solution for heat flow through a general harmonic network. Phys. Rev. E, 90:042128, Oct 2014.

[351] Inbal Oz, Hod Oded, and Abraham Nitzan. Evaluation of dynamical properties of open quantum systems using the driven liouville-von neumann approach: methodological considerations. Molecular Physics, 117:2083, Mar 2019.

[352] Gregory Bulnes Cuetara, Massimiliano Esposito, and Gernot Schaller. Quantum thermodynamics with degenerate eigenstate coherences. Entropy, 18(12):447, 2016.

[353] Juzar Thingna, Felipe Barra, and Massimiliano Esposito. Kinetics and thermodynamics of a driven open quantum system. Phys. Rev. E, 96:052132, Nov 2017.

[354] Philipp Strasberg, Gernot Schaller, Tobias Brandes, and Christopher Jarzynski. Second laws for an information driven current through a spin valve. Phys. Rev. E, 90:062107, Dec 2014.

[355] Herbert Schoeller and Gerd Schön. Mesoscopic quantum transport: Resonant tunneling in the presence of a strong coulomb interaction. Phys. Rev. B, 50:18436–18452, Dec 1994.

[356] R. B. Saptsov and M. R. Wegewijs. Fermionic superoperators for zero-temperature nonlinear transport: Real-time perturbation theory and renormalization group for anderson quantum dots. Phys. Rev. B, 86:235432, Dec 2012.

[357] R. B. Saptsov and M. R. Wegewijs. Time-dependent quantum transport: Causal superfermions, exact fermion-parity protected decay modes, and pauli exclusion principle for mixed quantum states. Phys. Rev. B, 90:045407, Jul 2014.

[358] CNRPC Caroli, Ro Combescot, Ph Nozieres, and D Saint-James. Direct calculation of the tunneling current. Journal of Physics C: Solid State Physics, 4(8):916, 1971.

[359] Horacio M. Pastawski. Classical and quantum transport from generalized landauer-büttiker equations. ii. time-dependent resonant tunneling. Phys. Rev. B, 46:4053–4070, Aug 1992.

[360] Antti-Pekka Jauho, Ned S. Wingreen, and Yigal Meir. Time-dependent transport in interacting and noninteracting resonant-tunneling systems. Phys. Rev. B, 50:5528–5544, Aug 1994.

[361] Liliana Arrachea. Green-function approach to transport phenomena in quantum pumps. Phys. Rev. B, 72:125349, Sep 2005.

[362] Liliana Arrachea and Michael Moskalets. Relation between scattering-matrix and keldysh formalisms for quantum transport driven by time-periodic fields. Phys. Rev. B, 74:245322, Dec 2006.

[363] J. Rammer and H. Smith. Quantum field-theoretical methods in transport theory of metals. Rev. Mod. Phys., 58:323–359, Apr 1986.

[364] Janine Splettstoesser, Michele Governale, Jürgen König, and Rosario Fazio. Adiabatic pumping through a quantum dot with coulomb interactions: A perturbation expansion in the tunnel coupling. Phys. Rev. B, 74:085305, Aug 2006.

[365] Liliana Arrachea, Eduardo R. Mucciolo, Claudio Chamon, and Rodrigo B. Capaz. Microscopic model of a phononic refrigerator. Phys. Rev. B, 86:125424, Sep 2012.

[366] Liliana Arrachea, Gustavo S. Lozano, and A. A. Aligia. Thermal transport in one-dimensional spin heterostructures. Phys. Rev. B, 80:014425, Jul 2009.

[367] Gianluca Stefanucci and Carl-Olof Almbladh. Time-dependent partition-free approach in resonant tunneling systems. Phys. Rev. B, 69:195318, May 2004.

[368] J. M. Luttinger. Theory of thermal transport coefficients. Phys. Rev., 135:A1505–A1514, Sep 1964.

[369] G. Tatara. Thermal vector potential theory of transport induced by a temperature gradient. Phys. Rev. Lett., 114:196601, May 2015.

[370] Doron Cohen. Quantum pumping in closed systems, adiabatic transport, and the kubo formula. Phys. Rev. B, 68:155303, Oct 2003.

[371] M. R. Wegewijs and Yu. V. Nazarov. Resonant tunneling through linear arrays of quantum dots. Phys. Rev. B, 60:14318–14327, Nov 1999.

[372] H. Sprekeler, G. Kießlich, A. Wacker, and E. Schöll. Coulomb effects in tunneling through a quantum dot stack. Phys. Rev. B, 69:125328, Mar 2004.

[373] W. Mao, P. Coleman, C. Hooley, and D. Langreth. Spin dynamics from majorana fermions. Phys. Rev. Lett., 91:207203, Nov 2003.